

Precision Measurement of the Proton Electric to Magnetic Form Factor Ratio with BLAST

by

Christopher Blair Crawford

Submitted to the Department of Physics
in partial fulfillment of the requirements for the degree of

Doctor of Philosophy in Physics

at the

MASSACHUSETTS INSTITUTE OF TECHNOLOGY

May 2005

© Massachusetts Institute of Technology 2005. All rights reserved.

Author
Department of Physics
May 19, 2005

Certified by
Haiyan Gao
Associate Professor of Physics
Thesis Supervisor

Accepted by
Thomas J. Greytak
Chairman, Department Committee on Graduate Students

Precision Measurement of the Proton Electric to Magnetic Form Factor Ratio with BLAST

by

Christopher Blair Crawford

Submitted to the Department of Physics
on May 19, 2005, in partial fulfillment of the
requirements for the degree of
Doctor of Philosophy in Physics

Abstract

We have measured G_E^p/G_M^p at $Q^2 = 0.15\text{--}0.65$ (GeV/c)² in the South Hall Ring of the MIT-Bates Linear Accelerator Facility. This experiment used a polarized electron beam, a pure hydrogen internal polarized target, and the symmetric Bates Large Acceptance Spectrometer Toroid (BLAST) detector. By measuring the spin-dependent elastic $\vec{H}(\vec{e}, e'p)$ asymmetry in both sectors simultaneously, we could extract the form factor ratio independent of beam and target polarization. This was the first experiment to measure G_E^p/G_M^p using a polarized target, which is complementary to recoil polarimetry experiments.

Thesis Supervisor: Haiyan Gao
Title: Associate Professor of Physics

Acknowledgments

I would like to express gratitude to my advisor, Haiyan Gao, for giving me interesting, challenging problems to work on, and making sure that I had the resources to be successful in my endeavors. She has been a strong advocate, and her optimistic attitude has motivated me to improve. I also thank my thesis committee members, Bob Redwine and Ernie Moniz, for their thoughtful comments and suggestions. I acknowledge Professors Ricardo Alarcon, Bill Bertozzi, John Calarco, Haiyan Gao, June Matthews, Richard Milner, and Bob Redwine for their vital role in the development and guidance of the BLAST physics program. This work was supported by a grant from the U.S. Department of Energy.

I was very privileged to work on this experiment with the exceptionally talented and friendly staff at Bates Linear Accelerator Center and MIT including Taylan Akdogan, Tancredi Botto, Karen Dow, Manouch Farkhondeh, Bill Franklin, Doug Hasell, Ernie Ihloff, Jim Kelsey, Michael Kohl, Hauke Kolster, Tim Smith, Stan Sobczynski, Chris Tschalar, Genya Tsentalovich, Bill Turichnetz, Townsend Zwart, the accelerator operators, and radiation protection officers. They were always willing to go out of their way to help me with problems. Their creative ideas, stimulating conversations, and encouragement have helped to make Bates a wonderful learning environment that I will remember with fondness. The engineers and technicians at Bates did an outstanding job designing and building the BLAST detector, solving problems with the experiment, and keeping it running smoothly. Thanks to Ernie Bisson for maintaining our computers, for his immediate response and quick solutions when anything went wrong.

I would like to acknowledge the tireless efforts of my fellow graduate students working on BLAST: Ben Clasie, Adam Degrush, Tavi Filoti, Eugene Geis, Pete Karpnius, Aaron Maschinot, Nikolas Meitanis, Jason Seely, Adrian Sindile, Yuan Xiao, Chi Zhang, and Vitaliy Ziskin. Each person made major contributions to the experiment, and spent countless hours on shift commissioning the detector and taking production data. I learned a lot by working together with Chi Zhang and Tim Smith on the

BLAST reconstruction software and benefited from many enlightening conversations with them.

Thanks to Vitaliy Ziskin, Aaron Maschinot, Ben Clasie, Jason Seely, Taylan Akdogan, Akihisa Shinozaki, Tim Smith, Haiyan Gao, John Calarco, and Joy Gurrie for contributing figures in this thesis, and to Karen Dow and Haiyan Gao, Michael Kohl for the many helpful comments while reviewing it.

Thanks to Ernie Ihloff for bringing me up to speed in construction of the laser-driven target, for helping with the many problems we faced with the target, and for his helpful advice in general. Michael Grossman machined most of the custom components of the target, always promptly and accommodating last minute changes. George Sechen provided valuable assistance in the lab. Our research group, Tim Black, Ben Clasie, Jason Seely, Dipankar Dutta, Feng Xiong, and Wang Xu made valuable contributions to the target. Ben and Jason took over the target and made dramatic improvements to get the high figure of merit quoted herein. Thanks, Ben and Jason, for being such good friends, and for all you have done for me.

I feel the deepest gratitude for my wife Kimberly, for her unwavering support and faith in me during our extended time in graduate school. She has given me the strength and encouragement I needed to complete this work. Thanks, Curtis, Nicole, and Elizabeth, for being understanding while I have been away for such long hours finishing this thesis. Curtis has inspired me by writing his own book at the same time I was writing. I thank our parents for their encouragement and support. This has truly been an accomplishment of our whole family, and I could not have done it without them.

Contents

1	Physics Overview	17
1.1	Formalism	20
1.1.1	Kinematics	22
1.1.2	Form Factors	24
1.1.3	Dynamics	26
1.2	Existing Data	28
1.2.1	Rosenbluth Separation	29
1.2.2	Proton RMS Radius	30
1.2.3	Higher Q^2 Unpolarized Data	33
1.2.4	Polarized Data	36
1.2.5	Global Analysis	38
1.2.6	Two-photon Contribution	42
1.3	Theoretical Descriptions of the Nucleon Form Factors	47
1.3.1	Perturbative QCD	48
1.3.2	Constituent Quark Models	48
1.3.3	VMD Models	51
1.3.4	Lattice QCD	53
1.4	Current Experiment	56
1.4.1	Experimental Overview	56
1.4.2	Physics Impact	57
2	Experimental Setup	59
2.1	Polarized Beam	59

2.1.1	Polarized Source	59
2.1.2	Storage Ring	60
2.1.3	Compton Polarimeter	64
2.2	Polarized Targets	66
2.2.1	Atomic Beam Source	68
2.2.2	Laser Driven Source	73
2.3	The BLAST Detector Package	86
2.3.1	BLAST Toroid	91
2.3.2	Drift Chambers	93
2.3.3	TOF Scintillators	98
2.3.4	Čerenkov Detectors	102
2.4	Electronics and Software	104
2.4.1	Trigger	104
2.4.2	Data Acquisition	106
2.4.3	Online Monitor	108
2.4.4	Reconstruction Library	109
3	Data Analysis	113
3.1	Event Selection	114
3.1.1	Elastic TOF Cuts	115
3.1.2	Elastic WC Cuts	116
3.1.3	Q^2 Determination	119
3.1.4	Yields	119
3.1.5	Luminosity	121
3.2	Asymmetry	123
3.2.1	Raw Asymmetry	125
3.2.2	Background Correction	128
3.2.3	Radiative Correction	129
3.3	Form Factor Ratio	130
3.3.1	Single Asymmetry Extraction	131

3.3.2	Super-ratio Extraction	133
3.3.3	Global Fit Extraction	134
3.4	Systematic Errors	135
3.4.1	Drift Chamber Q^2 Determination	136
3.4.2	TOF Q^2 Determination	137
3.4.3	Target Spin Angle	139
3.4.4	Monte Carlo Simulation	140
3.4.5	Binning and Cuts	143
3.4.6	False Asymmetry	143
3.4.7	Pion Contamination	147
4	Results and Discussion	149
4.1	Form Factor Ratio	149
4.2	Individual Form Factors	151
4.3	Discussion of Errors	156
4.4	Outlook	157
A	Linear Calibrations	161
A.1	Least Squares Fit	161
A.1.1	Generalizations of the Linear Fit	163
A.1.2	Minimum χ^2 from a Least Squares Fit	166
A.2	TOF Scintillator Offsets	168
A.2.1	Cosmic Coincidences	169
A.2.2	Elastic Coplanarity	172
A.3	Drift Chamber Time-to-Distance Function	173
A.3.1	Garfield Simulation	173
A.3.2	Iterative Relaxation Method	174
A.3.3	Least Squares Linear Calibration	175
B	Cross Section Data	181

List of Figures

1-1	Diagrams of the lowest-order ep scattering amplitudes.	21
1-2	Kinematics of the polarized elastic scattering OPE amplitude.	22
1-3	The ep -helicity asymmetry for different target spin angles.	28
1-4	The G_E and G_M world unpolarized data.	31
1-5	The first measurement of the $\vec{H}(\vec{e}, e'p)$ asymmetry.	37
1-6	The $\mu G_E/G_M$ world data on the proton.	39
1-7	Phenomenological fits to the $\mu G_E/G_M$ world data.	42
1-8	Scaling of the Dirac and Pauli form factors at large Q^2	49
1-9	Diagram of the Vector Meson Dominance (VMD) amplitude.	51
1-10	Models of $\mu G_E/G_M$ based on dispersion theory and VMD.	54
2-1	Plan of the BATES Linear Accelerator Center.	61
2-2	Yield and asymmetry results of the Compton polarimeter.	64
2-3	Time-dependence of the beam polarization.	65
2-4	Compton measurements in conjunction with the spin flipper.	66
2-5	Schematic of the Bates Atomic Beam Source (ABS).	69
2-6	Polarization-dependent simulation of the ABS magnetic optics.	70
2-7	Hyperfine structure of hydrogen and deuterium.	71
2-8	Optical pumping cycle with an intermediary alkali species.	74
2-9	Optical pumping of the potassium D1 line.	75
2-10	Laser-Driven Source (LDS) Schematic.	76
2-11	LDS Components.	80
2-12	Spin-cell, oven, and vacuum seal mount to the chamber.	81

2-13	Stand-alone dissociator performance.	82
2-14	Drawing of the complete LDS apparatus.	85
2-15	Temperature dependence of LDS dissociation.	87
2-16	Laser wavelength scan of the potassium D1 resonance.	87
2-17	The BLAST detector package.	90
2-18	Magnetic field map of BLAST.	92
2-19	Steps of track reconstruction from hits in the drift chambers.	96
2-20	An application of the Newton-Rhapson method to track fitting.	97
2-21	Drift chamber tracking efficiency.	98
2-22	Timing vs. coplanarity for TOF paddle L9B.	101
2-23	TOF efficiency.	102
2-24	Schematic of the trigger logic.	105
2-25	Integration of online display (NSED) with ROOT analysis package.	109
3-1	TOF scintillator timing and coplanarity cuts.	116
3-2	Drift chamber offsets and cuts based on redundant track parameters.	118
3-3	Invariant mass (W) and missing mass squared (M_X^2) spectra.	119
3-4	Yield for each run normalized by charge.	120
3-5	The normalized yield in each Q^2 bin.	121
3-6	Pressure in the UGBS as a function of time.	123
3-7	Comparison of the ABS yield with a Monte Carlo (MC) simulation.	124
3-8	Raw experimental asymmetries in each sector.	126
3-9	Comparison of three methods of extracting $\mu G_E/G_M$	130
3-10	Single-asymmetry extraction of $\mu G_E/G_M$	132
3-11	Extraction of the target spin angle from a fit of A_L and A_R	133
3-12	The P and β -dependence of the χ^2 fit function.	136
3-13	Discrepancy in Q^2 between electron and proton kinematics.	138
3-14	Comparison of Q^2 from the TOFs and the drift chambers.	139
3-15	Analysis of Monte Carlo data.	142
3-16	Asymmetry and form factor ratio analyzed in fine bins.	144

3-17	Analysis of data divided into six sequential run periods.	145
3-18	Beam and target single spin asymmetries.	146
3-19	Pion yields as a function of M_X^2 and W	147
4-1	BLAST results of $\mu G_E/G_M$ based on Q_{WC}^2	150
4-2	Rosenbluth separation of G_E and G_M constrained by $R = G_E/G_M$. . .	153
4-3	BLAST extraction of G_E and G_M from the world unpolarized data. . .	154
4-4	Recent results of G_E^n from polarization experiments.	155
4-5	BLAST results of $\mu G_E/G_M$ based on TOF corrections to Q_{WC}^2	158
A-1	Robust fit by separation of slope and offset	165
A-2	Timing peaks of cosmic coincidences in each paddle combination. . .	171
A-3	Widths and residuals of cosmic coincidence timing peaks.	172
A-4	Garfield simulation of time-to-distance function.	174
A-5	Hyperbolic parametrization of the time-to-distance function.	176
A-6	Stub types used in linear calibration of the T2D function.	177
A-7	Fit to the vertex of a stub crossing the wire.	178
A-8	Test of the hyperbolic T2D functions.	179

List of Tables

2.1	South Hall Ring (SHR) specifications.	62
2.2	Comparison of the ABS and LDS targets.	68
2.3	Optimal spin-cell parameters.	78
2.4	Figure of merit (FOM) results from the MIT-LDS target.	88
2.5	BLAST coil specifications.	91
2.6	Drift chamber specifications.	94
2.7	Time-of-flight (TOF) scintillator specifications.	100
2.8	Čerenkov detector specifications.	103
2.9	Left and right sector Memory Lookup Unit (MLU) trigger logic.	107
2.10	Cross sector Memory Lookup Unit (MLU) trigger logic.	107
2.11	Summary of physics triggers.	107
2.12	ROOT functionality used in the BlastLib2 reconstruction library.	110
2.13	BlastLib2 reconstruction library classes.	111
3.1	Conditions of the three BLAST hydrogen run periods.	114
3.2	Integrated beam current, yields, and asymmetries.	127
3.3	Radiative corrections for three cut-off parameters.	129
3.4	Values for $\mu G_E/G_M$ from each method of extraction.	131
3.5	Systematic uncertainties of $\mu G_E/G_M$	137
3.6	Effect of δQ^2 on the form factor ratio uncertainty.	140
3.7	Summary target spin angle (β) measurements.	141
4.1	Extraction of G_E and G_M from world unpolarized data.	155

A.1	Statistical measures of central tendency.	164
B.1	World data used for the extraction of G_E and G_M	181

Chapter 1

Physics Overview

Although the atomic constituents, the electron and nucleons, are all spin $\frac{1}{2}$ particles of charge $-e$, $+e$, and 0 , they are fundamentally different. In the standard model, the electron is a point Dirac particle which interacts electromagnetically by exchanging virtual photons, as described by Quantum Electrodynamics (QED). The weak coupling to the photon, $\alpha \approx 1/137$, guarantees that interaction amplitudes can be calculated perturbatively. As a result, QED is very well understood and has been tested to 3 ppb [1] in experiments like the hydrogen Lamb shift.

In contrast, the proton is 1836 times more massive than the electron and has internal structure, first observed through its anomalous magnetic moment. In a simplistic picture, it is composed of three bound valence quarks which interact through Quantum Chromodynamics (QCD) by the exchange of virtual gluons. Unlike QED, the coupling to gluons $\alpha_S \approx 1$ is strong and increases as the energy decreases. In fact, the gluons interact among themselves further enhancing the nonperturbative nature of QCD. Quarks and gluons cannot exist in isolation, but only in bound states as mesons and baryons, a property known as confinement.

Due to confinement, the proton and neutron are the only stable hadronic states. But even in a simplistic picture, these states have the complex structure of three valence quarks mediating gluons in a sea of quark-antiquark pairs and gluon loops. The valence quarks only account for a small part of the proton's spin and charge distributions. The strong coupling of QCD at low energy prevents perturbative expansions as

done in QED, and no exact analytic solution of QCD is known, so the nonlinear field equations must be solved numerically on a discrete lattice of space-time. Thus, the very force responsible for complex structure of the nucleon eludes our understanding of it.

But a detailed understanding of the nucleon is essential. The nucleon form factors provide a stringent test of QCD in the nonperturbative region which has not been experimentally verified to the same extent as the asymptotically free high energy region. The low energy region is important for the structure of baryons and mesons, and also for the nucleon-nucleon potential, which is used to calculate the properties of nuclei. Finally, precision data on the proton are important for physics input to other atomic and nuclear processes such as the QED calculation of the hydrogen Lamb shift and parity violating (PV) experiments on the proton.

Experimentally, electron scattering is a very clean probe of the structure of the nucleon. The electromagnetic interaction is well known and is sufficiently weak that the interaction is dominated by the one-photon-exchange (OPE) amplitude. While the QCD details of the proton structure are not well understood, the ep cross section can be parametrized by only two structure functions of the proton in the OPE approximation. For elastic scattering these are the form factors G_E and G_M , which are functions of a single variable, the momentum transfer squared Q^2 of the virtual photon. Electron scattering experiments have had a rich history over the past half century, progressing from measurements of the charge radius of the proton to a detailed mapping of the elastic form factors over a wide range of Q^2 . Inelastic scattering has been used to measure the properties of nucleon resonances and culminated in experimental evidence of the partonic (quark and gluon) structure of the nucleon in Deep Inelastic Scattering (DIS).

In the last two decades, advances in the technology of intense polarized beams, polarized targets, and polarimetry have ushered a new generation of electron scattering experiments relying on spin degrees of freedom. Although these experiments measure the same nucleon form factors as unpolarized experiments, they have several distinct advantages over traditional cross section measurements. First, they have increased

sensitivity to small effects by observing the interference between a large amplitude and the small amplitude of interest. For example, the polarized cross section for ep -scattering contains a mixed term proportional to $G_E G_M$, which is absent in the unpolarized cross section. Second, spin-dependent experiments involve the measurement of polarizations or helicity asymmetries, both of which are independent of the cross section normalization. To first order, this eliminates the effect of luminosity, acceptance, and detector efficiency. Other systematics such as beam and target polarization or polarimeter analyzing power can be canceled by measuring a ratio of polarization observables.

The form factors $G_E(Q^2)$ and $G_M(Q^2)$ can be extracted from the elastic ep cross section at fixed Q^2 by observing the change in the cross section as a function of other kinematic variables. The unpolarized elastic cross section depends on only two parameters: the beam energy and electron scattering angle, which must both be varied under the constraint of fixed Q^2 to extract G_E and G_M . But variation of the beam energy is problematic, both in determining the energy-dependent spectrometer acceptance, and accounting for variations in the cross section, which can be several orders of magnitude. At high Q^2 the unpolarized cross section is dominated by the magnetic contribution, making the extraction of G_E difficult; at low Q^2 it is dominated by the electric part, making the extraction of G_M difficult. In contrast, polarized experiments have the leverage of spin degrees of freedom which can be varied instead of beam energy, avoiding difficulties of the latter. The longitudinal and transverse terms of the polarized cross section containing $G_E G_M$ and G_M^2 , respectively, can be completely isolated by tuning the target spin orientation or by observing the corresponding component of the recoil polarization. Also note that the deuteron, a spin-1 particle, has three elastic form factors, two of which can only be extracted from spin observables in conjunction with the unpolarized cross section.

Recent measurements of the form factor ratio $\mu G_E/G_M$ using recoil polarimetry at Jefferson Lab (JLab) [2, 3], which are of higher precision than the corresponding unpolarized extractions, deviated dramatically from the unpolarized data. This has prompted intense theoretical and experimental activity to resolve the discrepancy.

The validity of analyzing data in the OPE approximation has been questioned, and higher order amplitudes are now thought to have greater significance. Even if the polarized data are more reliable than the unpolarized data, the discrepancy must be understood in order to extract G_E and G_M individually. If higher order corrections are significant, they must be applied to all electron nuclear scattering cross sections.

Toward this resolution, the first double helicity asymmetry measurement of the of the proton form factor ratio has been conducted in the South Hall Ring (SHR) of the MIT-Bates Linear Accelerator Center. The experiment used an intense polarized stored electron beam, an internal polarized gas target, and the Bates Large Angle Spectrometer Toroid (BLAST) detector package. The experiment takes advantages of many unique features of this setup to minimize systematic errors. Furthermore, the systematic errors are different from those of recoil polarization experiments. Thus it is an important cross check of recoil polarimetry. The results from this experiment are presented herein.

1.1 Formalism

The utility of electron scattering lies in the ability to separate the interaction mechanism from the underlying hadronic structure. The latter, represented by form factors, is the ideal meeting point between experiment and theory. Consider the non-relativistic scattering of plane waves from an extended charge distribution $\rho(\mathbf{x})$ with electrostatic potential $\phi(\mathbf{x})$, where $\rho = -\nabla^2\phi$. The cross section is proportional to the square of the transition amplitude

$$\langle \mathbf{k}' | \mathcal{H} | \mathbf{k} \rangle = \int d^3\mathbf{x} e^{-i(\mathbf{k}-\mathbf{k}')\cdot\mathbf{x}} \nabla^{-2}\rho(\mathbf{x}) = \frac{F(\mathbf{q}^2)}{\mathbf{q}^2}, \quad (1.1)$$

where $\mathbf{q} = \mathbf{k} - \mathbf{k}'$ is the three-momentum transfer and $\nabla^{-2}\rho$ is the solution of $\rho = -\nabla^2\phi$. The form factor

$$F(\mathbf{q}^2) \equiv \int d^3\mathbf{x} e^{-i\mathbf{q}\cdot\mathbf{x}} \rho(\mathbf{x}) = 1 - \frac{1}{6}\langle r^2 \rangle \mathbf{q}^2 + \mathcal{O}(\mathbf{q}^4) \quad (1.2)$$

is the Fourier transform of $\rho(\mathbf{x})$ normalized such that $F(0) = \int d^3\mathbf{x}\rho = 1$. The Taylor expansion in Eq. 1.2 relates the root-mean square (RMS) charge radius $r_p = \sqrt{\langle r^2 \rangle}$ to the slope of $F(\mathbf{q}^2)$ at $\mathbf{q}^2 = 0$.

The proton is a spin- $\frac{1}{2}$ particle and therefore has two independent form factors, G_E and G_M , representing the charge and magnetic distributions. They are defined in terms of the nucleon transition current in Sec. 1.1.2. Given that the hydrogen nucleus is a single proton, the formalism for extracting G_E and G_M from the elastic $H(e, e'p)$ cross section is straightforward. The lowest order amplitudes of the QED perturbative expansion of the ep -cross section are shown in Fig. 1-1. The form factors are defined in Sec. 1.1.2 in terms of the nucleon current of the OPE amplitude (a). In an electron scattering experiment, one needs to take into account radiative corrections in addition to the OPE. The electron radiative corrections of the next four amplitudes (b)–(e) are model-independent and can be calculated exactly in terms of G_E and G_M . The proton radiative corrections (f)–(h) are suppressed by the mass of the proton, and the two-photon box (i) and cross (j) amplitudes are suppressed by α^2 . However, the model-dependent amplitudes are now being actively re-investigated in an attempt to reconcile the form factor ratio extraction between polarized and unpolarized data.

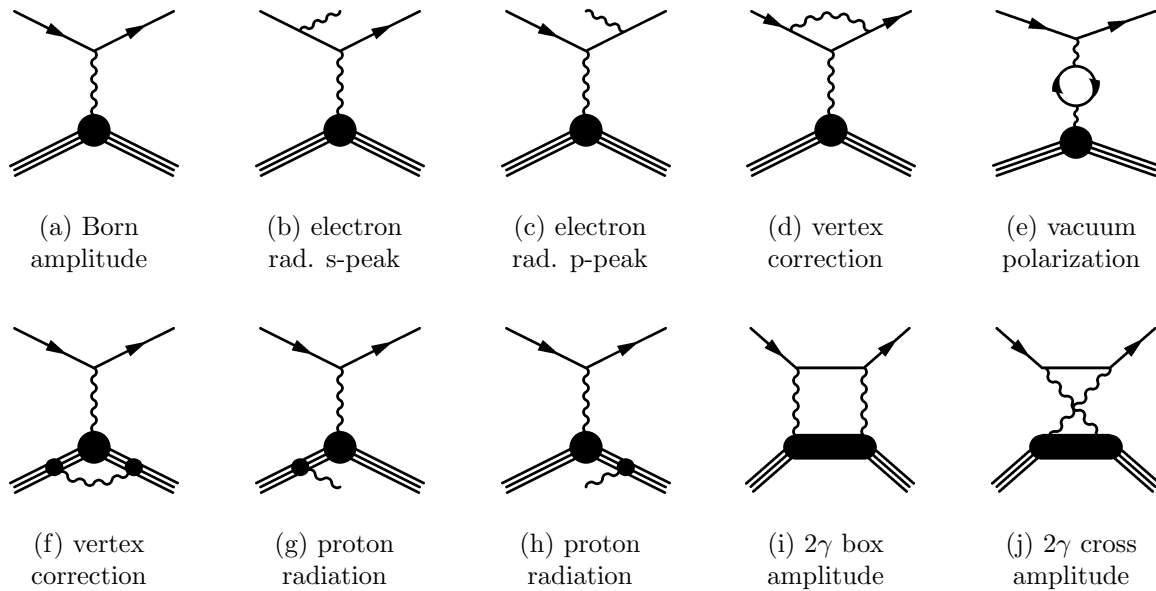


Figure 1-1: Diagrams of the lowest-order ep scattering amplitudes.

1.1.1 Kinematics

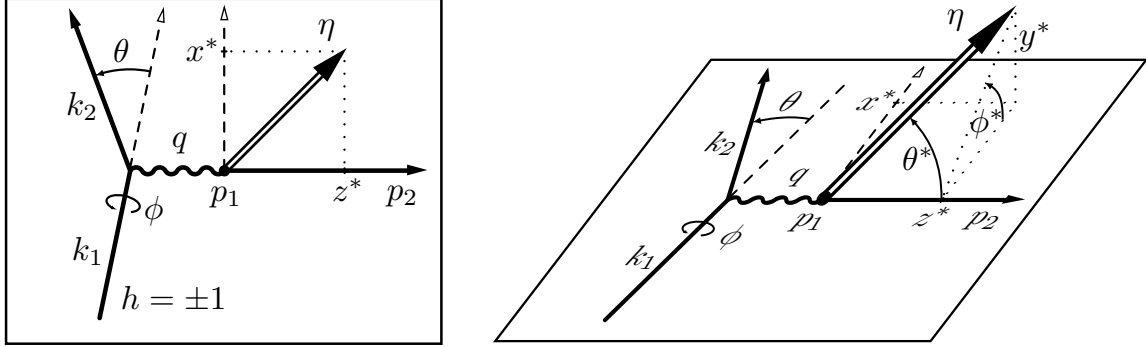


Figure 1-2: Kinematics for the polarized elastic scattering OPE amplitude in the scattering plane (left), and in three dimensions (right). The polar angles (θ^* , ϕ^*) and components (x^* , y^* , z^*) of the target polarization vector η are also shown.

The kinematics for the Born one-photon exchange (OPE) amplitude are illustrated in Fig 1-2. All variables are in the laboratory frame in units where $\hbar = c = 1$, and $g_{00} = \epsilon_{0123} = 1$. In the extreme relativistic limit (ERL), the incident electron with momentum $k_1 = (E, E\hat{z})$ is scattered in the direction $\Omega = (\theta, \phi)$ with momentum $k_2 = (E', E'\hat{\Omega})$. The virtual photon transfers its 4-momentum $q \equiv k_1 - k_2 = (\nu, \mathbf{q})$ to the target proton, initially at rest $p_1 = (M, \mathbf{0})$, where M is the proton mass. Unpolarized elastic scattering has three degrees of freedom: E , θ , and ϕ . At a fixed beam energy E , the cross section is azimuthally symmetric and is a function of a single variable, which may be taken as θ , E' , ν , $|\mathbf{q}^2|$, or more commonly, the space-like Lorentz-invariant 4-momentum transfer squared

$$Q^2 \equiv -q^2 = \mathbf{q}^2 - \nu^2 = 4EE' \sin^2 \frac{\theta}{2} > 0. \quad (1.3)$$

The elastically recoiling proton has momentum $p_2 = (M+\nu, \mathbf{q})$. From conservation of momentum on the proton vertex, $q^2 = -2p_1 \cdot q$,

$$Q^2 = 2M\nu \quad \text{and} \quad E' = \frac{E}{1 + \frac{2E}{M} \sin^2 \frac{\theta}{2}}, \quad (1.4)$$

or in terms of the dimensionless quantity $\tau \equiv Q^2/4M^2$,

$$v^2 = \tau Q^2 \quad \text{and} \quad \mathbf{q}^2 = (1 + \tau)Q^2. \quad (1.5)$$

The longitudinal polarization of the virtual photon is

$$\epsilon = \left(1 + 2(1 + \tau) \tan^2 \frac{\theta}{2}\right)^{-1}. \quad (1.6)$$

We also define $K \equiv k_1 + k_2$ and $P \equiv p_1 + p_2$, and note that $K \cdot q = P \cdot q = 0$.

The polarized cross section has additional spin degrees of freedom. We only consider longitudinally polarized electrons with helicity $h = \pm 1$, which is equal to the helicity of the scattered electron in the ERL. The target polarization vector $\eta = (0, \hat{\boldsymbol{\eta}})$ is most conveniently represented in the coordinate system of the scattering plane (x^*, y^*, z^*) , where z^* is in the direction of \mathbf{q} , y^* is in the direction of $\mathbf{k}_1 \times \mathbf{k}_2$, perpendicular to the scattering plane, and x^* is in the scattering plane, perpendicular to z^* , forming a right-handed system. The spin orientation in the polar coordinates is (θ^*, ϕ^*) , where

$$x^* = \sin \theta^* \cos \phi^*, \quad y^* = \sin \theta^* \sin \phi^*, \quad \text{and} \quad z^* = \cos \theta^*. \quad (1.7)$$

The spin of the recoil proton is fixed by conservation of angular momentum. In the Born approximation, the cross section vanishes for a target polarized along y^* (Sec. 1.2.6). In the laboratory, the target polarization angle β is defined with respect to the beam in the scattering plane and positive in the left sector (Sec. 2.3).

The radiative kinematics of Fig. 1-1 (c) and (d) have three additional degrees of freedom for the outgoing momentum \mathbf{k} of the radiated photon. Consequently, the experimental determination of Q^2 from the leptonic vertex $Q_l^2 = -(k_1 - k_2)^2$ differs with that from the hadronic vertex $Q_h^2 = t = -(p_2 - p_1)^2$. In the following we use the leptonic vertex for our analysis, $Q^2 \equiv Q_l^2$. The photon 3-momentum \mathbf{k} is parametrized by the inelasticity $v = (k + p_2)^2 - M^2 = 2k \cdot p_2$, the projection of the photon momentum along q , $\tau_k = k \cdot q / q \cdot p_1$, and the azimuthal angle ϕ_k . The elastic

condition $Q^2 = 2M\nu$ becomes $Q^2 + v = 2M\nu$. In terms of these variables, the photon phase space is [4]

$$\int \frac{d^3k}{2k_0} = \int_0^{v_m} \frac{dv}{4\sqrt{\lambda_q}} \int_{\tau_{min}}^{\tau_{max}} \frac{d\tau_k v}{(1 + \tau_k)^2} \int_0^{2\pi} d\phi_k \quad (1.8)$$

with limits

$$v_m = \frac{\sqrt{\lambda_s}\sqrt{\lambda_m} - 2m^2Q^2 - Q^2S}{2m^2} \approx S - Q^2 - \frac{M^2Q^2}{S}, \quad (1.9)$$

$$\tau_{min}^{max} = \frac{v + Q^2 \pm \sqrt{\lambda_q}}{2M^2}, \quad (1.10)$$

where

$$\lambda_q = S_x^2 + 4M^2Q^2, \quad \lambda_s = S^2 - 4m^2M^2, \quad \lambda_m = Q^2(Q^2 + 4M^2). \quad (1.11)$$

In terms of $R = 2k_1 \cdot p_1 = 2Mk$ (used interchangeably with v), $R\tau_k = 2k \cdot q$. The Lorentz invariants $S = 2k_1 \cdot p_1$ and $X = 2k_2 \cdot p_2$ are the same as those of the OPE amplitude, and $S_x \equiv S - X = Q^2 + v$.

1.1.2 Form Factors

The Born invariant amplitude contains the transition currents of the electron j^μ and proton J^ν joined by the photon propagator $g^{\mu\nu}/q^2$,

$$\mathcal{M} = j_\mu \frac{1}{q^2} J^\mu, \quad \text{where} \quad j^\mu = -e \bar{u}_{k_2} \gamma^\mu u_{k_1}, \quad J^\mu = e \bar{u}_{p_2} \Gamma^\mu u_{p_1}, \quad (1.12)$$

and $u = (\sqrt{E+M}, \boldsymbol{\sigma} \cdot \mathbf{p} / \sqrt{E+M})^T \chi$. Here, $\boldsymbol{\sigma}$ are the Pauli matrices, and χ a two-component spinor. The electron has pure Dirac coupling, while the proton vertex is parametrized by the most general non-parity-violating, Lorentz-invariant conserved current,

$$\Gamma^\mu = F_1 \gamma^\mu + \frac{\kappa}{2M} F_2 i \sigma^{\mu\nu} q_\nu. \quad (1.13)$$

The Dirac form factor $F_1(Q^2)$ describes an extended Dirac particle of which the spin is preserved in the ERL. The Pauli form factor F_2 accounts for the anomalous magnetic moment of the proton $\kappa = \mu - 1$ associated with a spin flip.

While F_1 and F_2 are preferred in Vector Meson Dominance (VMD) models (Sec. 1.3.3) and in describing the perturbative QCD high Q^2 limit of proton structure (Sec. 1.3.1), the Sachs form factors

$$G_E = F_1 - \tau \kappa F_2 \quad \text{and} \quad G_M = F_1 + \kappa F_2 \quad (1.14)$$

are a more natural description of the nucleon current densities and their coupling to the virtual photon. Using the Gordon decomposition $\Gamma = \gamma G_M + \kappa F_2 P/2M$ in the Breit frame, defined by $P_B \equiv p_1 + p_2 = (2E_B, \mathbf{0})$ so that $\nu_B = 0$,

$$\Gamma_B^\mu = \gamma^\mu G_M + \delta_0^\mu \frac{M}{E_B} (G_E - G_M), \quad (1.15)$$

$$J_B = e \chi_{p_2}^\dagger (2M G_E, i\boldsymbol{\sigma} \times \mathbf{q} G_M) \chi_{p_1}. \quad (1.16)$$

Thus the proton transition current $J_B(Q^2)$ in the Breit frame corresponds to the charge and magnetic moment distributions in the proton [5]. The Sachs form factors G_E and G_M are the $C0$ and $M1$ multipole form factors [6] which couple to longitudinal and transverse polarization of virtual photon respectively. Accordingly, they normalize to the charge and magnetic moments of the proton, $G_E(0) = 1$ and $G_M(0) = \mu$ in units of e and μ_N , respectively. In contrast to the Dirac and Pauli form factors, the cross term $G_E G_M$ vanishes in the unpolarized cross section.

Although the transition current takes on such a simple form in the Breit frame, the Sachs form factors cannot be rigorously identified as Fourier transforms of spatial charge and magnetization densities in the proton because the Breit frame varies with Q^2 . However, at $Q^2 \ll M^2$ the energy transfer is negligible and the identification of $G_E(Q^2)$ with the Fourier transform of the charge distribution is valid. Thus the charge and magnetic radius of the proton can still be extracted from the derivative of G_E and G_M at $Q^2 = 0$. Kelly [7] has investigated the use of relativistic inversion

to extract spatial densities from the form factors at higher Q^2 .

1.1.3 Dynamics

The unpolarized elastic $p(e, e')p$ cross section was first derived by Rosenbluth [8], who used an effective charge $e'(q^2)$ and an effective anomalous magnetic moment $\mu'(q^2)$ for F_1 and $(1 + \kappa)F_2$, respectively. Dombey [9] and Alkezier [10] did early calculations of the polarized cross section, which is also given in [11, 6, 4]. From Eq. 1.12, the Born cross section factorizes into leptonic and hadronic tensors

$$\frac{d\sigma}{d\Omega} = \frac{\sigma_M}{L_M^2} L_{\mu\nu} W^{\mu\nu}, \quad \text{where} \quad \sigma_M = \frac{\alpha^2 \cos^2 \frac{\theta}{2}}{4E^2 \sin^4 \frac{\theta}{2}} \frac{E'}{E} \quad (1.17)$$

is the Mott (non-structure) cross section including the recoil factor with corresponding $L_M^2 = L_{\mu\nu}^M L_M^{\mu\nu} = 16M^2 E E' \cos^2 \frac{\theta}{2}$. The leptonic and hadronic tensors are

$$L^{\mu\nu} = \sum_{h'} j^{\mu*} j^\nu = \left(2k_1^{(\mu} k_2^{\nu)} + q^2 g^{\mu\nu} \right) - ih \left[\epsilon^{\mu\nu}{}_{\alpha\beta} k_1^\alpha k_2^\beta \right], \quad (1.18)$$

$$W^{\mu\nu} = \sum_{\eta'} J^{\mu*} J^\nu = \left(G_M^2 L_p^{\mu\nu} + \kappa F_2 (2F_1 - (1-\tau)\kappa F_2) P^\mu P^\nu \right) - i\eta_\alpha \left[2MG_M^2 \epsilon^{\mu\nu\alpha\beta} q_\beta - \frac{1}{M} \kappa F_2 G_M \epsilon^{\mu\alpha\beta[\gamma} P^{\nu]} q_\beta p_{1\gamma} \right], \quad (1.19)$$

where $a^{(\alpha\beta)} \equiv a^\alpha b^\beta + a^\beta b^\alpha$, $a^{[\alpha\beta]} \equiv a^\alpha b^\beta - a^\beta b^\alpha$, $L_p^{\mu\nu} = 2p_1^{(\mu} p_2^{\nu)} + q^2 g^{\mu\nu}$, and $\epsilon^{\alpha\beta\gamma\delta}$ is the completely antisymmetric tensor.

Both tensors have symmetric (in μ, ν) unpolarized terms and antisymmetric polarized terms. Therefore in the Born approximation, $\frac{d\sigma}{d\Omega} = \Sigma + h\Delta$, there are no single-spin asymmetries. The polarized cross section is proportional to the product $P=P_b P_t$ of beam and target polarizations and changes sign with either electron or target spin reversal. From the four different combinations of beam and target spin configuration, one may extract the polarized and unpolarized cross sections and two independent false asymmetries.

The unpolarized part of the cross section is

$$\Sigma = \sigma_M \left[(F_1^2 + \tau(\kappa F_2)^2) + 2\tau(F_1 + \kappa F_2)^2 \tan^2 \frac{\theta}{2} \right] \quad (1.20)$$

$$= \sigma_M \left(\frac{G_E^2 + \tau G_M^2}{1 + \tau} + 2\tau G_M^2 \tan^2 \frac{\theta}{2} \right) \quad (1.21)$$

$$= \sigma_M \frac{\tau G_M^2 + \epsilon G_E^2}{\epsilon(1 + \tau)}, \quad (1.22)$$

The transverse and longitudinal response functions are G_M^2 and G_E^2 , and ϵ is the longitudinal polarization of the virtual photon. The polarized cross section is

$$\Delta = -\sigma_M v_p \frac{p_1}{M} \cdot (Kq G_M^2 + (PK - Kq) G_E G_M) \cdot \boldsymbol{\eta} \quad (1.23)$$

$$= \sigma_M v_p \left(K^0 \mathbf{q} G_M^2 + \frac{1}{\nu} \mathbf{q} \times (\mathbf{K} \times \mathbf{q}) G_E G_M \right) \cdot \boldsymbol{\eta} \quad (1.24)$$

$$= \sigma_M \left(v_z z^* G_M^2 + v_x x^* G_E G_M \right), \quad (1.25)$$

where

$$\begin{aligned} v_p &= -\tan^2 \frac{\theta}{2} / [2M^2(1 + \tau)], \\ v_z &= v_p K^0 |\mathbf{q}| = -2\tau \tan \frac{\theta}{2} \sqrt{\frac{1}{1+\tau} + \tan^2 \frac{\theta}{2}}, \\ v_x &= v_p 2M |\mathbf{K}| (1 + \tau) = -2 \tan \frac{\theta}{2} \sqrt{\frac{\tau}{1+\tau}}, \end{aligned} \quad (1.26)$$

and z^* and x^* are the longitudinal and transverse components of the target spin unit vector with respect to \mathbf{q} in the scattering plane. The asymmetry is zero for the normal component (y^*). This formula is consistent with Donnelly and Raskin [6] except their response functions lack the factor $\mathbf{q}^2/Q^2 = 1 + \tau$, which is the exact correction to a relativistic approximation used throughout their derivation, following the method of Carlson and Gross [11]. Afanasev *et al.* [4, Eqs. 9–13,17–21] use a simpler form for the hadronic tensor which gives the same cross section.

The physics asymmetry is

$$A \equiv \frac{\sigma_+ - \sigma_-}{\sigma_+ + \sigma_-} = \frac{\Delta}{\Sigma} = \frac{v_z z^* G_M^2 + v_x x^* G_E G_M}{(\tau G_M^2 + \epsilon G_E^2) / [\epsilon(1 + \tau)]} \quad (1.27)$$

where σ_h is indexed by the beam helicity $h = \pm 1$, and $\sigma_+(-\eta) = \sigma_- (+\eta)$. Figure 1-3 shows the asymmetry as a function of θ and the target spin angle β using the Höhler form factor parametrization [12] as input. The asymmetry goes from 0 at $\theta = 0^\circ$ (purely longitudinal) to 100% at $\theta = 180^\circ$, confirming that the spin of the electron is preserved in the ERL.

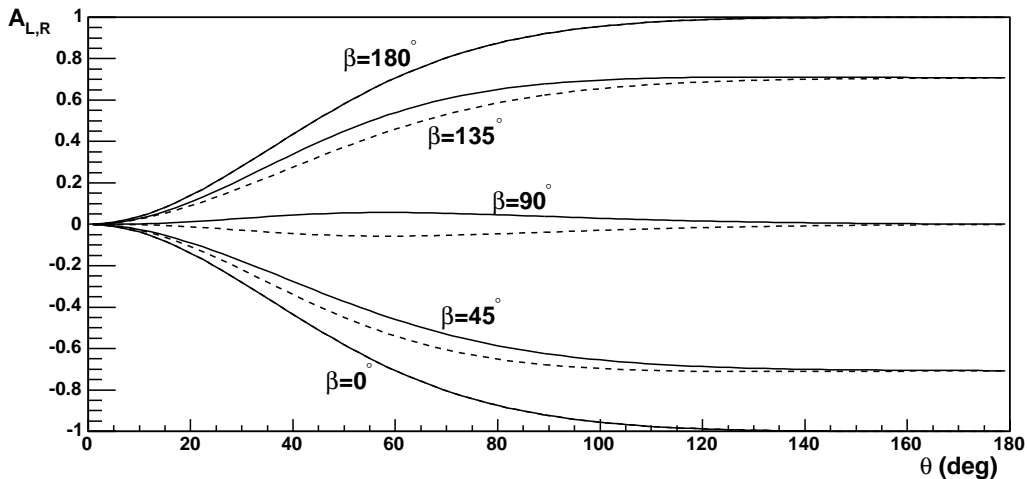


Figure 1-3: The ep -helicity asymmetry for an electron scattering into the left sector (A_L , solid curve) and right sector (A_R , dashed curve) of BLAST, shown for five different spin angles (β). By symmetry, $A_L = A_R$ at $\beta = 0^\circ, 180^\circ$; and $A_L(\beta) = -A_R(180^\circ - \beta)$ so that $A_L = -A_R$, at $\beta = 90^\circ$. A_L and A_R are most different from each other at $\beta \approx 45^\circ$ or 135°

1.2 Existing Data

The first hint of structure in the nucleon came in 1932 from the experiments of Stern [13] using the same molecular beam method used to separate the spin states of silver atoms a decade earlier. Passing H_2 and HD molecules through a gradient magnetic field for angular momentum dispersion, he measured the magnetic moment of the proton to be $\mu_p \approx 2.5 \pm 10\%$ in units of $\mu_N = e\hbar/2M$, close to the present value $\mu_p = 2.792847351(28)$ [14]. The anomalous magnetic moment $\kappa = \mu - 1 = 1.79$ is larger than the Dirac moment μ_N , the contribution from a point-like spin- $\frac{1}{2}$ particle. Twenty years later, electron scattering experiments by Hofstadter *et al.* [15] at Stanford confirmed the extended structure of the proton as a distribution of electric charge and magnetic moment. These experiments using unpolarized electrons and protons were refined and extended to higher Q^2 . Higher energy resonances of the nucleon such as the $\Delta(1232)$ and the $N(1440)$, were discovered by inelastic electron scattering experiments. In the deep inelastic region $Q^2 \rightarrow \infty$ at finite $x \equiv Q^2/2M\nu$, Friedman, Kendall, Taylor, *et al.* [16] discovered that the cross section scaled as a

function of the momentum fraction of the struck parton x , independent of Q^2 . This confirmed the partonic structure of the nucleon and the existence of quarks.

In the last decade, a new generation of polarization experiments have measured $\mu G_E/G_M$ to higher precision; however the results are in conflict with the unpolarized data. There has been a considerable effort to reconcile these two sets of data. This section provides a summary of the different experiments used to measure the form factors of the proton.

1.2.1 Rosenbluth Separation

The standard method of extracting $G_E(Q^2)$ and $G_M(Q^2)$ from the unpolarized elastic $p(e, e')$ cross section is by a Rosenbluth separation. At a given Q^2 , the cross section must be measured at different kinematics in order to separate G_E from G_M . The only other parameter to vary is the beam energy E . In terms of the Dirac and Pauli form factors F_1 and F_2 , the cross section of Eq. 1.20 has the form $aF_1^2 + bF_1F_2 + cF_2^2$. Early extractions were done using the “ellipse method,” by plotting the elliptical constraints on F_1 and F_2 of cross section measurements at different energies. The form factors F_1 and F_2 were extracted from the intersection of all ellipses, although the same result could have been obtained algebraically.

A practical advantage of the Sachs form factors G_E and G_M is the disappearance of this cross term. The reduced cross section

$$\frac{d\sigma}{d\Omega} \frac{\epsilon(1+\tau)}{\sigma_M} \equiv \sigma_R = \tau G_M^2 + \epsilon G_E^2 \quad (1.28)$$

is linear in ϵ , so τG_M and G_E are the intercept and slope, respectively, of σ_R as a function of ϵ . Early separations also fit reduced cross sections as a function of $\tan^2(\frac{\theta}{2})$ or $\cot^2(\frac{\theta}{2})$, which are also linear. Assuming that G_E and G_M are of the same order of magnitude, the factor $\tau = Q^2/4M^2$ implies that the reduced cross section is dominated by G_E at low Q^2 and by G_M at high Q^2 , making Rosenbluth separations difficult at these extremes. This is reflected in the unpolarized data.

Initial measurements of the Dirac and Pauli form factors performed at the Stanford

Linear Accelerator by Hofstadter [15] confirmed the extended structure of the proton. Their results of both F_1 and F_2 were consistent with dipole form factors, which correspond to exponential charge and magnetic distributions,

$$\rho(r) = e^{-r/r_0}, \quad (1.29)$$

each with an RMS radius of 0.75 fm. Subsequent separations of G_E and G_M [17, 18, 19] confirmed the dipole form

$$G_E(Q^2) = \frac{1}{\mu} G_M(Q^2) = G_D(Q^2) \equiv \frac{1}{(1 + Q^2/\Lambda^2)^2}, \quad (1.30)$$

with $\Lambda^2 = 0.71 (\text{GeV}/c)^2$. Usually G_E and G_M are quoted in units of G_D . The world unpolarized data of G_E and G_M , normalized to G_D are shown in Fig. 1-4

1.2.2 Proton RMS Radius

An early physics goal of elastic scattering since the first measurements of Hofstadter was to determine the RMS charge radius r_p of the proton. This is a fundamental static property of the nucleon as is its magnetic moment. It is also an important physics input into the QED calculation of the hydrogen Lamb Shift, a precision test of QED. The importance of r_p is further discussed in [20].

The ideal method of extracting r_p from unpolarized data is to do a Rosenbluth separation of G_E and G_M , and fit for the slope of G_E at $Q^2 = 0$ to get r_p . However because the cross section is dominated by G_E at low Q^2 , one must make the assumption that $\mu G_E/G_M \approx 1$. Also, r_p is determined strictly by the behavior of G_E near $Q^2 = 0$ regardless of the shape of form factors at higher Q^2 , and the slope must be measured at $Q^2 \ll (\hbar c/r_p)^2 \approx 0.05 (\text{GeV}/c)^2$, well below any structure due to the shape of the proton. From the dipole form factor, $r_p = \sqrt{12/\Lambda^2} = 0.811$ fm, a little short of the currently accepted value of $r_p = 0.8750(68)$ fm [14].

Early unpolarized data were taken mostly at low Q^2 and were sensitive to r_p . Hand *et al.* [21] reanalyzed the results of eight early experiments at $Q^2 < 1.8 (\text{GeV}/c)^2$

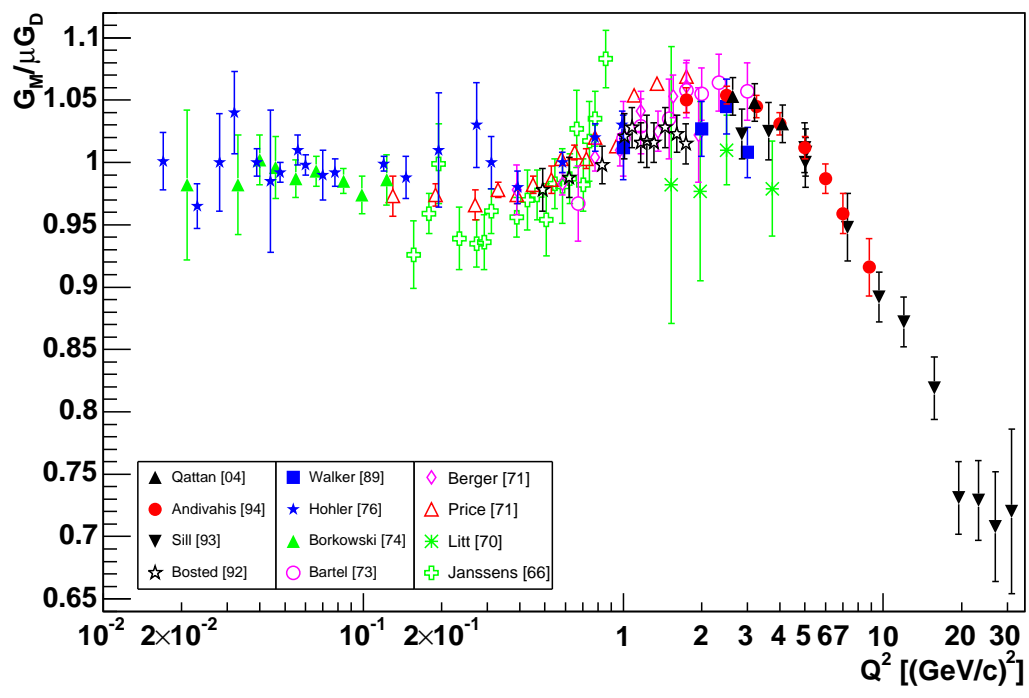
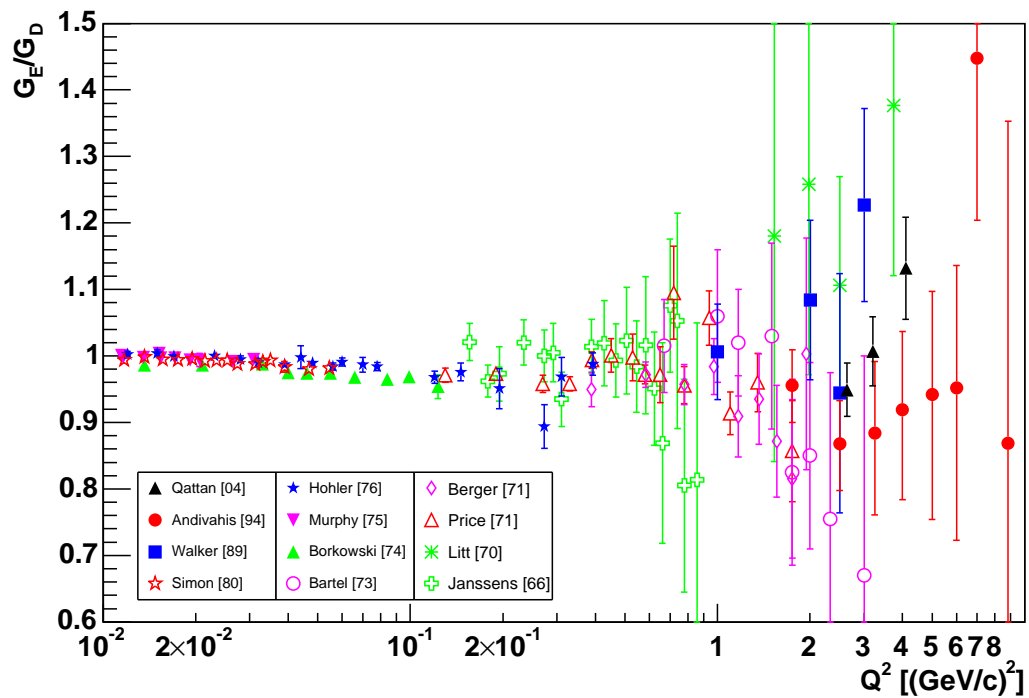


Figure 1-4: The G_E and G_M world unpolarized data.

by interpolating all cross section data in clusters of Q^2 to a single point and performing Rosenbluth separations. They fit the $Q^2 < 3 \text{ fm}^{-2}$ data to the quadratic form $G_E^p = 1 - \frac{1}{6}\langle r^2 \rangle Q^2 + A Q^4$, to obtain the RMS radius of the proton $r_p = 0.805 \pm 0.011 \text{ fm}$, in agreement with the standard dipole form factor. They also noted that the data on G_M were consistent with the dipole form with $\Lambda^2 = 18.5 \text{ fm}^{-2} = 0.72 (\text{GeV}/c)^2$, which yields the same magnetic radius.

An independent L-T separation by Murphy *et al.* [22] at the Saskatoon Linear Accelerator at $Q^2 = 0.15\text{--}0.8 \text{ fm}^{-2}$ obtained similar results $r_p = 0.810 \pm 0.040 \text{ fm}$. The cross sections were measured by detecting the proton, which had the advantage of easier collimation, smaller background signals, and a smaller radiative correction. However, higher precision data taken about the same time at Mainz [23, 24] at low Q^2 yielded r_p about 10% higher than the fit of Hand.

In response to these discrepancies, Simon *et al.* [25] performed another experiment at Mainz at Q^2 up to 1.4 fm^{-2} using a pressurized gas target to limit the normalization uncertainty to 0.5%, significantly smaller than previous experiments. They reanalyzed the data up to $Q^2 < 2 \text{ fm}^{-2}$ from the experiments at Saskatoon, Mainz, and Orsay, and obtained the much larger value of $r_p = 0.862 \pm 0.012 \text{ fm}$. Gao [26] showed that the discrepancy between Simon and Hand could be explained by the different range of Q^2 used in each fit. Specifically, a refit of the Hand data set restricted to $Q^2 < 2 \text{ fm}^{-2}$ yielded $r_p = 0.868 \pm 0.105 \text{ fm}$, in agreement with Simon. This indicates that the two analyses are consistent with each other and illustrates the sensitivity of the extraction to data at low Q^2 . It also shows how restricting the Q^2 range severely affects the error in r_p both from lost data, and from smaller leverage to constrain the slope. It is clearly desirable to be able to fit a larger Q^2 region in a model-independent manner.

Mergell [27] did a dispersion analysis of the form factors following the method of Höhler [12], which resulted in the slightly lower value $r_p = 0.847 \text{ fm}$. This analysis included information from πN scattering amplitudes and pion form factors (see Sec. 1.3.3). Sick [28] did a reanalysis of world data fitting the world data below $Q^2 = 4 \text{ fm}^{-2}$ to a continued fraction, but not refitting the acceptance normalization for each experiment. He quoted $r_p = 0.895 \pm 0.018 \text{ fm}$, in good agreement with the

most recent atomic physics extraction [20]. His analysis included Coulomb distortion effects, arising from multiple soft photons transferred along with the hard virtual photon of momentum transfer q . This effect was shown to increase the radius by about 0.01 fm. The current standard accepted value of the proton RMS radius, influenced by these fits, is $r_p = 0.8750(68)$ fm [14].

There are new proposals for precision measurements of r_p . RpEX, [26] the sister experiment of this experiment was proposed to measure both the form factor ratio and relative cross section at 22 points between $0.13 < Q^2 < 2.26 \text{ fm}^{-2}$. These would be used in conjunction with polarization data measured in the same range to extract $G_E(Q^2)$, normalized by $G_E(0) = 1$. The proposal projected an increase in the precision of r_p by a factor of 3, compared to the combined world data.

Another experiment, Exp. R-98-003 [29], is being carried out at the Paul Scherrer Institute (PSI) to measure the 2S Lamb shift from muonic hydrogen (μp). The muon is more massive than the electron, and its wave function has more overlap with the proton. Therefore, the muonic Lamb shift is more sensitive to the proton radius, and the extraction of r_p has a projected uncertainty of 0.1%, a factor of 20 increase in precision.

1.2.3 Higher Q^2 Unpolarized Data

Subsequent unpolarized experiments focused on extending the measurements of G_E and G_M to higher Q^2 and higher precision, with higher beam energy and more sophisticated detectors. Two physics motivations of these experiments were: a) the investigation whether $\mu G_E/G_M \approx 1$ scaling continues to higher Q^2 , and b) the asymptotic dependence of F_1 and F_2 as predicted by perturbative QCD.

Some dedicated L-T separation experiments measured cross sections at many values of ϵ for each Q^2 point, while other data were taken simply as calibration measurements for other electron scattering experiments. For data at $Q^2 > 10 (\text{GeV}/c)^2$, the electric contribution to the cross section is so small that G_M could be extracted without performing a Rosenbluth separation. Other experiments assumed scaling ($G_E = G_M/\mu$) to extract G_E and G_M . Some experiments combined their data with

earlier experiments in order to perform separations. Thus although some experiments can be presented as independent measurements, a more meaningful picture comes from global analyses such as those of Walker *et al.* [30] and Arrington [31]. The following is a description of the data used in those references.

Two experiments carried out at the Cambridge Electron Accelerator (CEA), one by Goitein *et al.* [32] at forward angles, and the other by Price *et al.* [18] at backward angles, were combined to extract G_E and G_M at $Q^2 = 7\text{--}45 \text{ fm}^{-2}$, in the same range as the analysis of Hand [21]. From the $d(e, e'p)$ data of Hanson [33], the ratio of the deuteron quasielastic to proton elastic cross section was 0.80–0.95 depending on Q^2 .

An independent L-T separation was performed at the 2.5 (GeV/c) Bonn synchrotron by Berger *et al.* [34] in approximately the same Q^2 range. They measured cross sections at multiple energies for each Q^2 value, most notably 15 energies at $Q^2 = 0.58 \text{ (GeV/c)}^2$, and found good linear dependence. They reported $\mu G_E/G_M$ to drop significantly below 1.

Another independent L-T separation was also done at DESY by Bartel *et al.* [35] at $Q^2 = 0.67\text{--}3.0 \text{ (GeV/c)}^2$. Cross sections were taken with one spectrometer at forward angles and the other one at 86° . These data also showed a significant drop in $\mu G_E/G_M$. In addition, the proton was detected at forward angles for some Q^2 values. This was also compared with $d(e, e'p)$ to show that deuteron binding effects in the quasielastic cross section were small. Earlier experiments at DESY [36, 17, 37] measured cross section data up to $Q^2 = 9 \text{ (GeV/c)}^2$, but at only a single beam energy.

The bulk of the proton unpolarized cross section data has come from SLAC. Janssens *et al.* [38] did an extensive set of L-T separations in the range $Q^2 = 4\text{--}30 \text{ fm}^{-2}$ using the 1 (GeV/c) spectrometer. Litt *et al.* [39] also did independent L-T separations at higher Q^2 values ($1.0\text{--}3.75 \text{ (GeV/c)}^2$), and the results were consistent with scaling ($\mu G_E/G_M \approx 1$). In the same experiment, Kirk *et al.* [19] measured G_M to $Q^2 = 25 \text{ (GeV/c)}^2$ under the assumption of continued scaling ($\mu G_E/G_M \approx 1$).

There are four other cross section sets with insufficient data for independent L-T separations. Stein *et al.* [40] measured the cross section at $Q^2 = 0.1\text{--}1.8 \text{ (GeV/c)}^2$ with beam energy up to 20 GeV as part of a comprehensive DIS program with a 20 GeV

electron spectrometer fixed at $\theta = 4^\circ$. Rock *et al.* [41] measured the cross section at $Q^2 = 2.5\text{--}10 \text{ (GeV/c)}^2$ as calibration for $d(e, e'n)$ cross section measurements. Bosted *et al.* [42] measured the same, but using a $\theta = 180^\circ$ spectrometer, for which kinematics the cross section only depends on G_M . Sill *et al.* [43] repeated the measurements of Kirk *et al.* up to even higher Q^2 (31 (GeV/c)^2) in search of scaling predicted by pQCD.

Two more recent L-T separations have been performed at SLAC. Andivahis *et al.* [44] doubled the Q^2 range of Rosenbluth separations to 8.8 (GeV/c)^2 , taking data with both the 1.6 and 8 GeV spectrometers. The spectrometers were cross-normalized with a simultaneous measurement at the same kinematics. The world data for $Q^2 > 3 \text{ (GeV/c)}^2$ is dominated by this single experiment. An earlier experiment by Walker *et al.* [30] measured G_E and G_M at the four points $Q^2 = 1.0, 2.0, 2.5,$ and 3.0 (GeV/c)^2 with a single detector, the 8 GeV spectrometer, avoiding the problems of normalization. However Ref. [31] claims the data for $\theta < 20^\circ$ did not have the proper corrections applied, as was done in Ref. [44].

The latest unpolarized data have been taken at Jefferson Lab. Dutta *et al.* [45] (JLab Exp. E91-013) measured hydrogen cross sections as part of an investigation of nuclear transparency and the nuclear spectral functions of carbon, iron, and gold nuclei. Experiment E94-110 [46, 47] measured the elastic hydrogen cross section at 28 points in the range $0.4 < Q^2 < 5.5 \text{ (GeV/c)}^2$ as part of a program to measure $R = \sigma_L/\sigma_T$ in the resonance region. Finally, experiment E01-001 [48] was a dedicated high precision Rosenbluth separation of the hydrogen form factors at $Q^2 = 2.64, 3.20,$ and 4.10 (GeV/c)^2 . In this experiment, the proton was detected instead of the electron to minimize systematic errors. At fixed Q^2 , the recoil proton has the same momentum regardless of the beam energy, thus avoiding uncertainty due to momentum dependence of the spectrometer acceptance. Also, the cross section $d\sigma/d\Omega_p$ for detecting protons is much larger and slower-varying than that of the electron $d\sigma/d\Omega_e$ because the proton angle does not change as rapidly. The experiment used the second spectrometer to simultaneously measure the cross section at $Q^2 = 0.5 \text{ (GeV/c)}^2$ for normalization purposes, although these data were not reported in Ref. [48].

1.2.4 Polarized Data

Recent advances in polarized beams, polarized targets, and polarimetry have made possible a new generation of precision measurements of $\mu G_E/G_M$. Such experiments benefit from interference terms between G_E and G_M in the polarized response functions. The extra spin degree of freedom allows for direct measurement of $\mu G_E/G_M$ at a single beam energy.

In the extreme relativistic limit (ERL), the electron helicity is conserved, and it is much easier to prepare polarized beams than to detect the scattered electron polarization. Furthermore, in the OPE approximation, single polarization asymmetries with either polarized beam and unpolarized target or vice versa are parity-violating and very small. This leaves two double-polarization measurements from ep -elastic scattering: $\vec{p}(\vec{e}, e'p)$ and $p(\vec{e}, e'\vec{p})$.

The first polarization experiment was an asymmetry measurement at $Q^2 = 0.765$ (GeV/c)² by Alguard *et al.* [49] at SLAC. The asymmetry for longitudinally polarized electrons from a longitudinally polarized target is

$$A = \frac{\epsilon\tau \left(\frac{2M}{E} G_E G_M + \left(\frac{2\tau M}{E} + 2(1 + \tau) \tan^2 \frac{\theta}{2} \right) G_M^2 \right)}{\epsilon G_E^2 + \tau G_M^2}. \quad (1.31)$$

For their experiment they used a dynamic nuclear polarized (DNP) butanol target ($P_t = 0.50 - 0.65$) illuminated with a polarized electron beam ($P_e = 0.51$), produced by photo-ionization of a polarized ⁶Li atomic beam. They measured $A = 0.138 \pm 0.031$, and determined the sign of G_E/G_M to be positive. However, it was not feasible to extract $\mu G_E/G_M$ from this experiment. At their kinematics, the asymmetry in Eq. 1.31 has a maximum at $\mu G_E/G_M = 0.78$, as shown in Figure 1-5, making the asymmetry insensitive to $\mu G_E/G_M$. The asymmetry lies within 1σ of the measured value for the form factor ratio anywhere in the range $0.41 < \mu G_E/G_M < 1.20$. Double polarization asymmetries have also been measured in the resonance region and in deep inelastic scattering.

The form factor ratio has been measured by recoil polarimetry at Bates [50], Mainz [51], and Jefferson Lab [52, 53, 3]. The form factor ratio can be extracted from

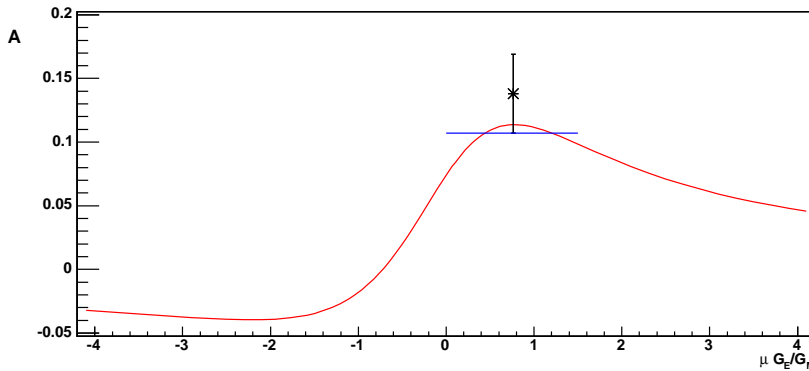


Figure 1-5: The asymmetry as a function of $\mu G_E/G_M$ for longitudinally polarized electrons scattering from a longitudinally polarized proton target, with data from [49]. The kinematics for this experiment maximize the magnitude of the asymmetry; thus, the asymmetry is insensitive to the value of $\mu G_E/G_M$. The (blue) horizontal line shows the range of $\mu G_E/G_M$ corresponding to 1σ error in A .

the ratio of the transverse (P_t) to longitudinal (P_l) polarization of the recoil proton, according to

$$\frac{G_E}{G_M} = -\frac{P_t}{P_l} \frac{E + E'}{2M} \tan \frac{\theta}{2}. \quad (1.32)$$

The recoil proton polarization is measured by a secondary reaction with an analyzer (carbon) in the focal plane of the polarimeter. The azimuthal distribution of yields from the analyzer is sinusoidal with an amplitude proportional to the polarization and a phase shift equal to the angle of polarization in the plane transverse to the velocity of the proton. The largest systematic error comes from determining the proton spin precession angle inside the magnetic spectrometer.

Eyl *et al.* [54] measured the longitudinal recoil polarization from hydrogen. The first extraction of $\mu G_E/G_M$ with a focal plane polarimeter was done by Milbrath *et al.* [50] at MIT-Bates at the two points $Q^2 = 0.35$ and $0.5 (\text{GeV}/c)^2$. Pospischil *et al.* [51] constructed a focal plane polarimeter at Mainz and measured $\mu G_E/G_M$ at $Q^2 = 0.37, 0.40$, and $0.44 (\text{GeV}/c)^2$. The same FPP was used by Dieterich *et al.* [55] for an independent measurement at $Q^2 = 0.40 (\text{GeV}/c)^2$ in comparing the recoil polarization ratio P_x/P_t from ^3He versus ^4He . The data from these experiments agreed with the unpolarized results.

The FPP measurements were extended to higher Q^2 at Jefferson Lab Hall A by Jones *et al.* [2] with the unexpected result of a dramatic linear decrease in the form factor ratio down to $\mu G_E/G_M = 0.6$ at $Q^2 = 3.5(\text{GeV}/c)^2$. These results were reproduced in a subsequent calibration of the FPP [53] for two other experiments on $D(\vec{\gamma}, \vec{p})n$ and $H(\vec{\gamma}, \vec{p})\pi^0$. Gayou *et al.* [3] extended the measurement to $Q^2 = 5.5(\text{GeV}/c)^2$, and observed the same trend. The form factor ratio continued to decrease linearly down to 0.27 at $Q^2 = 5.5(\text{GeV}/c)^2$. There is another experiment approved for JLab Hall C to extend the range to $Q^2 = 9(\text{GeV}/c)^2$. The world data of the form factor ratio are shown in Fig. 1-6

The discrepancy between FPP and unpolarized data has renewed interest in the proton form factors. It prompted considerable theoretical activity, both to reconcile the polarized and unpolarized data (Sect. 1.2.6), and to understand the intriguing Q^2 dependence of $\mu G_E/G_M$ (Sect. 1.3). Experiment E01-001 [48] was performed at Jefferson Lab to test for possible systematic effects in the previous unpolarized experiments, but the results were consistent with the unpolarized world data. A whole new set of experiments have been proposed to test for higher-order processes which may contribute to this discrepancy.

1.2.5 Global Analysis

Many global fits to the world data have been performed [21, 18, 34, 25, 30, 56, 57, 31, 58, 59]. In addition, there are fits to theoretical models which will be discussed in the next section. We consider here the most recent fits. Walker *et al.* [30] extracted G_E and G_M at 17 values of Q^2 from the world data with improved radiative corrections. They also fit a normalization constant for each of the 11 experiments. Bosted [56] fit this global analysis to an inverse polynomial in $Q = \sqrt{Q^2}$, and obtained the results

$$G_E(Q^2) = \frac{1}{1 + 0.62Q + 0.68Q^2 + 2.80Q^3 + 0.83Q^4}, \quad (1.33)$$

$$\frac{G_M(Q^2)}{\mu} = \frac{1}{1 + 0.35Q + 2.44Q^2 + 0.50Q^3 + 1.04Q^4 + 0.34Q^4} \quad (1.34)$$

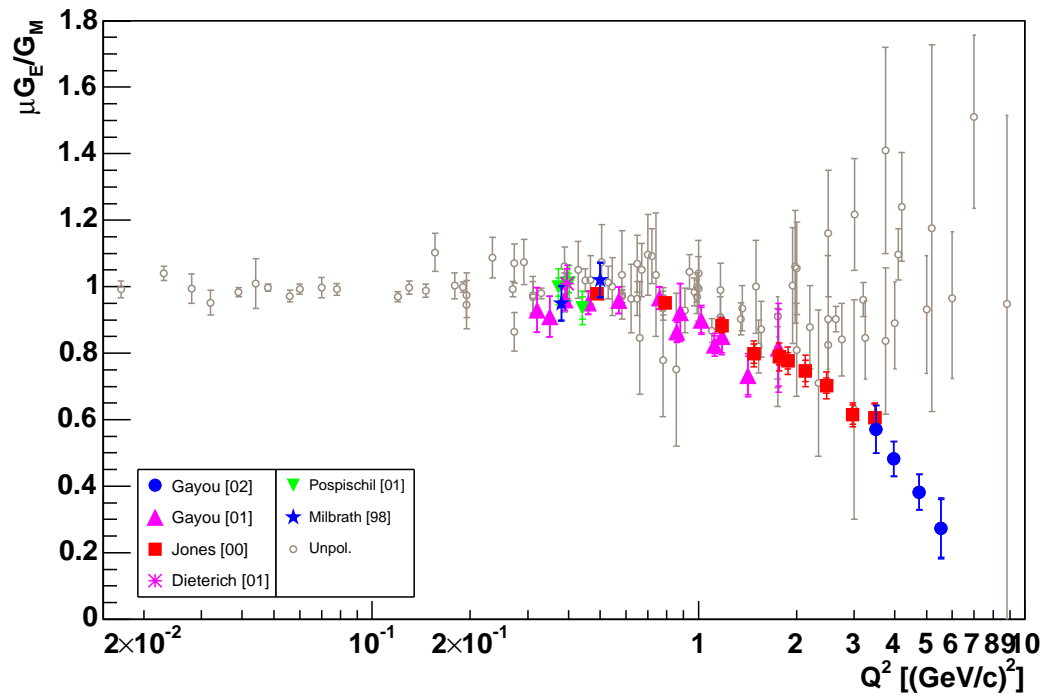
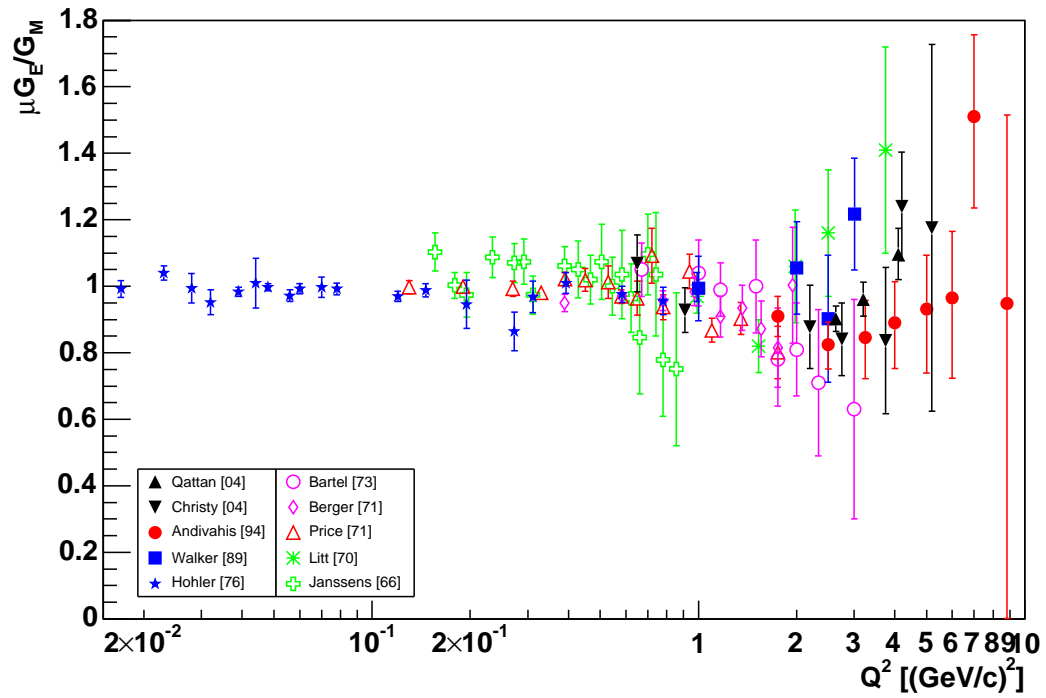


Figure 1-6: The $\mu G_E / G_M$ world data on the proton, unpolarized data only (top) and including polarized data (bottom).

The odd powers of Q allow for oscillation about the dipole form G_D at the expense of a singular derivative as $Q^2 \rightarrow 0$.

In response to the new behavior of the Hall A polarized data, Brash *et al.* [57] fit the new form factor ratio data to the linear equation

$$\mu G_E/G_M = 1.0 - (0.130 \pm 0.005)[Q^2 - (0.04 \pm 0.09)], \quad (1.35)$$

for $Q^2 = 0.04\text{--}5.6 \text{ (GeV/c)}^2$ and used this new constraint to extract G_M from the world data. They refit their data for the same function of Ref. [56], and concluded that G_M was systematically 1.5–3% larger than the extraction from unpolarized data alone. However, as pointed out in Ref. [58], a form factor extraction combining Rosenbluth separations with polarized data is inherently inconsistent, and yields both the wrong extraction of G_E and G_M in the Born approximation, as well as incorrect unpolarized cross sections.

Arrington [31] performed a reanalysis of the unpolarized cross section data of Ref. [30], adding the experiments [40, 41, 37], and updating data to the newly published results [42, 44]. He updated radiative corrections, split up data sets from more than one spectrometer, and fit all of the cross section data directly to the same polynomial functions of [56]. In addition, he reanalyzed L-T separations from single-extraction experiments with enough data [39, 30, 44, 34, 38]. He also used the global fit to normalize the cross sections and to interpolate them into 26 Q^2 points up to 6 (GeV/c)^2 and extracted global G_E and G_M points similar to [30]. He concluded that the world unpolarized data set is self-consistent, but statistically incompatible with the new form factor ratios from polarized data.

In a later paper [58], Arrington refit the world data including low Q^2 data [23, 22, 25], and recent Jefferson Lab cross sections [45, 47, 46]. He used an inverse polynomial in Q^2 with coefficients up to Q^{12} . He also fit the polarized and unpolarized data together assuming a 6% linear ϵ correction to all cross section to take into account the discrepancy between the two types of measurements. As expected, the former fit is very similar to [56], while the latter yields an enhancement in G_M even compared

to [57].

Kelly [59] fit both polarized and unpolarized data to the simple form

$$G_E(Q^2) = \frac{1 - (0.24 \pm 0.12)}{1 + (10.98 \pm 0.19)\tau + (12.82 \pm 1.1)\tau^2 + (21.97 \pm 6.8)\tau^3} \quad (1.36)$$

$$\frac{G_M(Q^2)}{\mu} = \frac{1 + (0.12 \pm 0.04)}{1 + (10.97 \pm 0.11)\tau + (18.86 \pm 0.28)\tau^2 + (6.55 \pm 1.2)\tau^3} \quad (1.37)$$

This gives the correct $1/Q^4$ dependence at high Q^2 , is well behaved as $Q^2 \rightarrow 0$, and gives the RMS proton radius $r_p = 0.863 \pm 0.004$ in agreement with the currently accepted value.

Motivated by a bump structure at $Q^2 \approx 0.2\text{--}0.3$ (GeV/c)² in the neutron electric form factor, Friedrich and Walcher [60] have put forth a phenomenological model of the form factors

$$G_N(Q^2) = G_s(Q^2) + a_b Q^2 G_b(Q^2). \quad (1.38)$$

The model parametrizes the smooth high Q^2 dependence with a pair of dipoles,

$$G_s(Q^2) = \frac{a_{10}}{(1 + Q^2/a_{20})^2} + \frac{a_{11}}{(1 + Q^2/a_{21})^2}, \quad (1.39)$$

and adds a Gaussian bump at low Q^2 ,

$$G_b(Q^2) = e^{-\frac{1}{2}\left(\frac{Q-Q_b}{\sigma_b}\right)^2} + e^{-\frac{1}{2}\left(\frac{Q+Q_b}{\sigma_b}\right)^2}, \quad (1.40)$$

where $Q = \sqrt{Q^2}$. The second exponential is small and restores the analyticity of $G(Q^2)$ as $Q^2 \rightarrow 0$. Two dipoles were needed in order to get the right asymptotic Q^2 dependence of the form factors, but their amplitudes are related by the normalization at $Q^2 = 0$, satisfying $a_{10} + a_{11} = G_N(0)$. They discovered that not only G_E^n , but also the “standard” form factors G_E^p , G_M^p , and G_M^n fit well to this ansatz. Noting that the bump has the effect of shifting charge to the outside of the nucleon, they give it the physical interpretation of a pion cloud. The fits of Arrington, Kelley, and Friedrich and Walcher are shown in Fig. 1-7.

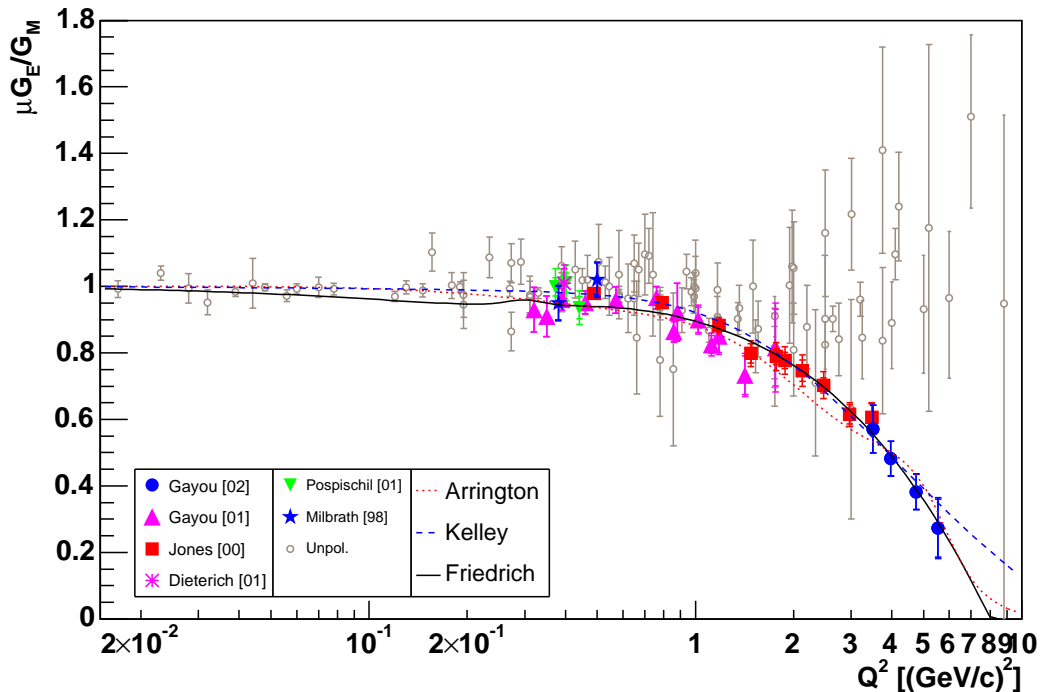


Figure 1-7: Phenomenological fits to the $\mu G_E / G_M$ world data.

1.2.6 Two-photon Contribution

In the current Born OPE framework, the form factor ratio $\mu G_E / G_M$ extracted from unpolarized cross section measurements is incompatible with the Hall A extraction from recoil polarization data. As previously mentioned, the unpolarized data from many experiments performed at laboratories around the world are consistent with each other. Therefore, the discrepancy is probably not caused by experimental systematics, such as ϵ -dependence in acceptance, or normalization errors. Also, recoil polarization measurements from three different laboratories agree at low Q^2 . At Jefferson Lab, high Q^2 extractions from three separate experiments using different beam energies are also consistent.

This discrepancy is an important problem not only for elastic form factors, but for other hadronic properties determined from lepton scattering as well. Even if the polarized data are considered to be more reliable, one must still combine them with unpolarized cross sections to extract G_E and G_M . This separation is not reliable until

the form factor contributions to the cross section are known well enough to reconcile the two methods [58]. While the current Rosenbluth separations give an adequate parameterization of the cross section data, it is not meaningful to compare the extracted form factors with theoretical predictions. Another unresolved question is why the systematic deviation of the unpolarized cross sections is linear in ϵ , conspiring to give false confidence in the Rosenbluth extraction.

The most likely candidate to resolve this discrepancy is the two photon exchange contribution from the box and cross diagrams of Fig. 1-1. This effect along with the other radiative effects must be corrected for in the extraction of the form factors, which are defined as matrix elements in the OPE approximation. However, the two photon effect is model-dependent and difficult to calculate. Although these effects had been considered as early as in the 1960's [61], most unpolarized experiments were radiatively corrected within the framework of Mo & Tsai [62], in which peaking approximations were used for $q \rightarrow 0$ for one of the photons. The non-infrared divergent parts of the two-photon-exchange were even recently thought to be less than 1% [30, 63]. It has been shown that Coulomb distortion effects, arising from higher order diagrams with a hard virtual photon of momentum q and one or more soft virtual photons, have little effect on Rosenbluth separations [64].

The two-photon exchange term is equivalent to double virtual Compton scattering, with the virtual photons coupled to the scattered electron. This is complicated by the fact that the intermediate nucleon can be in any excited state, so that the amplitude is not just a function of the nucleon form factors. There have been many recent attempts to describe the effect qualitatively and quantitatively. They have had some success in reconciling the two methods. However, there are still conflicting statements among the authors, and a full calculation using realistic structure functions has yet to be done.

Guichon and Vanderhaeghen [65] developed a framework for the comparison of two photon effects between polarized and unpolarized experiments. Factoring all higher order scattering amplitudes into the nuclear current Γ , the most general current respecting Lorentz, parity, and charge conjugation invariance for a spin 1/2 particle

is

$$\Gamma^\mu = \tilde{G}_M \gamma^\mu - \tilde{F}_2 \frac{P^\mu}{M} + \tilde{F}_3 \frac{\gamma \cdot K P^\mu}{M^2}, \quad (1.41)$$

where \tilde{G}_M , \tilde{F}_2 , and \tilde{F}_3 are complex functions of Q^2 and ϵ , which equal G_M , F_2 , and 0 respectively in the Born approximation. \tilde{G}_E is defined analogous to Eq. 1.14. Using standard techniques, they computed both the unpolarized cross section and recoil polarization from this nucleon current. The form factor ratios, as extracted from the unpolarized and polarized cross sections, both had corrections containing the dimensionless two-photon exchange characterization

$$Y_{2\gamma}(Q^2, \epsilon) = \mathcal{R} \left(\frac{K \cdot P \tilde{F}_3}{M^2 |\tilde{G}_M|} \right). \quad (1.42)$$

Using the difference between polarized and unpolarized extraction of $\mu G_E/G_M$, they were able to extract $Y_{2\gamma}$ and the corrected Born OPE form factor ratio. $Y_{2\gamma}$ turned out to be a small correction (2–4% depending on Q^2) with very little ϵ dependence, and the actual $\mu G_E/G_M$ was a little higher than, but very close to the polarized results. Thus the two-photon effects were shown not to alter the linearity of the Rosenbluth separation. A similar analysis also using e^-p and e^+p data to separate G_E and G_M has also been done [66]. The $Y_{2\gamma}$ contribution is expected to change sign when switching between e^-p and e^+p scattering.

In a general analysis of model-independent properties of two-photon exchange, Rekaló and Tomasi-Gustafsson [67] started with the same nucleon current as Eq. 1.41. However, taking into account C-invariance of the electromagnetic interaction of hadrons, they showed that the first two terms could only involve an odd number of photons, while the third term involved only an even number of photons. Thus the phases of \tilde{G}_M and \tilde{F}_2 were of order α^2 and so these were essentially the elastic form factors. They also confirmed that the amplitudes of \tilde{G}_M , \tilde{F}_2 , and \tilde{F}_3 should be the same for both e^-p and e^+p scattering. In addition, applying crossing symmetry between the s-channel ($e^+e^- \rightarrow p\bar{p}$) and the t-channel ($ep \rightarrow ep$), they concluded that the 1γ - 2γ interference contribution should be nonlinear in ϵ and depend on the

variable $x = \sqrt{(1 + \epsilon)/(1 - \epsilon)}$ to first order at least.

The first model-dependent calculation of the two photon effect, by Blunden, Melnitchouk, and Tjon [68] assumed the intermediate nucleon state to stay in the ground state, with both γp interactions described by the standard proton current operator of Eq. 1.13. They used monopole form factors $G_E = G_M/\mu = G \equiv (1 + Q^2/\Lambda^2)^{-1}$ in their calculation. The resulting correction was about 2% in addition to the approximations of Mo and Tsai [62]. It was almost linear in ϵ , with slope increasing slightly with Q^2 . Thus this calculation was able to explain half of the discrepancy between polarized and unpolarized form factor ratios.

Chen *et al.* [69] evaluated the two photon exchange contribution in a partonic model. The intermediate nucleon included excited states and was modeled with generalized parton distributions (GPD), which are also useful for describing Virtual Compton Scattering (VCS). Using input of $\mu G_E/G_M$ from the polarized JLab data, they were able to reproduce the approximate ϵ -dependence of the unpolarized cross sections of Ref. [44]. The two-photon exchange contribution increased the slope of $\mu G_E/G_M(\epsilon)$ as desired, but also introduced nonlinearities into the ϵ dependence. They also predict the cross section e^+/e^- ratio for $2 < Q^2 < 5$ (GeV/c) to be 0.98 at large ϵ , crossing 1 at about $\epsilon = 0.35$. While a full extraction of G_E and G_M within this model still needs to be done, this work appears to resolve most of the discrepancy between the form factor ratio extracted from unpolarized and polarized data.

Experimentally, the effects of the two photon exchange diagram are accessible through its possible nonlinear ϵ -dependence, or its C -odd and T -odd (parity conserving) properties [70]. Experiments of all three types have been carried out in the past with limited precision, and new precision measurements of each have been proposed. Although there have been many single-experiment Rosenbluth separations, the ϵ ranges were typically insufficient for a conclusive test of linearity. There is a Jefferson Lab proposal to do a high precision test of linearity at $Q^2 = 1.12$ and 2.56 (GeV/c)² of the Rosenbluth cross section [71], and also in the recoil polarizations P_x and P_y [72].

The e^\pm cross sections are identical except for a sign change in the interference

between the one and two-photon exchange amplitudes (C -odd). Therefore, the ratio $R = \sigma(e^+p)/\sigma(e^-p)$ is highly sensitive to the two-photon effect. Previous measurements of R have been done in the 1960's, but either at low statistics or at a large value of ϵ where the sensitivity is much smaller [73]. Precision measurements of R have been proposed at VEPP-3 [74] and at Jefferson Lab Hall B [75]. The latter experiment uses two radiators: the first to create real photons which are converted into e^+/e^- pairs in the second. These pairs are focused by a 4-dipole chicane magnet around a photon barrier and back to the beam line, where the cross sections of each on an unpolarized LH_2 target are measured in the CLAS detector. By measuring both cross sections simultaneously and switching the polarity of the chicane magnets, the systematic normalization uncertainty can be greatly reduced.

The parity conserving T -odd symmetry is manifest in the single-spin asymmetry A_y from $\vec{p}(e, e'p)$, or as an induced polarization P_y from $p(e, e'\vec{p})$, which are equivalent by time reversal invariance. These measurements probe the imaginary part of the two-photon exchange amplitude, while second order corrections to the linear Rosenbluth equation and C -odd effects depend on the real part of the amplitude. Early experiments [70] were only able to place upper bounds on this effect at the 1% level, but their kinematics were in an insensitive region. Recently parity conserving single beam asymmetries $p(\vec{e}, e'p)$ have been observed in SAMPLE [76] and the Mainz A4 Parity Violation [77] experiments. New experiments are being proposed at Jefferson Lab to study A_y [78] and P_y [72, 79, 80], and the transverse beam asymmetry [80].

In conclusion, the discrepancy in extractions of $\mu G_E/G_M$ between unpolarized and polarized experiments have motivated intense theoretical and experimental activity. The difference is believed to be caused by interferences between the two-photon (box and cross diagrams) and Born amplitudes, confirmed by preliminary model-dependent calculations. Although there are no compelling experimental data in favor of two-photon effects, many new experiments have been proposed or approved to search for this effect.

1.3 Theoretical Descriptions of the Nucleon Form Factors

As confirmed by deep inelastic scattering (DIS), the nucleon is composed of point-like partons: three valence quarks in a sea of quark-antiquark pairs and gluons. The most naive model in which the electromagnetic properties of the nucleon are determined by its valence quarks was ruled out by DIS experiments of the Spin Muon Collaboration (SMC) at CERN [81], which showed that the valence quarks were responsible for only 25% of the spin of the nucleon, giving rise to the nucleon “spin crisis” of the 1980’s. Since the magnetic moment of the nucleon is not just the sum of the static moments of its constituent point charges, there is no reason to expect identical distributions of charge and magnetization. This illustrates the important contributions of the sea quarks and gluons to the structure of the nucleon. In contrast to the QED dynamics of the leptonic probe, the QCD running coupling constant

$$\alpha_s(Q^2) = \frac{\alpha_s(0)}{1 + \frac{\alpha_s(0)}{16\pi^2} \left(11 - \frac{2}{3}N_f\right) \ln\left(\frac{Q^2}{\Lambda_{QCD}^2}\right)} \quad (1.43)$$

is strongest at low energy (confinement), and decreases at higher energy (asymptotic freedom). The energy scale associated with this shift is $\Lambda_{QCD} \approx 200$ MeV. Thus perturbative QCD (pQCD) expansions are only valid at very high Q^2 . The low energy ($M = 0.938$ (GeV/ c^2)) static properties of the nucleon are determined by QCD in the nonperturbative region. There are no exact analytical solutions to QCD, and the only alternative is numerical calculations of lattice QCD, which is limited by present computing power. However, predictions of the asymptotic behavior of the form factors can be derived from pQCD.

There are many effective theories and models of the nucleon describing the form factors in different Q^2 regions. Some examples are, increasing in Q^2 : Chiral Perturbation Theory (χ PT), dispersion relations, Vector Meson Dominance (VMD) models, and Constituent Quark Models (CQM). However, these models require form factor data as input and thus have little predictive power. Also, each is valid in a limited

Q^2 range consistent with the modeled degrees of freedom. Many of these models have been reviewed in [20]. In this section, we will briefly discuss general properties and few examples of each type, with emphasis on low- Q^2 models relevant to the current experiment.

1.3.1 Perturbative QCD

The asymptotic behavior of G_E and G_M as $Q \rightarrow \infty$ can be deduced from general properties of QCD. Based on dimensional scaling and the assumption of hard scattering from point-like quarks, Brodsky and Farrar [82] proposed that exclusive cross sections should scale as $d\sigma/dQ^2 \sim (Q^2)^{2-n}$ at large Q^2 , where n is the number of point-like particles ($n = 8$ for ep scattering). Thus the asymptotic behavior of the form factors should be

$$F_1(Q^2) \sim (Q^2)^{-2}, \quad F_2(Q^2) \sim \frac{F_1}{Q^2}, \quad \text{and} \quad \frac{\mu G_E}{G_M} \sim \text{const}, \quad (1.44)$$

where F_2 is suppressed by helicity conservation. The same prediction was confirmed by two independent pQCD analyses [83, 84], the former showing only logarithmic deviations from the dimensional scaling law. While this scaling law predicted the previously available data very well, the new polarized data appear to scale as $\sqrt{Q^2}F_2/F_1$ as shown in Fig. 1-8. In response, to the new data, Brodsky, Hwang, and Hill have reproduced this trend by adding higher twist contributions while maintaining hadron helicity conservation. Other possible explanations include taking into account the orbital angular momentum of the quarks L_z [84, 85], or simply that the scaling has not set in yet in this range of Q^2 . The relativistic formalism of Light-Front Constituent Quark Model (LFCQM) calculations (Sec. 1.3.2) [86, 87] also implies components of the quark wave function with $L_z \neq 0$.

1.3.2 Constituent Quark Models

At large momentum transfer, the electron scatters from individual partons in the nucleon, and effective models must address these degrees of freedom. For elastic scat-

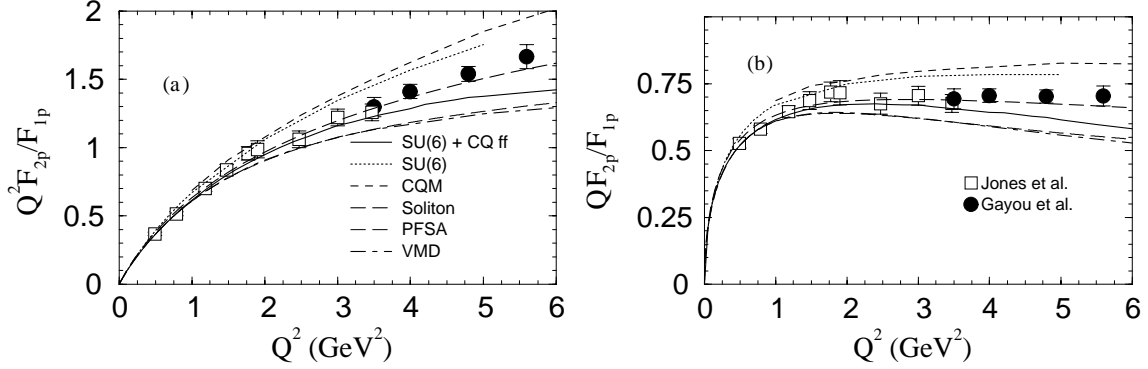


Figure 1-8: From [3]: the scaling of the Dirac and Pauli form factors at large Q^2 . The unpolarized data seemed to scale as $Q^2 F_2/F_1$, while the JLab polarized data shown above favor $Q F_2/F_1$. The models [88, 88, 89, 90, 91, 92] (from top to bottom) are explained below.

tering, there must also be some mechanism to redistribute the momentum among the rest of the nucleon. Constituent quark models (CQM) approximate QCD by absorbing gluonic degrees of freedom into the (dressed) valence quark mass and an effective confining potential. Realistic CQM's must include relativistic effects. As described in Ref. [93], there are three classes of Hamiltonian quantum dynamics proposed by Dirac which satisfy Poincaré invariance: the instant form, light-front form, and point form. They correspond to particle states being defined on a space-like hyperplane at some fixed time, on a tangent to the light cone, or on a Lorentz-invariant hyper-surface (hyperbola), respectively.

In the light-front dynamics, the space-time variables x and t are transformed to $x^\pm = \frac{1}{\sqrt{2}}(t \pm x)$ with corresponding canonical momenta p^\pm . This system has the advantage of a simple Hamiltonian without negative energies, the ability to separate the center of mass from the relative motion of particles, and boosts which are independent of the interactions. The difficulty comes in boosting spin vectors into this infinite momentum frame, which is done with Melosh rotations. On the other hand, the point form has the property of covariance, and simple coupling of spin and orbital angular momentum.

A simplified LFCQM model (CQM in light-front dynamics) was introduced by Chung and Coester [94], and applied by Schlumpf to compute a wide variety of

hadronic properties [95]. These models reproduced the form factor scaling of the unpolarized data, failing to describe the polarized data. However, another calculation by Frank, Jennings, and Miller [89] using the model of Schlumpf agrees well with the complete polarized data set. Agreement was attributed to the limiting QF_2/F_1 dependence caused by imposing Poincaré invariance [96], in potential violation of the quark helicity conservation rule. Calculations by Cardarelli *et al.* [88] were also carried out in light-front dynamics with a one-gluon exchange potential to study SU(6) symmetry breaking. Their predictions for G_E and G_M with and without form factors for the constituent quarks, also agree well with the polarized data.

A variant of the CQM model is the diquark model of Kroll *et al.* [97]. Two of the constituent quarks are tightly-bound into a spin-0 or 1 diquark with a phenomenological form factor which allows the diquark to behave as free quarks at high Q^2 . The electron may scatter from either the quark or diquark, and helicity-flip amplitudes are generated by scattering from the spin-1 diquark. Ma, Qing, and Schmidt [98] did calculations of a quark spectator-diquark model in light-front dynamics. Wagenbrunn *et al.* [91, 99] constructed a model in point form dynamics, following the point form spectator approximation (PFSA) of Klink [100]. This model also uses a Goldstone boson exchange potential, and is in good agreement with the form factors from polarized data.

Another class of quark models based on the MIT Bag Model has three valence quarks confined to a finite spherical well. Historically, these models were not able to reproduce the static properties of the nucleon. Lu and Thomas [101] included a pion field in the model to restore chiral symmetry and reproduce the low- Q^2 properties of the form factors with agreement up to $Q^2 < 1 \text{ (GeV/c)}^2$. Miller applied the relativistic dynamics of the quarks in the LFCQM to the pion cloud of the Cloudy Bag Model (CBM) to create the so-called hybrid LFCBM [86]. The model describes all four nucleon form factors using only four tunable parameters. It also has the correct low Q^2 behavior as required by chiral perturbation theory and therefore is very useful for chiral extrapolations in lattice QCD (see Sec. 1.3.4). This model is one of the most complete in terms of its incorporation of both meson and quark degrees of freedom,

although it only has four parameters.

1.3.3 VMD Models

Initial deviations of the form factor data from $G_D(Q^2)$ were parameterized by pure phenomenological fits using constraints of dispersion analysis. Under the assumption that the form factors are analytic functions over the entire physical region, they are uniquely determined by analytic continuation, [21]

$$F(q^2) = \frac{1}{\pi} \int \frac{\text{Im } F(q'^2)}{q'^2 - q^2 - i\epsilon} dq'^2. \quad (1.45)$$

The utility in this expression comes from approximating the continuous spectral function $\text{Im } F(q'^2)$ with discrete poles, taken from πN resonances, leading to a sum of monopole terms [44]

$$F(Q^2) = C + \sum_i \frac{C_{\gamma V_i}}{Q^2 + M_{V_i}^2} F_{V_i N}(Q^2), \quad (1.46)$$

where C is chosen to satisfy the normalization at $F(0)$. The physical interpretation of this approximation is that the nuclear structure is described by the exchange of vector mesons, as shown in Fig. 1-9. In this vector meson dominance (VMD) model, $F_{V_i N}(Q^2)$ is a simple form factor (usually monopole or dipole) of the bare nucleon (a Dirac particle), and $C_{\gamma V_i}$ is the coupling strength of the virtual photon to a vector meson of mass $M_{V_i}^2$.

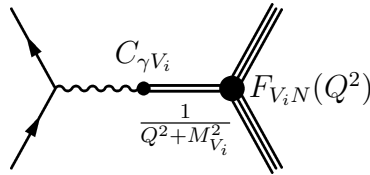


Figure 1-9: Diagram of the Vector Meson Dominance (VMD) amplitude.

As the ρ -meson is an isovector, while ω and ϕ are isoscalars, the VMD model applies to the isospin form factors F^s and F^v , related to the conventional form factors

by

$$F^p = F^s + F^v \quad \text{and} \quad F^n = F^s - F^v. \quad (1.47)$$

As F_1 and F_2 , or G_E and G_M , cannot all satisfy Eq. 1.46, a choice must be made of which pair to model, and the Dirac and Pauli form factors are preferred in the literature. Early data, e.g. [38, 21], were fit to the three resonance poles with considerable improvement over the simple dipole fit. The dipole form comes naturally from two resonances of similar mass and equal but opposite strengths, i.e. the derivative.

Later fits have included the width $\Gamma = 150$ MeV of the ρ meson through dispersion relations and have include higher mass poles such as $\omega(1420)$ and $\rho(1450)$. In addition to the large width of ρ , there is a substantial non-resonance contribution to the isovector dispersion spectrum between the two pion threshold and the ρ peak, which is strong enough to affect the low Q^2 behavior of the form factors and consequently r_p [25, 27].

Iachello *et al.* [102] fit all four nucleon form factors with a VMD model including the width of ρ . They also modeled the bare nucleon with dipole, eikonal, and monopole intrinsic form factors and included photon interaction with the bare nucleon. Höhler *et al.* [12] calculated the ρ contribution using an analytic continuation of πN scattering amplitudes and π form factor data instead of fitting the nucleon form factor data with a single pole. They also introduced the isovector meson $\rho'(1250$ MeV) much below its physical mass. This model was improved by Mergell *et al.* [27], updating the π form factors to account for ρ - ω mixing. They also matched the asymptotic Q^2 dependence to pQCD by constraining the free parameters with a set of super-convergence relations.

The basic VMD model was also extended by Gari and Krümpelmann [103, 104] with an additional term to guarantee the correct pQCD behavior at large Q^2 . Lomon [92] updated this model with the width of ρ and the additional meson $\rho'(1450)$. Later, in order to explain the Hall A data, he extended the model [105] to include $\omega'(1419)$, and excluded unpolarized data which was in conflict with the new polarized data to get reasonable agreement. Hammer *et al.* [106] did a dispersion fit including form

factor data from the time-like region, and Kubis *et al.* [107] included vector mesons in a fit using chiral perturbation theory, but neither of these calculations reproduce the data at high Q^2 .

With the exception of Refs. [12] and [27] at low Q^2 , these VMD models are phenomenological fits to the form factors with physics-inspired functions and constraints. Therefore comparisons with new experimental data have limited meaning, since the parameters must be returned to explain new data.

Holzwarth [90] investigated a topological soliton model of the nucleon based on an effective nonlinear Lagrangian with mesonic degrees of freedom. Like the LFCBM [86], this model was constructed as simple as possible from the essential elements required to gain a physical understanding of the nuclear structure and make meaningful comparisons with the data. The first of three important parts of this model is a pionic soliton created from a standard Skyrme term in the Lagrangian. A single vector meson pole ρ is coupled to both the isovector and isoscalar form factors with an interpolation parameter λ ranging from 0 for pure Skyrme to 1 for pure VMD. The third essential component is a relativistic boost to the Breit frame, which is also important in constituent quark models. The resulting spectral function shows the same behavior as Refs. [12, 27] between the two-pion threshold and ρ pole. This model reproduces G_E^p and G_M^p including the form factor ratio very well, although it underestimates G_E^n and overestimates G_M^n above $Q^2 = 1 \text{ (GeV/c)}^2$. This model has been updated [108] to include loop corrections.

1.3.4 Lattice QCD

Lattice QCD promises pure numerical calculations of the form factors straight from the QCD Lagrangian without effective theories, models, or assumptions. Indeed the hadron mass spectrum has been calculated on the lattice with success [109]. However, these calculations are limited by computing power, and many approximations must be made [110]. First, calculations are done on a discrete space-time with lattice spacing a , and must be extrapolated to the continuum limit $a \rightarrow 0$. This limit is under control with improved actions such that $O(a)$ errors are eliminated, and lattice spacings up

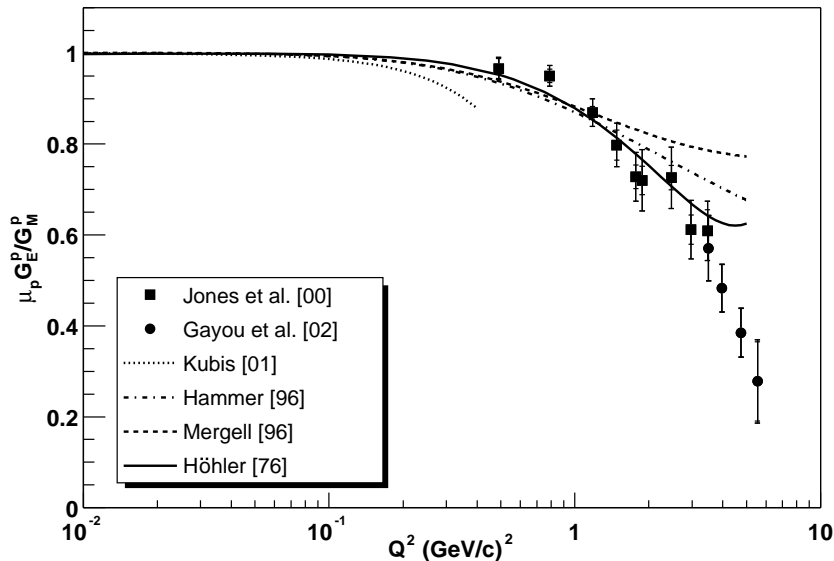


Figure 1-10: From [20]: polarized $\mu G_E/G_M$ data from Jefferson Lab with fits using dispersion theory and VMD.

to $a = 0.1$ fm can be used with little error. The second, extrapolation to infinite volume, is more difficult. Current computing power does not permit large enough lattices to fully contain the pion cloud that arises from chiral symmetry breaking, and the effects of this are unclear. The third, chiral extrapolation, is the continuation to small quark masses, or equivalently small pion mass. The difficulty is compounded by spontaneous symmetry breaking of QCD, which introduces non-analytic dependence of observables on m_π . Current lattice calculations use a pion mass of 6–10 times the physical pion mass, though this may be soon reduced to 2–3 times with the next generation of supercomputers. The prohibitively high cost of including quark-antiquark loops (the sea) in the action requires many calculations to be done in the quenched approximation. Further studies are needed to understand the effect of quenching.

The chiral extrapolation to physical masses is a very difficult problem and has lately attracted a lot of attention. Simple model-independent (for example, linear) extrapolations give wrong results due to the non-analytic effect of symmetry breaking. Chiral perturbation theory (χ PT) is effective in extrapolating from small masses, and

captures the leading non-analytic behavior of QCD; however the radius of convergence for χ PT expansions is small compared to the calculated mass scale. Thus model-dependent extrapolations are needed to respect the chiral symmetry for the current range of m_π^2 imposed by state-of-the-art lattice calculations. Such a model must have a tunable m_π^2 and satisfy the leading non-analytic (LNA) behavior and other formal constraints of QCD. One suitable model, the CBM, is discussed below.

The QCDSF collaboration performed a quenched calculation [111] in 2003 of the nucleon form factors up to $Q^2 \approx 2(\text{GeV}/c)^2$ at 3 different lattices from $16^3 \times 32$ to $32^3 \times 48$ and different spacings. They used $O(a)$ improved Wilson fermions (clover) with mass scale in the range $0.4 < m_\pi^2 < 1.3 \text{ GeV}^2$. Previous lattice QCD calculations of the nucleon [112] had focused on the magnetic moments and charge radii.

Ashley *et al.* [113] have reported a chiral extrapolation of these new calculations which satisfies the LNA behavior and other formal constraints of QCD. As the calculations are not precise enough to distinguish between the Q^2 dependence of different models, they fit the calculations to isoscalar and isovector dipole form factors with the mass scale Λ a continuous function of m_π^2 . In the case of the isoscalar form factors, with no LNA behavior, they did linear extrapolations of $\Lambda(m_\pi^2)$, while for the isovector case the functional form of the extrapolation was inspired from studies of the CBM.

Thomas and collaborators [114] have successfully used the light-front cloudy bag model (LFCBM) [86] for chiral extrapolation. The model was constructed to both respect chiral symmetry through the pion cloud and Lorentz invariance through the use of light-front dynamics. It was able to reproduce the m_π^2 and also Q^2 dependence of the lattice calculations, and also has the proper LNA behavior QCD. They found that the pion cloud was not important at the mass range of the lattice calculations, but very significant near the chiral limit. Their extrapolation agrees well with experimental form factors, and through a severe extrapolation of $Q^2 > 2(\text{GeV}/c)^2$, they predict that $\mu G_E/G_M$ crosses 0 at about $Q^2 \approx 6(\text{GeV}/c)^2$. While these results are promising, there is clearly a need to test extrapolation with other suitable models to investigate the model dependence.

The Lattice Hadron Physics Collaboration (LHPC) has performed an unquenched calculation [115] of the hadron form-factors using a hybrid scheme with staggered sea quarks and domain wall valence quarks. Their calculation was done on a $20^3 \times 64$ lattice with spacing $a = 0.125$ fm using a PC cluster at JLab. The results were in agreement with the QCDSF calculation.

Rapid progress in lattice QCD has been made in the use of sophisticated actions, extrapolation techniques, and also in sheer computing power. In the near future Lattice QCD calculations will progress to the point where they can be tested with precision form factor measurements in the Q^2 region of the current experiment.

1.4 Current Experiment

We have measured double-spin asymmetries of the elastic $\vec{p}(\vec{e}, e'p)$ channel at $0.15 < Q^2 < 0.65$ (GeV/c) 2 . These high-precision asymmetries have been used to extract the form factor ratio $\mu G_E/G_M$ of the proton for the first time from this reaction. The only prior measurement of this asymmetry [49] was performed at the single point $Q^2 = 0.765$ (GeV/c) 2 and with large statistical uncertainty. The kinematics of that experiment maximized the asymmetry, but minimized its sensitivity to $\mu G_E/G_M$. However, the sign of G_E/G_M was determined to be positive.

1.4.1 Experimental Overview

From Eq. 1.27, the experimental double-spin asymmetry for elastic $\vec{p}(\vec{e}, e'p)$ scattering is the product of the beam and target polarization, P_b and P_t , and the ratio of the polarized over the unpolarized hydrogen elastic cross section [6]

$$A_{exp} = P_b P_t \frac{z G_M^2 + x G_E G_M}{\tau G_M^2 + \epsilon G_E^2}, \quad (1.48)$$

where $\tau = Q^2/4M^2$, and $\epsilon = 1/(1 + 2(1+\tau) \tan^2 \frac{\theta}{2})$ is the longitudinal polarization of the virtual photon. The terms including the kinematic factors z and x are proportional to the longitudinal and transverse components of the proton polarization z^* and x^*

with respect to the momentum transfer, \mathbf{q} .

By simultaneously measuring the asymmetry for two different spin orientations at fixed Q^2 , one can form a super-ratio R_A of the asymmetries in which the beam and target polarization and the unpolarized cross section cancel. Given a symmetric detector, both asymmetries can be measured at the same time by orienting the target spin at the angle $\beta = 45^\circ$ to the left of the beam, so that the asymmetry A_L (A_R) for electrons scattering into the left (right) sector is predominantly transverse (longitudinal). The super-ratio of these two independent asymmetries is

$$R_A \equiv \frac{A_L}{A_R} = \frac{z_L + x_L R}{z_R + x_R R}. \quad (1.49)$$

The form factor ratio $R = G_E/G_M$ can be extracted from the solution of Eq. 1.49.

From the two asymmetries A_L and A_R at each Q^2 point, one may also extract the product of beam and target polarization $P = P_b P_t$. A comparison of the values of P at each Q^2 point gives a measure of data quality. By constraining each P to be the same, one may effectively apply extra statistics toward the form factor ratio, the quantity of physical interest. By using some model of $\mu G_E/G_M$ at the lowest Q^2 point to fix the polarization, one may also extract $\mu G_E/G_M$ from a single asymmetry measurement, although with lower statistical precision. The experimental setup and detailed analysis are described in the following chapters.

1.4.2 Physics Impact

The purpose of this experiment was to map out the form factors in the low- Q^2 region of the pion cloud. These data may be used to test the various form factor models which are applicable in this region, or may be used to tune their low Q^2 dependence. Particularly important will be the test of ab-initio lattice QCD calculations once they are precise enough for comparison. Precise measurements of G_E and G_M are also important as physics input for parity violating experiments on the proton [76, 116, 117, 118, 77].

In light of the discrepancy between unpolarized extractions of $\mu G_E/G_M$ and the

FPP results from JLab, this experiment is an independent verification of the validity of form factor extraction from the polarized asymmetry. Although formally both experiments measure the same observable, the systematic uncertainties from each method are very different. The FPP analysis hinges on a careful determination of the spin precession of the recoil proton through the optics of the spectrometer, while our data are most sensitive to the determination of the momentum transfer \vec{q} and the spin angle of the polarized target. There are high statistics FPP data from MIT-Bates, Mainz, and JLab in the region of this measurement allowing for a rigorous cross-check of the FPP results at low Q^2 .

This experiment also includes data up to $Q^2 = 0.9 (\text{GeV}/c)^2$ from the backward angle TOFs, which are not included in this thesis. This is at the threshold where the JLab data depart from $\mu G_E/G_M \approx 1$ scaling. With data from backward angle TOFs, not included in this thesis, the BLAST measurement of $\mu G_E/G_M$ extends to $Q^2 = 0.9 (\text{GeV}/c)^2$, high enough in Q^2 that the JLab measurement of $\mu G_E/G_M$ at the same value of Q^2 has dropped significantly below 1. There is a deferred proposal to measure $\mu G_E/G_M$ from elastic $\vec{p}(\vec{e}, e'p)$ at JLab in Hall C [119]. Just as FPP measurements of $\mu G_E/G_M$ were pioneered at MIT-Bates and then repeated at JLab, our experiment may provide valuable input into future polarized target JLab measurement, which can be done to much higher Q^2 . Finally, as higher order radiative corrections are developed to reconcile the polarized and unpolarized data, our measurements at low Q^2 can constrain the theory at the point where the corrections are small.

Chapter 2

Experimental Setup

The measurement of $\mu G_E/G_M$ was performed in the South Hall Ring (SHR) of the Bates Linear Accelerator Center, using the Atomic Beam Source (ABS) and the BLAST detector package. These three key components (the polarized beam, polarized target, and detectors) are described below.

2.1 Polarized Beam

2.1.1 Polarized Source

The polarized electron source [120] uses a strained GaAs crystal photo-cathode illuminated by a circularly polarized laser, similar to polarized sources at JLab and SLAC. The strain in the GaAs crystal removes the degeneracy in energy levels, increasing the maximum polarization from 50% to 100% at the expense of low quantum efficiency. In practice, the polarization is limited to about 80% by electron depolarization during diffusing to the surface and by strain relaxation. Therefore the active layer must be very thin, on the order of 100 nm. The work function of the crystal is decreased by mono-layer coating of cesium, which must be restored about once a week.

The high polarization is gained at the expense of low quantum efficiency, about 0.1%. Thus it is necessary to illuminate the photocathode with an intense laser beam. The Bates polarized source uses a commercially available 150 W fiber-coupled diode

array laser system at the fixed wavelength of 808 nm. Special GaAs crystals optimized for this higher wavelength have been grown by Bandwidth Semiconductor and a group in St. Petersburg, and crystals from both groups generate a polarization in excess of 75%. Also a pre-prebuncher was installed to increase the electron capture efficiency from 30% to 50%. With these improvements, the source was able to inject 6 mA into the accelerator.

The laser beam is passed through a linear polarizer and a $\lambda/4$ wave-plate before being focused on the photo-cathode. The beam helicity is reversed by the mechanical insertion of a $\lambda/2$ wave-plate into the beam. This is controlled automatically by the beam-fill software. A Wien filter in the polarized source selects the spin direction such that after acceleration, recirculation, and transport, the beam is longitudinally polarized in the region of the internal target.

The beam polarization at the source is periodically measured with a transmission polarimeter [121], consisting of a bremsstrahlung radiator followed by a 6" steel core absorber magnet. The longitudinal polarization of the beam is transferred to the bremsstrahlung photons, which are monitored before and after the absorber with scintillators. The beam polarization is extracted from the asymmetry in the helicity dependent transmission of bremsstrahlung photons through the absorber. The transmission polarimeter was cross-calibrated against the S-Line Møller polarimeter during the SAMPLE experiment [122].

2.1.2 Storage Ring

The polarized electrons are accelerated up to 1 GeV by the linear accelerator and injected into the South Hall Ring (SHR). The linac has 190 m of RF cavities with a duty factor of 1%, capable of energies up to 540 MeV. A recirculator transports the beam back to the beginning of the accelerator for a second pass through the RF cavities, nearly doubling the beam energy. Figure 2-1 shows a plan of the MIT-Bates Linear Accelerator Facility with the accelerator, SHR, and experimental halls.

The SHR [123] may either be operated in pulse stretcher mode for external targets or as a storage ring for internal targets. The ring specifications during this experiment

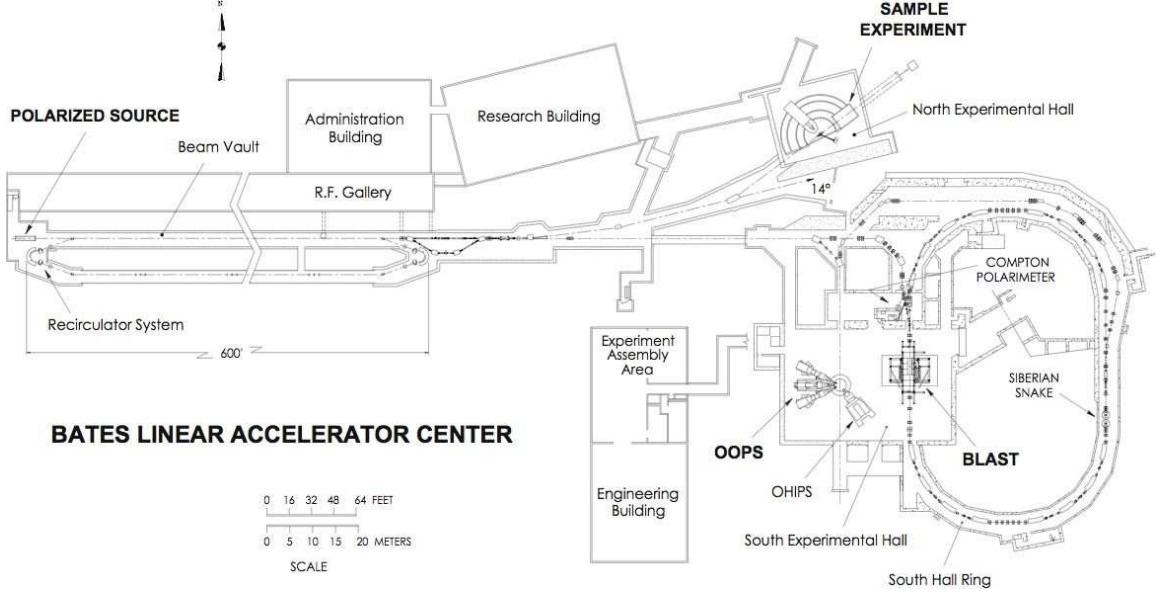


Figure 2-1: Plan of the BATES Linear Accelerator Center.

are listed in Table 2.1. The SHR has a symmetric race track design with 16 dipole magnets each bending the beam 22.5° . An RF cavity in the ring compensates for energy loss due to synchrotron radiation and stabilizes the energy in the ring. There are 32 beam position monitors (BPM) throughout the ring, a synchrotron light monitor to measure the beam profile in x and y , and a tune sweeper, which is a destructive monitor. Four plastic scintillator beam quality monitors (BQM) are placed around the beam pipe close to the interaction region to help the operators to tune the ring and reduce the background radiation in the detectors. There are also top, bottom, left, and right beam scrapers to reduce the beam halo, and a 10 mm diameter aperture tungsten collimator placed immediately before the target cell to protect it from injection flash and synchrotron radiation damage.

The spin vector S of electrons in the ring precesses according to the Bargmann, Michel, and Telgdi (BMT) equation [121]

$$\frac{d\mathbf{S}}{dt} = \frac{e}{\gamma mc} \mathbf{S} \times ((1 + a_e \gamma) \mathbf{B}_\perp - (1 + a_e) \mathbf{B}_\parallel), \quad (2.1)$$

where $a_e = \frac{1}{2}(g - 2) = 0.001159652187(4)$ is the electron gyromagnetic anomaly. The

Beam energy	E	$850.0 \pm 0.8 \text{ MeV}$ ($\gamma = 1663.$)
Beam spread	ΔE	0.20 MeV
Sync. Loss/Turn	U_0	5.1 keV
Max. Current	I	230 mA
Lifetime	τ	30 min
Beam Polarization	P_b	$0.6558 \pm 0.0007 \pm 0.04$
Ring length	L	190.205 m
Harmonic number	h	1812
Rev. Frequency	$\beta c/L$	1.577 MHz
RF frequency	$\approx h\beta c/L$	2856 MHz
RF Wavelength	$\approx L/h$	10.5 cm
Bending radius	ρ	9.144
Magnetic rigidity	$B\rho$	2.8353 T m

Table 2.1: South Hall Ring (SHR) specifications.

magnetic field of the dipoles $\int B_y ds = 2\pi B\rho = 17.814 \text{ Tm}$ precesses the spin in the plane of the ring. Due to momentum spread of the beam, it also diffuses the spin of individual electrons, depolarizing the beam. To maintain longitudinal polarization at the interaction point, the ring includes a full Siberian snake on the opposite side of the ring from the internal target. The snake, designed at the Budker Institute of Nuclear Physics in Novosibirsk, is composed of two superconducting solenoids with maximum combined integrated field of $\int ds B_{\parallel} = 10.5 \text{ Tm}$ and additional quadrupole magnets to restore the optical transparency of the system. The solenoids rotate the spin 180° about the beamline so that the spin precession in the north half of the ring compensates for that in the south half. In the second pass, the residual precession of the spin at the interaction point is also rotated about the beam line, compensating for differences between the two halves of the ring.

The beam energy $E = 850.0 \pm 0.8 \text{ MeV}$ was calibrated from a precise field-map of the integrated magnetic field along the dipoles in the ring [124]. This calibration was cross-checked to a precision of 6×10^{-6} at $E = 370 \text{ MeV}$ by measuring the spin precession in the ring without the snake [121]. The RMS energy spread in each RF bucket is $\Delta E/E = 0.024\%$.

The beam current is measured non-destructively with the Lattice DC Current

Transformer (LDCCT), a parametric current transformer developed by Unser [125]. The technology used to measure DC currents is a saturatable core primary winding around the beam with a nonlinear magnetic response to current. It is coupled to a secondary winding which is driven with a fixed signal. Pickup electronics measure the second harmonic generated by the nonlinear response, which is proportional to the absolute beam current passing through the coil with absolute accuracy of 0.05%.

The LDCCT signal is output to both a 16 bit ADC, which is read as an EPICS variable (Sec. 2.4.2), and to a voltage-to-frequency (V2F) converter. The number of oscillations of the V2F, proportional to the integrated beam current, are counted in two scaler channels, DCCT and BDCCT. The latter is gated by the trigger supervisor inhibit signal when the data acquisition is busy, when the target is in a transition between well-defined states, or when the high voltage trips or is put to standby. Thus the BDCCT scaler measures the actual charge passing through the target while the experiment is taking data, which eliminates the need to be correct the yields for deadtime. This is important in the case where correctable false asymmetries prevent applying an overall deadtime dilution factor to the physics asymmetry. The DAQ deadtime fraction, $1 - \text{BDCCT}/\text{DCCT}$, is determined from these two scalers.

The LDCCT is monitored regularly with current injected into a calibration loop and measured with an ammeter with 1 pA resolution, also output to EPICS. The beam scalers were calibrated during fake runs in which the beam was turned off and currents ranging from 0–200 mA in steps of 5 mA were injected in the calibration loop. The calibration from this data, good to 0.5% for currents over 20 mA, is

$$Q = (2.90027 + 3.01409 \times 10^{-4} S + 6.18094 \times 10^{-10} S^2) \text{ mC}, \quad (2.2)$$

where S is the DCCT or BDCCT scalers value after a pedestal subtraction of 2400 counts. Currents up to 300 mA have been stored in the ring, but to prevent radiation damage to windows and to the target cell, our experiment was limited to 195 mA in the ring until the last few days, when it was increased to 225 mA.

2.1.3 Compton Polarimeter

The absolute beam polarization in the ring is passively monitored with a Compton polarimeter [126, 127], which measures the helicity asymmetry of polarized photons backscattered from the beam. The analyzing power of this process is below 3% at energies less than 1 GeV. In addition, the Compton edge (the maximum kinetically allowed backscattering energy) is very low compared to the maximum bremsstrahlung energy, making background separation difficult, especially at large beam currents.

The polarimeter uses a 532 nm laser circularly polarized by a helicity Pockels cell with fast helicity reversal and chopped with a mechanical wheel to simultaneously measure the background. The laser interacts with the beam with a crossing angle less than 2° , made possible with four remotely steered mirrors placed in a polarization-preserving configuration. The interaction point is upstream of the target to reduce backgrounds. The photons are backscattered in a narrow cone, detected by a CsI scintillator crystal, selected for its fast timing and good energy resolution.

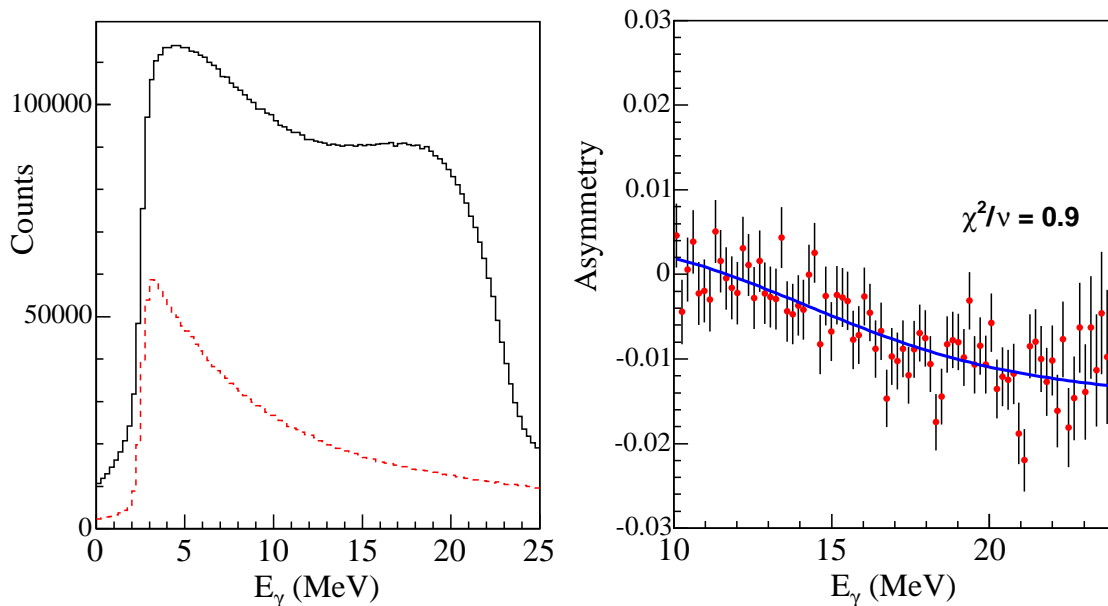


Figure 2-2: The yield (left) and asymmetry (right) of the Compton polarimeter during one fill of the storage ring. The total yield (solid black curve) is shown with the the background (dashed red curve). The laser helicity asymmetry is fit to the theoretical asymmetry to extract the beam polarization.

To handle the high rates (on the order of 100 kHz), the phototube signal is digitized into a 12-bit flash ADC with 100 MHz sampling. The pulses are energy resolved, helicity-sorted, and histogrammed in the CPU of the readout controller. The raw histograms are fed into the CODA data-stream and also analyzed in detail online. The typical energy dependent cross section and helicity asymmetry from one fill is shown in Fig. 2-2. With this setup, the beam polarization in a single fill could be measured to a statistical accuracy of 5%. The systematic error is 4%, mainly due to uncertainty of the analyzing power and beam alignment. The beam polarization measured by the Compton polarimeter over the duration of this experiment are shown in Fig. 2-3. The average polarization was $P_b = 0.6558 \pm 0.0007$ (stat) ± 0.04 (sys).

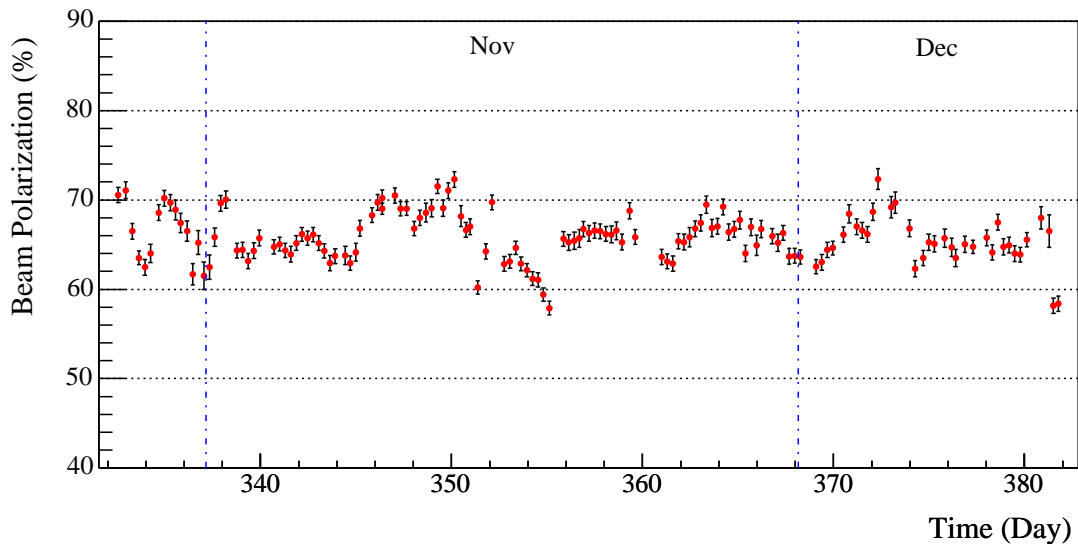


Figure 2-3: Time-dependence of the beam polarization.

The Compton polarimeter reported a small difference between the polarization of the two beam helicities. Unequal polarizations of the two helicity states would have affected the $H(e, e'p)$ asymmetry as a dilution. However, this difference was a false asymmetry and could be minimized by adjusting the tune of the ring, the alignment of the laser, and the position of the collimator before the scintillator. To verify that the two polarizations were indeed the same, a spin flipper [128] was installed downstream of the target. The helicity of the beam was flipped by ramping the frequency of an

RF dipole magnet through an RF-induced depolarizing resonance. By comparing the polarization before and after the spin flip for injections of both helicities (Fig. 2-4), the polarizations of both beam helicity states were verified to be the same within error.

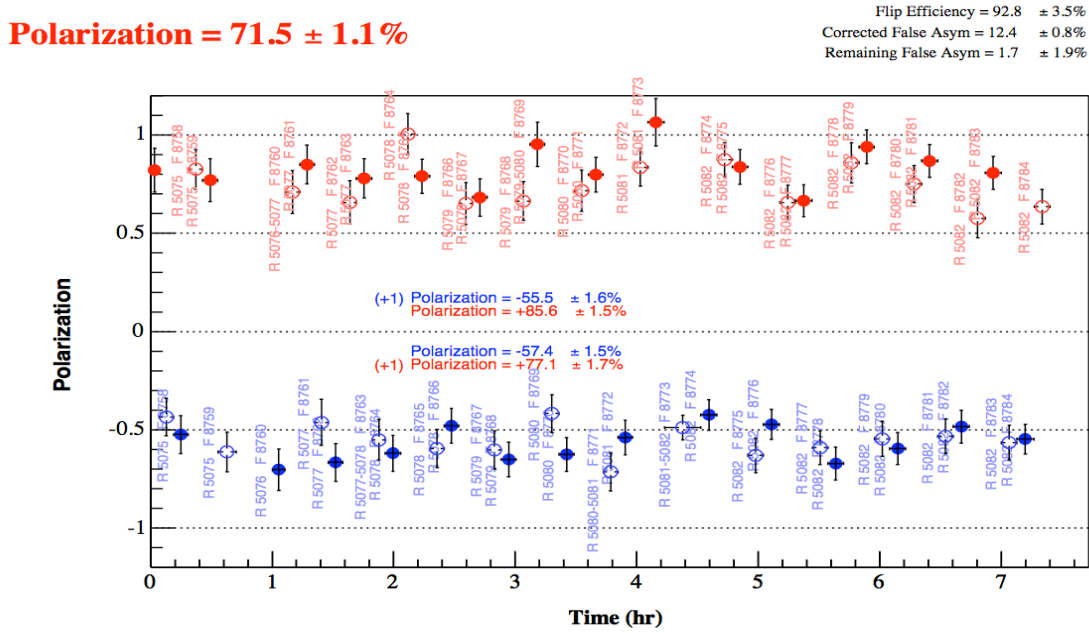


Figure 2-4: Beam polarization fill by fill during runs with the spin flipper. The solid points are for new fills, and the hollow points are for after the spin has been flipped.

2.2 Polarized Targets

Two polarized hydrogen/deuterium sources have been developed for use at BLAST: an Atomic Beam Source (ABS), and a Laser Driven Source (LDS). Polarized atoms from either type of source are injected into an open-ended cylindrical cell in the beam line to form an internal target. An internal target has several nice features:

- High polarization for both hydrogen and deuterium. In addition, systematic errors due to the beam current and target density variations are reduced by frequent reversal of the target polarization.

- Low backgrounds as the target is a pure atomic species. Also, there are no beam entrance or exit windows.

However, the thickness of internal targets is limited and must be compensated by an intense electron beam and a large acceptance spectrometer in order to attain practical event rates.

The ABS is based on standard technology and has been used in numerous nuclear and high energy physics laboratories, including NIKHEF (AmPS), DESY (HERMES), IUCF, BNL (RHIC), and COSY. An intense atomic beam is formed of dissociated hydrogen/deuterium directed through a cryogenic nozzle, skimmer, and collimator. The atoms are nuclear polarized passively by a series of Stern-Gerlach type spin filters and RF transitions before being injected into the storage cell. This source produces very high target nuclear polarization P_t , but with limited target thickness ρ .

The LDS is a novel source which actively polarizes hydrogen/deuterium atoms via the transfer of angular momentum from a circularly polarized laser. There is no need for spin filtering and all of the gas passes through to the target cell. As a result, the polarization is lower, but the target thickness is substantially greater, allowing for a higher overall figure of merit. An LDS was used at IUCF for polarized pd scattering [129]. Although not as common for polarized hydrogen/deuterium targets, optical pumping is the standard method of polarizing the noble gases He and Xe.

A comparison of the performance of both types of targets is shown in Table 2.2. The figure of merit (FOM) $\mathcal{F} = \rho \cdot P_t^2$ is a measure of the statistical precision obtained from a given experimental run time. Only the atomic polarization P_e was measured in our LDS, but the nuclear polarization P_t is related by

$$P_t = \frac{P_e f_\alpha}{f_\alpha + \sqrt{2}(1 - f_\alpha)} \quad (2.3)$$

under the assumption of spin temperature equilibrium (STE), which has been established by experiments at Erlangen [130] and IUCF [129]. We assume the worst case, that hydrogen atoms are completely depolarized after recombining into molecules.

The experimental data for this thesis were measured using an ABS target; however, we also describe the LDS because of our major role in its development.

	HERMES ABS [131]		IUCF LDS [132]		BLAST ABS		MIT LDS
	H	D	H	D	H	D	H
Gas							
Φ [10^{16} atoms/s]	4.4	2.4	100	72	2.6	2.6	110
ρ [10^{13} atoms/cm ²]	11.	10.5	30	30	4.9	4.5	150
f_α			~ 0.48	~ 0.48			0.56
P_e (atomic)			~ 0.45	~ 0.45			0.37
$\langle P_t \rangle$	0.78	0.85	0.145	0.102	0.80	0.86	[.175]
\mathcal{F} [10^{13} atoms/cm ²]	6.7	7.6	0.63	0.31	3.1	3.3	4.7

Table 2.2: A comparison of the figure of merit of ABS and LDS targets including those developed for BLAST. $\langle P_t \rangle$ for the MIT LDS was not measured, but calculated using Eq. 2.3.

2.2.1 Atomic Beam Source

The BLAST Atomic Beam Source is described in detail in Ref. [133]; in this section we give only a brief overview of the ABS and a few details specific to the hydrogen data. The ABS was originally built at NIKHEF, and was moved to Bates after the electron accelerator and AmPS storage ring at NIKHEF were closed. Since then most of the components were redesigned or replaced to adapt the ABS for operation in the restricted geometry and large magnetic field of the BLAST environment.

The components of the ABS are illustrated in Fig. 2-5. Molecular hydrogen is dissociated by the intense radio frequency (RF) field of the dissociator in the first chamber. A cryogenic nozzle at the outlet of the dissociator forms an atomic beam. A small amount of oxygen flows through the dissociator, combining with the hydrogen to form an ice coating on the nozzle and increase the degree of dissociation. The beam intensity was optimized by adjusting the nozzle temperature and hydrogen flow rate. The atomic beam is further collimated by a skimmer between the first two chambers. The chambers are differentially pumped by three turbo pumps located on the mezzanine above BLAST. The beam is filtered in the desired spin states though

a series of sextupole magnets and RF transitions, described below. The sextupole magnets also serve to focus the polarized beam into the storage cell, where the electron scattering occurs. The gas target is monitored from a small sampling hole below the holding cell. The relative intensity of the molecules and of the two atomic spin states in the sampling beam are measured using a gradient dipole and three compression tubes with ion gauges.

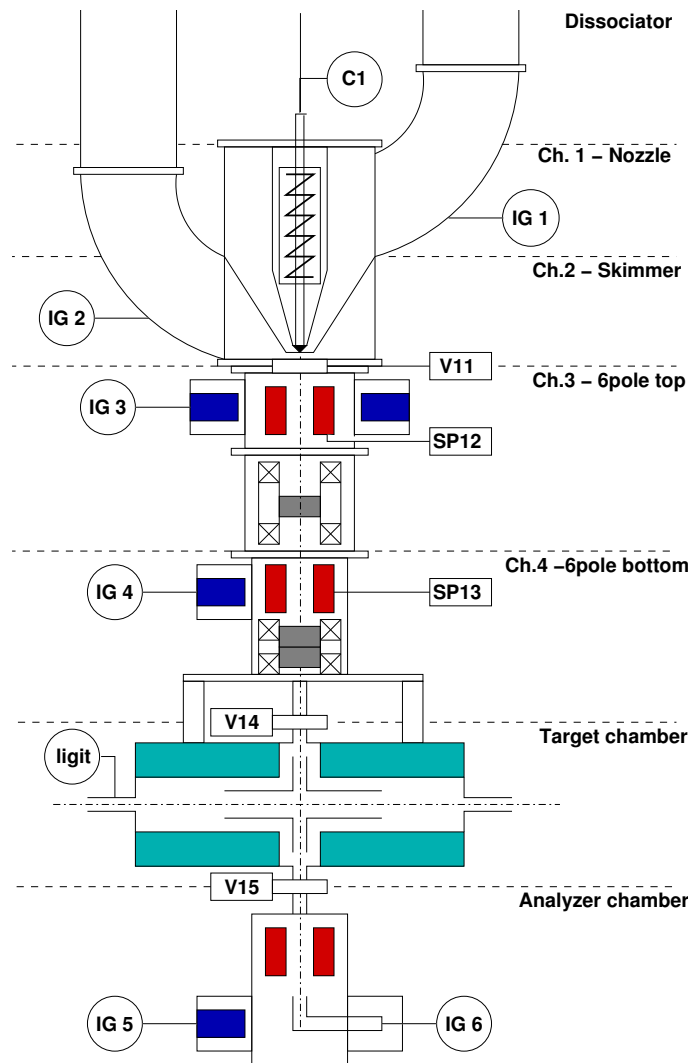


Figure 2-5: Schematic of the Bates Atomic Beam Source (ABS).

The atomic states are filtered by two sets of sextupole magnets. As the beam

passes through the sextupole, the spin of the atoms are adiabatically aligned to the radial field. The strong magnetic gradient of the sextupole exerts the force

$$\mathbf{F} = \nabla(\boldsymbol{\mu} \cdot \mathbf{B}) \quad (2.4)$$

on the atomic electrons, focusing the atomic states with electron spin up and defocussing the spin down states. A simulation of the atomic beam passing through the sextupole optics of the ABS is shown in Fig. 2-6.

The ABS is embedded in the BLAST toroidal magnetic field, and it was discovered that the ABS intensity was reduced by almost a factor to two while the toroid was energized. Although the constant BLAST field did not change the magnitude of the gradient force, it did affect its direction. As a result the atoms were not properly focused into the target cell. This was problem was solved by placing magnetic shielding around the sextupoles, which restored the nominal thickness of the ABS. Other improvements to the ABS system included adding extra pumping and replacing the weak sextupole magnets with stronger ones which could tolerate higher temperatures.

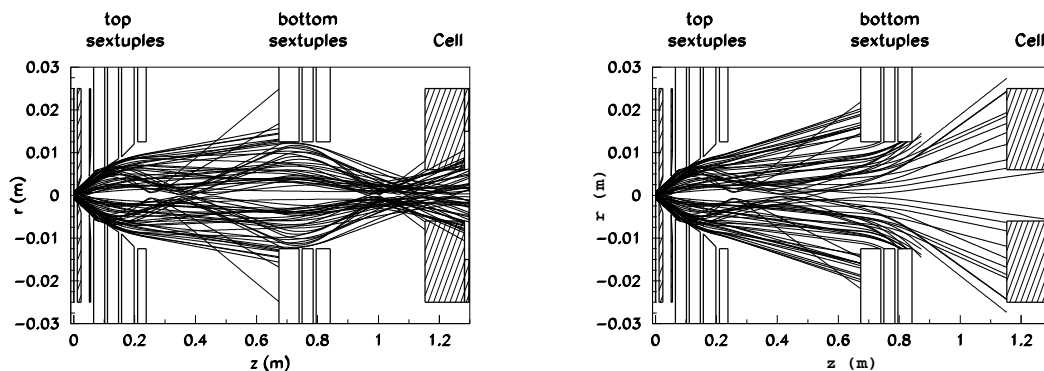


Figure 2-6: Simulations of the atomic beam passing through the ABS optics [133]. The first sextupole system focuses atoms in hyperfine states with $m_S = \frac{1}{2}$ ($B \gg B_c$). In the left figure the electron spin transitions from $m_S = +\frac{1}{2}$ to $m_S = -\frac{1}{2}$ between the two sets of sextupoles and get defocused in the second. In the right figure the atoms keep their electron spin and get focused in the second sextupole set.

Only atomic spin states can be selected by the sextupoles, since the magnetic

moment of the electron is three orders of magnitude larger than the nuclear magnetic moment; thus, adiabatic RF transitions are also needed to polarize the atomic beam in a specific state. In a static magnetic field, the degeneracy of the hyperfine multiplets of the hydrogen atom is broken. The energy splitting increases linearly with the magnetic field until near the critical field $B_c = E_{hf}/g\mu_B = 507$ Gauss, where hyperfine coupling is broken. E_{hf} is the separation of hyperfine multiplets at $B = 0$, and $g \approx 2$ is the electron gyromagnetic ratio (Eq. 2.1). The energy levels of hydrogen and deuterium are shown in the Breit-Rabi diagrams of Fig. 2-7. The addition of a time-varying RF field of frequency $h\nu = \Delta E$ will cause a resonance between two hyperfine states separated by energy ΔE , and the spin will oscillate between these two eigenstates. To ensure an efficient transition even for atoms spending different amounts of time in the transition region, a gradient magnetic field is added along the path of the atomic beam. This guarantees that adiabatic passage between two states occurs exactly once, resulting in close to 100% efficiency.

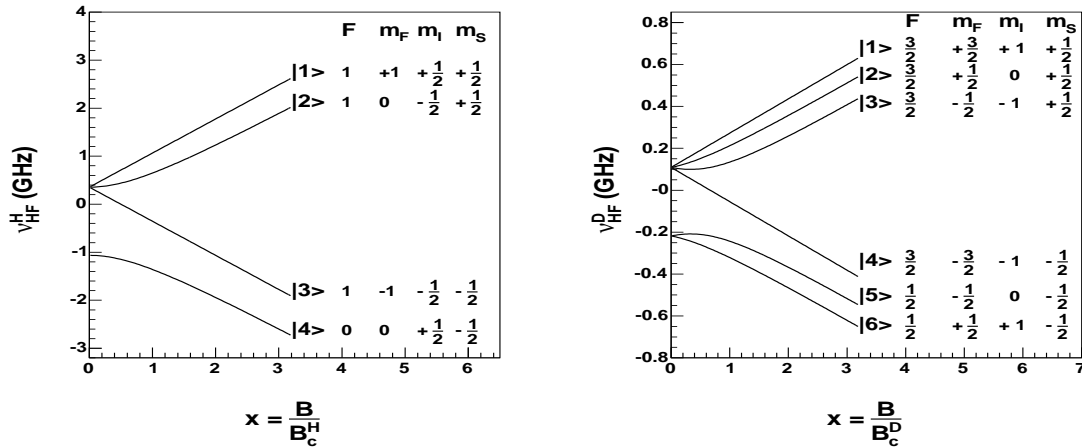


Figure 2-7: Breit-Rabi diagram of the energy levels of hydrogen (left) and deuterium (right) in the presence of a magnetic field.

There are three types of RF transitions (SFT, MFT, WFT) characterized by ΔF , Δm_F , the direction of the RF field, and the strength of the static field. An RF field parallel to the static field induces a σ -transition ($\Delta m_F = 0$), while a perpendicular field induces a π -transition ($\Delta m_F = 1$). Strong field transitions (SFT) are charac-

terized by $\Delta F = 1$, while medium and weak field transitions (MFT, WFT) exchange states among the same hyperfine multiplet ($\Delta F = 0$). Only the MFT and WFT are used to polarize hydrogen.

In strong magnetic fields where $B \gg B_c$, the nuclear and electronic spin states decouple, and the nuclear spin is a good quantum number: $m_I = \frac{1}{2}$ for states $|1\rangle$, $|4\rangle$, and $m_I = -\frac{1}{2}$ for states $|2\rangle$, $|3\rangle$. However if the holding field is not strong enough, there is a residual hyperfine interaction which lowers the polarization of states $|2\rangle$ and $|4\rangle$. Therefore, our experiment was carried out using single state injection of the pure states $|1\rangle$ and $|3\rangle$, which do not mix via the hyperfine interaction. State $|3\rangle$ is prepared through the series of sextupole filters and RF transitions

$$\begin{pmatrix} n_1 \\ n_2 \\ n_3 \\ n_4 \end{pmatrix} \xrightarrow{6-pol} \begin{pmatrix} n_1 \\ n_2 \\ 0 \\ 0 \end{pmatrix} \xrightarrow{MFT \pi_{23}} \begin{pmatrix} n_1 \\ 0 \\ n_2 \\ 0 \end{pmatrix} \xrightarrow{6-pol} \begin{pmatrix} n_1 \\ 0 \\ 0 \\ 0 \end{pmatrix} \xrightarrow{WFT \pi_{13}} \begin{pmatrix} 0 \\ 0 \\ n_1 \\ 0 \end{pmatrix}, \quad (2.5)$$

where n_i are the initial population density of each state. For state $|1\rangle$ injection, the last transition (π_{13}) is omitted; this is the only difference between the preparation of the two target polarization states. The WFT requires a lower gradient field, improving the transition efficiency; therefore asymmetry in the intensity and polarization of the two target states is expected to be small. Indeed this was observed in measurements of the target false asymmetry (Sec. 3.4.6).

The atomic beam is injected into a cylindrical storage cell, which increases the target thickness in comparison to a pure atomic beam. The inlet of the storage cell is also a cylinder with approximately the same conductance as either half of the storage cell. The cell is cooled to about 100 K. The experiment was commissioned with a 40 cm long storage cell, while the the production data were taken with a 60 cm cell.

There are transverse and longitudinal coils wound around iron yokes above and below the scattering chamber to create a holding field of arbitrary direction. The spin orientation of the target is adjusted by varying the current in each set of coils. Data were taken at two spin angles, $\beta = 47.2^\circ$ and $\beta = 31.4^\circ$. After the production run, the

magnetic field was measured every 2 cm along the target using a three dimensional Hall probe. The alignment of the probe was only known to 1° , but plans are underway to calibrate the alignment better than 0.3° after the 2005 deuterium run.

2.2.2 Laser Driven Source

Laser driven sources have been developed at Argonne National Laboratory [134], the University of Illinois at Urbana-Champaign (UIUC) in 1994 [135] and at the University of Erlangen in 1995 [136]. The UIUC target was moved to IUCF and used in experiments CE-66 and CE-68 [129, 137, 138]. The current LDS developed for BLAST has improved the figure of merit by optimizing the spin-cell geometry [139, 140]. We describe the general technique of the LDS, the setup of the MIT target, and its performance.

Optical Pumping and Spin Exchange

The LDS is based on the technique of optical pumping, in which atoms are polarized through the transfer of angular momentum from a circularly polarized laser beam to the valence electrons. The σ_+ photon couples to the $m_j = -\frac{1}{2} \rightarrow \frac{1}{2}$ transition from the ground state to an excited state. The excited state decays to $m_j = +\frac{1}{2}$ as in Fig. 2-9, polarizing the ground state after many cycles. For hydrogen atoms, the ground state transitions are in the XUV range ($L_\alpha = 12.1$ nm) for which there are no high-powered lasers or efficient optics. Thus hydrogen must be polarized through an intermediate species. The three steps in this process, optical pumping, spin exchange collisions, and nuclear polarization via hyperfine interactions, are illustrated in Fig. 2-8.

Alkali vapors are ideal for pumping because they are atomic, they have a single valence electron, and their ground state is $J = \frac{1}{2}$. The optimal alkali atom to use is a compromise between several factors. The low Z atoms have a small hydrogen spin-exchange cross section, must be operated at higher temperatures, and react more strongly with the spin-cell coating, which is used to preserve the hydrogen atomic dissociation and polarization. However, the Møller cross section is proportional to Z^2 .

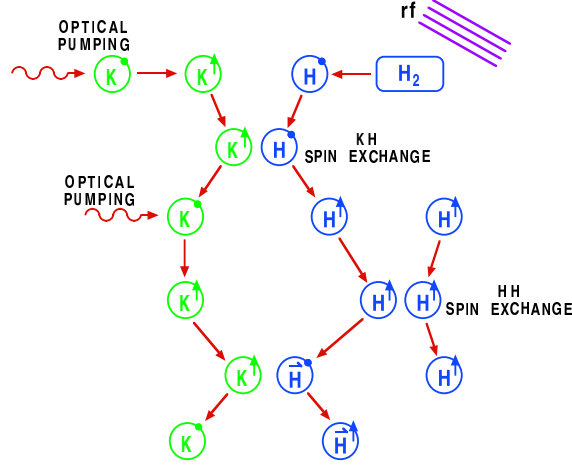


Figure 2-8: The hydrogen pumping cycle: a) alkali atoms are optically pumped and b) transfer their polarization to hydrogen atoms via spin-exchange collisions, and c) the nucleus is polarized through H-H hyperfine interactions.

Møller scattering reduces the stored beam lifetime and is a background to the $H(e, e'p)$ process. Considering these requirements, the optimum alkali for optical pumping is potassium. Potassium atoms are pumped with the $(3p)^6(4s)^2S_{1/2} \rightarrow (3p)^6(4p)^2P_{1/2}$ transition (D_1) of wavelength 770.121 nm in vacuum, illustrated in Fig. 2-9.

Consider the σ_+ transition from $m_j = -\frac{1}{2} \rightarrow +\frac{1}{2}$, which decays to the $m_j = -\frac{1}{2}$ and $\frac{1}{2}$ ground states with the branching ratios $\frac{2}{3}$ and $\frac{1}{3}$, respectively. For $m_j = +\frac{1}{2}$, there is no net increase in the potassium polarization and the radiated photon is still polarized. For $m_j = -\frac{1}{2}$, the radiation may depolarize other K atoms. Walker and Anderson [141] showed that this radiation trapping can be weakened by optical pumping in a strong magnetic field. The Zeeman shift in a 1 kG field is 0.0036 nm, large enough to separate the Doppler-broadened profiles of the σ_+ and σ_- resonances. Negative polarization is achieved by reversing the helicity of the laser and tuning to the $\sigma_- D_1$ transition.

Polarization is transferred from the potassium to the hydrogen atoms and then protons via spin exchange collisions. In time, the system approaches spin temperature equilibrium (STE), in which the hydrogen atomic and nuclear polarizations are equal. In a strong magnetic field, the atomic and nuclear spins decouple and as a result, the

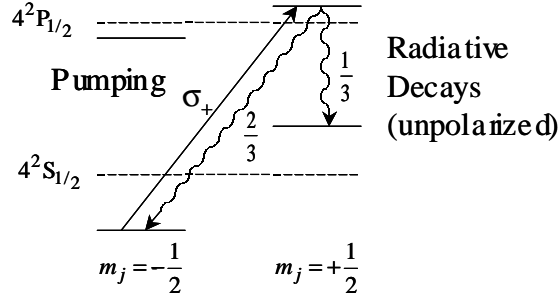


Figure 2-9: Optical pumping of potassium, the energy levels of the D1 line without a magnetic field (dashed lines) are split in a strong magnetic field. Absorption of right circularly polarized photons leads to depopulation of the $m_j = -1/2$ state.

hyperfine interaction is weak. However, the H-H collision rate per atom is proportional to the H density, and even in a strong field, a dense enough target will have enough hyperfine interactions to approach STE [141].

The performance of an LDS target depends critically on the atomic polarization. Most depolarization occurs during wall collisions, as the atoms temporarily stick to the surface, where fluctuating magnetic fields can cause spin flips. Also, the kinetic energy is low enough on the surface to recombine with other atoms, forming (unpolarized) molecules. The spin exchange cell and storage cell are coated with drifilm (SC-77) [142] to prevent H from sticking on the walls. The cells must be heated to prevent potassium condensation, which would react with the coating. A magnetic holding field is also needed in the spin cell and target cell regions to keep the polarization of each atom from drifting in random directions, and also to decouple the nuclear and atomic spins.

Optimization of Spin-cell

The spin-cell design was optimized using a simple dynamical model assuming molecular flow through spin-cell, transport neck, and target cell system. Following [143], the conductance of a component $C = V/t$, or the volume V of gas passing through it

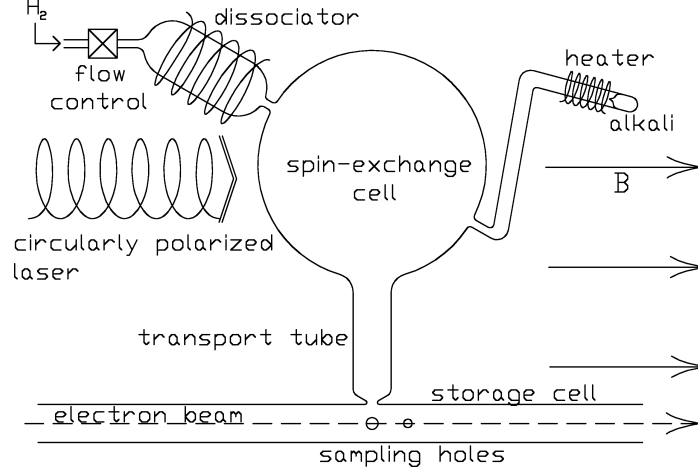


Figure 2-10: Laser-Driven Source (LDS) Schematic.

per time t is

$$C = \frac{\bar{v}A}{4} \times \begin{cases} 1, & \text{thin aperture of cross-sectional area } A; \\ \frac{4d}{3l}, & \text{tube of length } l \text{ and diameter } d, \end{cases} \quad (2.6)$$

In steady state, the gas flow rate $\Phi = N/t = nC$ through each component connected in series is conserved. The average particle speed is

$$\bar{v} = \sqrt{\frac{8k_B T}{\pi m}} = 1.455 \times 10^5 \text{ cm/s} \sqrt{\frac{T}{M}}, \quad (2.7)$$

where k_B is Boltzmann's constant, T is the temperature (in K), m is the mass, and M the atomic mass (in amu). Therefore H_2 is denser than H_1 at the same atomic flow rate, and the combined density is

$$n_H = \frac{\Phi}{C} (f_\alpha + \sqrt{2}(1 - f_\alpha)). \quad (2.8)$$

where $f_\alpha = 1/(1 + N_w \alpha_r)$ [144] is the fraction of hydrogen atoms in atomic state (per time, not volume) and C is the atomic conductance. The wall collision rate per atom (thought of in terms of conductance into the surface area A_S of the cell) is

$$\gamma_w = \frac{n C_{A_S}}{N} = \frac{\bar{v} A_S}{4 V}. \quad (2.9)$$

The dwell time of an atom in the spin-cell is $t_{dw} = V/C$ making the total number of wall collisions $N_w = \gamma_w t_{dw} = C_{A_S}/C$, where C is the total conductance from the spin-cell through the remainder of the system. A spin-cell of spherical geometry was chosen to minimize the surface area to volume ratio, although any compact geometry with rounded edges would have been effective.

The atomic polarization P_e of hydrogen is pumped through spin-exchange interactions with the potassium (polarization P_k) and depleted by wall collisions and by the replenishment of unpolarized gas,

$$\langle P_e \rangle = P_k \frac{\gamma_{se}}{\gamma_{HK} + \alpha_d \gamma_w + t_{dw}^{-1}} \frac{f_\alpha + \sqrt{2}(1 - f_\alpha)\alpha_m}{f_\alpha + \sqrt{2}(1 - f_\alpha)}. \quad (2.10)$$

The coefficients α_r and α_d are the probabilities of recombination and depolarization, respectively, during a wall collision; and α_m , the probability of remaining polarized after recombination, is negligible. The spin-exchange collision rate with potassium is

$$\gamma_{HK} = n_K \langle v_{rel} \sigma_{HK} \rangle, \quad (2.11)$$

where v_{rel} is the relative velocity between a hydrogen and a potassium atom.

In order to achieve $P_t \approx P_e$, the dwell time in the spin-cell must exceed the STE time,

$$t_{st} = \frac{1 + \left(\frac{B}{B_c}\right)^2}{n_H \langle \sigma_{HH} v_{rel} \rangle}, \quad (2.12)$$

where $B_c = 507$ Gauss is the critical field of the hyperfine interaction and $\langle v_{rel} \rangle = \sqrt{2}\bar{v}$ is average relative velocity between hydrogen atoms.

The figure of merit \mathcal{F} for optimization of the target a measure of the effective statistics measured under a given beam condition. For a physics asymmetry A measured with beam times target polarization $P = P_b P_t$, the measured asymmetry is $A_{exp} = PA$ and the statistical error is

$$\delta A^2 = \frac{\delta A_{exp}^2}{P^2} = \frac{1 - A_{exp}^2}{NP^2} = \frac{1 - P^2 A^2}{NP^2}. \quad (2.13)$$

The number of counts N depends on the target thickness ρ , so the figure of merit is

$$\mathcal{F} = \frac{\rho P^2}{1 - P^2 A^2} \rightarrow \rho P_t^2. \quad (2.14)$$

The target has a triangular density profile

$$n = n_0(1 - |2z/L|)(f_\alpha + \sqrt{2}(1 - f_\alpha)) \quad (2.15)$$

with both f_α and P_t decreasing along the length of the target cell due to wall collisions.

Table 2.3 lists the results from the spin-cell optimization computer simulation.

region		spin-cell	transport	target cell
geometry		sphere	cylinder	cylinder
dimensions		r=2.5 cm	l=5 cm d=7 mm	l=40 cm d=12.5 mm
number of wall collisions	N_w	640	96	768
number of K-H collisions	N_{KH}	11.1	0.4	3.0
number of H-H collisions	N_{HH}	444	25	120
dwel time in spin-cell	t_{dw}	6.8 ms	0.38 ms	3.9 ms
STE relaxation time	t_{st}	0.075 ms		
hydrogen flow rate	Φ	1.0×10 ¹⁸ atoms/s		
potassium fraction	n_K/n_H	0.67%		
potassium polarization	P_K	95%		
recombination coefficient	α_r	4.0×10 ⁻⁴		
depolarization coefficient	α_d	7.3×10 ⁻⁴		
spin-exchange cross section	σ_{HK}	7.4×10 ⁻¹⁵ cm ²		
hyperfine cross section	σ_{HH}	2.0×10 ⁻¹⁵ cm ²		

Table 2.3: Optimal spin-cell parameters.

The spin-cell, transport tube, and target cell were also modeled with a sophisticated Monte Carlo code [140], in which the atoms move ballistically until a wall collision, where they are emitted with a $\cos(\theta)$ distribution. The code includes the effects of optical pumping, radiation trapping, spin-exchange, depolarization, recombination, iterated on the atomic and nuclear and potassium polarizations and the atomic density. It calculates the polarization, density, degree of dissociation, and figure of merit. The resulting optimum configuration from this code was a cylindrical

spin-cell of length $3\frac{1}{2}''$ and diameter $3.5''$. The larger geometry has more potassium atoms at the same density to make more efficient use of the laser power.

Magnetic Field

The magnetic field in the spin-cell and target cell serves two purposes: a) it defines the spin quantization axis, and b) it breaks the degeneracy of the σ_+ , σ_- transitions to prevent radiation trapping. The requirement for non-overlapping σ_+ , σ_- transitions in potassium is that the Zeeman shift in frequency be larger than the Doppler-broadened line width. In a weak field, J is a well-defined quantum number, and the energy levels of an atomic state are split by

$$\Delta E = g \mu_B \mathbf{J} \cdot \mathbf{B}, \quad (2.16)$$

where $\mu_B = e\hbar/2m_e$ (Bohr magneton) and $g = 1 \pm \frac{1}{2}l + 1$ for $J = L \pm \frac{1}{2}$ (Landau factor). The D1 transition is split by $\Delta\lambda^Z = \frac{4}{3}\lambda^2\mu_B B/hc = 0.0036 \cdot B$ (nm/kG). The Doppler-broadened line shape for a Maxwellian velocity distribution is Gaussian with a FWHM of

$$\Delta\lambda_{1/2}^D = 7.16 \times 10^{-7} \lambda \sqrt{\frac{T}{M}},$$

where T is the temperature in K, and M is the atomic mass (amu). At 220°C , the Doppler line width of the D1 transition is 0.0020 nm; thus the field must be on the order of 1 kG in the spin-cell region for a clean line separation.

The condition for adiabatic transport requires a much smaller field, on the order of 20 G. It is important to minimize gradients in the holding field, which cause depolarization [145]. The spin relaxation time due to transverse gradients in the holding field is

$$\frac{1}{t_g} = \frac{\langle v^2 \rangle}{3} \frac{|\nabla B_x|^2 + |\nabla B_y|^2}{B_0^2} \frac{\tau_c}{1 + w_0^2 \tau_c^2}$$

where $w_0 = \gamma B_0$ is the Larmor frequency of hydrogen in the magnetic field, $\gamma = 4.258$ MHz/kG, $v = 3.1 \times 10^6$ cm/s is the average velocity of the H atoms at $T=500$ K, and $\tau_c = 1.53 \times 10^{-5}$ s is the mean time between collisions. The holding field coils

were designed to have gradients less than 13 G/cm, in which case the spin relaxation time is $t_g = 0.26$ s. This is much longer than the dwell time in the target, 3.9 ms.

Hardware Setup

The components of the LDS are shown in Fig. 2-11.

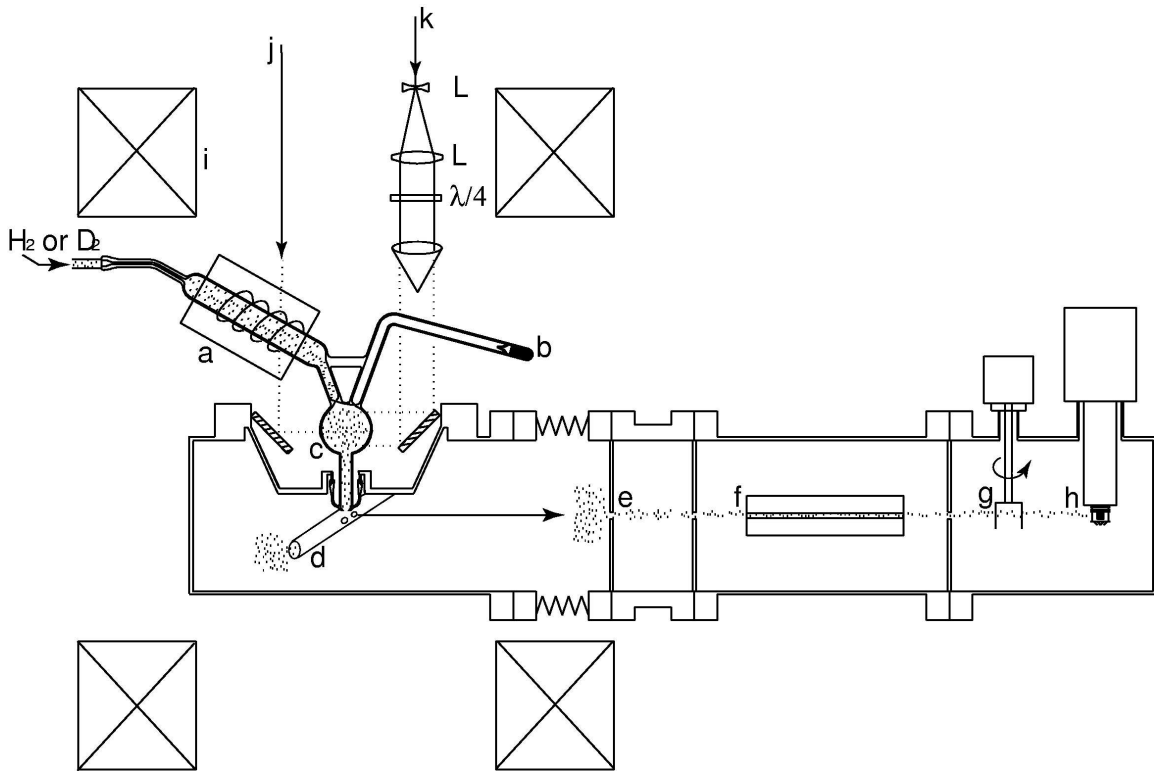


Figure 2-11: LDS Components: a) dissociator, b) potassium ampule, c) spin-cell (oven not shown), d) target cell, e) blank gasket apertures, f) permanent sextupole magnet, g) chopper, h) quadrupole mass analyzer, i) 0.1T holding field coils, j) laser beam for Faraday monitor, k) 3W Ti:Sapphire laser beam for optical pumping, l) beam expanding optics. The laser and magnetic field are shown in the plane of the page for illustration purposes, but are actually rotated by 90° so as to extend out of the page.

The Pyrex spin-cell has two inlets, one for hydrogen, and the second for potassium. It is connected to the target cell via a transport tube (neck). The end of the transport tube is shaped to fit tightly against the storage cell. The spin-cell and target cells are coated with a organosilane (SC-77 Drifilm) to prevent recombination and depolarization on the cell walls. The entire spin-cell and target cell must be uniformly heated

to over 180° to prevent condensation of potassium vapor on the walls. The spin-cell is enclosed in an oven made of high-temperature Torlon. The oven extends down into the entire transport tube region and is heated by forced air to reduce temperature gradients. The spin-cell and oven are mounted in the target test chamber with a $2\frac{3}{4}$ " Conflat flange welded to a glass-metal seal, as shown in Fig. 2-12. The potassium ampule is wrapped with heating tape and aluminum, and the storage cell is mounted in contact with a rod heater. During operation, the potassium density in the spin-cell is adjusted by heating the ampule, with the spin-cell and target cell kept at least 10° warmer to prevent condensation.

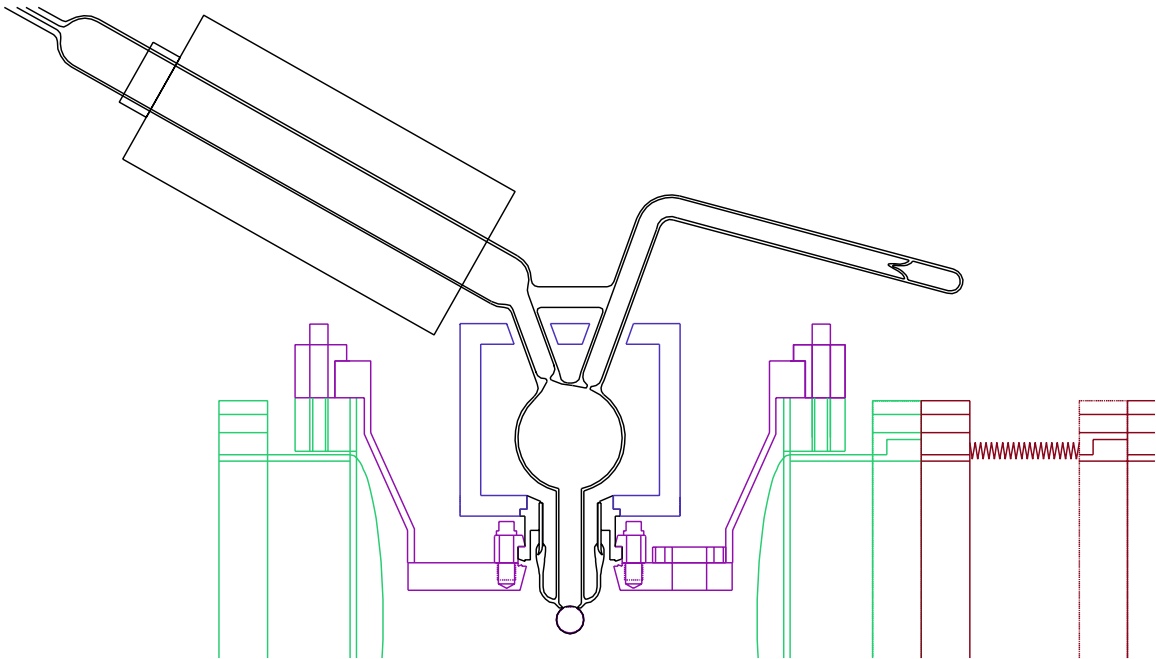


Figure 2-12: Spin-cell, oven, and vacuum seal mount to the chamber. The design allowed the entire spin-cell and transport tube to be heated by forced air, while maintaining a vacuum in the spin-cell and target chamber. The spin-cell is mounted to the chamber by a glass-metal seal and $2\frac{3}{4}$ " Conflat vacuum flange.

The gas distribution panel has two channels, one for H_2/D_2 , and the other for O_2 , which enhances the performance of the dissociator. The H/D flow is set by a MKS mass flow control unit, while the O_2 flow is adjusted with a needle valve. The entire panel can be evacuated via a pump line connected in between the two channels. A Baratron gauge measures the pressure downstream of the flow control.

The molecular H₂ gas is dissociated in an RF resonant cavity before entering the spin-cell. The gas panel is connected to the dissociator by flexible $\frac{1}{8}$ " metal tubing, a glass-metal seal, and a 12" long \times 1 mm inner diameter capillary to contain the plasma in the dissociator tube.

The RF resonator [146] has a 15 turn coil around the hydrogen tube with 1 turn coupling to an external RF source. The coil is connected at one end to the inside of a cylindrical brass grounding shield to form a distributed LC circuit/waveguide. The resonator is driven with 30 W of RF power at 100-160 MHz. The cavity is air-cooled on the inside and water-cooled on the outside, which improves the degree of dissociation. We unsuccessfully tried a double-walled dissociator with cooling water flowing through the outer layer of glass.

The restriction at the inlet to the spin-cell was adjusted to optimize the H₂ pressure in the dissociator. The efficiency of the dissociator was studied with standalone dissociators mounted directly to the target chamber in line with the polarimeter. The results of these studies are shown in Fig. 2-13.

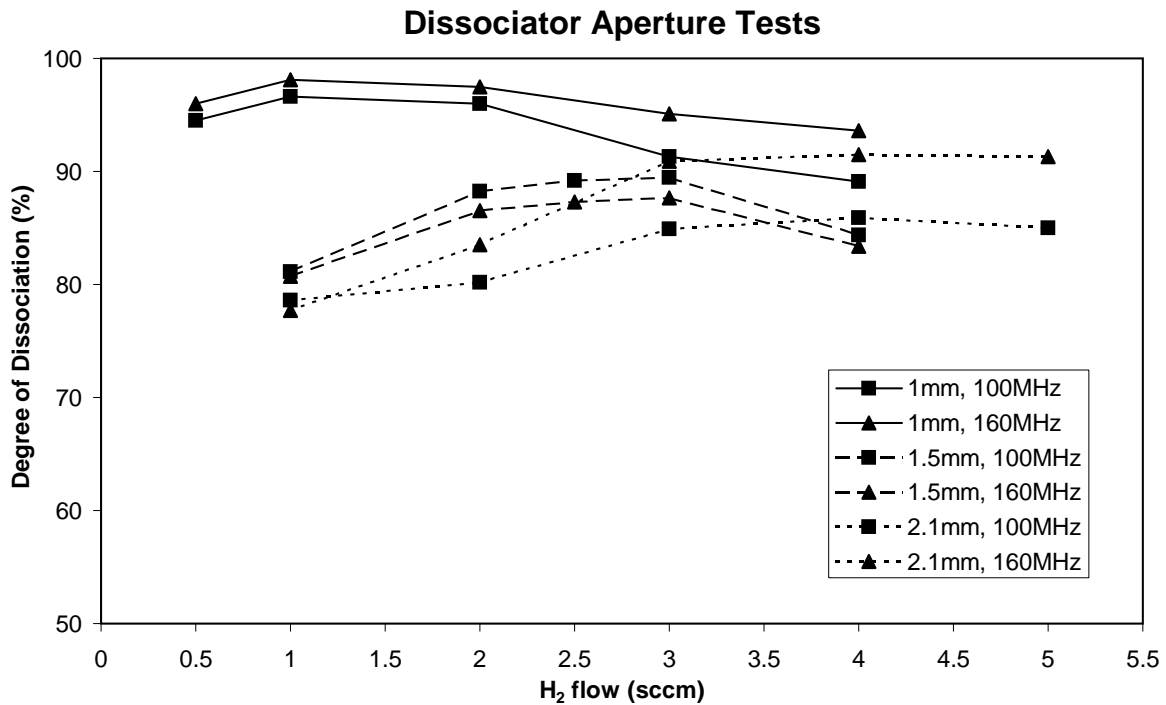


Figure 2-13: Performance of stand-alone dissociators with conductance limiters of different diameter apertures at the exit, and operated at two RF frequencies.

The target chamber was designed for flexibility to accommodate various configurations. The vacuum chamber has six way cross with 10" Conflat (CF) flanges on the top and bottom, and 8" CF flanges on each side. The rear port is connected to a Varian 1000HT turbo pump separated from the chamber and magnetic field by a 1 m extension pipe. The port on the right side couples to the polarimeter, and the other two side ports are used for feed-throughs and access to the chamber. The chamber is equipped with Granville-Phillips thermocouple and Stabil-Ion pressure gauges, and power and thermocouple feed-throughs for control of the target cell temperature. The spin-cell is mounted to an inverted cone on the top, recessing down into the chamber. The turbo pump and polarimeter are isolated by MDC 8" gate valves. The entire system of gas valves, vacuum gauges and valves, pumps, shutters, and Quadrupole Mass Analyzer (QMA) are automated by a custom electronic interface to LabVIEW with hardwired interlock circuits to protect the components in the case of power failure or software errors.

The LDS has two Helmholtz-like coils 12" apart with an 18" inner diameter. Each of the two coils is composed of 144 turns of $\frac{3}{8}$ " hollow water-cooled copper conductor. The coils draw 286 A at 50 V for a 1 kG field in the center of the spin-cell.

The laser system comprises a Spectra Physics 3900 Ti:Sapphire laser pumped with a 20 W Argon laser. The Ti:Sapphire laser has three elements for tuning the wavelength: a birefringent filter for coarse tuning, a thin etalon, and a thick etalon for fine tuning. The thick etalon is heated in an oven to control the wavelength up to 0.001 nm, and has line spacing of 0.040 nm. The oven temperature controller electronics were modified to accept an analog control signal from the computer. Thus the wavelength can be scanned through the σ_+ and σ_- D1 resonance lines. The thin etalon has a line thickness of 0.040 nm and has a manual threaded adjustment to select the range of the thick etalon. Similarly the birefringent filter angle is adjusted by hand to select the range of thin etalon line. A small fraction of the beam is split into a power meter and a wave-meter which is accurate to 0.001 nm. The line width is also monitored with a spectrum analyzer. All three diagnostics are recorded in LabVIEW.

The laser beam is passed through a Conoptics M360-50 Electrical-Optic Modulator (EOM) to broaden the narrow line-width to match the Doppler-broadened profile of the potassium absorption line. The EOM contains two crystals of Lithium Tantalate (LiTaO_3) with a diameter of 1.25 mm and combined length of 40 mm. It can handle up to 2.5 W of beam which must be focused fine enough to pass through the crystal, but diffuse enough not to burn the crystal. The modulator is driven by 20-450 MHz white noise from an Accu-Noise generator amplified to 20 W by a Minicircuits LZY-1 amplifier. The resulting line-width is about 1 GHz FWHM, which enhances the absorption of laser power by about 30%.

The beam is expanded to a diameter of 5 cm to fill the cross sectional area of the spin-cell. It passes through a linear polarizer and a $\lambda/4$ wave-plate to achieve circular polarization. The beam is periscoped down into the sunken spin-cell with two 45° polarization preserving mirrors, as there is no room for a polarization compensating optical setup. The transmitted beam through the spin-cell is monitored on the other end with a power monitor.

Both the dissociation fraction f_α and atomic polarization P_e are measured with a Stern-Gerlach type polarimeter. The polarimeter has two chambers separated by blank Conflat gaskets with a 3 mm hole in the center of each to collimate the atoms which escape from the sampling holes in the target cell. The apertures also serve as conductance limiters, and the polarimeter is differentially pumped with a Varian 300 L/s ion pump in each chamber and a NEG pump in the final chamber. The polarimeter is coupled to the target chamber by a 6" metal bellows section for two way alignment. The polarimeter is supported by a gimbal connected around the bellows to the target chamber, and balances on two load-bearing frictionless pads.

The first chamber has a shutter and a sextupole for filtering spin-states. The sextupole is 10 cm long with an outer diameter of 25 mm and a 5 mm tapered bore. The field strength at the pole tips is about 1.5 T. Simulations were done to determine the optimum distance of the sextupole from the detector.

The second chamber contains a chopper and Quadrupole Mass Analyzer (QMA) for measurement of the beam intensity. The chopper is a $3/8''$ steel rod with a slot

just larger than the beam profile, and is coupled to an external 1/4 W D.C. motor by a ferrofluidic seal. The frequency of the chopper is detected with an external optical interrupt circuit. The hydrogen and deuterium atomic and molecular beam intensities are detected with a Balzers Prizma QMA, with a cross beam ion source. The electronics for the QMA output a digitally synthesized analog signal with inadequate timing resolution for our chopper frequency. Therefore, we modified the electronics to extract the analog signal directly after the preamplifier. The QMA and chopper signals are fed into a DSP Lock-in Amplifier which interfaces with the LabVIEW computer automated control and measurement system.

The dissociation fraction and polarization are monitored via two sampling holes in the target cell: one directly at 90° to the input aperture and the second hole 2 cm downstream, to ensure that atoms were being sampled from the storage cell and not directly from the spin-cell. Background measurements taken by aligning the polarimeter away from the sampling holes are more accurate than the background measurements taken by closing the shutter. The typical signal to noise ratio is 30:1.

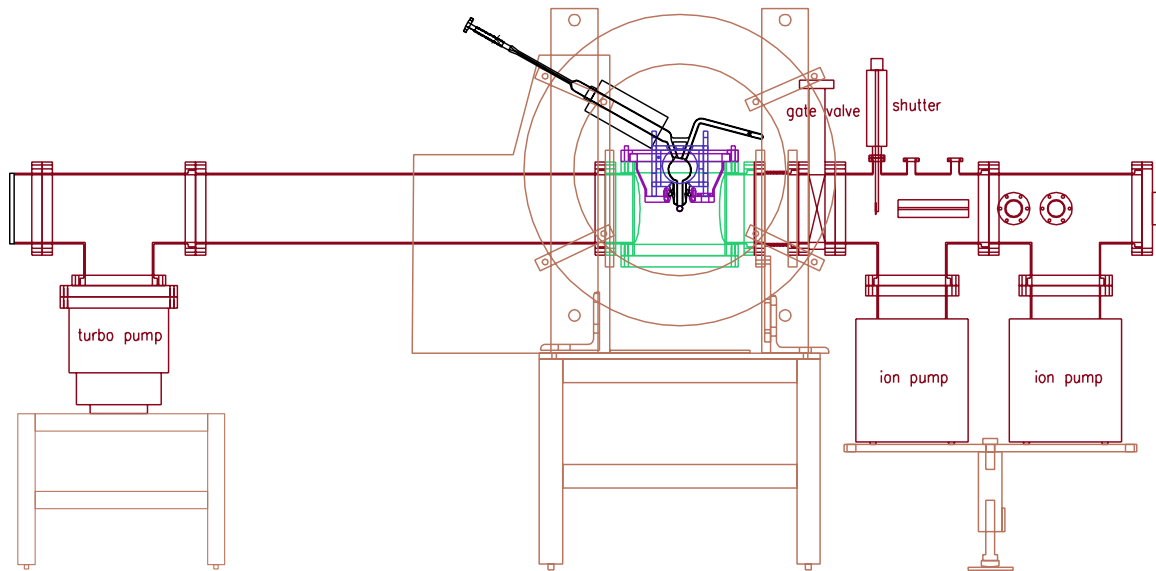


Figure 2-14: Drawing of the complete LDS apparatus including the target chamber, pumps, and holding field coils, and the polarimeter. The polarimeter is connected to the target chamber by metal bellows for alignment to the sampling holes in the target.

LDS Performance

The degree of dissociation and the atomic polarization are

$$f_\alpha = \frac{Y^2 - Y_r^2}{Y^2 - Y_b^2} \quad \text{and} \quad P_e = \frac{Y_r^1 - Y_{r\ell}^1}{Y_r^1 - Y_b^1}, \quad (2.17)$$

respectively, where Y^1 and Y^2 are the QMA yields for atomic mass 1 and 2 averaged over 30 s. The subscripts r , ℓ , and b refer to the RF turned on, the laser turned on, and the polarimeter misaligned, respectively. The background yields $Y_b^{1,2}$ are measured at the beginning of the run with the polarimeter misaligned from the sampling holes. The RF-off yields $Y^{1,2}$ were only measured before potassium was introduced into the spin-cell because of the difficulties in re-igniting the plasma in the presence of potassium. In order to detect RF interference in the QMA, the ratio

$$\frac{Y_r^1 - Y^1}{Y_r^2 - Y^2} \quad (2.18)$$

of the QMA sensitivities to mass 1 versus mass 2 was monitored for abrupt changes.

During test measurements, the atomic fraction was monitored as the spin-cell was heated up to 220° C. Afterward, potassium was introduced into the spin-cell by slowly heating the ampule. Measurements of atomic polarization were made as a function of the ampule temperature. The procedure was repeated at different flow rates in search of the optimum figure of merit. Figure 2-15 shows the effects of the oven temperature and potassium density on the degree of dissociation. Figure 2-16 shows a wavelength scan of the D1 σ_+ and σ_- resonances with potassium vapor in the cell during an early polarization measurement of the LDS. Finally, the best results are shown in Table 2.4 as a function of hydrogen flow rate.

2.3 The BLAST Detector Package

The few-body nuclear physics program using internal targets in the SHR has many detector requirements [147]:

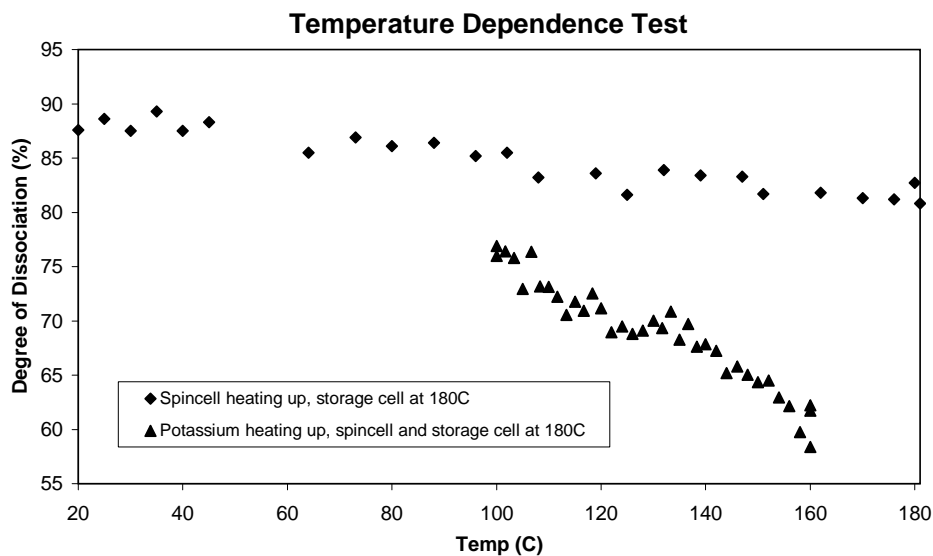


Figure 2-15: Temperature dependence of dissociation in the target cell. Diamonds represent the spin-cell being heated without potassium. Triangles show the dependence on the potassium ampule temperature, with the spin-cell at 180°C.

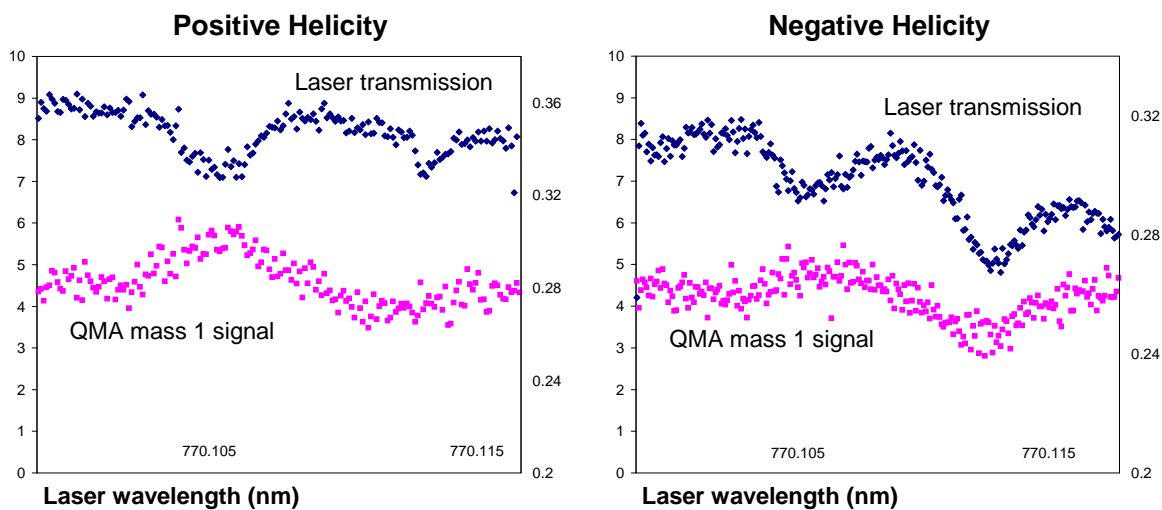


Figure 2-16: Preliminary polarization results. The units for both laser transmission and the QMA signal are arbitrary. The Ti:Sapphire laser is scanned over the potassium D1 transition, first with right circular polarization, and then with left-circular polarization.

Flow	Φ (sccm)	1	1.2	1.35	1.5	2
	Φ (10^{18} atoms/s)	0.90	1.08	1.22	1.35	1.80
Temperature	T_K ($^{\circ}\text{C}$)	205	205	210	205	127
	T_C ($^{\circ}\text{C}$)	210	210	220	210	222
Dissociation	f_{α} (%)	59	56	52	47	46
Polarization	P_e ($h = +1$) (%)	36.0	37.3	36.1	36.0	29.4
	P_e ($h = -1$) (%)	37.0	37.3	—	36.0	27.4
FOM	\mathcal{F} (10^{17} atoms/s)	0.41	0.47	0.42	0.38	0.30

Table 2.4: Best figure of merit achieved by the MIT LDS as a function of flow rate. These results were obtained without the EOM, which would have increased P_e by approximately 30%. The two temperatures were measured in the potassium ampule T_K and in the spin-cell T_C , and the atomic polarization P_e was measured for both atomic spin states, corresponding to the two helicities of the laser.

- Large acceptance to compensate for the low luminosity associated with the internal target, even in the intense stored beam. Two important side benefits are the detection of out-of-plane angles, and the all Q^2 points are measured under the same beam and target polarization conditions.
- The detector should be azimuthally symmetric to allow for coincidence measurements, and also for super-ratio experiments which are independent of P . A full $\Delta\phi = 2\pi$ detector would be ideal to separate the response functions, especially for deuterium, but at least the left and right sectors should be instrumented.
- Resolution of the vertex and initial momentum (\mathbf{p}) of each scattered particle at the 1% level, requiring a spectrometer magnet and wire chambers. The spectrometer should be integrated around the SHR beampipe and the internal target. In particular, it should have large fields to resolve the high momentum forward scattered electrons, and extremely small fields and gradients at the internal target and beamline.
- Particle Identification (PID) of e^{\pm} , π^{\pm} , p, n, and d. Precise timing resolution is needed for mass identification. A Čerenkov detector is needed for pion rejection, especially for inelastic kinematics and for the inclusive trigger. Efficient neutron detection is also important for the complete few-body nuclear physics program

including neutron form factors.

In conformance with these requirements, the detector package was designed around eight coils of the Bates Large Acceptance Spectrometer Toroid (BLAST) magnet. The two horizontal sectors are instrumented with, from the beam line radially outward: drift chambers, Čerenkov detectors, time-of-flight (TOF) scintillators, and two sets of neutron scintillators. The top and bottom sectors contain the ABS and diagnostics. To minimize costs the other four sectors are left open. Both the BLAST coils and detector sub-packages are installed on rails to open for maintenance. The spectrometer toroid and each of these detectors are shown in Fig. 2-17. Each detector except the neutron scintillators [133] is explained in further detail in this section.

The BLAST detector was built using conventional technology for cost reduction and reliability. The scintillators, Čerenkov detectors, and wire chambers were all based on standard designs. The trigger was based on the trigger for Hall A at JLab. The data acquisition software CODA was written at JLab and most of the trigger and readout electronics were based on the VME and FASTBUS hardware also used at JLab. All computing power was based on inexpensive PCs running Linux, including the 40 CPU analysis cluster. The slow control system is based on the industry standard EPICS used elsewhere throughout the lab. Finally, the simulation, reconstruction, and analysis software is based on the CERN packages GEANT and ROOT.

The BLAST coordinate system is defined with the origin at the center of the internal target, the z-axis pointing downstream along the beamline, the y-axis pointing straight up, and the x-axis in the horizontal plane outward in the left sector (looking downstream). Spherical and cylindrical coordinates in the BLAST frame are defined as usual:

$$x = \rho \sin \phi, \quad y = \rho \cos \phi, \quad z = r \cos \theta, \quad \text{and} \quad \rho = r \sin \theta. \quad (2.19)$$

Each detector element also has its own coordinate system with the origin in the center of the detector, the x' -axis running horizontally along the face of the detector in the direction of increasing θ , the y' -axis pointing either up or down in the direction of

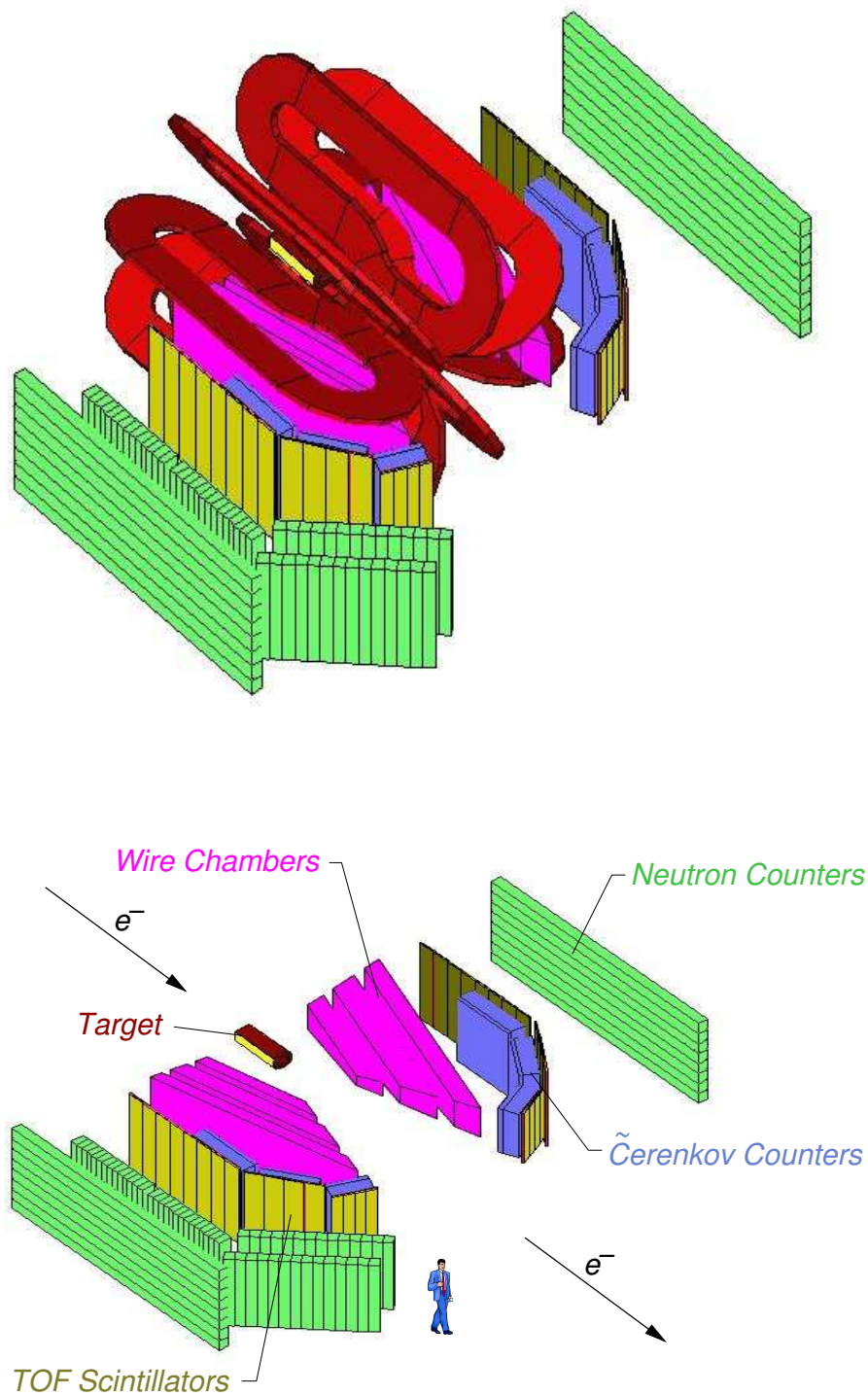


Figure 2-17: The BLAST detector package shown with and without the magnetic coils of the toroid.

increasing ϕ , and the z' -axis in the general direction of particles passing through the detector component.

2.3.1 BLAST Toroid

The spectrometer uses a toroidal magnetic field to minimize fringe fields in the target holding field in the PMTs of the Čerenkov and TOF scintillators. The large acceptance in both solid angle and momentum prevents a focal plane design, but the wire chamber positional information throughout the field is complete enough to uniquely reconstruct tracks. The field also shields Møller scattered electrons, bending them inward of the wire chamber acceptance. Positrons are deflected outward into the backward region of the spectrometer and although they increase the event rate and deadtime, they are easily identified by their tight curvature.

The coils are shaped to give maximum dispersion to forward electrons and have a 1 m inner diameter opening in the back to accommodate the internal target and scattering chamber. The coils are wound with a hollow copper conductor with water coolant circulating through the core. The sides are reinforced with G10 plastic. The coils are supported in the toroid configuration by an aluminum frame with a maximum deflection of 7–8 mm with to the field energized at full strength. The specifications are given in Tab. 2.5.

Max. Field	B	0.38 T
Num. Coils	N_c	8
Num. Turns	N_t	26
Max. Current	I	6730 A
Power Output	P	1.5 MW

Table 2.5: BLAST coil specifications.

For Monte Carlo testing, the BLAST field was modeled both in TOSCA and by an analytic Biot-Savart calculation. The field was also carefully mapped before the wire chambers and other detectors were installed [148]. The mapping was done automatically with an EPICS controlled x-y-z table with resolution 0.05 mm, (the

absolute probe position was known to 1 mm) and two Sentron three-dimensional Hall probes with precision 0.1%. The orientation of the x-y-z table was surveyed at each new position, and the field-map was interpolated into a rectangular grid of 5 cm between points in each direction. The field-map agreed within 1% of both the TOSCA and Biot-Savart calculations. The field was analytically continued past the measured points and past the physical region of the wire chambers to make the track-fitting more robust. The field is predominantly azimuthal so that tracks lie approximately in planes extending radially outward from the beamline; however this is modified by small fringe effects near the coils. The field-map of B_y in the central horizontal plane is shown in Fig. 2-18. This map does not include the effect of magnetic materials in the ABS, internal target, detectors, or heavy iron shielding of the Čerenkov PMTs, which may be the cause of systematic shifts in the reconstructed momentum of tracks (Sec. 3.4.1).

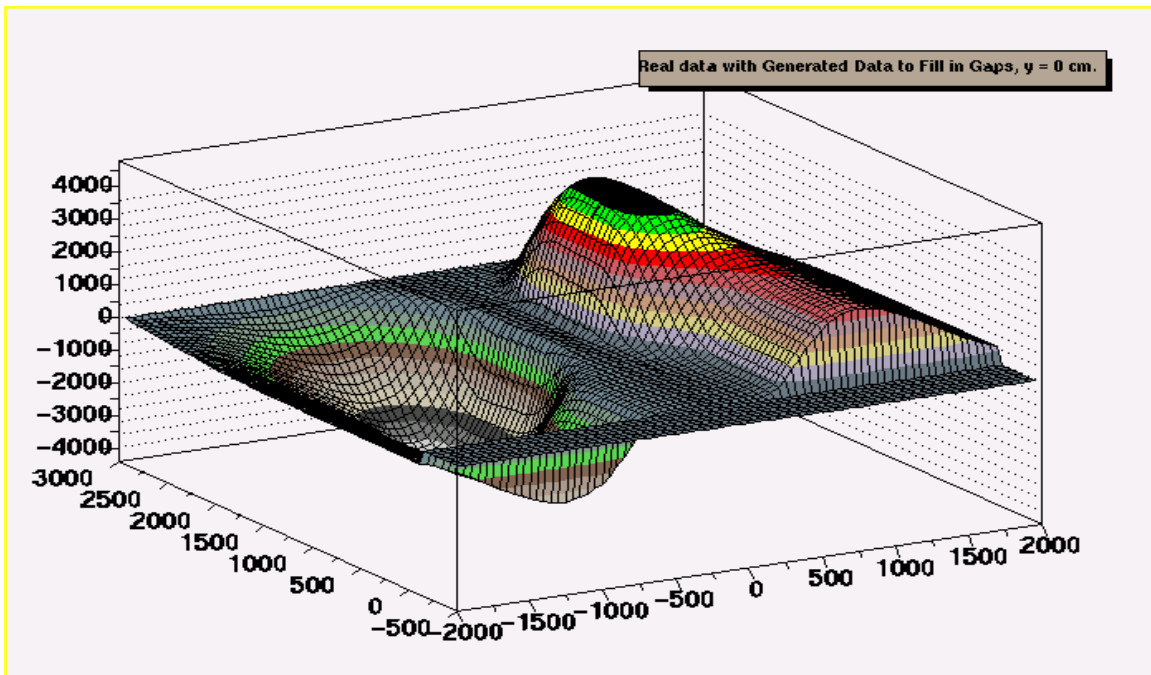


Figure 2-18: Magnetic field map of BLAST.
Magnetic field map of B_y in the central horizontal plane of BLAST.

2.3.2 Drift Chambers

The drift chambers (WC) are embedded in the $\phi = \pm 22.5^\circ$ horizontal sectors between the toroid coils and were designed to maximize the acceptance within these constraints. The three chambers in each sector were constructed of one-piece aluminum frames joined together with spacers to form a single airtight chamber. A mixture of helium and isobutane flows through the chambers at just above atmospheric pressure. This single-chamber aluminum construction was chosen over lower-cost G10 layered frames because of its strength against deformation from the wire tension. Multiple scattering is reduced by the elimination of windows between each chamber, by the use of field and guard wires instead of foil cathodes, and the use of helium instead of air as the quenching gas. The chambers are planar at an angle of $\alpha = 16.5^\circ$ with respect to the beam-line, and the frame has a trapezoidal shape on all 6 faces.

In general, a particle track through the spectrometer has 5 degrees of freedom: its momentum $\mathbf{p} = (p, \theta, \phi)$ and position $\mathbf{x} = (x, y, z)$ at a fixed point along the trajectory modulo one free parameter along the length of the track. We use the interaction vertex parameters (p, θ, ϕ, z, d) for physics analysis and the trajectory at the wire chamber entrance plane $(p_w, \theta_w, \phi_w, x_w, y_w)$ for reconstruction purposes. The parameter z is the location of the interaction vertex in BLAST coordinates, calculated as the closest point to the track along the beamline. The distance d of closest approach to the z -axis (beam line) is fixed at $d = 0$, since the beam position is known much better than the wire chamber resolution. Likewise, there is a constraint between ϕ_w and y_w . Therefore the wire chambers must determine four independent track parameters. Hits are required in each of the three chambers for momentum resolution. In practice, at least 12 hits are required for adequate track reconstruction. In the wire chamber (WC) coordinates, x_w is along the face of the wire chamber in the horizontal plane and increases with θ (toward upstream), y_w points straight up or down and increases with ϕ , and z_w is perpendicular to the wire planes directed away from the beamline.

Each chamber contains two superlayers of cells rotated about the z_w -axis by the stereo angles $+5^\circ$ (inner) and -5° (outer) for two dimensional track coordinates in

each plane. The stereo angles are small because the coordinate x_w determines p , θ , and z , while y_w only gives ϕ . Each cell has three sense wires with the center wire staggered 1 mm upstream to distinguish between tracks on the left and right sides of the cell. The multiplicity of wires in each cell gives extra information on the wire resolution and the slope of the track through each chamber, although slope resolution is poor since the layers are only separated by 1 cm. Thus of the 18 layers per sector, there are effectively 6 independent measurements, which overdetermine the track parameters by two. A single sense wire is indexed by the key (se=0–1, ch=0–2, su=0–1, la=0–2, ce=0–34). The wire chamber specifications are in Table 2.6.

parameter	p [MeV]	θ [°]	ϕ [°]	z [cm]
nominal acceptance	100–1000	22–75	-17–17	-50–50
resolution	25 MeV	0.5°	0.6°	1 cm
gas mixture	82.3% helium, 17.7% isobutane			
stereo angle	$\pm 5^\circ$			
wire stagger	± 0.5 mm			
mid-plane separation	1 cm (layers), 6 cm (superlayers), ~ 42 cm (chambers)			
cells/superlayer	(su=0) 18, 19, 26, 27, 34, 35 (su=5)			
sense wires	954 total, \varnothing 25 μm			
guard wires	1272 total, \varnothing 100 μm			
field wires	7332 total, \varnothing 100 μm			
drift velocity	20 $\mu\text{m}/\text{ns}$			
TDC resolution	0.5 ns/ch			
position resolution	200 μm (nominal)			
acceptance/sector	401 msr (nominal)			

Table 2.6: Drift chamber specifications.

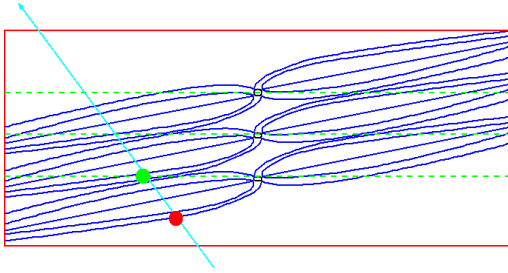
Each cell is bounded by HV field wires creating an electric gradient toward the three sense wires. A charged particle passing through the cell ionizes the gas, and the resulting electron avalanche while drifts toward the sense wires. The sense wire signals are preamplified and discriminated in readout cards mounted on the chamber, and are digitized by the FASTBUS TDCs in common stop mode with up to 16 hits per trigger. In the jet-style cell where ions drift horizontally toward the sense wires, tracks with an impact angle greater than $\sim 60^\circ$ have reduced resolution. This affects the resolution of forward electron tracks. The drift lines are shifted by about 5° due

to the Lorentz force from the BLAST field. In comparison, the CLAS drift chambers in Hall B of JLab have 4 or 6 layers of hexagonal cells, with more redundancy and without the $\sim 60^\circ$ impact angle limit [149]. The limited redundancy of the BLAST wire chambers presents a difficulty in calibration.

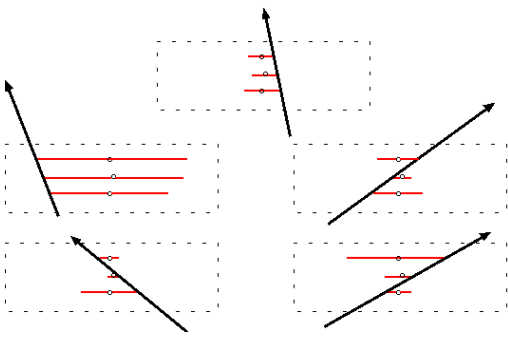
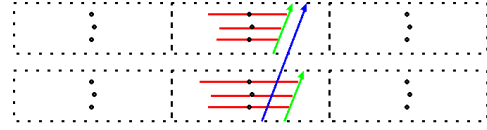
The calibration of each drift chamber wire is specified in terms of the functions $x_w(t)$ defined as the x_w coordinate of the track where it crosses that layer as a function of the wire TDC value t . This is a convenient meeting point between raw hit data and track simulations. It is a double-valued function (for both sides of the wire) which also depends on the magnetic field, track impact angle, and gas composition. It has four regions: the low-resolution crossover region in the vicinity of the wire, the nonlinear region within 4 mm of the wire, the linear region, and the unpredictable fringe region near the edge of the cell. It may be approximated by $x_w(t) = x_0 + k d(t_0 - t)$, where the time-to-distance function $d(t)$ is determined from a Garfield simulation. In this case the calibration coefficients for each wire are its position x_0 , the TDC maximum t_0 , and a factor k to account for variations in the drift velocity. Details of the wire chamber calibrations are given in Appendix A.3.

The steps in the reconstruction of wire chamber tracks are illustrated in Fig. 2-19. In a single cell, all wires are parallel to each other and so the reconstructed “stub” is a plane parallel to the wires. The intersection of two stub planes in a chamber forms a track segment, a point (x_w, y_w) in the plane of the chamber together with crude directional information. Three stubs are linked to form a track which is approximately circular within the wire chambers. The fast fitter calculates the track momentum from the radius of this circle.

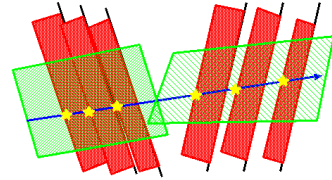
Due to multiple hits, noise, and left/right ambiguities, there are many stubs, segments or tracks in software associated with the same physical track. In order to reduce the combinatorics, only the best candidates are kept at each stage in reconstruction. In the track fitter, all track candidates are iterated together, discarding bad tracks every few iterations. Also, stubs or hits may be missing due to inefficient wires or bad readout cards. Using the limited redundancy in the wire chambers, the reconstruction software is able to reconstruct 3 hit, 2 hit, 1 hit, or 0 hit stubs. Up to



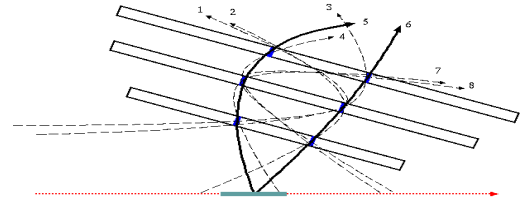
(a) Time-to-distance function calculates the perpendicular distance of the track from the wire.



(b) Stub-finder determines which side of each wire the track passed.



(c) In each chamber, the intersection of two stubs planes forms a line segment.



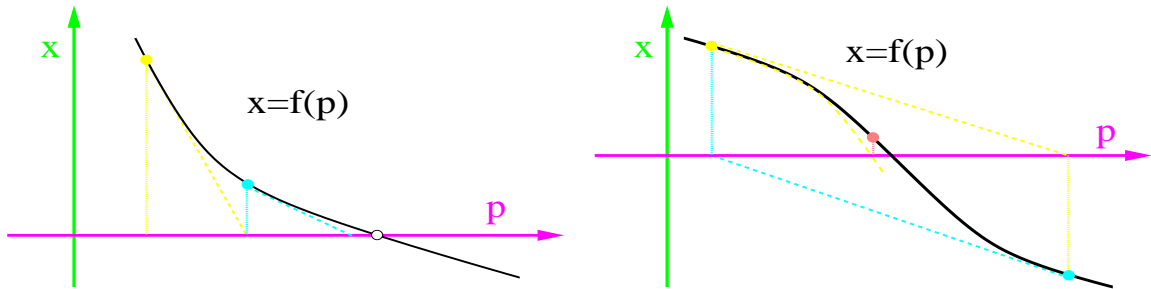
(d) The line segments are linked to form the most likely tracks.

Figure 2-19: Steps of track reconstruction from hits in the drift chambers.

two fake (0 hit) stubs in separate chambers can be reconstructed using information from the other stubs, although such tracks have poor resolution.

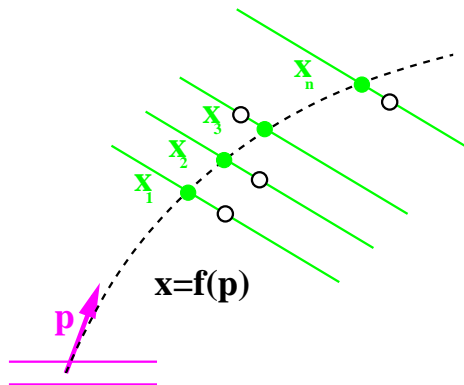
Once a track has been linked, its segments and stubs are no longer needed. Track fitting is done at the hit level by finding the root of the function $\mathbf{x}_0 = \mathbf{f}(\mathbf{p})$, where $\mathbf{p} = (p, \theta, \phi, z)$ and \mathbf{x}_0 contains the 18 coordinates of the wire hits. The function $\mathbf{x} = \mathbf{f}(\mathbf{p})$ is evaluated numerically by simulating a track with initial parameters \mathbf{p} through the field of the wire chamber. The root is solved numerically using a modification of the Newton-Rhapson method of Ref. [150, §9.6], which is illustrated in Fig. 2-20. The modifications to this method are as follows: Because the space $\{\mathbf{x}\}$ is of higher dimension than \mathbf{p} , the inverse of \mathbf{f} is only well defined on its image in $\{\mathbf{x}\}$. For values of \mathbf{x} out of the image, we project perpendicularly onto the image

space before inverting. In the Newton-Rhapon method, this is done by computing the least squares inverse of the Jacobian $J = d\mathbf{f}/d\mathbf{p}$ defined by $J^{-1} \equiv (J^T J)^{-1} J^T$, as discussed in Appendix A. As long as \mathbf{x}_0 lies closer to the image of \mathbf{f} than its radius of curvature, the inverse converges using this method. While this problem could be treated as a minimization of $\chi^2 = ((\mathbf{f}(\mathbf{p}) - \mathbf{x}_0)/\Delta x)^2$, much more information is retained by solving the root directly. For example χ_{min}^2 should be close to 0, and $\mathbf{f}(\mathbf{p}) - \mathbf{x}_0$ has more information than χ^2 . The Newton-Rhapon method tends to pass right over local minima in search of the global minimum. Ideally χ^2 should converge to zero by a factor of 1000 per iteration, but this fitter converges by a factor of 10-100 per iteration due to the extra dimensions of $\{\mathbf{x}\}$.

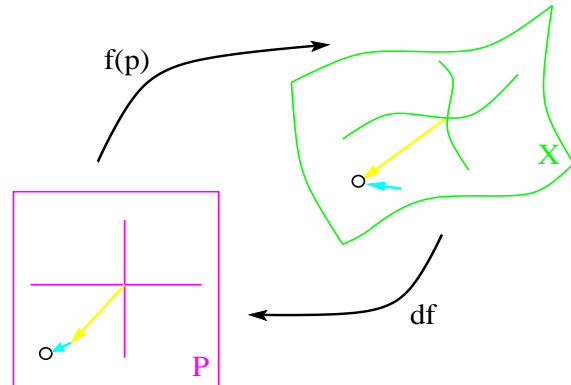


(a) In one dimension, the derivative of f maps the deviation dx from the initial guess to the adjustment dp , and so forth.

(b) In some cases the Newton method may fail to converge, and it is necessary to backtrack to a smaller correction dp .



(c) For track fitting, the function f maps the 4-dimensional track trajectory \mathbf{p} to the 18-dimensional vector of wire hits \mathbf{x} .



(d) In each iteration the trajectory \mathbf{p} is corrected by $d\mathbf{p} = J^{-1}d\mathbf{x}$, where J is the Jacobian derivative and $d\mathbf{x}$ is the deviation of the simulated track from the wire hits.

Figure 2-20: An application of the Newton-Rhapon method to track fitting.

The drift chamber tracking efficiency was measured by selecting non-biased elastic ep events from the TOF scintillator cuts. To determine the tracking efficiency of protons, the percentage of missing tracks was tabulated for non-biased events as a function of Q^2 calculated from the electron, with an additional cut on W . The electron efficiency was calculated similarly, with a cut on the proton momentum versus theta. The tracking efficiency, which includes both detector response and reconstruction robustness, is shown in Fig. 2-21

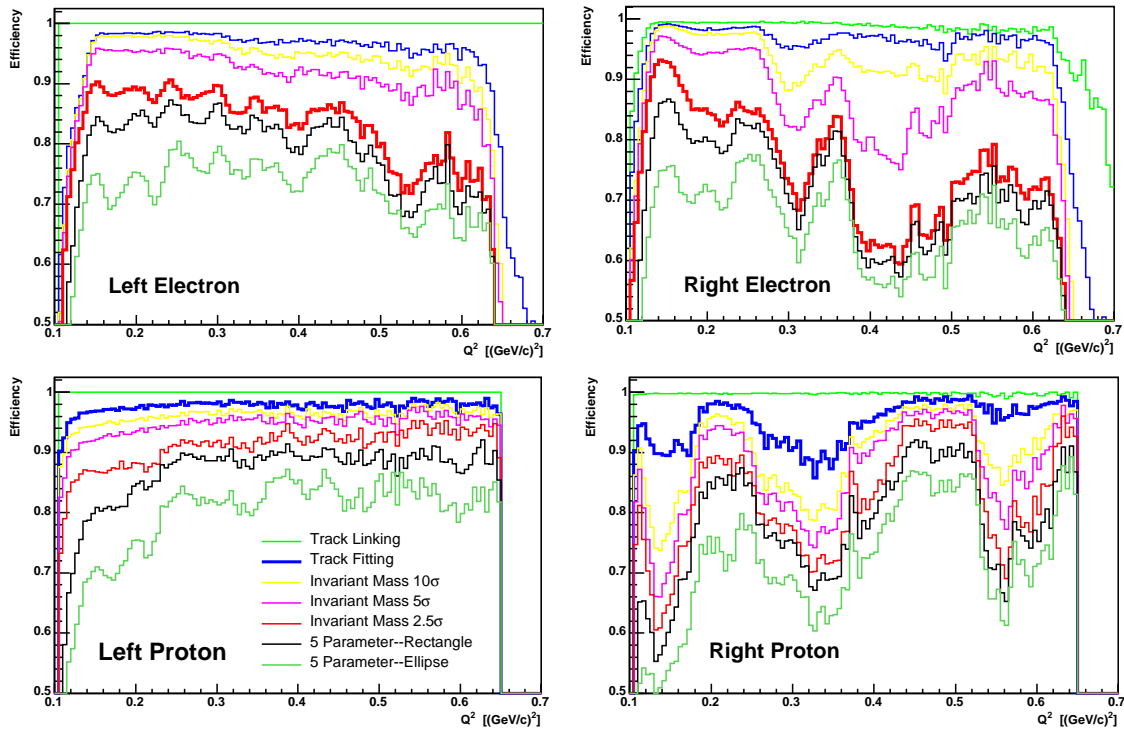


Figure 2-21: Drift chamber tracking efficiency for electrons and protons in the left and right sectors. The curves, listed in the same order in the legend as they appear in the plot, correspond to different standards of an acceptable track.

2.3.3 TOF Scintillators

Timing for the trigger and particle identification is provided by the time-of-flight (TOF) scintillators. There are photomultiplier tubes (PMT) on each end of the scintillator bar, which reduces random background rates, provides positional information along the length of the paddle, and improves the statistical timing information by a

factor of $\sqrt{2}$. Also, assuming the velocity of light is constant along the scintillator, the meantime of the two PMT signals will be independent of the hit position. The meantime of the earliest TOF hit is used to define the trigger timing. For coplanar events, the four PMT readings combine to give two peaks (timing difference and coplanarity) as well as track azimuthal angle ϕ and the trigger timing. These peaks are used for efficient elastic kinematic cuts.

The BLAST detector does not have a start counter. Instead the timing measurements are made in common start mode, triggered by the first detector to be hit. Therefore, only time differences between scintillators, where the common start cancels, can be observed. Timing of the vertex is obtained by simulating each particle backward from the TOFs. Particle identification for coincident events is obtained from the combination of masses which best reproduces the observed time difference. Assuming that the triggering particle is ultra-relativistic ($\beta = 1$), the timing difference determines the velocity of the heavier particle. The mass can be determined from the velocity in combination with momentum information of the wire chambers. For singles events, the TOFs only provide a self-timing peak (the same hit causes both the start and stop in the TDC module) and the position of the track in the scintillator.

A detailed description of the theory and construction of the BLAST TOFs is given in [151], and the specifications in Table 2.7. The Bicron-408 scintillator was chosen for its long attenuation length and fast timing response, and the thickness is an optimization between efficiency and timing resolution. The scintillators are wrapped in two layers of aluminum foil and an exterior Kapton sheath. All but the last four TOFs have 10 mil of lead shielding in front of the scintillator material. There are 16 TOFs in each sector, covering the entire acceptance of the drift chambers. The forward four TOFs are smaller because they are closer to the beamline and also have larger rates. Four additional backward angle TOFs (BATs) were installed in each sector at electron angles $95^\circ < \theta < 115^\circ$ behind the wire chamber acceptance to increase the Q^2 range of the $\mu G_E/G_M$ measurement. They were constructed identical to the original large TOFs.

	TOF Scintillator Number															
	0	1	2	3	4	5	6	7	8	9	10	11	12	13	14	15
θ_e [°]	26.0	28.8	31.7	34.4	37.7	41.8	45.6	50.0	54.6	58.3	62.2	66.2	71.0	76.2	83.0	86.9
θ_p [°]	—	—	—	—	—	27.2	31.4	35.8	40.7	44.6	48.7	52.8	57.6	61.9	65.0	67.0
$\langle Q_e^2 \rangle$.142	.169	.197	.225	.261	.305	.345	.389	.433	.465	.497	.525	.560	.592	.615	.626
$\langle Q_p^2 \rangle$	—	—	—	—	—	.660	.622	.573	.509	.453	.390	.324	.257	.196	.158	.149
dim.	47" × 6" × 1"				180.0 cm × 26.2 cm × 1"											
scintillator	Bicron BC-408 polyvinyl toluene with organic fluors															
index of refraction n	1.58															
rise time	0.9 ns															
attenuation length	210 cm															
phototubes	3" Electron Tubes 9822B02															
TDC resolution	50 ps/channel															
timing resolution (σ)	350 ps															
position resolution (σ)	3 cm															

Table 2.7: Time-of-flight (TOF) scintillator specifications. Units of Q^2 are $(\text{GeV}/c)^2$.

Lucite light guides at each end of the scintillator are bent perpendicular to BLAST field, and the PMTs were shielded with μ -metal one radius past the photocathode. During commissioning runs, an extra layer of μ -metal was added which extended a full diameter past the photocathode. The bases have actively stabilized voltage dividers at ~ -2000 V, gain-matched using cosmic rays. The timing is extracted independent of signal strength (no walk effect) using constant fraction discriminators (CFD), and is sent to the TDC and the trigger logic.

Special care is taken to have a clean trigger. The top and bottom PMT signals are averaged in a mean-timer, removing the positional time-dependence. The final trigger is strobed with an OR of all TOF meantimes to remove jitter from all of the trigger logic units. During commissioning, the programmable delay for each TOF was adjusted relative to a temporary start counter placed adjacent to the target chamber in order to synchronize the physical TOF signals from channel to channel in each sector. However, this was unnecessary because all timings are relative in the BLAST detector. The clean trigger can simply be taken in software from the self-timing peak of the fastest (triggering) particle. The TDC values from every other detector are relative to this trigger TDC.

A flasher system is used to monitor drifts in the timing of each detector, using an LSI model VSL-337ND-S ultraviolet nitrogen laser. A single laser pulse is split into multiple fiber optic cables, each of which is attenuated and coupled to the center of a TOF, Čerenkov, or neutron scintillator. The laser is pulsed at about 1 Hz and the flasher events trigger the DAQ system using a photodiode detector. The mean timing offset of each TOF is calibrated relative to the other TOFs using cosmic rays which trigger left-right sector coincidences. Also, the position along each TOF is calibrated by enforcing the coplanarity of elastic $H(e, e'p)$ events. These methods, described in Appendix A.2, were extended to calibrations of the neutron detectors relative to the TOFs [133]. These calibrations are relative to some global undetermined trigger offset.

During the analysis, we discovered that the bottom PMT discriminator of left sector TOF #9 had an abnormally high threshold (~ 100 mV) and jitter (~ 10 ns), as shown in Fig. 2-22, This jitter was random and could not be corrected for in software. It only affected electrons, which are minimum ionizing particles. The discriminator module was replaced after the current experiment, but reasonable timing may still be obtained from the top PMT in conjunction with positional information from the wire chamber track.

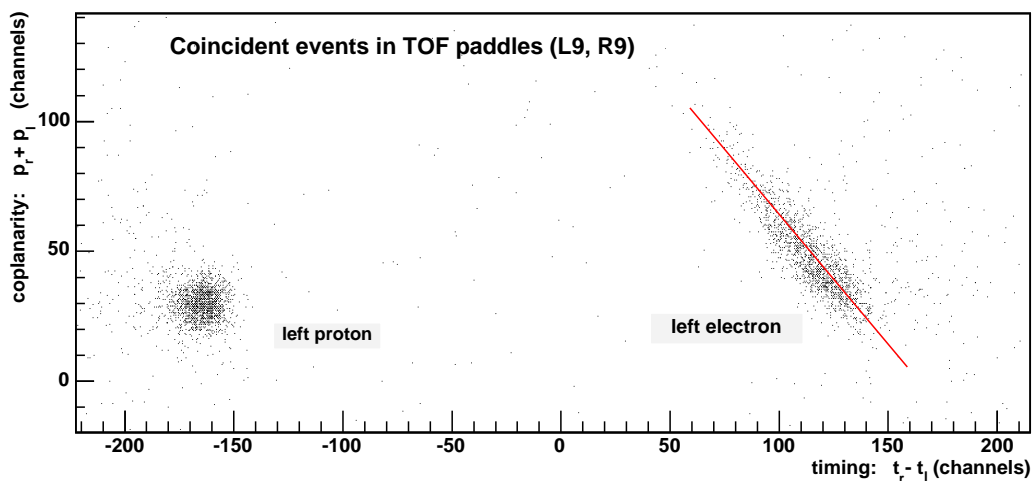


Figure 2-22: Timing vs. coplanarity for TOF paddle L9B. The variables are explained in Sec. 3.1.1.

The TOF efficiency is shown in Fig. 2-23. Candidate tracks are chosen from all triggers which were independent of the TOF in question, e.g. neutron detector triggers or $H(e,p)e'$ events. For protons, singles electron triggers are used. For the efficiency of electrons forward of the neutron detectors, a special proton trigger was added which required a TOF hit on the proton side in coincidence with a Čerenkov hit on the electron side to reduce the accidental background rate.

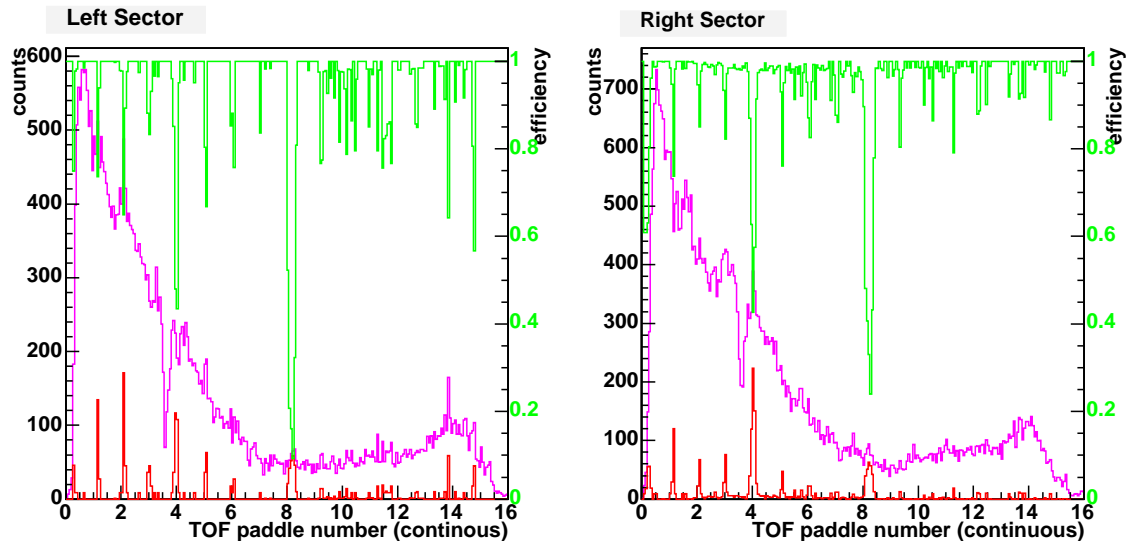


Figure 2-23: Efficiency of each TOF along the width of the scintillator.

2.3.4 Čerenkov Detectors

The Čerenkov detectors (CC) distinguish between relativistic electrons and pions with momenta up to 700 MeV. They are also important for reducing backgrounds, especially in the high count rate singles trigger. They are described in Ref. [152], and a brief summary is presented here, with the specifications given in Table 2.8.

Čerenkov radiation is produced by ultra-relativistic particles traveling faster than the speed of light in the medium, similar to the sonic boom of acoustics. The light is emitted in a characteristic forward cone. The BLAST Čerenkov boxes consist of a thin layer of highly transparent silica Aerogel in a diffusely reflective light collecting box. The thickness and index of refraction represents a balance between complete

pion rejection and sufficient light output. A reflector in each box is angled to reflect the light toward sets of PMTs at either end. The signals from all PMTs in a single box are passively added before they are sent to TDC and ADC channels and the trigger logic. Each tube was individually gain-matched by disabling the voltages of all other tubes in the box during a short calibration run.

Since they are in the BLAST fringe field of ~ 100 Gauss, the PMTs are shielded with two concentric tubes of low-carbon steel which extend at least one diameter beyond the phototubes. Before the present experiment, it was observed that residual fields of 3–5 Gauss severely reduced the Čerenkov efficiency, so additional iron shielding was added around the PMT support frame, and the Čerenkov efficiency is now $\sim 85\%$. This shielding may affect the magnetic field inside the drift chambers, which is not accounted for in the present field-map (Sec. 3.4.1).

Čerenkov box	0	1	2	3
Index of refraction n	1.020	1.030	1.030	1.030
Aerogel thickness	7 cm	5 cm	5 cm	5 cm
# of phototubes	6	8	12	12
TOFs subtended	0–3	4–7	8–11	BATs
nominal θ range	20°–35°	35°–50°	50°–70°	95°–115°
\langle photoelectrons/event \rangle	2.8			
phototube model	5" Photonis XP4500B			
max. tolerable field	0.5–1 Gauss (50% efficient)			
reflective coating	LabSphere, NH			
Aerogel manufacturer	Matsushita, Japan			

Table 2.8: Čerenkov detector specifications.

The size of the Čerenkov boxes varies so that each covers the acceptance of 4 TOF scintillators. The fourth box was initially intended to subtend TOFs 12–15; however, it was removed to allow low-momentum backward deuterons to reach the TOFs without being absorbed in the Čerenkov detector. It was used in front of the BATs instead. Thus the singles triggers in these backward TOFs are heavily prescaled and require coincidence with a neutron detector.

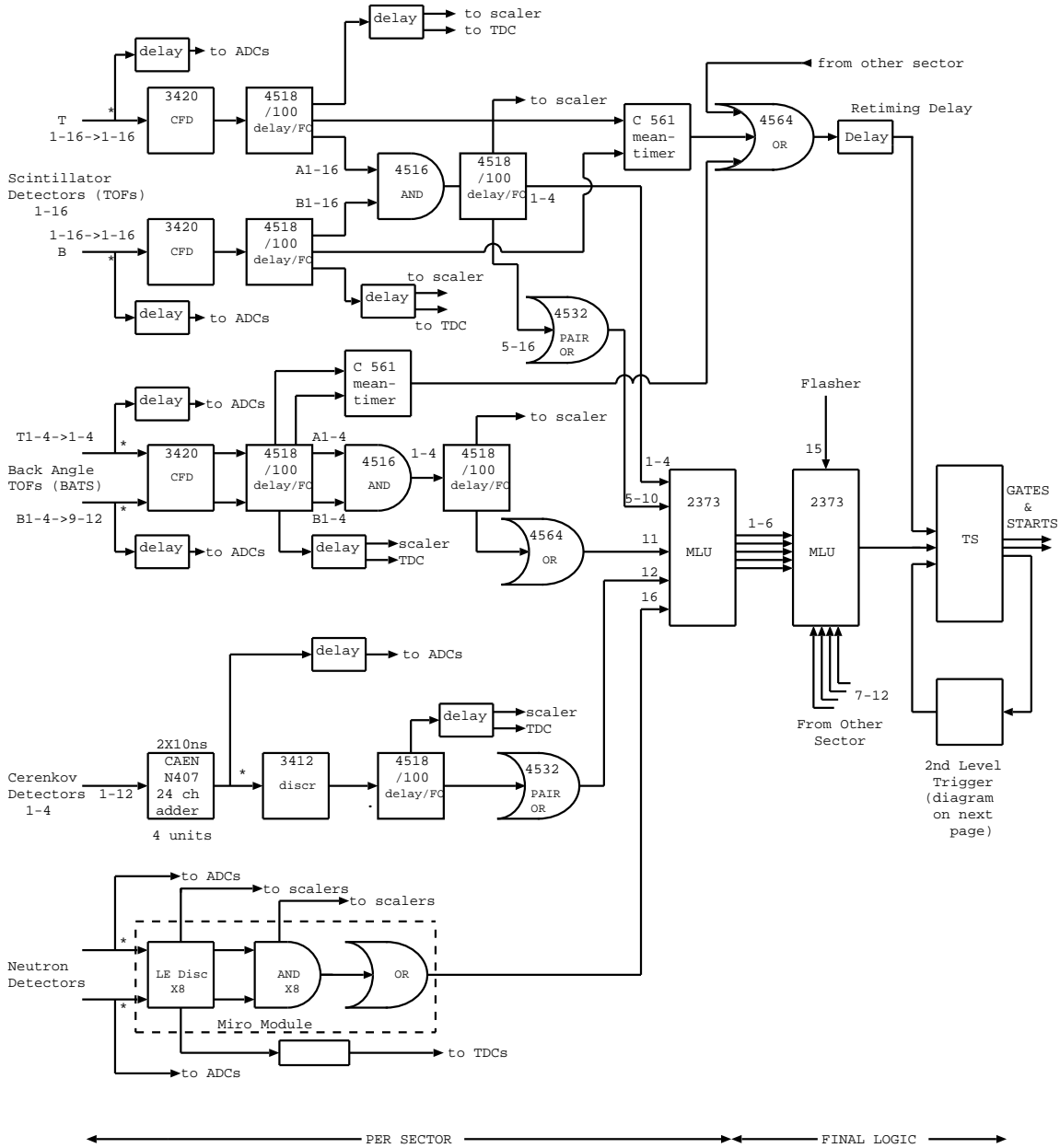
2.4 Electronics and Software

2.4.1 Trigger

The BLAST trigger is versatile, programmable, and can accept the multiple physics channels present in a large-angle spectrometer. The trigger software and design were developed in conjunction with JLab Hall A and tested there prior to their use in BLAST. Software improvements for BLAST were also sent back to Hall A. Figure 2-24 is a schematic of the electronic components. The raw signals from each detector are split off to the ADC channels, and to the timing components (discriminators, programmable delays, mean-timers). The latter signal is sent to the TDC modules and also to input bits of the trigger logic. All except for the 4 most forward TOFs are paired, and the entire Čerenkov and neutron sub-detectors are each combined into one input bit per sector. The programmable logic is implemented with LeCroy 2373 Memory Lookup Units (MLUs). The MLU is a real-time look up table with multiple output bits for each combination of input bits (signals). There are too many input signals for one 16-bit MLU so the logic is split into left and right sector MLUs. The output bits of both sector MLUs are combined in the cross MLU, which defines the eight separate trigger types listed in Table 2.11. Each trigger type can be individually prescaled. Multiple physics channels can be assigned to the same trigger bit, but they will have the same prescale factor.

There is a second level wire chamber trigger which is too slow to start the TDCs and ADCs, but instead accepts or rejects readout. This reduces the deadtime of noise events from $835 \mu\text{s}$ for read out down to $5 \mu\text{s}$ for a start trigger and fast clear. The second-level trigger, implemented in a custom designed electronics module, requires at least one hit in each of the three wire chambers in one sector. Midway through our experiment, the DAQ deadtime was further decreased by enhancing the logic to require the above wire chamber pattern in each sector with a TOF hit.

The trigger distribution, common strobe, prescaling, external inhibit, internal busy inhibit, event synchronization, and up to three levels of triggers are all managed by the trigger supervisor (TS) module. The TS was developed at JLab and is



note: * all analog signal division in matched impedance passive splitters

Figure 2-24: A schematic of the trigger logic. Only one circuit is shown for each detector, and only the left sector is shown. The logic from the left sector MLU and right sector MLU are combined in the cross MLU to form the final trigger processed by the trigger supervisor.

controlled by the CODA software.

The physics trigger setting used during our experiment, `newphys_kd_BATS`, is summarized in Tables 2.9–2.11. The two changes to the trigger, described above and in Sec. 2.3.3, did not affect the analysis.

The rates for each trigger type input to the TS are recorded in scaler channels, read out every second. There are also scalers channels for each raw PMT, for coincidences in the two ends of the scintillator, busy-inhibited rates, beam quality monitor (BQM) rates, wire chamber rates, and integrated current, as mentioned in Sec. 2.1.2. The scaler information is viewed online and also recorded into the CODA data-stream for subsequent analysis.

2.4.2 Data Acquisition

BLAST uses the modular Cebaf Online Data Acquisition (CODA 2.2.1) system from JLab. Digitization of the physics data is handled in two FASTBUS crates, one for each sector. The PMT signals are read out by LeCroy 1881M ADC and 1875A TDC modules, and the wire chambers by LeCroy 1877 TDC modules with up to 16 hits per trigger. The data are read out and buffered in a FASTBUS interface module (SFI) readout controller (ROC) and sent via the local DAQ Ethernet to a Linux host computer in the counting bay, which runs three main CODA processes: The event builder (EB) assembles fragments from each ROC into a raw CODA event. Events are buffered in the event transfer system (ET), which has input pipes for merging events from the scalers, EPICS, and Compton polarimeter, and also output pipes for online monitors. The events are written to disk by the event recorder (ER), and transferred in duplicate to RAID disks on the analysis farm.

Slowly varying settings such as the drift chamber and PMT high voltages, current in the ring, ABS settings, target holding field currents, BLAST toroid current, vacuum pressures, and temperatures are controlled and monitored by the Experimental Physics and Industrial Control System (EPICS V3.13.4). These EPICS variables are recorded into the CODA data-stream every second. The variables are only read out at the beginning and end of runs or when they have changed beyond some threshold.

bits	input description	cnN bTt	output bits description
0-3	single TOFs 0-3	001	single TOF
4-9	paired TOFs 4-15	011	multiple TOFs
10	OR of BATs	101	BAT
11	OR of Čerenkov	111	BAT + TOFs
12	not used	000 xxx	no CC, no NC, any TOF
13	not used	010 xxx	no CC, yes NC, TOF<12
14	not used	110 xxx	no CC, yes NC, TOF≥12
15	OR of neutrons	100 xxx	yes CC, no NC, any TOF
		000 000	no CC, no NC, no TOF
		001 000	no CC, yes NC, no TOF

Table 2.9: Detail input and output bits of the left and right MLU. The bits marked with ‘xxx’ represent one of the above four TOF patterns.

	coinc				neutron	double	bats			singles
A	cn0xx1				cn0xx1	cn0x11	cn0xx1			cn0001
B	cn0xx1				001000	000000	cn0100			000000
cn	10	11	01	00	00	00	10	01	00	00
10	0,6	0,5,6	0,5,6	0,6	1,6	2,6	4,6	4,5,6	4,6	6
11	0,5,6	0,5	0,5	0,5	1,5	2,5	4,5,6	4,5	4,5	5
01	0,5,6	0,5	0,5	0,5	1,5	3,5	4,5,6	4,5	4,5	—
00	0,6	0,5	0,5	0	1	3,5	4,6	4,5	4	—

Table 2.10: The trigger logic programmed for all of the physics channels (block columns) used for the hydrogen production data. The hardware triggers output from the XMLU are tabulated for different combinations of the six input bits ‘cnNbTt’ from each sector MLU. ‘A’ (rows) refers to either the left or right sector, and ‘B’ (columns) the other sector. Some triggers have multiple output bits, counted by each of the trigger scalers. The TS assigns the event type as the lowest set bit.

bit	prescale	label	description
0	1	coinc	1+ TOF in each sector $(e, e'p)$ $(e, e'd)$ $(e, e'\pi)$
1	1,2	neutron	1+ TOF in one sector, a NC in the other $(e, e'n)$
2	10	double	2+ TOFs in the same sector with CC $(e, e'\pi)$
3	100	double	2+ TOFs in the same sector, prescaled (calib)
4	1	bats	1+ TOF in one sector, a BAT in the other $(e, e'p)$
5	1000	singles	1+ TOF≥12 one sector, prescaled (calib)
6	9	singles	1+ TOF in one sector with CC (e, e')
7	1	flasher	flasher diode trigger (calib)

Table 2.11: Summary of the physics triggers corresponding to output bits of the XMLU. The detailed bit patterns of each trigger are in tables 2.9 and 2.10.

Physics events must be sandwiched by both EPICS and scalers events to be valid. All events are timestamped by the ROCs, which are synchronized to the CODA host computer `dblast07` every minute by a fast Network Time Protocol (NTP) with 40 time samples. The overall synchronization is better than 10 ms, typically 5 ms. The same protocol is used to synchronize the scaler readout times. The EPICS server and `dblast7` are synchronized using a common server at bates (`locus`).

Each CODA run is automatically logged in the electronic logbook (`elog`), which was modified from the Jefferson Lab Hall A logbook to include a MySQL database of entries. Run parameters such as the run number, target gas, holding field, data quality, and trigger, electronics, epics and scaler maps are recorded in a searchable RUN table in the database. The logbook also has manual entries including special shift summary report forms.

2.4.3 Online Monitor

There were several online monitors to ensure data quality. All EPICS variables were guarded by the `AlarmHandler` program. The `DataAlarm` script checked every 10 seconds that physics, scalers, EPICS, and Compton events in the CODA data-stream were being recorded to disk. The raw rates were also monitored with online scalers, including the BQM and wire chamber scalers, which were used to improve the beam tune and reduce backgrounds.

The TDC and ADC spectra from each detector were monitored directly from the CODA ET data-stream with the program `onlineGui`. This root-based graphical monitor is based on the reconstruction library, and also histograms wire chamber track parameters p , θ , ϕ , z , q , W , and p_X for a subset of the events. In addition, the data were fully reconstructed into ntuples by the offline farm within about 8 hours. These ntuples were analyzed daily for preliminary physics results, including the target polarization.

The event display utility `nseed` has been particularly useful for visually inspecting the quality of online data and for debugging the reconstruction code. It is used for verification of the electronics map by making sure all hits in a track line up. It

is based on the same reconstruction library the ntuples are generated from. It can display events selected by a graphical cut in an arbitrary histogram, and mark the current event with a triangle in all histograms that are currently being displayed, as illustrated in Fig. 2-25.

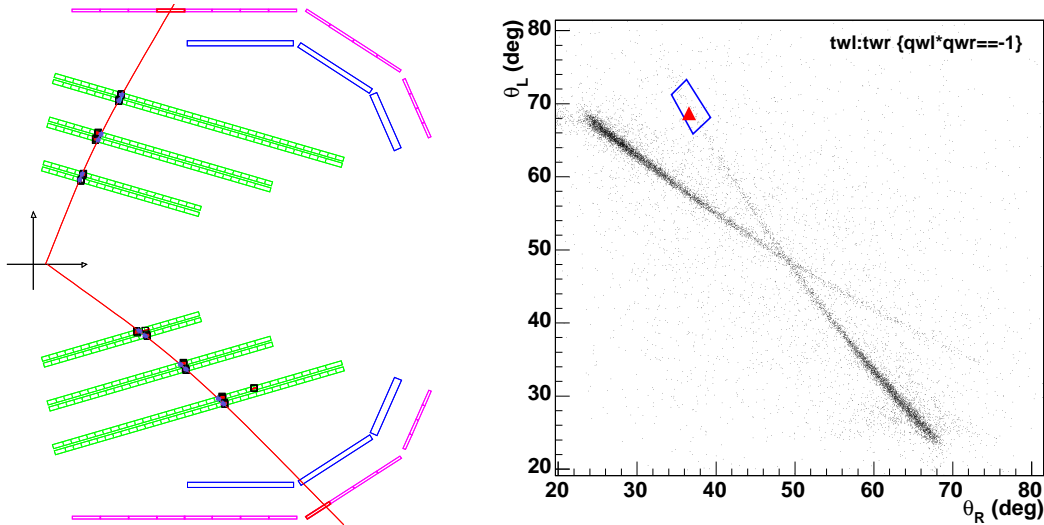


Figure 2-25: Integration of online display (NSED) with ROOT analysis package.

2.4.4 Reconstruction Library

All reconstruction software (`lrn`, `lrd`, `nused`, `onlineGui`, analysis scripts) is based on the common library, `BlastLib2`, which provides uniformity and efficiency. Reconstructed ntuple values can be verified in the online display, and all programs recognize the same options and settings. The open-source library is written in C++ using standard UNIX utilities `autoconf`, `make`, and `gcc`. The current version `v3.4.4` contains 37500 lines of code and is maintained in the BLAST CVS repository. It is built on the framework of ROOT and uses many of its basic features, listed in Table 2.12.

The key functions of the library and its corresponding classes are listed in Table 2.13. The library decodes raw CODA data-files into detector hits using an electronics map configuration file, which maps the ROC addresses, crate slots, and module channels into physical detector components. The data for each individual detector are

Functionality	ROOT Class
script/command-line interface	CINT
persistence (storage)	TFile, TTree
analysis/histogramming	TH1, TNtuple
graphics interface	TCanvas
linear algebra	TVector3, TMatrix
resource environment	TEnv
database interface	TMySQL

Table 2.12: ROOT functionality used in the BlastLib2 reconstruction library.

reconstructed as explained in Secs. 2.3.2–2.3.4. The library combines the detector information for each physical track and performs basic particle identification. Finally, all tracks are integrated into a single physics event. The reconstructed events are recorded in a Data Summary Tape (DST) file and also into physics ntuples, which may be easily analyzed. The DST records the complete reconstruction state of each event, so that re-crunches with new calibrations or an updated library can be done 10–20 times faster than from the original CODA file.

Functionality	BlastLib2 Class
Geometry	TBLGeometry, TBLGeomGeneral, TBLGeomWC, TBLGeomSC, TBLGeomSB, TBLGeomCC, TBLGeomNC, TBLGeomLD, etc.
Magnetic Field	TBLMagField, TBLHoldField, TBLFieldCoil, TBLFieldMap, TBLFieldHarmonic, etc.
CODA data parsing	TBLRaw, TCodaRead, TCodaEvio, etc. TBLMonteCarlo, TBLElectronicsMap, etc.
Outer Detectors	TBLEpics, TBLScalers, TBLCompton, etc. TBLDetRecon, TBLDetCalib, TBLScRecon, tof_hit, cc_hit, nc_hit, tof_calib, cc_calib, nc_calib, etc.
WC reconstruction	TBLWc1Key, TBLWc1WireCal, TBLWc1Time2Distance, TBLWc1Hit, TBLWc1Cluster, TBLWc1Stub, TBLWc1Segment, TBLWc1Track, etc.
Track Fitting	TBLSimTrack, TBLFitTrack, TBLNewt, TBLNewtDer, TBLLazy, TBLLinear, etc.
Particle ID	TBLDetTrack, TBLPidRecon, etc.
Track/Event Integration	TBLRecon, TBLTrack, TBLKineFit, TBLAcceptance
Slow Controls	TBLEpicsRecon, TBLComptonRecon, etc.
DST input/output	TBLDst, fillheader, dstheader, wchvheader, TBLEvent, TBLEvTrack, TBLEvMC, TBLEvWC, TBLEvTof, TBLEvCC, TBLEvNC, TBLEvL15, TBLEvL20, TBLEvBat, TBLMCEvent, TBLEpicsEvent, TBLScalerEvent, etc.
Graphics, NSED	TBLEventDisplay, TBLUtilPad
General Utilities	TOpt, TPid, TBLUtil
Configuration Files	blastrc, blast.geom, bgrid2.blast electronics.map, Epics.map, scaler.label epics.cal, blast.sc_cal, Wire.Cal, WC_pos_vs_t_parameters, etc

Table 2.13: BlastLib2 reconstruction library classes.

Chapter 3

Data Analysis

Data for this experiment were taken during three run periods, listed in Table 3.1. The first run was taken with the BLAST magnetic field reversed (electrons out-bending) to extend the acceptance to lower Q^2 . The rates are higher at lower Q^2 , allowing an accurate measurement of the target polarization in less time. Data were taken with the ABS target. Between the second and third run periods, the ABS performance was greatly improved, which affected both the target thickness and polarization. Also, the 40 cm long cell was replaced with a 60 cm long cell (cell #3) of the same diameter. As a result the third run period yielded over 13 times the effective statistics of the first two run periods combined. The majority of the data in the third run were taken with the magnetic holding field oriented at 47° with respect to the beam line. Between the second and third run periods, deuterium data with 450 kC of accumulated charge were also taken, and even more deuterium data are being taken in the 2005 deuterium run. One can also extract the proton form factor ratio from quasi-elastic scattering from deuterium, although it is complicated by nuclear effects such the deuteron structure and final state interactions (FSI). However, for the scope of this thesis, only the results of the hydrogen data from run 3 with the holding field at 47° are presented.

	Run 1	Run 2	Run 3	
start date	2003/12/09	2004/02/15	2004/10/28	2004/11/01
run numbers	3787–4208 4696–4744	4747–4857 6273–7001	12144–12183 12184–12229	12244–12292 12297–13266
beam charge	q 20 kC	57 kC	25 kC	291 kC
target length	l 40 cm	40 cm	60 cm	60 cm
thickness [cm ⁻²]	ρ 2.7×10^{13}	2.7×10^{13}	4.9×10^{13}	4.9×10^{13}
int. luminosity $\int dt \mathcal{L}$	3.4 pb^{-1}	9.6 pb^{-1}	7.7 pb^{-1}	89.8 pb^{-1}
beam pol.	P_b 0.65	0.65	0.65	0.65
target pol.	P_t 0.48	0.42	0.80	0.80
pol. angle	β 47.1°	47.1°	31.4°	47.1°
BLAST polarity	reversed	nominal (electrons inbending)		

Table 3.1: Beam, target, and spectrometer conditions for the three data-taking periods of BLAST with the ABS H₂ target.

3.1 Event Selection

A set of cuts on information provided by the time-of-flight (TOF) scintillators, drift chambers (WC), and Čerenkov detectors were applied to obtain a clean elastic event selection. Preliminary event selection was done in the reconstruction code, requiring a good wire chamber track in each sector, one with positive charge (curvature) and the other with negative charge. The additional cuts described below were imposed on the reconstructed ntuples. These cuts were used to form the yields for comparison with Monte Carlo simulations and for forming the raw asymmetry.

In addition to the TOF and WC cuts described below, Čerenkov cuts were also possible due to greatly improved detection efficiency during run 3. Cuts were tested on both the proton (veto) and electron (coincidence) tracks. For the 2004 run, the last Čerenkov box covering TOF paddles 12–15 was moved in front of the Backward Angle TOFs (BATs) so as not block the detection of low-momentum elastic deuterons in the last four TOF paddles. Therefore cuts were only applied to TOF paddles 0–10. Also, the left forward-most box was noisy, so only protons in TOF paddles 0–4 were vetoed by the most forward Čerenkov box in either side. The Čerenkov cuts had no significant impact on the extraction of the form factor ratio, and were not used in the final analysis. This is consistent with the fact that the pion threshold

in W is separated from the elastic peak by five times the wire chamber resolution (Sec. 3.4.7), so that pions can be cleanly separated by kinematics alone. Also, the Čerenkov detector only differentiates ep coincidences from π^-p events, which are rare on a hydrogen target because they are only produced from 2π -production or from the cell wall.

3.1.1 Elastic TOF Cuts

The TOF cuts were based on the timing and coplanarity of elastic scattering. The elastic kinematics span a ridge of 48 paddle combinations of proton-electron coincidences with the electron scattering into the left sector and 48 combinations with the electron scattering into the right sector, as shown in Fig. 3-1. For each paddle combination, there are four TDC values $u^{L,R}$ and $d^{L,R}$, coming from the top and bottom phototubes, respectively, in the left and right sectors. Of these, two combinations (trigger offset and azimuthal scattering angle) are random while the other two (coplanarity $p \equiv d^R - u^R + d^L - u^L$, and proton timing $t \equiv d^R + u^R - d^L - u^L$) are sharply peaked. Histograms of $\mathbf{x} = (p, t)$ were fit to the 2-D Gaussian distribution

$$f(\mathbf{x}) = f_0 e^{-\frac{1}{2}(\mathbf{x}-\mathbf{b})^t C^{-1}(\mathbf{x}-\mathbf{b})}, \quad (3.1)$$

where the f_0 is the maximum at $\mathbf{b} = (p_0, t_0)$, and C is the symmetric covariance matrix. Ideally there should be no correlation between p and t ; however, the cross-term of C was needed, for example, to fit TOF combinations with paddle 9 on the left, which had a bad discriminator on the bottom PMT. Elliptical cuts of n_σ standard deviations from the mean were formed from the constant contours defined by $f(\mathbf{x}) = f_0 e^{-\frac{1}{2}n_\sigma^2}$. The timing resolution for paddle combinations with the electron scattering into the left sector are shown in Fig. 3-1 with an example histogram of p versus t and its corresponding $n_\sigma = 2.5$ cut in the inset. The timing and coplanarity projections for the same paddle combination (left TOF #2, right TOF #13) are also shown on the two sides the cut.

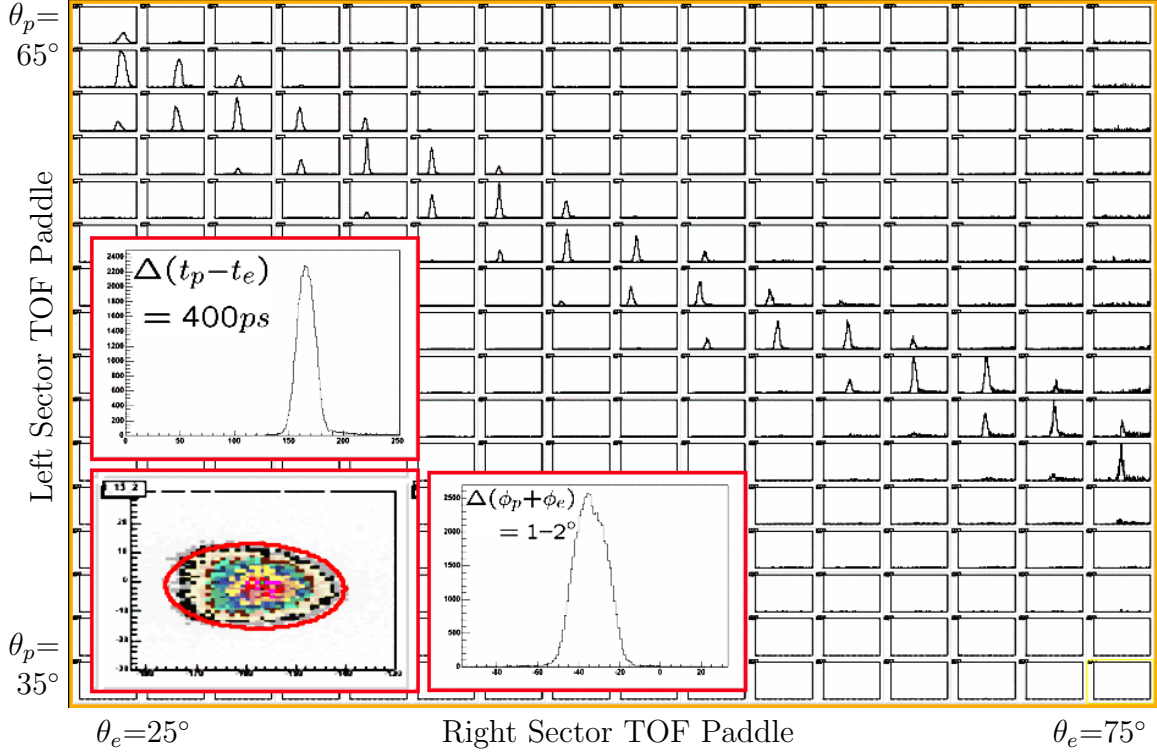


Figure 3-1: An illustration of the TOF timing and coplanarity cuts. Spectra of the proton timing delay are shown for each combination of the 16 TOFs in the right sector (vertical) and the 16 TOFs in the left sector (horizontal). The coplanarity vs. timing peak is also shown in the inset for the combination (left TOF #2, right TOF #13), with the 2.5σ elliptical cut, and timing and coplanarity projections shown on the sides.

3.1.2 Elastic WC Cuts

The most significant cuts were based track parameters from the drift chambers. The drift chambers provide 4 coordinates (p, θ, ϕ, z) for both the electron and proton, while elastic kinematics can be determined from only three coordinates, for example, (θ_e, ϕ_e, z_e) . Elastic relations between these and the other five coordinates are used to make cuts, specifically on $p_e(\theta_e)$, $p_p(\theta_p)$, $\theta_p(\theta_e)$, $\phi_p(\theta_e)$, and $z_p(z_e)$. For example for $p_e(\theta_e)$, the difference $\Delta_{p_e}(\theta_e) \equiv p_e - p_e(\theta_e)$ between the measured momentum and the kinematically determined momentum from θ_e was histogrammed as a function of θ_e . In each θ_e bin (1° wide), Δ_{p_e} was fit to a Gaussian with mean μ_{p_e} and RMS deviation σ_{p_e} . The mean and width were in turn fitted to a polynomial in θ_e , to obtain

the momentum offset $\mu_{p_e}(\theta_e) \equiv \langle \Delta_{p_e} \rangle$ and the relative deviation $\chi_p(\theta_e) \equiv (\Delta_{p_e} - \mu_{p_e})/\sigma_{p_e}$ of each event from elastic kinematics, with the associated cut $|\chi_p| < n_\sigma$. We investigated the dependence of the asymmetry and polarization on the width of the cut n_σ , and found very little variation. We chose to use independent 2.5σ cuts on each of the five redundant wire chamber variables. The distributions of Δ for each relation are shown in Fig. 3-2 with curves for the average, 1σ resolution, and the 2.5σ cuts.

The cut on $p_e(\theta_e)$ is equivalent to a cut on invariant mass $W^2 \equiv (q + p_2)^2 = M^2 + 2M\nu - Q^2$, except that it varies along with the width of the peak as a function of θ_e . For radiative corrections (Sec. 3.2.3), it was necessary to use a cut on inelasticity $v = W^2 - M^2$. In order to obtain a clean cut on W , the electron momentum was corrected by the offset $-\mu_{p_e}$. Likewise, the three cuts on $p_p(\theta_p)$, $\theta_p(\theta_e)$, $\phi_p(\theta_e)$ are equivalent to cuts on the missing 4-momentum $p_X \equiv k_1 - k_2 + p_1 - p_2$ which has three independent components when constrained by W . In elastic scattering p_X should be zero. The invariant mass (W) and missing mass squared ($M_X^2 \equiv p_X^2$) spectra are shown in Fig. 3-3. After the above corrections, \mathbf{p}_X is centered exactly about the origin. The widths of the two components of the scattering plane $\delta p_X^x = 27$ MeV and $\delta p_X^z = 29$ MeV are much wider than $\delta p_X^y = 6.7$ MeV due their stronger dependence on the reconstructed momentum resolution. Also, the former two are smeared by the s - and p -peaks of the radiative tail in the scattering plane (Fig. 1-2b,c). The final cut on $z_p(z_e)$ is not an elastic cut, but rather a cut on reconstruction. It reduces accidental coincidences by ensuring that tracks originate from the same vertex.

Additional boundaries were imposed on the range of each variable. The electron and proton angles were restricted to $23^\circ < \theta_e < 76^\circ$, $28^\circ < \theta_p < 69^\circ$, and $-14^\circ < \phi < 14^\circ$ to reduce the effect of wire chamber mis-reconstruction, especially at forward angles of the measured acceptance. A vertex cut of -20 cm $< z < 20$ cm was also used. Even though data were taken with a 60 cm long target cell, the holding field was only constant in the region of the cell included in the cut. However, the target is thickest in the center and only $1/16^{\text{th}}$ of the events are come from the last 10 cm at either end of the target.

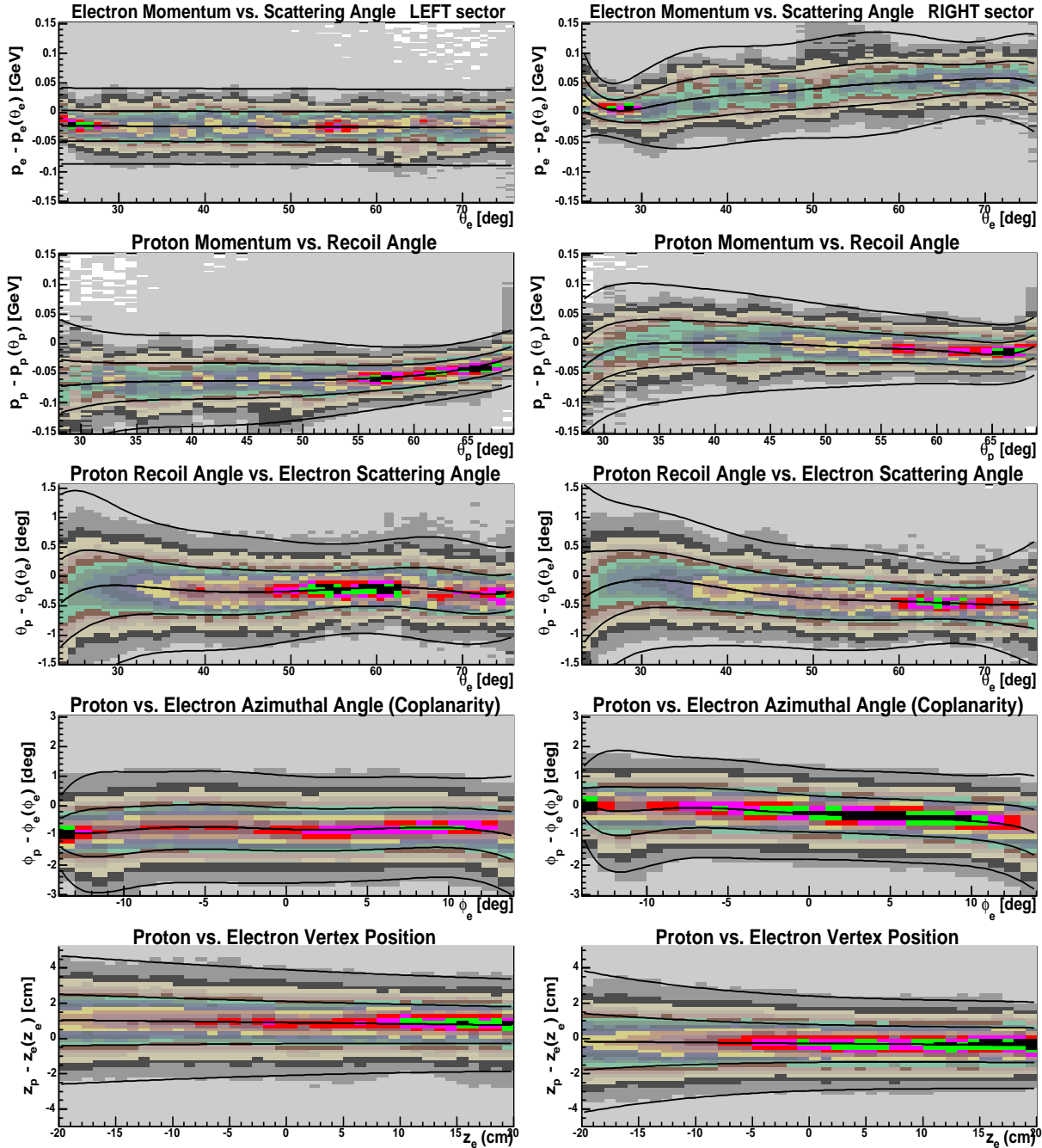


Figure 3-2: Drift Chamber cuts based on the five overdetermined track parameters: p_e , p_p , θ_p , ϕ_p , and z_p . Each plot is a histogram of the difference between one of these variables and the same, calculated from another track parameter using elastic kinematics. The left [right] panels correspond to electrons scattering into the left [right] sector. For example, in the top left panel, the electron momentum p_e in the left sector is calculated as a function $p_e(\theta_e)$ of its scattering angle θ_e , and the difference is histogrammed against θ_e . The five curves correspond to fits to the average kinematic correction, and 1σ and 2.5σ resolution. The 2.5σ band was used for drift chamber cuts.

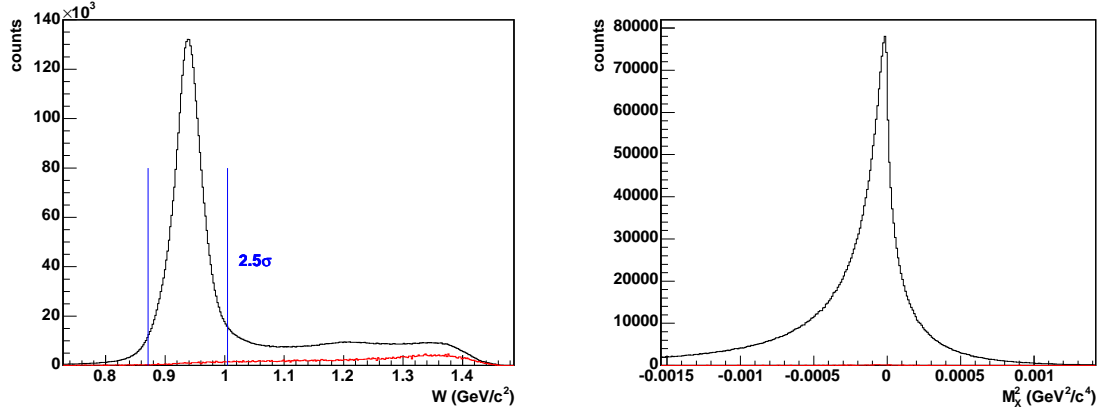


Figure 3-3: Invariant mass W (left) and missing mass squared M_X^2 (right) spectra, including the empty target background (red). For the W spectrum, the cut only required a positive track in one sector and a negative track in the other sector. The cut on W shown on the left was also applied to the M_X^2 spectrum and was used for the final analysis.

3.1.3 Q^2 Determination

From the kinematics of a coincidence measurement of the elastic reaction, there were four independent measures of Q^2 , using either momentum or scattering angle from either the electron or proton. However, the angular resolution of the wire chamber is much better than momentum resolution, so only the angles were used. As seen in Fig. 3-2, there is some discrepancy between the value of Q^2 determined from the electron scattering angle, and the value of Q^2 determined from the proton recoil angle. The effect of this on the systematic errors is discussed in Secs. 3.4.1 and 3.4.2. The discrepancy between these two determinations will be resolved after the 2005 run, but for the present work, the average Q^2 from these two determinations was used.

3.1.4 Yields

The total yield for each run normalized to the collected charge is shown in Fig. 3-4. There is a slowly varying trend which reflects changes in the thickness of the ABS target. Runs which varied from the average by more than 2.5σ were rejected.

The data were divided into 8 bins in Q^2 for compatibility with the systematic

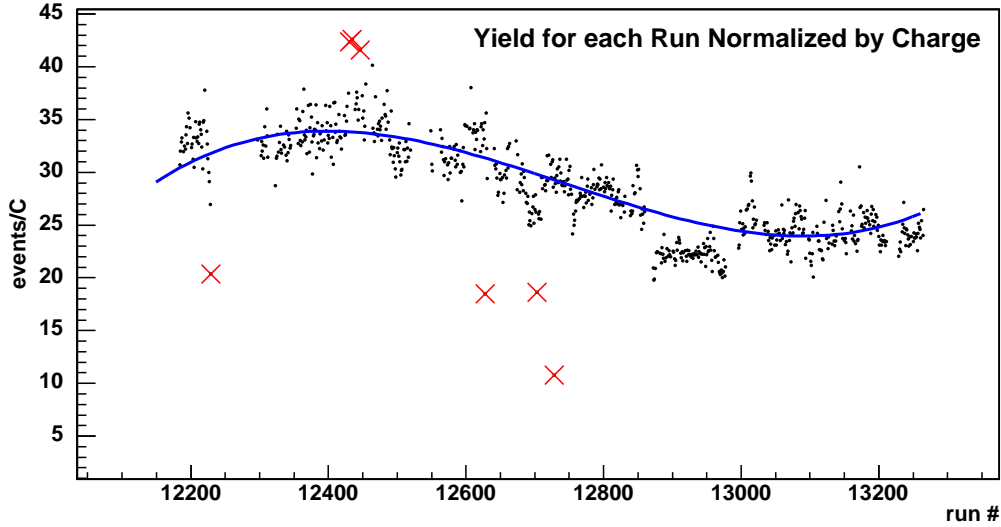


Figure 3-4: The total yield for each run, normalized by charge but not target thickness. Rejected runs are crossed out.

errors. The bins are progressively wider at higher Q^2 to compensate for the lower statistics. The Q^2 range of each bin is given in Table 3.2.

Figure 3-5 shows the yield in each Q^2 bin separately as a function of the run number. The sum of the yields in all Q^2 bins was normalized to unity. The yields in each bin were fit to a constant line to check for variations in time. Only the fourth ($Q^2 = 0.28 \text{ (GeV/c)}^2$) bin in the left sector showed any time dependence. This problem was caused by an inefficient PMT in the bottom of TOF 5 in the left sector. The PMT finally broke from the scintillator during run 12520, and was repaired before run 12549. In order to investigate the effect of this on the asymmetry and form factor ratio extraction, the data were divided into six sequential subsets, each analyzed separately (Sec. 3.4.5). Both the asymmetry and form factors from all six data sets were consistent with each other as expected, since efficiencies are supposed to cancel in the asymmetry.

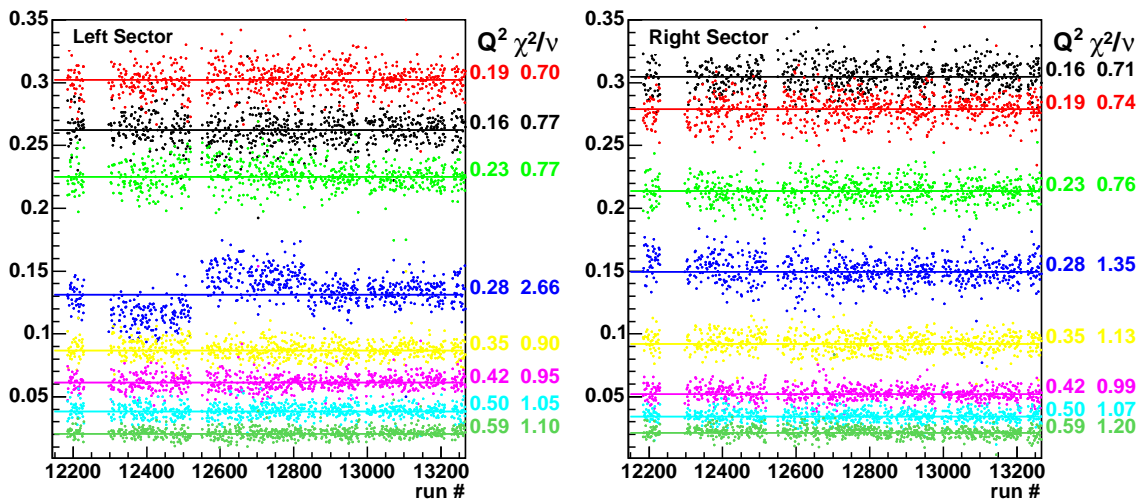


Figure 3-5: The yield in each Q^2 bin (Q^2 is in units of $(\text{GeV}/c)^2$). The total yield in all bins has been normalized to unity in each sector for each run. The run period is broken into 6 run sets (separated by vertical bars) to investigate the discontinuities in the $Q^2 = 0.28 (\text{GeV}/c)^2$ bin in the left sector (Sec. 3.4.5).

3.1.5 Luminosity

The thickness of the ABS target cannot be measured directly; however there are two methods of determining the luminosity using the yields: by comparison with either Monte Carlo simulations, or with the yields from the Unpolarized Gas Buffer System (UGBS). These methods have uncertainties from detector efficiencies and radiative corrections for MC simulations, or from the target cell conductance and buffer volume calibration of the UGBS. We take the approach of calibrating the absolute target thickness using the UGBS, and then compare our yields with MC simulations as a consistency check.

It is possible to obtain an absolute calibration of the UGBS target thickness. This can be used to normalize the elastic event yield by luminosity and thereby calibrate the target thickness of the ABS. In this system, a buffer of volume V and temperature T is filled every half hour with H_2 gas, which flows passively through a length of low conductance tubing into the target cell, so that the pressure P drops exponentially.

The UGBS flow rate Φ can be accurately determined using the ideal gas law,

$$\Phi = -\frac{V}{k_B T} \frac{dP}{dt}, \quad (3.2)$$

where k_B is the Boltzmann constant. In Fig. 3-6, the buffer pressure during runs 11870–11873 was fit to an exponential function of time to extract the average flow rate, $\Phi = (8.11 \pm 0.34) \times 10^{15}$ molecules/s. The density of gas in the cell was determined from the conductance of the target cell as in Sec. 2.2.2. The target cell used for production data for this experiment was a 60 cm long cylinder of diameter 1.5 cm, connected in the center to a cylindrical feeding tube 15 cm long with a diameter of 1.27 cm. The unpolarized gas was injected into the center of the cell, and saw the conductance of three cylinders in parallel with total conductance $C = 8.03$ L/s. The areal density (target thickness) of the UGBS, $\rho = 5.33 \times 10^{13}$ cm⁻², was obtained by integration of the triangular density profile from $z = -20$ cm to $z = 20$ cm, the region of the target used for the analysis of data. The integrated luminosity for these UGBS runs was $\mathcal{L}_{UGBS} = \int dt \rho I / e = 0.163$ pb⁻¹, where $\int dt I = 4.91$ kC was the integrated beam current. Multiplying by the normalization $Y_{ABS} / Y_{UGBS} = 550.9$, the ABS integrated luminosity was $\mathcal{L}_{ABS} = 89.8$ pb⁻¹ for 294.2 kC of beam used in the analysis of the form factor ratio, which corresponds to an average target thickness of $\rho = 4.89 \times 10^{13}$ cm⁻².

The error in the luminosity calibration is approximately 3%. The main errors include the buffer pressure (2%) and the buffer volume (2%), which will be remeasured to 1% accuracy at the end of the 2005 run. Other uncertainties include the calculation of the conductance (which could be significant but at the moment is not known conclusively), temperature variations (less than 0.3% because the hall temperature was included in the calculation), and a systematic shift in the detector efficiency between the UGBS and ABS runs, which were taken close together.

Using the luminosity from the UGBS, the normalized yield from the ABS target was compared with MC simulations (Sec. 3.4.4) in Fig. 3-7. The Monte Carlo events were generated from the elastic cross section with radiative corrections applied as

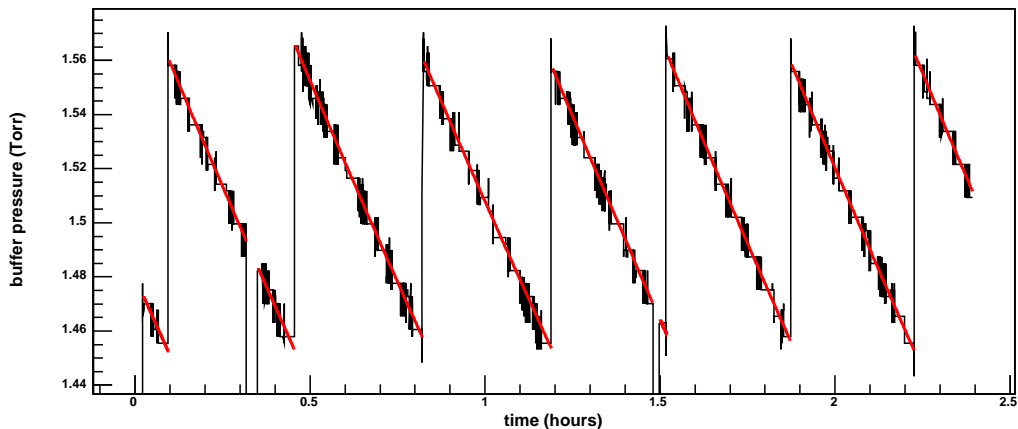


Figure 3-6: Pressure in the UGBS as a function of time.

described in Sec. 3.2.3. Events were generated with the same distribution as the cross section, as opposed to being generated uniformly across the phase space and being weighted by the cross section. The tracking resolution was smeared to have approximately the same drift chamber resolution as the real data, and the tracking efficiency, as measured in Sec. 2.3.2, was applied to the MC yield. The MC yield was decreased by 3.5% to account for a miscalculation of the beam current from the scalers at large currents. The MC yield was normalized by the number of events $N_{MC} = 10^7$ generated and the total cross section, $\sigma_{MC} = 161.5$ nb, of the phase space in which the events were generated, including both sectors. Although improvements still need to be made, the agreement between MC and the real data is reasonable, both in the overall normalization and in the shape of the yield as a function of Q^2 . The MC simulation is 7% lower than the real data in the left sector, and 13% lower in the right sector. The slight mismatch in the functional shape may be due to systematic shifts in Q^2 , which are further explored in Secs. 3.4.1 and 3.4.2.

3.2 Asymmetry

For elastic scattering, where the asymmetry depends only on the bin variable Q^2 , the experimental asymmetry can be extracted to high precision without Monte Carlo

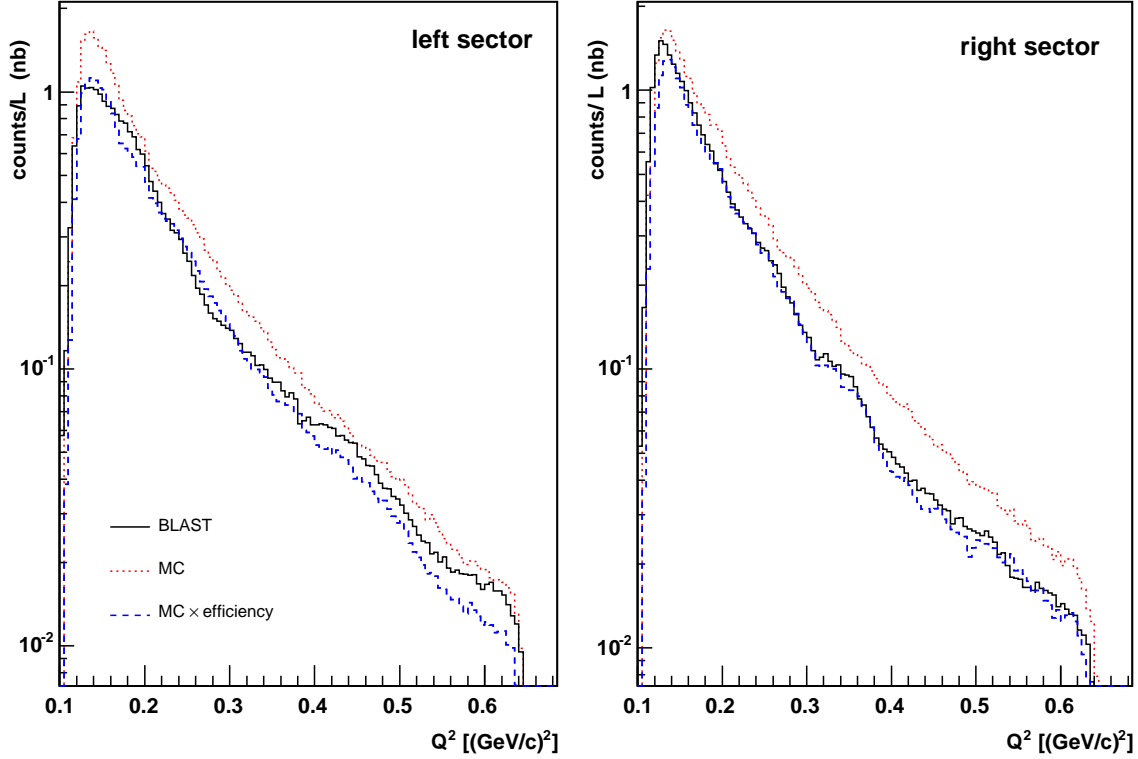


Figure 3-7: Comparison of the ABS yield (solid, black) and MC simulations, with (dashed, blue) and without (dotted, red) taking into account the detector efficiencies. The tracking efficiency of the electron and proton, radiative corrections, and a correction to the beam current were included in the efficiency.

simulation. The argument goes in two parts: First, the standard definition of the asymmetry applies both to a single point and to the weighted average of the asymmetry over a bin of finite width. The average asymmetry $\langle A \rangle$ over a bin in x is weighted by the unpolarized cross section since $\delta A \approx \frac{1}{\sqrt{N}}$, where N is the number of events. Since the helicity dependent cross section is related to the asymmetry by $\sigma_{\pm} \equiv \sigma(1 \pm A)$,

$$\langle A \rangle = \frac{\int dx \sigma A}{\int dx \sigma} = \frac{\frac{1}{2} \int dx (\sigma_+ - \sigma_-)}{\frac{1}{2} \int dx (\sigma_+ + \sigma_-)} = \frac{Y_+ - Y_-}{Y_+ + Y_-}, \quad (3.3)$$

where Y_{\pm} are the helicity dependent yields in that bin. Second, the average asymmetry can be associated with the asymmetry at the centroid of the bin. Let the true experimental asymmetry have the Taylor expansion $A(x) = A_0 + A_1 x + A_2 x^2 + \dots$,

then

$$\langle A \rangle = A_0 + A_1 \langle x \rangle + A_2 \langle x^2 \rangle \quad (3.4)$$

$$= A(\langle x \rangle) + \frac{1}{2} A'' \text{Var}(x), \quad (3.5)$$

where $A'' = 2A_2$ is the second derivative at an arbitrary origin in the bin, and $\text{Var}(x) = \langle x^2 \rangle - \langle x \rangle^2$. In our case, the correction would be largest at $Q^2 = 0.6 \text{ (GeV/c)}^2$, where $A''(Q^2) \approx 0.48 \text{ (GeV/c)}^{-4}$. Taking the worst case scenario of uniform Q^2 distribution in the bin of width 0.1 (GeV/c)^2 , the variance is $\text{Var}(Q^2) = (0.1 \text{ (GeV/c)}^2)/12$, and the correction would be less than 0.02%.

3.2.1 Raw Asymmetry

In this experiment, the yields from four double-polarized spin configurations labeled Y_{bt} , were measured. The beam helicity $b = \pm$ was flipped with every fill (10–15 minutes) and the target polarization $t = \pm$ was reversed every five minutes in a random manner. These four states are combined to form the unpolarized yield Y , the experimental asymmetry A_{raw} , and the beam and target single-spin asymmetries A_{beam} and A_{targ} , according to

$$Y \begin{pmatrix} 1 \\ A_{raw} \\ A_{beam} \\ A_{targ} \end{pmatrix} = \begin{pmatrix} 1 & 1 & 1 & 1 \\ 1 & -1 & -1 & 1 \\ 1 & 1 & -1 & -1 \\ 1 & -1 & 1 & -1 \end{pmatrix} \begin{pmatrix} Y_{++} \\ Y_{+-} \\ Y_{-+} \\ Y_{--} \end{pmatrix}. \quad (3.6)$$

Fast reversal of the target spin minimizes systematic errors in the asymmetry from slow drifts in the beam and target parameters or detector responses. Reversing both the beam and target polarization allows for an important cross-check of systematics, and more importantly cancels out false asymmetries to first order. To next order the false asymmetries appear only as a dilution.

The raw experimental asymmetries for electrons scattering into the left and right sectors are shown in Fig. 3-8 and Table 3.2. These asymmetries are fit to a parametriza-

tion using the Höhler form factors [12] to extract the product of beam and target polarization, $P = P_b \cdot P_t$. The difference in polarization between the left and right asymmetries is sensitive to the target spin angle, and the excellent agreement gives confidence in the measurement of the target magnetic holding field.

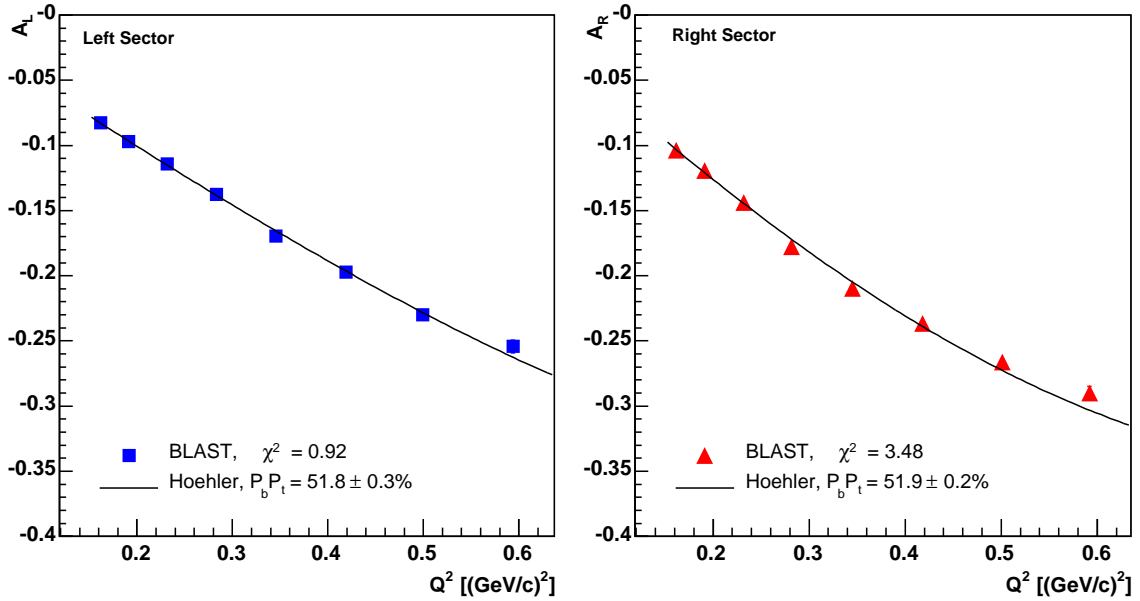


Figure 3-8: The experimental asymmetries measured for electrons scattering into the left (A_L) and right (A_R) sectors. The error bars are too small to be seen. Each sector was fit to the Höhler form factor parametrization to extract the product of beam and target polarization $P_b P_t$, which is consistent in the left and right sectors.

The extraction of $\mu G_E/G_M$ requires asymmetries in the left and right sectors at the same value of Q^2 . Even though the same bins are used in each sector, different distribution of events can cause a discrepancy of $Q_c^2 \equiv \langle Q^2 \rangle$ in each sector. Thus the asymmetries were adjusted to the average Q^2 of the left and right sector by scaling by the corresponding change in the asymmetries calculated from the Höhler form factor parametrization. This effect was very small.

The Höhler parametrization of the form factors was chosen because it was the state of the art fit to data mainly in the Q^2 range of our experiment. After this fit in 1976, most of the data were taken at higher Q^2 . Recent fits have had to accommodate newer data, which were at odds with the polarization data at $Q^2 > 1 (\text{GeV}/c)^2$. However,

beam	q_{++} [C]	q_{+-} [C]	q_{-+} [C]	q_{--} [C]
$\int I_{live}^{ABS} dt$	73692.6	73823.0	73337.4	72821.7
$\int I_{live}^{bkg} dt$	3777.1	3860.0	3678.1	3566.2

Q_{bin}^2	0.150	0.175	0.211	0.257	0.314	0.382	0.461	0.550	0.650
Q_c^2	0.162	0.191	0.232	0.282	0.345	0.419	0.500	0.593	
$\delta Q^2 \times 10^4$	0.069	0.100	0.152	0.237	0.336	0.509	0.702	0.978	

left sector

Y_{++}	117954	120493	83771	48730	33968	22534	13803	7662
Y_{+-}	140111	147687	106653	64290	47884	33771	21619	12589
Y_{-+}	137977	145025	104273	63746	47064	32999	21175	12202
Y_{--}	116942	119913	83717	48521	33799	22725	13558	7473
Y_{bkg}	163	207	221	210	203	192	176	108
Δ_{rc}	0.21	0.24	0.29	0.32	0.31	0.37	0.38	0.43
A_{beam}	0.16	0.16	0.19	-0.11	0.17	0.08	0.55	1.01
A_{targ}	-0.31	-0.48	-0.69	-0.22	-0.45	-0.90	-0.31	-0.51
A_{raw}	-8.20	-9.59	-11.26	-13.45	-16.49	-18.99	-21.79	-23.98
A_{exp}	-8.26	-9.69	-11.44	-13.71	-16.94	-19.69	-23.03	-25.38
δA_{exp}	0.14	0.14	0.16	0.21	0.24	0.29	0.37	0.49

right sector

Y_{++}	127503	112087	82604	52582	32309	16830	11072	6293
Y_{+-}	157989	143179	110227	74877	49528	27080	18939	11248
Y_{-+}	155940	140849	109062	73271	47961	26795	18344	11146
Y_{--}	126718	110863	81408	51092	31777	16804	10951	6224
Y_{bkg}	156	191	227	218	196	136	122	55
Δ_{rc}	0.11	0.12	0.16	0.16	0.11	0.14	0.10	0.11
A_{beam}	0.05	0.25	0.17	0.79	0.86	-0.08	0.78	0.06
A_{targ}	-0.31	-0.29	-0.06	-0.09	-0.68	-0.32	-0.81	-0.10
A_{raw}	-10.29	-11.83	-14.21	-17.45	-20.46	-22.92	-25.52	-28.09
A_{exp}	-10.37	-11.93	-14.38	-17.82	-20.99	-23.69	-26.58	-29.04
δA_{exp}	0.13	0.14	0.16	0.20	0.24	0.33	0.40	0.51

Table 3.2: Integrated beam current $q_{hh'}$ [C] (for beam helicity h and target polarization h'), Q^2 boundaries of bin, average Q^2 [(GeV/c)²] in bin, yields $Y_{hh'}$ [counts], radiative corrections Δ_{rc} [%] to the asymmetry, and asymmetries A [%], for each Q^2 bin. The raw asymmetry was corrected for empty target, beam blowup, radiative events, and Q^2 averaging between left and right sectors. The error δA_{exp} in the corrected experimental asymmetry is statistical only.

these form factors are only used as systematic checks of the data and to bin center Q^2 , so their impact on the analysis is minimal.

3.2.2 Background Correction

There is a small contribution to the raw yields from quasi-elastic scattering from the aluminum target cell wall, and shower events from the collimator upstream of the target. However, almost all events from the collimator are reconstructed upstream of the vertex cut, and can be differentiated by their low momentum. In addition, the collimator reduces the background from the cell wall to less than 0.5% in all Q^2 bins with a 2.5σ cut on the elastic peak in the invariant mass (W) spectrum. Both of these processes are helicity independent and can be corrected as a dilution to the asymmetry. The only background from the hydrogen target is radiative events, discussed below. The elastic peak is separated from the pion production threshold by 5 times the resolution of W , so the contribution to the asymmetry from inelastic scattering is insignificant.

The background was measured under the same conditions as the hydrogen data, but with the ABS gas flow turned off, and scaled by the ratio of integrated charge between the two datasets. However, gas in the target can affect the beam profile, possibly increasing the background rates at the same beam current [153]. This beam blowup effect was quantified in BLAST [133] through the $(e, e'n)$ quasi-elastic channel. Since there are no neutrons in the hydrogen target, this channel measures strictly the background, even in the presence of the hydrogen target. The ratio of $(e, e'n)$ yields from hydrogen Y_H^n versus empty target Y_{bkg}^n was $f_{beam} \equiv Y_H^n/Y_{bkg}^n \approx 1.05$. With the low backgrounds of BLAST, the beam blowup effect was insignificant. The raw asymmetry was corrected by

$$A = \frac{A_{raw}}{1 - f_{beam}Y_{bkg}/Y_H}, \quad (3.7)$$

where Y_H is the unpolarized elastic yield from the ABS hydrogen target and Y_{bkg} is the same from an empty target. The background distribution is shown with the

invariant mass distribution in Fig. 3-3, and the number of background events in each Q^2 bin are given in Table 3.2.

3.2.3 Radiative Correction

Radiative corrections were applied using the computer code MASCARAD [4] modified to accept an arbitrary orientation of the target polarization vector. This code, based on POLRAD, was chosen because it calculates spin-dependent radiative corrections. The unpolarized radiative corrections were tested against the computer code SIMC, used for unpolarized scattering in JLab Hall C. The corrections, calculated for different values of the cut-off parameter v (Sec. 1.1.1), are listed in Table 3.3. In order to ensure that the same cut-off was used in the analysis, a single cut on invariant mass W was used instead of cuts on each of the five overdetermined tracking parameters and on the TOF coplanarity and timing variables (Sec. 3.1.1). However the invariant mass cut yielded compatible results with the later more restrictive set of cuts. For the final analysis, a 2.5σ cut on W was used with the corresponding radiative corrections. As expected, the radiative corrections were very small, because most of radiative cross section σ_r can be factored as $\sigma_r = \sigma_0(1 + \delta)$, where σ_0 is the OPE cross section and δ is helicity-independent.

Q_c^2	0.162	0.191	0.232	0.282	0.345	0.419	0.500	0.593
$\delta(2.5)$	-.080	-.081	-.081	-.081	-.080	-.079	-.076	-.074
$\delta(5)$	-.046	-.045	-.045	-.044	-.042	-.040	-.036	-.033
$\delta(10)$	-.010	-.009	-.007	-.005	-.001	.003	.010	.018
$\Delta_L(2.5)$.0021	.0024	.0029	.0032	.0031	.0037	.0038	.0043
$\Delta_L(5)$.0040	.0046	.0054	.0062	.0062	.0074	.0078	.0084
$\Delta_L(10)$.0077	.0090	.0106	.0124	.0134	.0162	.0182	.0198
$\Delta_R(2.5)$.0011	.0012	.0016	.0016	.0011	.0014	.0010	.0011
$\Delta_R(5)$.0019	.0021	.0024	.0026	.0019	.0022	.0016	.0012
$\Delta_R(10)$.0022	.0024	.0026	.0027	.0015	.0018	.0006	-.0004

Table 3.3: Radiative corrections as a function of the cutoff $W - M$, in units of $\delta W = 0.027$ (GeV/c²). The corrections to the unpolarized cross section (δ) and to the asymmetry (Δ) are defined by $\sigma_r = \sigma_0(1 + \delta)$, and $A_r = A_0(1 + \Delta)$, respectively. The units of Q^2 are in (GeV/c)².

3.3 Form Factor Ratio

As mentioned in Sec. 1.4.1, there many ways to extract the proton form factor ratio $R = G_E/G_M$ from the asymmetry. From Eq. 1.27, the experimental asymmetry A_{ij} , for electrons scattering into sector $i=L,R$ and Q^2 bin j of average value Q_j^2 , depends on the product of beam and target polarization $P = P_b \cdot P_t$, and the form factor ratio $R_j = R(Q_j^2)$ by

$$A_{ij} = P \frac{z_{ij} + x_{ij} R_j}{\epsilon_j R_j^2 + \tau_j}, \quad (3.8)$$

where $z_{ij} \equiv \epsilon(1 + \tau)v_z z^*$ and $x_{ij} \equiv \epsilon(1 + \tau)v_x x^*$ are also evaluated at Q_j^2 . The target spin components x^* , z^* for the left ($i=L$) and right ($i=R$) sectors depend on Q_j^2 and the target holding field angle β . At least two asymmetries are needed to extract P and R_j in a single bin. The three methods presented below do this by grouping the asymmetries in different ways, and the advantages of each are discussed below. The extracted R and P from each method are listed in Table 3.4 and plotted in Fig. 3-9.

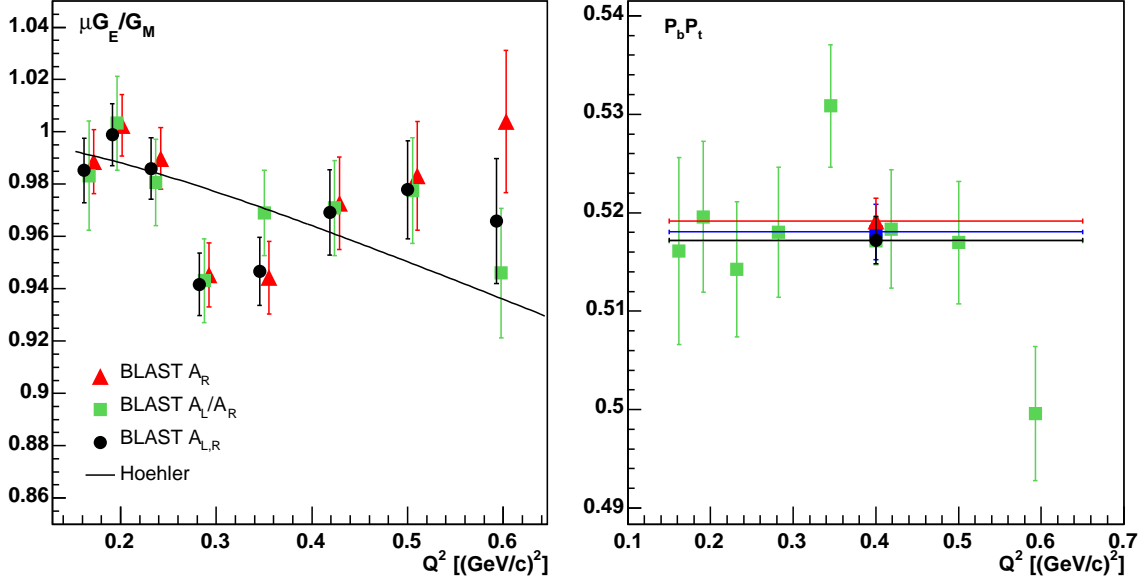


Figure 3-9: A comparison of the form factor ratio $\mu G_E/G_M$ and the product of beam and target polarization $P_b P_t$ extracted by the three methods described in the text: single-asymmetry (A_R), super-ratio (A_L/A_R), and global fit ($A_{L,R}$) methods.

Q_{ave}^2 [(GeV/c) ²]	0.162	0.191	0.232	0.282	0.345	0.419	0.500	0.593
$\mu G_E/G_M$ (A_R)	0.989	1.003	0.990	0.945	0.944	0.973	0.983	1.004
$\delta(\frac{\mu G_E}{G_M})$	0.012	0.012	0.012	0.012	0.014	0.018	0.021	0.027
$\mu G_E/G_M$ (A_L/A_R)	0.983	1.003	0.981	0.943	0.969	0.971	0.978	0.946
$\delta(\frac{\mu G_E}{G_M})$	0.021	0.018	0.017	0.016	0.016	0.018	0.020	0.025
$P_b \cdot P_t$	0.516	0.520	0.514	0.518	0.531	0.518	0.517	0.500
$\delta(P_b \cdot P_t)$	0.009	0.008	0.007	0.007	0.006	0.006	0.006	0.007
$\mu G_E/G_M$ ($A_{L,R}$)	0.985	0.999	0.986	0.942	0.947	0.969	0.978	0.966
$\delta(\frac{\mu G_E}{G_M})$	0.012	0.012	0.012	0.012	0.013	0.016	0.019	0.024

Table 3.4: Values for $\mu G_E/G_M$ with statistical errors from the three extraction methods: single asymmetry (A_R), super-ratio (A_L/A_R), and global fit ($A_{L,R}$). The polarization in each bin is also given for the super-ratio method.

3.3.1 Single Asymmetry Extraction

The straightforward extraction is to use Eq. 3.8 on a subset of the data (the polarimetry data) together with a model of the form factors to extract P . With this input, R can be solved for point by point from the rest of the data. We used the first Q^2 point as the polarimeter, measuring the form factor ratio in the rest of the bins. This method takes advantage of the large acceptance of BLAST, in that all Q^2 points are measured at the same time under the same target and beam conditions. However, we lose the form factor ratio for the first point when we use it as a polarimeter. Another problem is the model dependency introduced into the form factor ratio measurement. Fortunately $\mu G_E/G_M$ is constrained to 1 at $Q^2 = 0$, which minimizes the model dependency.

In principle, this method can be applied separately in the left and right sectors, giving independent measures of P in the first bin, and of R in subsequent bins. Figure 3-10 illustrates the asymmetry as a function of $\mu G_E/G_M$ in a separate panel for each Q^2 bin. The dashed horizontal line with an error band is the measured asymmetry A in the left sector and the dashed curve is of the function $A_L(R)$ at fixed P ; the solid lines are the same for the right sector. Due to our choice of spin angle, the left sector has essentially perpendicular kinematics, while in the right sector \mathbf{q} is

parallel to the target polarization:

$$x_L^* = 1, \quad z_L^* = 0 \quad \text{and} \quad x_R^* = 0, \quad z_R^* = 1. \quad (3.9)$$

As a result the numerator of A_L is proportional to R and the function $A_L(R)$ has a local minimum near the physical value of R , making the extraction difficult, especially at low Q^2 . The right sector is more sensitive to R . The numerator of A_R is constant, so that the form factor ratio is extracted from R^2 dependence of A_R in the denominator, the unpolarized part.

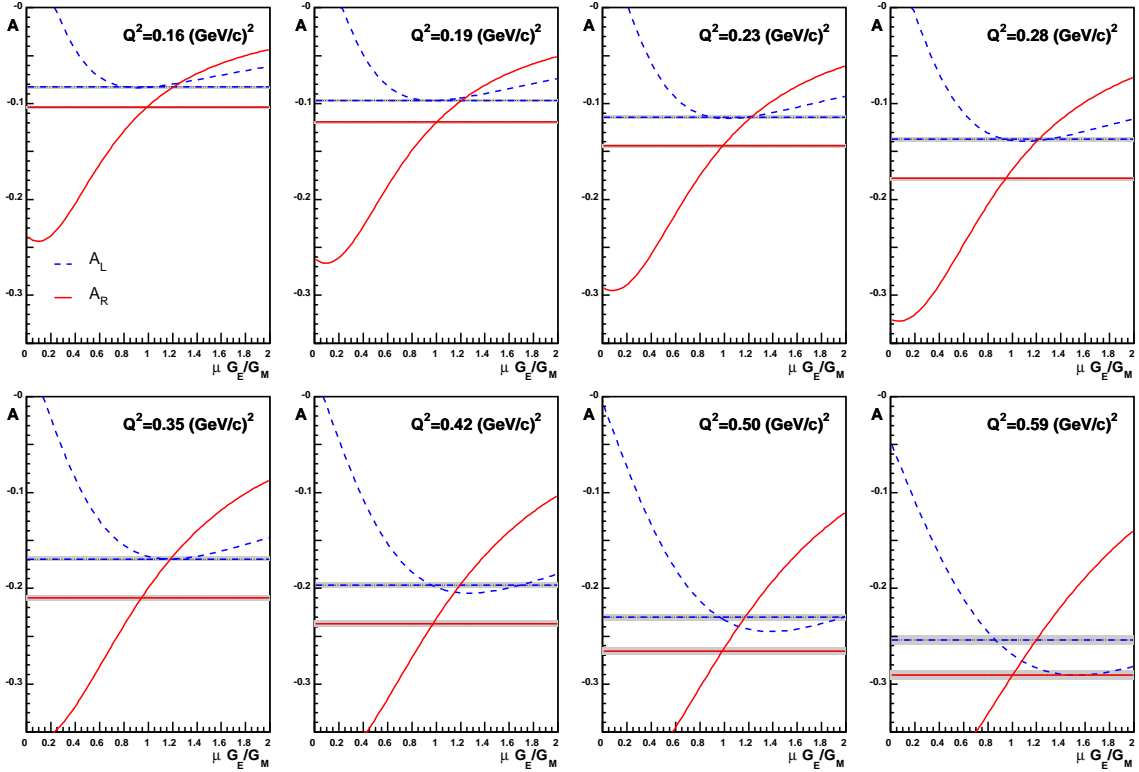


Figure 3-10: Single-asymmetry extraction of the form factor ratio. The asymmetries A_L (blue, dashed) and A_R (red, solid) are plotted as a function of $\mu G_E/G_M$ and compared with the measured asymmetry in each sector (constant lines with error bands).

Alternatively, the polarization can be extracted from a fit to all asymmetries in one sector, in which case the normalization of all R_j points is fixed by the model. This was done in Fig. 3-8 with the Höhler parametrization. The target spin angle

β can be verified by comparing P_i from the left and right sectors for different fixed values of β , as in Fig. 3-11. The results of this comparison, $\beta = 47.5 \pm 0.8^\circ$, are consistent with the measured spin angle $\beta = 47.1^\circ \pm 1^\circ$ from the target holding field map averaged over the vertex distribution.

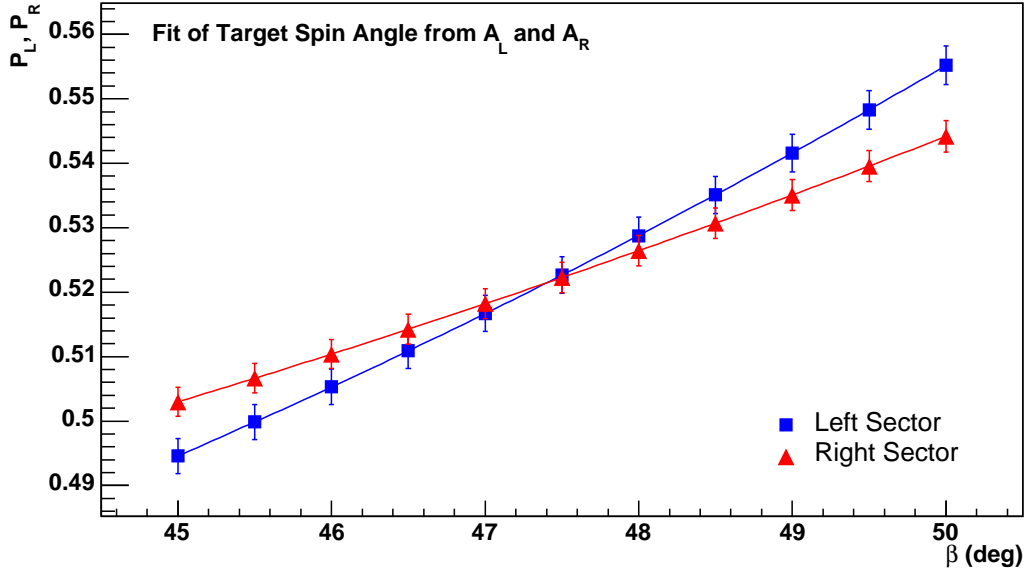


Figure 3-11: The target spin angle β , extracted from fits of A_L and A_R for the polarization in the left and right sectors, respectively, using the Höhler form factor parametrization. The spin angle β is extracted by requiring that the polarization $P = P_b P_t$ be the same in both sectors.

3.3.2 Super-ratio Extraction

The model dependence can be removed by forming a super-ratio $R_A = A_L/A_R$ of the left sector and right sector asymmetries in each Q^2 bin. The denominator of each asymmetry cancels in the super-ratio, as only x^* and z^* depend on the sector. In the ideal case with a pure transverse asymmetry in the left sector and longitudinal asymmetry in the right sector (Eq. 3.9), the super-ratio is proportional to R (not R^2)

$$R_A = \frac{z_L + x_L R}{z_R + x_R R} \approx \frac{v_x}{v_z} R. \quad (3.10)$$

R can be substituted back into Eq. 3.8 for either the left or right sector to extract the polarization.

Instead of directly forming the super-ratio as above, both R and P can be solved from A_L, A_R by transforming Eq. 3.8 for A_L and A_R into the linear equation

$$\begin{pmatrix} -x_L^* & A_L \\ -x_R^* & A_R \end{pmatrix} \begin{pmatrix} \frac{v_x R}{v_z} \\ \frac{\epsilon R^2 + \tau}{\epsilon(1+\tau)v_z P} \end{pmatrix} = \begin{pmatrix} z_L^* \\ z_R^* \end{pmatrix} \quad (3.11)$$

with the solution

$$R = -\frac{v_z}{v_x} \cdot \frac{z_L^* A_R - z_R^* A_L}{x_L^* A_R - x_R^* A_L} \quad (3.12)$$

and

$$P = \frac{\epsilon R^2 + \tau}{\epsilon(1+\tau)v_z} \cdot \frac{x_L^* A_R - x_R^* A_L}{x_L^* z_R^* - x_R^* z_L^*}. \quad (3.13)$$

Another advantage of the super-ratio method beside model independency is that an independent polarization P_j can be extracted in each Q^2 bin. This is an important check on systematic errors. Also, if an unanticipated dilution is the same in both sectors and depends only on Q^2 (not the spin angle), then it can be absorbed into P_j . In this case the extracted form factor ratio will still be accurate. However, from Eq. 3.13 it is apparent that one cannot compare polarizations from the left and right sector using this method. In Fig. 3-9, the polarization in all bins except possibly the last are consistent with each other.

3.3.3 Global Fit Extraction

The third extraction combines the strengths of the two previous methods by fitting both the left and right sector asymmetries for P . Instead of relying on a model for the form factors R_j in the fit, they are included as free parameters, extracted simultaneously with P . This method takes advantage of both the symmetric left and right sectors and the large acceptance of BLAST.

The fit makes optimal use of the asymmetry information in extracting P and R_j , and has the lowest statistical uncertainty in R_j of the three methods. Compared to the single asymmetry method, the fits of P in each sector are combined into a

single consistent fit which is model independent and does not sacrifice any points to polarimetry. Compared to the super-ratio method, the fit method consolidates P_j from each bin into a single P , applying the extra statistical information toward the form factor ratio results. For this reason, the final results are presented in terms of this fit. However, the other two methods are indispensable systematic checks because of their redundant polarization measurements in the left and right sectors, or in each Q^2 bin.

The fit method can also be used to extract the target spin angle, although with rather large uncertainty. Given n bins in Q^2 , there are $2n$ asymmetry measurements in the two sectors. The super-ratio method is equivalent to fitting for the $2n$ parameters P_j and R_j . Such a fit was used to double-check the super-ratio extraction and corresponding statistical errors. Fitting for a single P frees up $n - 1$ parameters, one of which can be used to fit for β . Such a $n + 2$ parameter fit was performed, yielding $\beta = 42^\circ \pm 3^\circ$. This value, well below the field map, is skewed by the highest Q^2 point, which has lower target polarization. If we omit it, we get the more reasonable value $\beta = 48^\circ \pm 4^\circ$. The statistical error in β is much better from the single asymmetry method due to the Höhler constraint. There is a strong correlation between β and P , while optimization of the two parameters together is very weak. Figure 3-12, which shows the χ^2 of the fit as a function of these two parameters, illustrates this as the long flat valley in (P, β) -space. This works to our advantage, since error in the measurement of β will be partially compensated for by a shift in the fitted P .

3.4 Systematic Errors

The major contributions to the systematic errors, listed in Table 3.5, come the determination of Q^2 and of the target spin angle β . Both of these uncertainties need to be improved in order to be comparable with the statistical errors. They will be investigated when BLAST is finished taking production data in 2005. These and other systematic checks are discussed below.

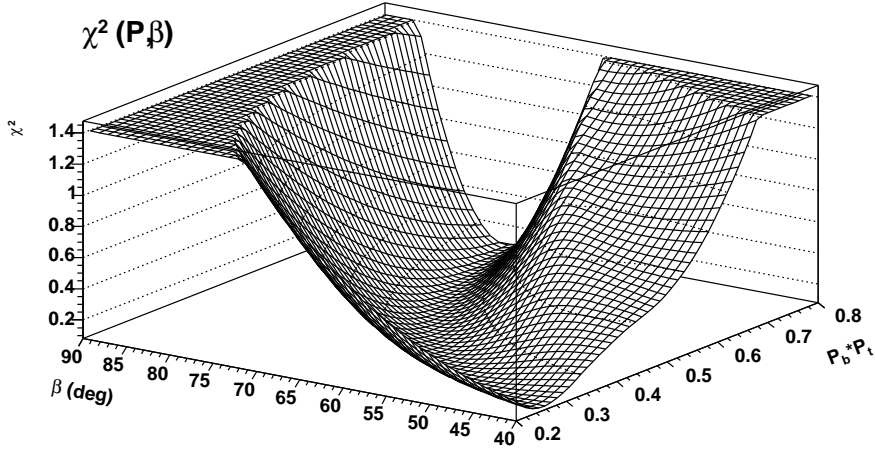


Figure 3-12: The P and β -dependence of the χ^2 function used in the $2+n$ -parameter fit of A_{ij} . Instead of a sharp minimum, χ^2 has a strong correlation between P and β along the valley.

3.4.1 Drift Chamber Q^2 Determination

A precise determination of Q^2 from the drift chambers is essential. Even though $\mu G_E/G_M$ varies slowly with Q^2 , the asymmetry decreases rapidly as a function of Q^2 . Also, kinematic factors used in the extraction of the form factor ratio depend on Q^2 . Systematic shifts in Q^2 affect the uncertainty in $\mu G_E/G_M$ much more than the Q^2 resolution of single events due to the large statistics in each bin. The shifts ΔQ_L^2 and ΔQ_R^2 in the two sectors are combined to form symmetric (ΔQ_S^2) and antisymmetric (ΔQ_A^2) shifts, where

$$\Delta Q_{L,R}^2 = \Delta Q_S^2 \pm \Delta Q_A^2. \quad (3.14)$$

Because $\mu G_E/G_M$ is approximately proportional to A_L/A_R and both asymmetries have a similar functional dependence on Q^2 , the systematic error contributed by ΔQ_A^2 is much larger than that from ΔQ_S^2 . Table 3.6 shows the effect of these two shifts on the extraction of the form factor ratio.

The magnitude of these shifts is estimated by comparing Q_e^2 (calculated from the electron scattering angle θ_e) to Q_p^2 (calculated from the proton recoil angle θ_p). The difference in these two determinations of Q^2 , shown in Fig. 3-13, increases with Q^2 and

Q_c^2 [(GeV/c) ²]	.162	.191	.232	.282	.345	.419	.500	.593
$\delta\beta$.008	.008	.008	.008	.008	.008	.008	.008
δQ_{WC}^2	.018	.018	.018	.018	.018	.018	.018	.035
total	.020	.020	.020	.020	.020	.020	.020	.020
δQ_{TOF}^2	.018	.022	.027	.032	.036	.043	.045	.047
total	.020	.023	.028	.033	.037	.044	.046	.048

Table 3.5: A list of contributions to the systematic error in $\mu G_E/G_M$. The uncertainty from the spin angle $\delta\beta$ is an overall normalization, while the error in δQ^2 varies point-to-point. The first set of errors for δQ^2 , used in Fig. 4-1, applies to reconstruction of Q^2 from the drift chambers only, but reflects the discrepancies in both the WC and TOF determinations of Q^2 . The second set, used in Fig. 4-5, comes from the uncertainty in the TOF correction to Q^2 . In each set, the error from $\delta\beta$ is added in quadrature with that from δQ^2 calculate the total systematic error.

is different in each sector. This is consistent with the discrepancies in the momentum offset corrections between the left and right sectors. Estimates of δQ_L^2 , δQ_R^2 , and $\delta(\mu G_E/G_M)$ from this method are shown in Table 3.6. The error in the form factor ratio is calculated by comparing extractions using the above two determinations of Q^2 . A systematic uncertainty in $\mu G_E/G_M$ of 0.018 due to δQ^2 is assigned to all data points except the highest Q^2 value, which is assigned 0.035.

It is believed that these discrepancies may be caused by a change in the BLAST field compared to the measured field-map. For practical purposes, the field-map was done without the wire chambers and outer detectors in position, even though they may have influenced the field during the experiment. Also, heavy steel magnetic shields were installed in front of the Čerenkov PMTs close to the BLAST field, and these could have an effect on the field. Possible changes in the BLAST field will be investigated after the the 2005 run is completed.

3.4.2 TOF Q^2 Determination

Timing information from the TOF scintillators can be used to get an independent measure of Q^2 using the kinematic relation

$$Q^2 = 2M\nu = 2M^2(\gamma - 1), \quad (3.15)$$

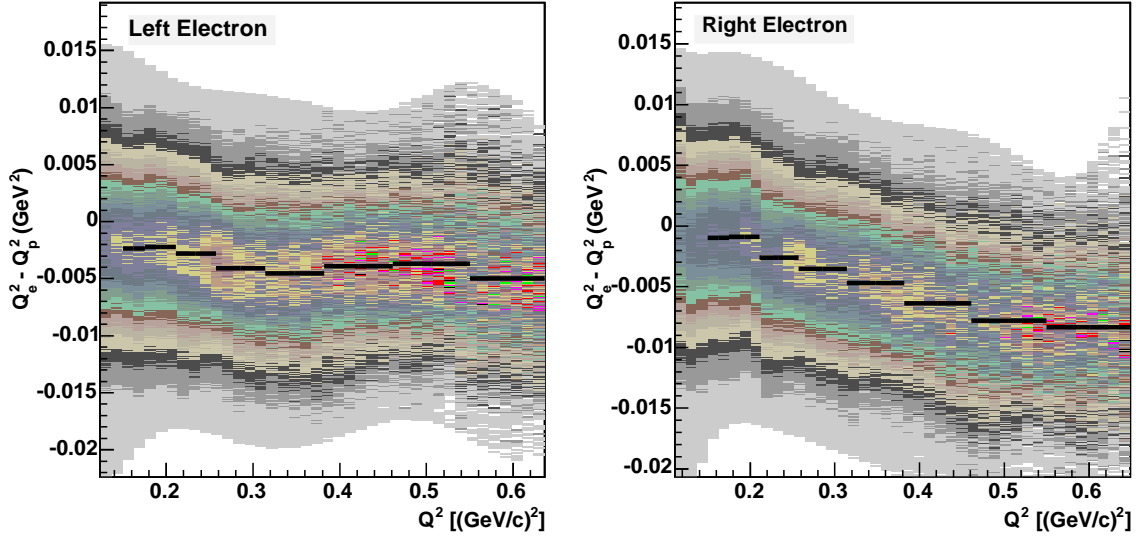


Figure 3-13: The discrepancy in Q^2 between calculations of Q^2 from the proton recoil angle and the electron scattering angle.

where $\gamma = 1/\sqrt{1 - \beta^2}$ is the recoil energy of the proton divided by its mass. The velocity of the proton is

$$\beta = \frac{v}{c} = \frac{d_p}{d_e + c\Delta t}, \quad (3.16)$$

where d_e and d_p are the path lengths of the electron and proton, respectively, and Δt is the timing delay between the electron and proton scintillator signals. The electron is assumed to be ultra-relativistic ($v = c$).

The difference between Q_{TOF}^2 (as determined above) and Q_{WC}^2 (from the drift chambers) is shown in Fig. 3-14. The antisymmetric part of the discrepancy ΔQ_A^2 is used to calculate a correction of $\mu G_E/G_M$ from the TOFS, given in Table 3.6. The Q^2 resolution of the scintillators is not as good as that of the drift chambers, especially at large Q^2 . However, there may be a systematic shift in Q^2 reconstructed from the drift chambers due to unknown variations in the BLAST field. The scintillator timing determination of Q^2 is more dependable at the present time, since the absolute scintillator timing was calibrated from an analysis of cosmic ray coincidence events. The error in the correction to $\mu G_E/G_M$ from the TOFs was calculated assuming

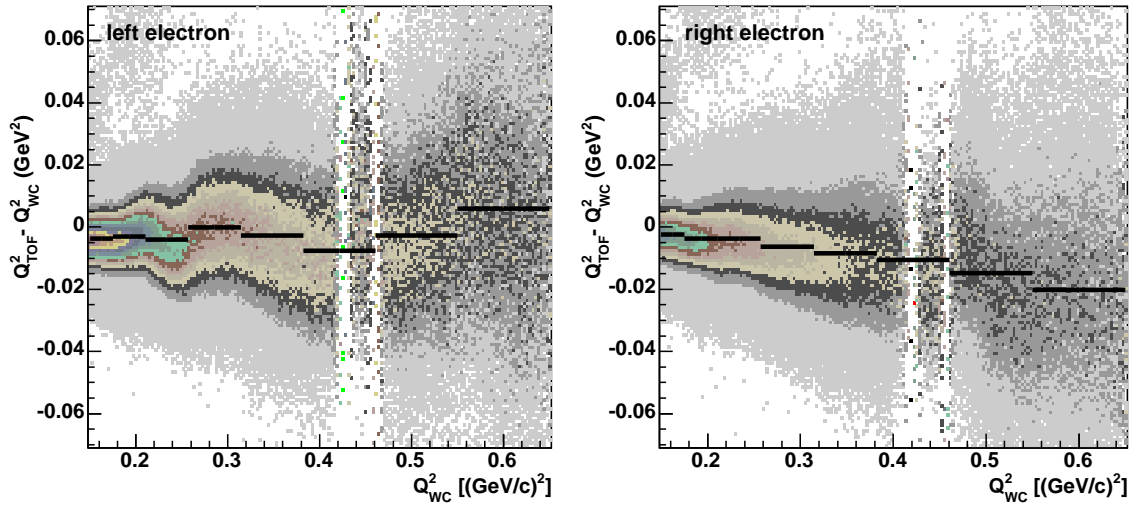


Figure 3-14: Comparison of Q^2 from the TOF scintillators and the drift chambers. The two vertical bands are caused by the omission of TOF 9 in the left and right sector.

150 ps systematic errors in timing. Work is being done to push this error down to 1 channel (50 ps) with a more thorough calibration of the timing offsets with cosmic rays.

There are plans to investigate the difference between TOF and drift chamber reconstruction after the 2005 run. After the cause of the discrepancies is understood and corrected, the systematics will be further reduced by performing a kinematic fit for Q^2 of each event with combined data from both the drift chamber and TOF scintillator hits.

3.4.3 Target Spin Angle

Precise knowledge of the target holding field angle is also important. After the hydrogen production run, a careful map of the holding field was done using a 3-D Hall probe and a special jig to align the probe with respect to the scattering chamber. The alignment of the Hall probe was measured by inserting it in a uniform dipole field. However, geometric restrictions prevented a precise measurement of one of the orientation angles of the Hall probe, which was unfortunately in the same direction as

Q^2 bin	0.162	0.191	0.232	0.282	0.345	0.419	0.500	0.593
$d\frac{\mu G_E}{G_M}/dQ_S^2$	2.8	1.9	0.9	0.1	-0.5	-0.9	-1.3	-1.5
$d\frac{\mu G_E}{G_M}/dQ_A^2$	-7.2	-6.6	-6.1	-5.5	-4.8	-4.3	-3.8	-3.3
$(Q_e^2 - Q_p^2)_L$	-0.0024	-0.0022	-0.0028	-0.0041	-0.0045	-0.0039	-0.0037	-0.0050
$(Q_e^2 - Q_p^2)_R$	-0.0010	-0.0009	-0.0026	-0.0035	-0.0047	-0.0064	-0.0078	-0.0083
$\frac{\mu G_E}{G_M e} - \frac{\mu G_E}{G_M p}$.018	.010	-.003	.002	.015	.019	-.001	.035
$(Q_{\text{TOF}}^2 - Q_{\text{WC}}^2)_S$	-0.0031	-0.0033	-0.0039	-0.0031	-0.0056	-0.0091	-0.0088	-0.0072
$(Q_{\text{TOF}}^2 - Q_{\text{WC}}^2)_A$	-0.0007	.0003	-0.0001	.0031	.0028	.0014	.0061	.0131
$\frac{\mu G_E}{G_M \text{ TOF}} - \frac{\mu G_E}{G_M \text{ WC}}$	-0.0047	.0021	-0.0007	.0169	.0135	.0062	.0231	.0431
$\delta(\Delta\frac{\mu G_E}{G_M})$.018	.022	.027	.032	.036	.043	.045	.047

Table 3.6: The effect of δQ^2 on the form factor ratio. The error in Q^2 is estimated by comparing determinations of Q^2 from θ_e , θ_p , and from timing. The last two lines list corrections to the form factor ratio and the associated errors using an absolute calibration of Q^2 from the TOF scintillators. Units of Q^2 are in $(\text{GeV}/c)^2$.

the holding field angle β . The uncertainty is estimated at 1° , which causes a systematic error of 0.73% in $\mu G_E/G_M$. A precision measurement of the holding field will be done after the current production run. A similar measurement has been performed at KEK [154], where the field angle in a spectrometer was mapped to better than 0.2° .

The target holding field angle has been extracted from the analysis of two different physics channels as a verification of the target field-map. Sections 3.3.1 and 3.3.3 reported extractions of β from the hydrogen data. The T_{20} observable from elastic electron scattering of a tensor polarized deuterium target is also sensitive to β . From an analysis of the limited deuterium dataset taken at the same holding field as the hydrogen data [155], β was determined to be $46.5^\circ_{-2.5^\circ}^{+3.5^\circ}$. The determinations of β are summarized in Table 3.7. Based on the consistency of these measurements, we estimate a 0.8% contribution to the $\mu G_E/G_M$ systematics from the spin angle uncertainty.

3.4.4 Monte Carlo Simulation

Although the asymmetry and form factor ratio extraction from this experiment are straightforward, we ran a Monte Carlo simulation as a check of the reconstruction and analysis codes, and to confirm the validity of the extraction. We used the standard

Method	β
Holding field map	$47.1^\circ \pm 1^\circ$
Höhler fit of Sec. 3.3.1	$47.5^\circ \pm 0.8^\circ$
Global Fit of Sec. 3.3.3	$42^\circ \pm 3^\circ$
(omit last Q^2 point)	$48^\circ \pm 4^\circ$
T_{20} analysis	$46.5^{+3.5^\circ}_{-2.5^\circ}$

Table 3.7: Summary target spin angle (β) measurements.

BLAST code `blastmc` based on GEANT 3.21 with the event generator `DGen` [155]. We generated events distributed according to the elastic e - p cross section, as opposed to a white generator with a uniform distribution across the phase space, tagging the cross section as a weight to each event. The Höhler form factors were used as input to the cross section. Each event is simulated through a realistic model of the BLAST detector. The simulation includes physical processes such as energy loss and multiple scattering of particles in the detectors. The tracks are digitized in each of the detectors they pass through, resulting in a CODA format data file which is compatible with output of the data acquisition system. The MC data are then reconstructed with the same code that analyzes the real data, with only a few technical differences such as a simplified electronics map. In addition, the generated track parameters are passed along for evaluation of the tracking performance.

For our simulation, 10^7 events were generated, and same analysis on them was performed as on the real data. One difference was that the beam and target polarization were set to 100%. The statistical errors were treated differently; `DGen` uses the pseudo-random Sobol sequence with errors that go as $\ln(n)$ instead of \sqrt{n} for the Poisson distribution. The results for the asymmetry and form factor ratio extraction from the Monte Carlo data are shown in Fig. 3-15. There was an unexplained drop in $\mu G_E/G_M$ at $Q^2 < 0.15 (\text{GeV}/c)^2$. This drop was not present for data analyzed straight from the `DGen` event generator, but arose from the acceptance of BLAST in `blastmc` and also in the reconstruction. Because of this, our results are reported with the first bin starting at $Q^2 = 0.15 (\text{GeV}/c)^2$.

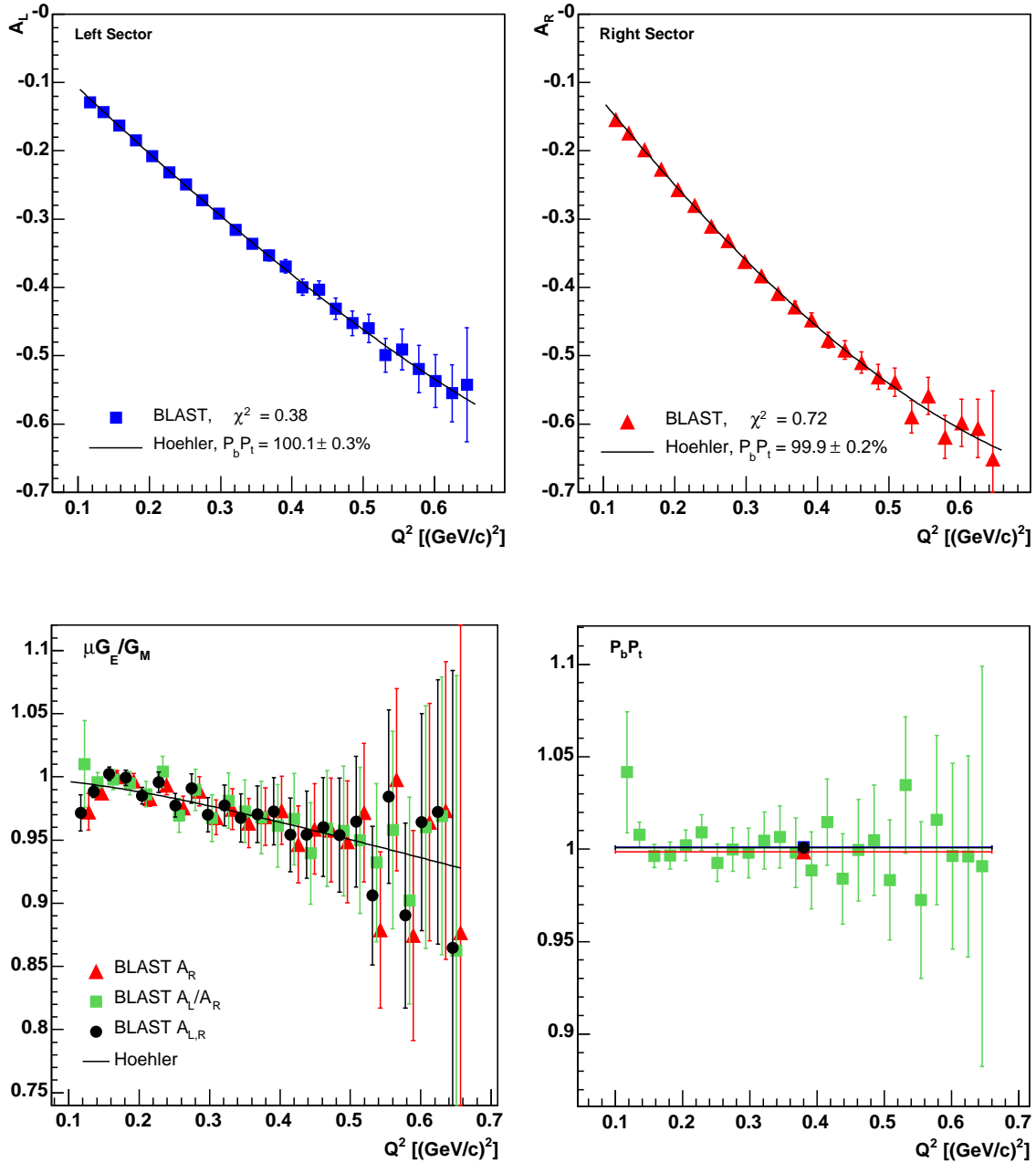


Figure 3-15: The asymmetry and form factor ratio from analysis of Monte Carlo data. Compare with Figs. 3-9 and 3-8.

3.4.5 Binning and Cuts

In order to check for binning effects, the analysis was repeated with 24 bins in Q^2 , as shown in Fig. 3-16. The discontinuities in the yield of the $Q^2 = 0.29 (\text{GeV}/c)^2$ bin (Fig. 3-5) were also investigated. As mentioned in Sec. 3.1.4, the whole dataset was broken into six sets, the first three sets separated by the above discontinuities, and the last three sets divided equally. The analysis was performed independently on each data set (Fig. 3-17), and the results of all sets were consistent with each other.

The choice of cuts also had a negligible effect on the asymmetry and extracted form factor ratio. The analysis was repeated for different combinations of TOF, Čerenkov, and drift chamber cuts, and the results from each combination were consistent with each other. Cuts on all five redundant tracking parameters from the drift chambers were compared with a single cut on invariant mass W . There was also little dependence of the width of cuts. A 2.5σ cut on W was used for the final analysis.

3.4.6 False Asymmetry

There are two independent measures of false asymmetries: the beam helicity asymmetry averaged over the two target spin states, and vice versa (Eq. 3.6). These measurements can detect asymmetries in the intensity or polarization between the two beam or target polarizations or asymmetries in the integrated beam current of each spin combination. The beam asymmetry A_b is negligible, but there is a small 0.4% target asymmetry A_t (Fig. 3-18). It is likely due to a difference in the intensity of the two ABS polarization states, as opposed to a true false asymmetry, since the beam asymmetry is small. There are a number of possible causes: an inefficient WFT in the ABS, spin-dependence of the target cell temperature due to interference of readout electronics with the WFT, or random intervals in which the ABS was temporarily unpolarized. The target asymmetry cancels to first order in the physics asymmetry by combining all four spin states, and has negligible systematic error.

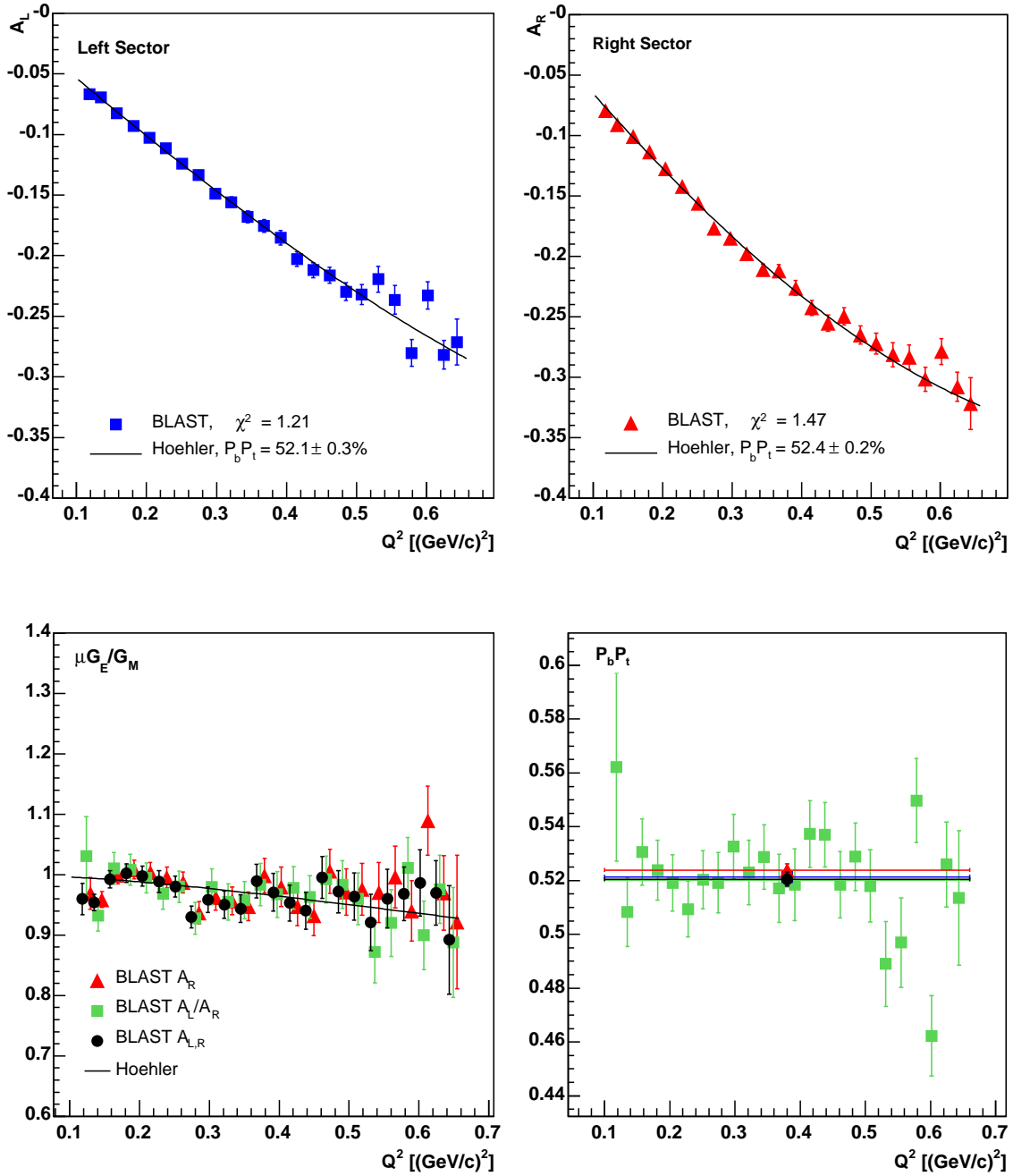


Figure 3-16: The asymmetry and form factor ratio in 24 bins. Compare with Figs. 3-9 and 3-8.

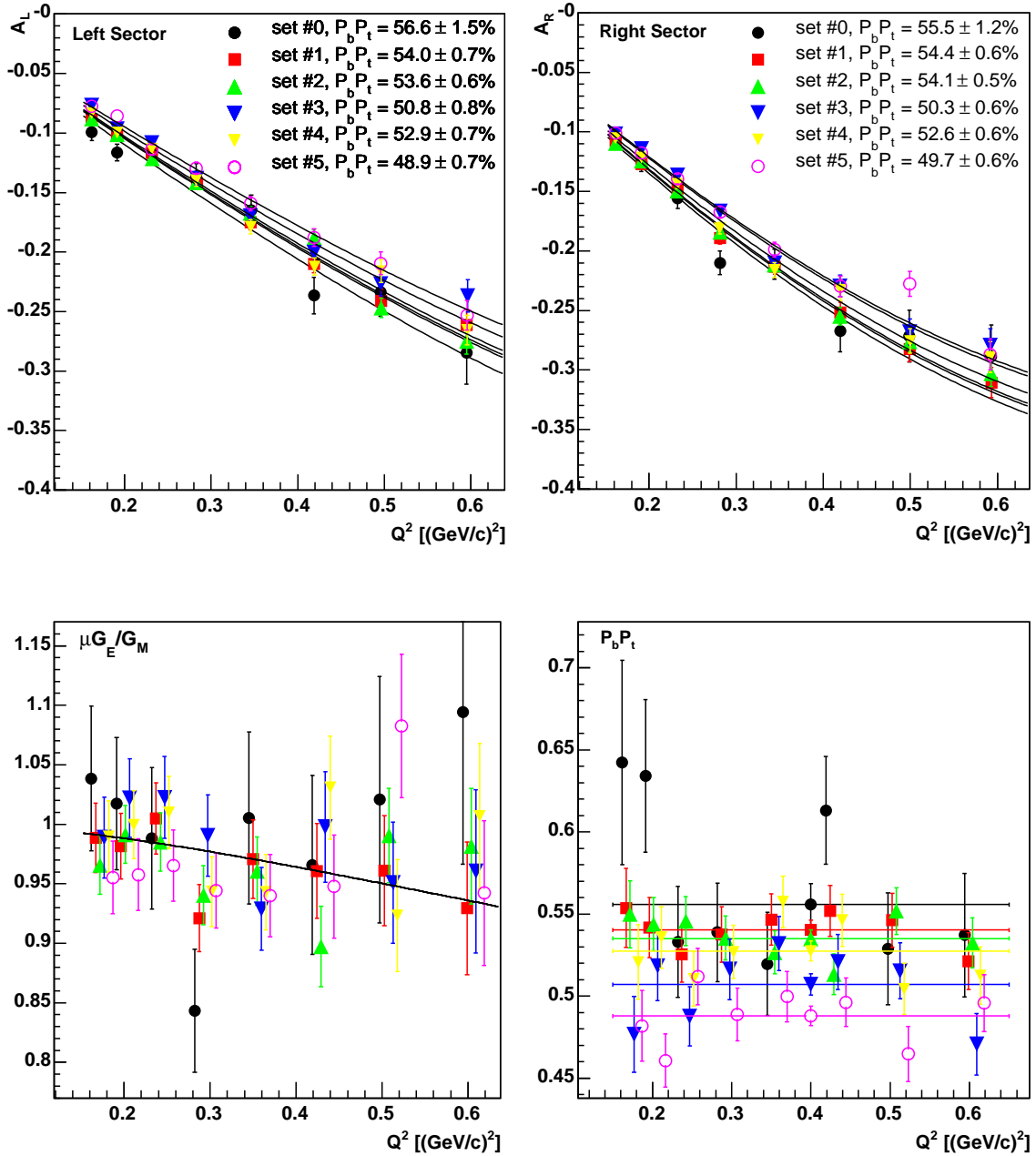


Figure 3-17: The asymmetry and form factor ratio from 6 subsets of the data compared. Compare with Figs. 3-9 and 3-8.

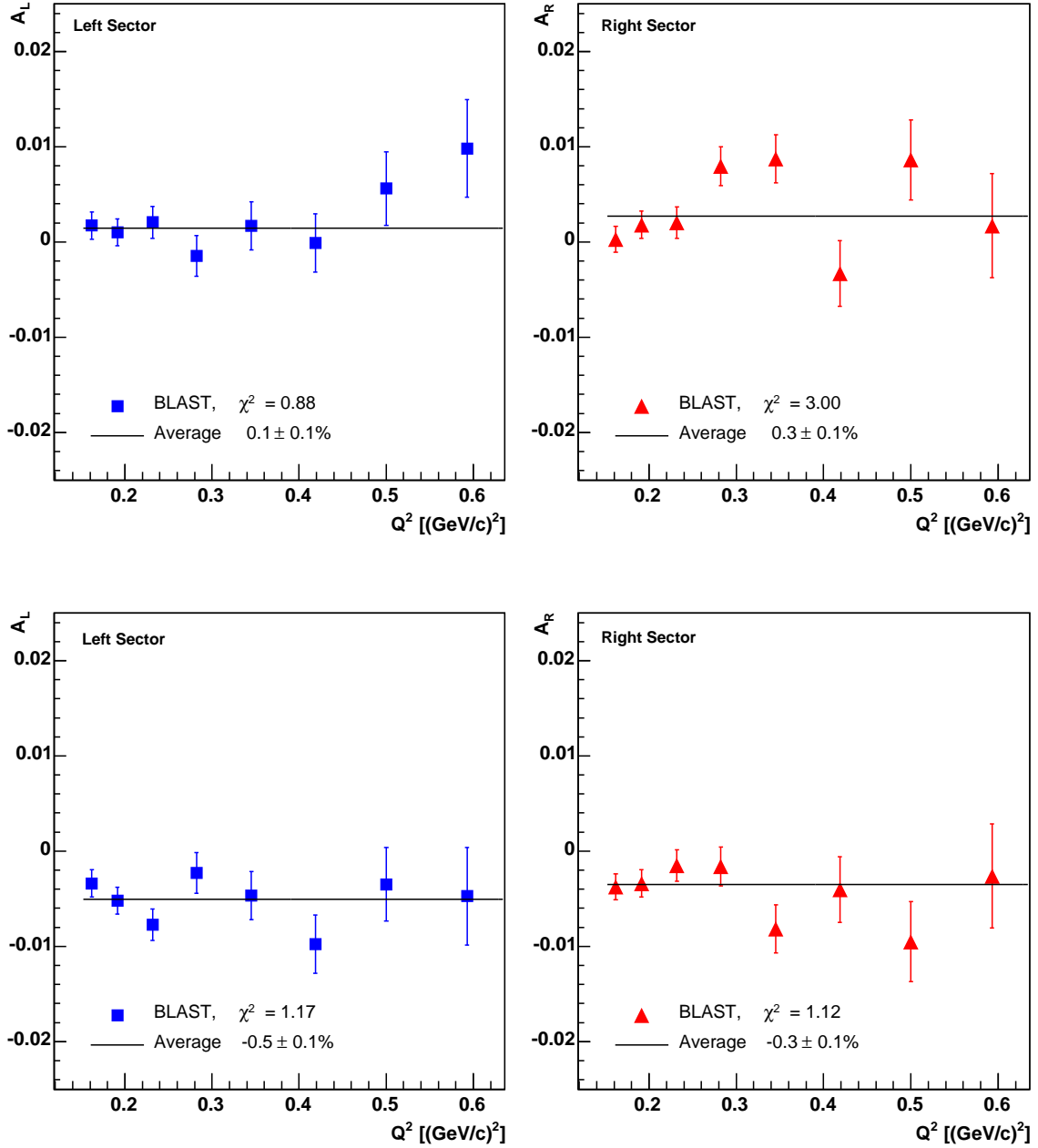


Figure 3-18: Beam and target single spin asymmetries.
Beam (top) and target (bottom) single spin asymmetries.

3.4.7 Pion Contamination

The inclusion of inelastic events in the yields would directly affect the asymmetries not just as a dilution because inelastic reactions carry an asymmetry of their own. However, the pion threshold is separated from the elastic peak by $m_\pi = 0.135$ (GeV/c²) in invariant mass W , five times the resolution in W , $\sigma_W = 0.027$ (GeV/c²). Figure 3-19 shows the inelastic yields between the elastic peak and the $\Delta(1232)$ resonance with cuts on Q^2 , E' , missing energy, vertex position, TOF timing and deposited energy. The histogram of missing mass M_X also includes anti-coplanar cuts to highlight the inelastic events, and the histogram of W includes the cut on M_X shown by vertical bars in the left panel. For the final results, the cut $|W - M| < 2.5\sigma_W$ was applied. By convoluting the inelastic cross section near threshold with the Gaussian resolution of W , the number of inelastic events passing the cut was found to be less than 50 in the left sector and 30 in the right sector, much less than background events from the cell wall and collimator.

The analysis was also repeated with Čerenkov cuts to differentiate pion from electron events, and asymmetry and form factor ratio results were the same as without the Čerenkov cuts. Therefore, we concluded that the inelastic contribution to the asymmetry is negligible.

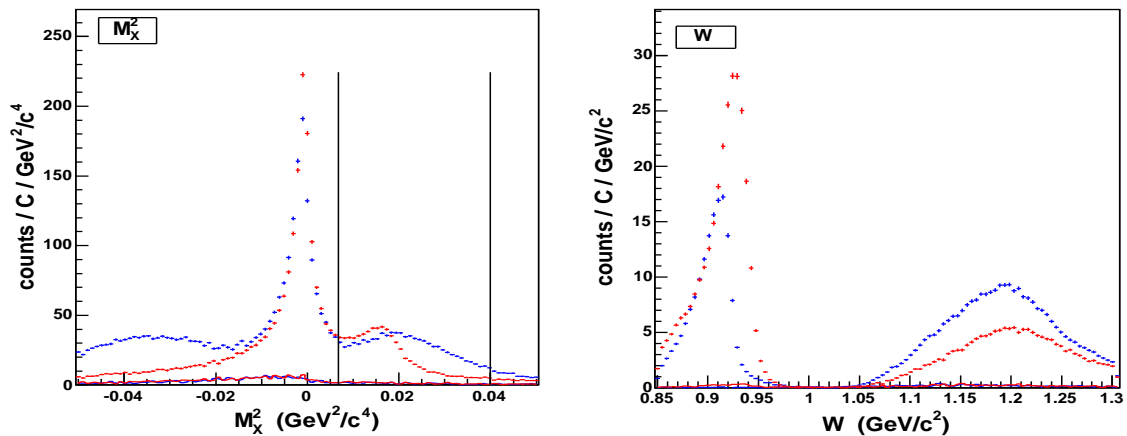


Figure 3-19: Pion yields as a function of M_X^2 and W for electrons scattered into the left (blue) and right (red) sectors.

Chapter 4

Results and Discussion

4.1 Form Factor Ratio

The results of $\mu G_E/G_M$ from this experiment are shown with the world polarization data in Fig. 4-1. For these results Q^2 was reconstructed solely from the drift chambers without any corrections from the Time-of-Flight scintillators. The relatively large systematic errors reflect the discrepancy between Q^2 as determined from the drift chambers and from the timing scintillators (Sec. 3.4.2), the discussion of which is deferred to Sec. 4.3.

The new results are consistent with both the unpolarized and polarized world data. They complement the mapping of $\mu G_E/G_M$ from $Q^2 = 0.5\text{--}5.6$ (GeV/c)² at JLab with measurements down to $Q^2 = 0.1$ (GeV/c)² of comparable precision. As shown in Table 4.1, the statistical uncertainty in $\mu G_E/G_M$ has been reduced from that of the unpolarized world data by roughly a factor of 2 in the lowest five Q^2 data points.

A narrow dip is observed in the form factor ratio around $Q^2 = 0.3$ (GeV/c)², which would correspond to structure in the proton on the order of $\hbar c/Q \approx 0.36$ fm. Many systematic checks have been performed to determine whether this feature is an artifact of the analysis. This issue will not be completely resolved until final calibrations of the drift chambers and magnetic field map are completed at the end of the 2005 deuterium run. However such a dip is consistent with the previous data.

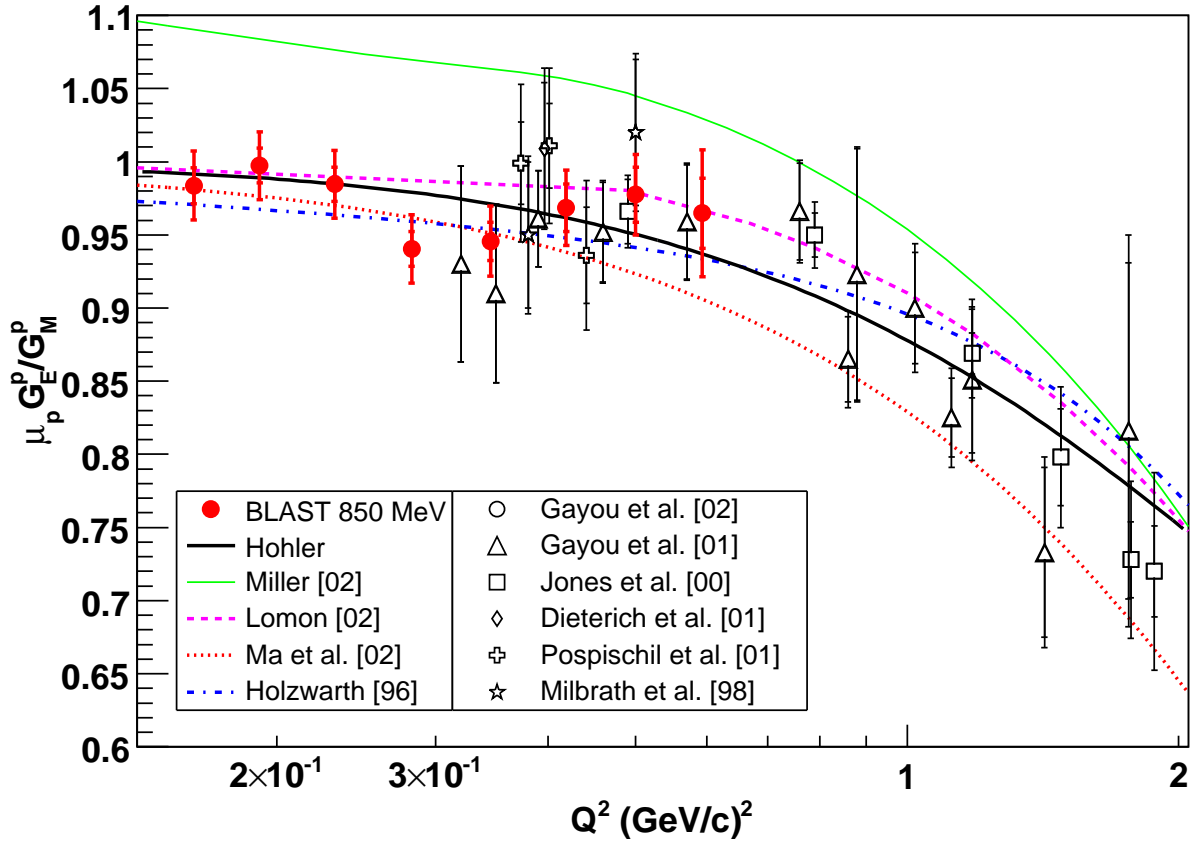


Figure 4-1: The BLAST results of $\mu G_E^p / G_M^p$ based on Q^2 determined from the drift chambers. Compare with Fig. 4-5, which includes corrections from the scintillator timing. Also shown are the world FPP data, and models which reproduce the higher Q^2 JLab results. The smaller error bars are statistical only; the outer error bars are for statistical and systematic errors added in quadrature.

The unpolarized data show hints of a similar structure, but without precision or coverage in the region to be conclusive. Almost all of the single-experiment form factor ratio extractions are from early measurements at Stanford [38] and are not precise enough to resolve a dip of the observed magnitude. There are two high statistics points from Bonn [34] which agree with our results, but they lack data on the low Q^2 side of the dip needed to be conclusive. The best quality data come from the global analysis of Höhler *et al.* [12], combining the data above with other experiments from 1962–1975. They also observe a small dip, although at slightly lower Q^2 . As seen, there is a lack of unpolarized data in the region of this experiment. Most recent

experiments have measured cross sections either at very low Q^2 to extract r_p or at high Q^2 to probe the asymptotic Q^2 dependence of $\mu G_E/G_M$.

The lowest five FPP calibration data points of Gayou *et al.* [53] show a systematic drop consistent with our observation; however, their errors are much greater, and these data do not extend below the dip. The two Bates FPP data [50] also show a dip, which is contradicted by the Mainz FPP data [51, 55], but these experiments also both have large error bars.

Figure 4-1 also includes some of the models which best describe the high Q^2 behavior of $\mu G_E/G_M$ measured at Hall A with polarized data [52, 3]. Of the constituent quark models, the fit is much better to Ma *et al.* [98] than Miller [86]. This is understandable, as the model of Miller was fit with only four free parameters, and thus it overshoots the data at low Q^2 . The dispersion, VMD, and soliton models of Höhler [12], Lomon [105], and Holzwarth [90], respectively, all do well at low Q^2 , with Lomon the closest to the data, except in the dip. None of the models, however, show any dip structure. Therefore, it is important to investigate whether the dip is real or is an artifact of the experiment, as discussed in Sec. 4.3.

4.2 Individual Form Factors

While interesting in their own right, one may also combine the measurements of $\mu G_E/G_M$ on the proton with the world elastic $e-p$ cross section data to extract G_E and G_M individually. At $Q^2 > 1$ (GeV/c)², there is an incompatibility in the form factor ratio extracted from the Rosenbluth versus Focal Plane Polarimetry method as explained in Sec. 1.2.6, and it is not yet understood how to combine these measurements into a single extraction of G_E and G_M . However, in the region of the BLAST experiment, the two methods are in agreement. Indeed, the unpolarized cross section, which appears in the denominator of the asymmetry formalism, was already used implicitly by the fit and single-asymmetry methods of extracting $\mu G_E/G_M$, though not in the super-ratio method.

The BLAST extraction of G_E and G_M uses the standard L-T separation of Eq. 1.28

with an additional constraint on $R = G_E/G_M$ from this experiment, minimizing the function

$$\chi^2 = \left(\frac{\epsilon G_E + \tau G_M - \sigma_R}{\delta\sigma_R} \right)^2 + \left(\frac{G_E/G_M - R}{\delta R} \right)^2, \quad (4.1)$$

where $\sigma_R \pm \delta\sigma_R$ are the world unpolarized reduced cross section data, and $R \pm \delta R$ are the data from our experiment.

The data used for the global fit are the same as those compiled by Arrington [58] (see Appendix B). They come from nine experiments, dominated by the early experiments at Stanford [38] and Bonn [34]. They were grouped in the same bins used for the BLAST data analysis, except for a cluster of cross sections near $Q^2 = 3.14 (\text{GeV}/c)^2$ which were shifted to the $Q^2 = 0.345$ bin to have enough statistics in the that bin. Also, we included cross sections down to $Q^2 = 0.1 (\text{GeV}/c)^2$ to have enough statistics in the first bin. In each bin, the cross sections were shifted to the centroid Q_c^2 of our own data point and scaled by the corresponding shift in the Höhler parametrization of the reduced cross section. The constrained L-T extractions are shown in Fig. 4-2 and Table 4.1.

As a check, two extreme values of δR were also used: $\delta R \approx \infty$ for a pure Rosenbluth extraction, and $\delta R \approx 0$ so that ratio was constrained exactly to our experimental value. The latter extreme gave very similar results to the combined fit with δR as the actual statistical errors, indicating the importance of our data in the extraction of G_E and G_M .

The form factor ratio agrees well with the L-T separation except for the three points at $Q^2 = 0.2\text{--}0.4 (\text{GeV}/c)^2$, in the region of the dip. This is the same region where there is less world data, with the exception of $Q^2 = .282 (\text{GeV}/c)^2$, where the bulk of the data are concentrated at low ϵ . At the lowest 5 values of Q^2 , our contribution of $\mu G_E/G_M$ reduces the statistical errors in both G_E and G_M roughly by a factor of two.

The new extractions of G_E and G_M are plotted with the world data in Fig. 4-3. Note that the Höhler data points are a global fit to all experiments listed after the Höhler entry in the legend, as well as several earlier experiments which are not

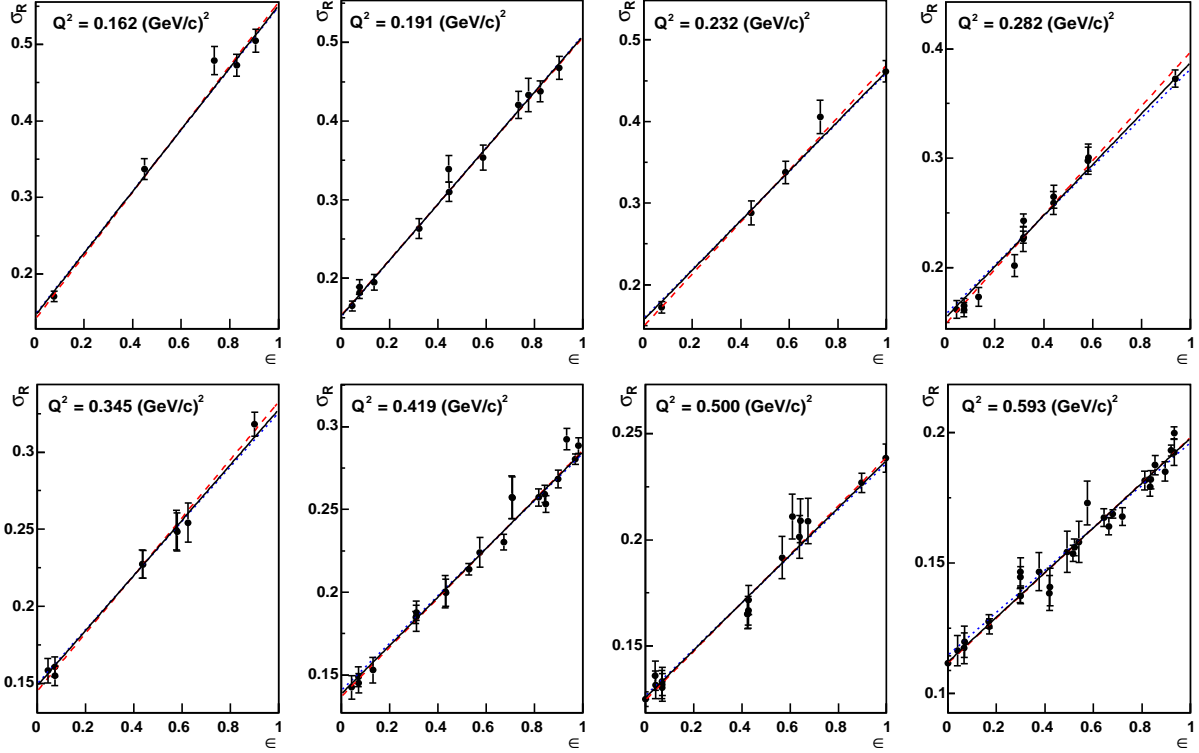


Figure 4-2: Rosenbluth separation of G_E and G_M constrained by $R = G_E/G_M$. For each Q^2 bin, the reduced cross section σ_R is plotted against ϵ . The dashed blue line is fit without any constraint on R . The dotted red line is fit with an exact constraint. The solid black line is the combined fit.

shown. The new results fill a gap between high statistics unpolarized measurements of G_E at low Q^2 and the high precision FFP data at higher Q^2 , although it is still not understood how to extract G_E from a combination of the polarized data and unpolarized cross sections at high Q^2 .

The observed narrow dip in the form factor ratio is correlated with a narrow dip in G_E , while G_M has little Q^2 dependence beside the broad shape well-described by unpolarized data. The extraction of G_M agrees well with previous data, although with substantially increased precision. None of the available models of G_E describe the dip observed in our data. However, a similar feature at $Q^2 = 0.3 (\text{GeV}/c)^2$ is observed in the G_E^n [133], but with positive instead of negative amplitude. Thus this dip could be attributed to the isovector form factor.

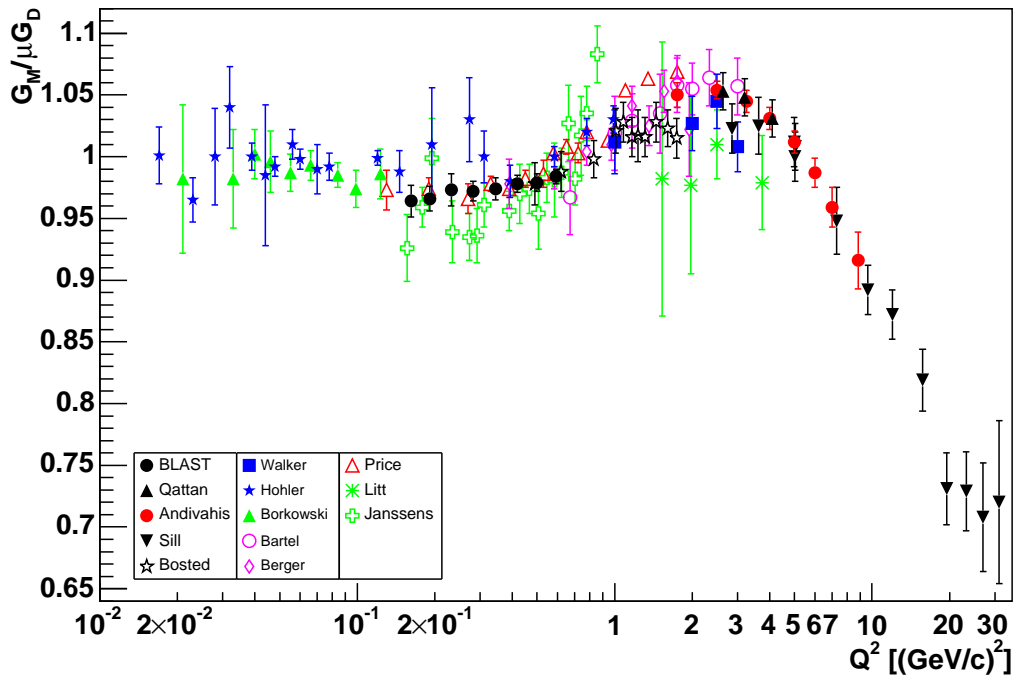
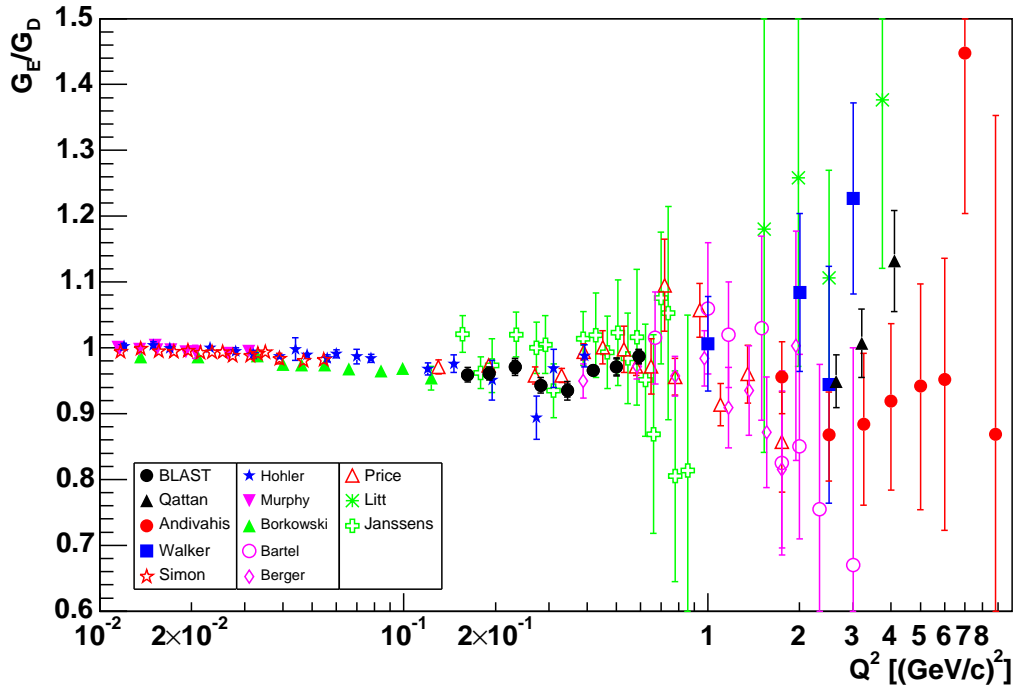


Figure 4-3: BLAST extraction of G_E and G_M plotted together with the world unpolarized data. The error bands show systematic and statistical errors combined in quadrature.

Q_c^2 (GeV/c) ²	n_ϵ	Unconstrained LT Separation			Combined LT + R Fit		
		G_E/G_D	$G_M/\mu G_D$	$\mu G_E/G_M$	G_E/G_D	$G_M/\mu G_D$	$\mu G_E/G_M$
.162	5	.970(17)	.948(24)	1.023(41)	.959(11)	.964(13)	0.994(19)
.191	12	.957(15)	.969(14)	.988(27)	.961(10)	.966(10)	0.995(17)
.232	5	.996(23)	.948(23)	1.050(46)	.971(13)	.973(13)	0.998(19)
.282	13	.974(18)	.954(11)	1.020(30)	.943(12)	.972(08)	0.970(17)
.345	9	.956(24)	.963(14)	.993(36)	.935(14)	.974(09)	0.959(19)
.419	21	.974(12)	.972(09)	1.001(21)	.966(09)	.978(07)	0.988(16)
.500	17	.982(20)	.975(09)	1.007(27)	.971(14)	.979(07)	0.992(19)
.593	30	.992(12)	.982(06)	1.010(18)	.987(11)	.984(06)	1.003(16)

Table 4.1: The extracted values of G_E and G_M , with and without the constraint of $\mu G_E/G_M$ from BLAST. n_ϵ is the number of reduced cross sections used for each fit. None of the cross sections were renormalized. The statistical and systematic errors combined in quadrature are indicated in parentheses.

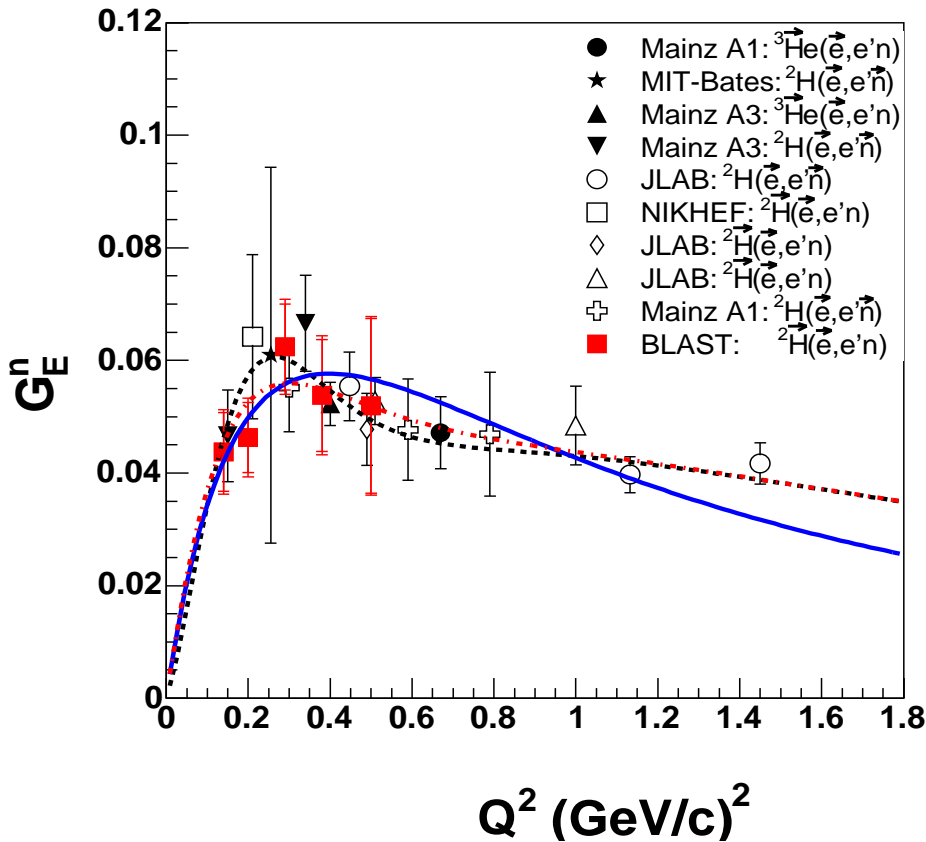


Figure 4-4: From [133]: recent results of G_E^n from polarization experiments including BLAST. The solid (blue) curve is a the Platchkov fit with a constraint on the neutron charge radius. The dashed (black) at dot-dashed (red) curves are Friedrich-Walcher fits without and with the BLAST data, respectively.

4.3 Discussion of Errors

We now return to the question of whether the observed dip is physical or is an artifact of the experiment. First consider statistical errors from drift chamber reconstruction only. We group the data in three sets: the first three points before the dip, the next two points in the dip, and the last three points after the dip. The average form factor ratio in these sets is $\mu G_E/G_M = 0.9887 \pm 0.0069$, 0.9429 ± 0.0088 , and 0.9708 ± 0.0110 respectively. The weighted difference between the average form factor ratio of the two middle points and the rest of the data is 0.0407 ± 0.0106 . Thus without consideration of systematic errors the dip is a 4σ effect.

A few checks were performed to ensure that the data were normally distributed and the the dip was not an anomaly. All three methods of the extracting the form factor ratio reproduce the dip. The single-asymmetry extraction and the global fit extraction are very close to each other at all Q^2 points. The super-ratio method extraction differs from the other two methods by 1.5σ at $Q^2 = 0.345$ and 0.592 . The extracted polarization also differs by the same amount at those points, indicating that there is a discrepancy between the left and right asymmetries at these points. But the super-ratio extraction of $\mu G_E/G_M$ is in agreement with the other methods at $Q^2 = 0.282$, the first point of the dip.

As discussed in Sec. 3.1.4, the efficiency of the left sector TOF paddle 9 changed twice during the experiment, potentially affecting the asymmetry at $Q^2 = 0.282$. However, the asymmetry and form factor ratio were analyzed in six sequential run periods (Fig. 3-17), and all periods were consistent with each other. The data were also analyzed in finer Q^2 bins in Fig. 3-16, and a dip was still observed in four bins. There we concluded that statistically, the dip is real.

Some of the systematic errors are overall normalization uncertainties, affecting $\mu G_E/G_M$ at each Q^2 by the same amount. These have no effect on the presence of a dip. For example, a one degree overestimation of the average target spin angle would raise $\mu G_E/G_M$ by 0.0073. False asymmetries due to improper beam current integration, or asymmetries in beam or target helicity states would also have the same

effect in each Q^2 bin. In Fig. 3-18, the beam and target false asymmetries show no strong Q^2 dependence, which would arise from detector-related false asymmetry.

This leaves us with only one systematic error, the determination of Q^2 , which could cause an artificial dip in the data. Non-uniform errors in Q^2 , especially asymmetric deviations in the left and right sector, could explain the dip. As mentioned in Sec. 3.4.1, there four independent determinations of Q^2 in each sector. The results of Sec. 4.1, relied on the average Q^2 from two of these determinations: from scattering angle of the electron and the recoil angle of the proton. The difference of Q^2 in these two determinations provided an estimate of the systematic error.

From Sec. 3.4.2, one can also determine Q^2 from the velocity of the recoil proton as determined by the TOF scintillators. The relative timing offsets of each scintillator was calibrated absolutely using the timing peaks of cosmic rays passing through both sectors of the TOFs. Thus the systematic errors in Q^2 are under better control for timing than from the drift chamber parameters. However, this timing losses precision at high Q^2 where the proton approaches the speed of light, and has its own systematic uncertainty associated with energy loss of detected particles. This effect is symmetric in the left and right sectors, so we can still use the timing as a measure of the dQ_A^2 error of the drift chamber Q^2 determination; a positive shift of Q^2 in one sector which is the same magnitude as a negative shift in the opposite sector. This correction is shown in Table. 3.6.

To see the effect of the systematic errors in Q_{WC}^2 as determined by timing, the BLAST results of $\mu G_E/G_M$ corrected by dQ_A^2 from timing are shown in Fig. 4-5. In this figure, the systematic error is due to the timing resolution in combination with half of the correction dQ_A^2 .

4.4 Outlook

We have shown that double spin-asymmetries are an effective tool in combination with the unpolarized cross section for extracting the electromagnetic form factors of the proton, especially in experiments with a large acceptance detector. This measurement

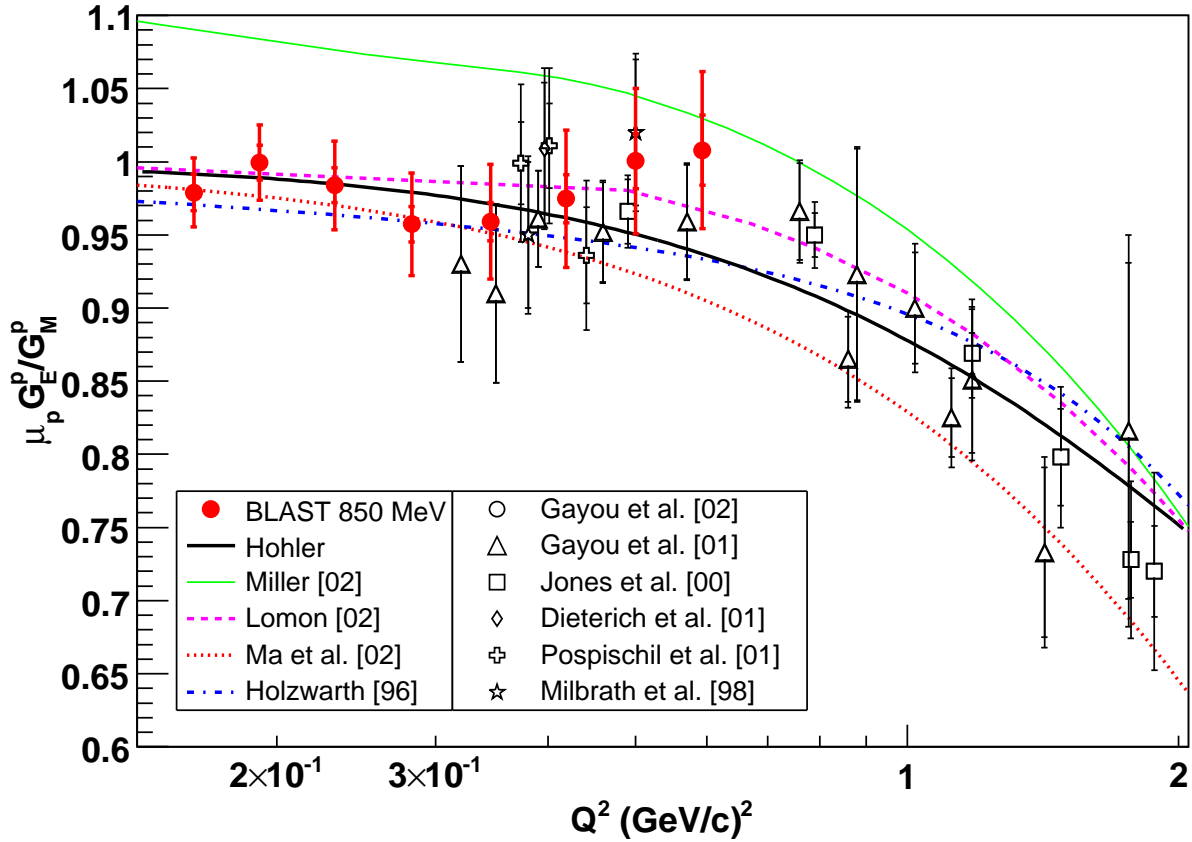


Figure 4-5: The BLAST results of $\mu G_E/G_M$ based on Q^2 reconstructed from the drift chambers with corrections from scintillator timing. Also shown are the world FPP data, and models which reproduce the higher Q^2 JLab results.

has substantially increased the precision of the G_E/G_M world data at $Q^2 = 0.15\text{--}0.6 (\text{GeV}/c)^2$, even in a region where Rosenbluth separations are still effective. A similar experiment was proposed at JLab [119] to extract G_E/G_M from double-spin asymmetries at higher Q^2 , and it would benefit from the methodology and results of the present work.

It would be interesting to push polarization measurements on the proton down to even lower Q^2 . Unpolarized data at lower Q^2 would benefit from spin observables to isolate the small magnetic contribution, which is difficult to determine accurately by Rosenbluth separation. This would allow a new level of precision measurement of the charge radius of the proton, which could be compared with forthcoming re-

sults of the muonic hydrogen Lamb shift experiment [29]. One could also perform a quality extraction of the magnetic radius of the proton, which is poorly known with unpolarized data alone.

The significance of this measurement is still limited by systematic errors mainly in the determination of Q^2 and the holding field angle β . Reduction of the uncertainty of Q^2 is important, since this is the only systematic error which could be responsible for the observed dip in $\mu G_E/G_M$ if it is unphysical. The extraction process is highly sensitive to Q^2 even though the form factors are fairly constant in Q^2 . There are contributions from both the Q^2 dependence of the asymmetry, and from the uncertainty in θ^* and kinematic factors. The first contribution is most serious, especially if the left and right sectors of BLAST are asymmetric such that the error in Q^2 is different in both sectors. There are indications from comparisons of independent measurements of Q^2 in each sector that this is indeed the case.

In order to resolve the discrepancy of Q^2 , an absolute calibration of the wire chambers is needed. All available information from the experimental data, cosmic rays, and detector surveys must be used to get a consistent calibration of the drift chambers. After the current physics run, the BLAST magnetic field will be measured with the target and all of the outer detectors in place and compared with the previous field map and TOSCA calculations. Extra cosmic ray data will also be taken at this time with zero magnetic field. These straight tracks will be useful for investigating the relative alignment of the three chambers within a sector and of one sector relative to the other. There may even be sufficient cosmic events in the existing physics data, although the wire chamber requirements in the trigger may be too restrictive.

After the most recent map of target holding field, the target polarization angle is reasonably well-known, and agrees well with the angle extracted from the data. Work is underway to increase the precision of the field map to less than 0.5° at the end of the current run, which will make the uncertainty in θ^* insignificant. By accomplishing the above tasks, it will be possible to reduce the systematic errors to the level of the statistical errors of this experiment.

While there is a great push to understand the recently discovered drop in G_E

at high Q^2 in terms of the dynamics of constituent quarks, and also to reconcile Rosenbluth and Focal Plane Polarimeter extractions of $\mu G_E/G_M$ in terms of higher order radiative corrections, there are also interesting features in the Q^2 range of this work. The first steps have been taken by Friedrich and Walcher [60] to parametrize the meson cloud of the nucleon by phenomenological fits of the low Q^2 dependence of the form factors. There is an opportunity to extend this investigation with more physical models.

If the observed dip in $\mu G_E/G_M$ turns out to be physical after reducing the systematic error in Q^2 and comparing the results with an analysis of the BLAST deuterium data, it would be a signature which could be tested against new models of the nucleon and direct calculations of Lattice QCD. This region is too high in Q^2 for effective field theories, but it would be interesting if they could reproduce similar features. Its effect on the nucleon-nucleon potential would also be interesting. These results are another piece of the puzzle in understanding hadronic structure in terms of the underlying quark and gluon degrees of freedom.

Appendix A

Linear Calibrations

Although some calibrations of the BLAST detector can be done with single measurements, for example using the flashers, additional information is available by considering physically motivated correlations between detector signals. In this appendix, we use such correlations to calibrate the TOF scintillator timing offsets and the time-to-distance function for wires in the drift chambers. Many of the correlations are linear or can be approximated by a linear function in the region of the calibration, which greatly simplifies the solution. We first review the formalism of linear least squares fitting based on the treatment in Numerical Recipes [150, §15], and discuss the robust fitting of multivariate correlations. This is applied to calibrations in the following sections.

A.1 Least Squares Fit

The least squares fit of data points (x_i, y_i) to the straight line $y = mx + b$ is obtained by minimizing the sum of squared deviations

$$\chi^2 = \sum_i (y_i - mx_i - b)^2 = (Y - Xa)^2, \quad (\text{A.1})$$

where the data and parameters are represented by the matrices

$$Y = \begin{pmatrix} y_1 \\ y_2 \\ \vdots \end{pmatrix}, \quad X = \begin{pmatrix} x_1 & 1 \\ x_2 & 1 \\ \vdots & \vdots \end{pmatrix}, \quad a = \begin{pmatrix} m \\ b \end{pmatrix}. \quad (\text{A.2})$$

The design matrix X is composed of rows of the coefficients of m and b for each data point. This can be generalized to any fit function which is linear in the fit parameters, $y = \sum_j X^j(x)a_j$, in which case the design matrix has components $X_i^j = X^j(x_i)$. The domain $\{x_i\}$ is arbitrary (discrete, continuous, vector space, or manifold). The range $\{y_i\}$ must be continuous, and if it is a vector space, X and Y are segmented into block rows containing the vector components of each data point. The minimum of χ^2 with respect to the parameters a has the solution

$$d\chi^2|_{\min} = 2 da^T X^T (Y - Xa) = 0, \quad (\text{A.3})$$

$$X^T Y = X^T X a, \quad (\text{A.4})$$

$$a = X^{-1} Y \quad \text{where} \quad X^{-1} \equiv (X^T X)^{-1} X^T. \quad (\text{A.5})$$

The matrix X^{-1} is defined as the least squares left sided inverse of X .

If the data points have Gaussian errors $y_i \pm \Delta y_i$, then the maximum likelihood fit is obtained by minimizing the chi-squared variable

$$\chi^2 = \sum_i \left(\frac{y_i - mx_i - b}{\Delta y_i} \right)^2 = (Y - Xa)^2. \quad (\text{A.6})$$

Each row of X and Y is divided by Δy_i , and the solution has the same form. The covariance matrix C of a has components

$$C_{ij} = \text{Cov}(a_i, a_j) = \sum_k \left(\Delta y_k^2 \frac{\partial a_i}{\partial y_k} \frac{\partial a_j}{\partial y_k} = X_{ik}^{-1} X_{jk}^{-1} \right) = (X^T X)^{-1}_{ij}. \quad (\text{A.7})$$

The design matrix does not have to be constructed from a single fit function of homogeneous data, but can be formed of arbitrary linear (or linearized) equations in

the fit parameters. Thus one can fit subsets of the data separately using individualized techniques and combine the results into a global linear fit, weighted by the errors in each subset of the data. The resulting system of weighted linear equations, $Y = Xa$, has the same form as above with the same least squares solution. This is the technique used in calibrating the TOF offsets (Sec. A.2) and the drift chamber wire time-to-distance functions (Sec. A.3.3).

Singular Value Decomposition (SVD)

Alternatively, one can compute the least squares inverse robustly by calculating the SVD [150, §2.6]. The matrix X can be decomposed as $X = RPS$ into a rotation R , a projection P , and a symmetric matrix S , which has the further decomposition $S = VWV^T$ with eigenvalues $W = \text{diag}(w_1, w_2, \dots, w_n)$ and eigenvectors $V = (V_1|V_2|\dots|V_n)$. Setting $U = RPV$ (with the same dimensions as X and P),

$$X = UWV^T \quad \text{and} \quad X^{-1} = VW^{-1}U^T, \quad (\text{A.8})$$

where U is orthonormal, V is a rotation, and W is diagonal. The least squares fit has the solution

$$a = X^{-1}Y = \sum_k V_k \frac{U_k \cdot Y \pm 1}{w_k}, \quad (\text{A.9})$$

where ± 1 indicates the uncertainty in a with each term added in quadrature, since C is diagonal in the basis $\{V_k\}$. In the case of a linear fit with $\bar{x} = 0$, the two columns of X are already orthogonal and $V = 1$. For large datasets where it is impractical to tabulate X , one can calculate the SVD of $X^T X$ instead.

A.1.1 Generalizations of the Linear Fit

Consider multiple data points at a single value x , and note that individual rows of X and Y can be added separately to $X^T X$ and $X^T Y$, weighted by Δy_i^{-2} . Therefore, it is equivalent to replace these rows with a single row of the average \bar{y} where $\bar{y}/\Delta y^2 \equiv \sum_i y_i/\Delta y_i^2$, weighted by $\Delta \bar{y}^{-2} \equiv \sum_i \Delta y_i^{-2}$. The importance of this observation is that

\bar{y} can be substituted with more robust estimators of the central tendency based on lower moments of the distribution, making them less vulnerable to instabilities from outlier points.

Method	Moment	Center	Spread
Least Squares	$(Y - Xa)^2$	Mean	Std. Dev.
Absolute Deviation	$ Y - Xa ^1$	Median	Abs. Dev.
Peak Fit	$(Y - Xa)^0$	Mode	FWHM

Table A.1: Three statistical measures of central tendency, listed in order of increasing robustness. Note that $(Y - Xa)^0$ is only the effective moment associated with the mode and FWHM, not actually used in calculations.

Three methods of evaluating the central tendency using different moments of the distribution are listed in Table A.1. The median is more robust than the mean because outlier points are not weighted by their deviation from the median [150, §15.7]. Calculation of the median only requires ranking the data, which is less computationally intensive than fitting a peak. The mode is only applicable to data of a discrete variable or binned data and can be vulnerable to statistical fluctuations depending on the binning. The same applies to the associated Full Width at Half Maximum (FWHM) spread, which is discontinuous and difficult to minimize (Sec. A.1.1). However, a fit to the peak can be considered the continuous analog of the mode, since both represent the maximum density of the distribution. A pure maximum likelihood Gaussian fit to unbinned data will just reproduce the mean and standard deviation; however, by parameterizing the background or cutting around the peak, one can essentially eliminate outliers. We consider such a fit as minimization of the zeroth moment, because outlier points have no weight, making this method the most robust. The drawback is that the choice of the cut is somewhat arbitrary and must be shown not to affect the fit.

Separation of Slopes and Offsets

Even if the data are not discrete or binned in x and there are not multiple points at each value of x , one can still perform a robust fit similar to that described above by

separating the fit into two parts: the offset and the slope. First project each data point (x, y) onto the y -axis by subtracting the fit function evaluated at x . The projection is a one-dimensional distribution of which the offset can be determined using one of the methods in Table A.1. Note that using the mean and variance to describe the offset is equivalent to the original linear least squares fit. Second, fit for the slope of the function by minimizing the spread of the projection. Thus the problem is reduced to a calculation or fit of the offset nested in a one-parameter fit for the slope, illustrated in Fig. A-1. The trade-off is that fit becomes nonlinear. Because the fit is divided into two levels, extra work is needed to calculate the covariance between offset and slope parameters. Also, care must be taken at the boundaries to cut only on x and not y , which would affect the distribution of the projection.

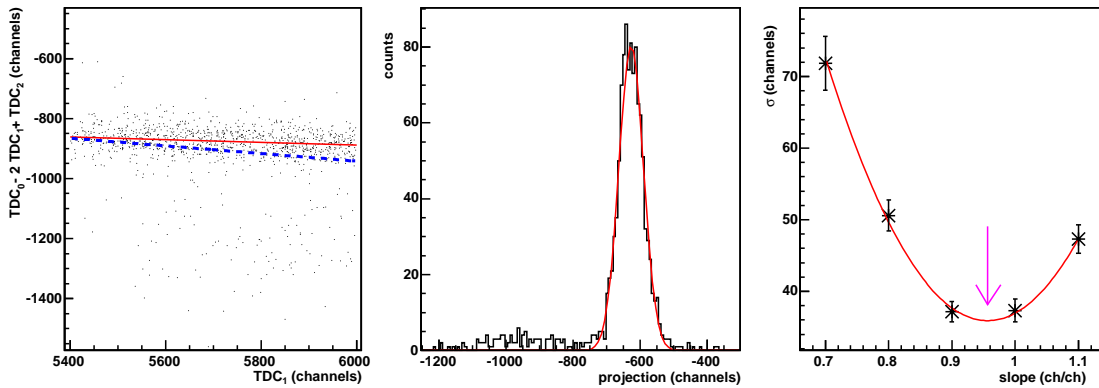


Figure A-1: Robust fit by separation of slope and offset. The first panel compares the robust fit (solid red) with a pure least squares fit (dashed blue). The second panel shows the projection to the y -axis along the best fit slope. The width of the projection is minimized as a function of slope in the third panel.

The separation of the slope and the offset can be generalized to fits of higher-dimensional surfaces. For an m -dimensional hyperplane in d -space with $(m+1)(d-m)$ parameters, there are $(d-m)$ offsets which can be fit from the projection of the data along fixed values of the remaining $m(d-m)$ slope parameters. As before, the slope parameters are fit by minimizing the widths of the offset peaks. If there are more than one offset, the peaks can be fit to a multidimensional Gaussian $f=e^{-\frac{1}{2}\chi^2}$, where χ^2 is given below in Eq. A.10.

The slope parameters can be determined by calculating χ^2 (width of the offsets projection) for each point on a grid of the slope parameters a and fitting for the minimum a_0 . Near a_0 , the function χ^2 can be fit to the quadratic form

$$\chi^2 = a^T A a + a^T b + c \quad (\text{A.10})$$

$$= (a - a_0)^T A (a - a_0) + a^T (b + 2Aa_0) + (c - a_0^T A a_0) \quad (\text{A.11})$$

with the new parameters grouped into a symmetric matrix A , a vector b , and a scalar c . In terms of these parameters, the minimum is

$$\chi_{\min}^2 = c + \frac{1}{2} b^T a_0 \quad \text{at} \quad a_0 = -\frac{1}{2} A^{-1} b. \quad (\text{A.12})$$

The covariance matrix for the slope parameters is $C = A^{-1}$ if the width of the projection χ^2 has been normalized by Δy_i . Otherwise, the best one can do is scale χ_{\min}^2 to equal $(d - m)$, resulting in the covariance matrix $C = A^{-1} \chi_{\min}^2 / (d - m)$.

A nonlinear parametrized m -dimensional surface S can also be fit using this method. The surface is re-parametrized to have $(d - m)$ offsets plus the remaining shape (slope) parameters by considering the intersection of S with a $(d - m)$ hyperplane extending out from a fixed point on the original surface. For the surface of a two-dimensional function $f(x, y; a_i)$ with parameters a_i , the natural offset parameter is $z = f(0, 0; a_i)$, and the data point (x, y, z) is projected onto the z -axis by subtracting $f(x, y; a_i)$. After adding the offset parameter z , one of the shape parameters a_i will be redundant and must be excluded from the fit.

A.1.2 Minimum χ^2 from a Least Squares Fit

Returning to the linear least squares fit, we substitute in the fitted value of a to get

$$\chi_{\min}^2 = (Y - X X^+ Y)^2 = Y^T P_{\perp} Y \quad (\text{A.13})$$

$$= Y^T Y - Y^T X (X^T X)^{-1} X^T Y, \quad (\text{A.14})$$

where $P_{\parallel} \equiv XX^+ = UU^T = P_{\parallel}^2$ is the 2-dimensional projection of points y_i onto the fitted line, and $P_{\perp} = 1 - P_{\parallel} = P_{\perp}^2$ is the $(n - 2)$ dimensional projection onto the residuals of y_i contributing to χ^2 . Substituting averages for Y^TY , Y^TX , and X^TX ,

$$\frac{1}{n}\chi_{\min}^2 = \overline{y^2} - \frac{(\overline{yx} \ \overline{y})}{\overline{x^2} - \overline{x}^2} \begin{pmatrix} 1 & -\overline{x} \\ -\overline{x} & \overline{x^2} \end{pmatrix} \begin{pmatrix} \overline{yx} \\ \overline{y} \end{pmatrix} \quad (\text{A.15})$$

$$= (\overline{y^2} - \overline{y}^2) - (\overline{yx} - \overline{y}\overline{x})^2 / (\overline{x^2} - \overline{x}^2) \quad (\text{A.16})$$

$$= \text{Var}(y) - \text{Cov}(y, x)^2 / \text{Var}(x) \quad (\text{A.17})$$

$$= \text{Var}(y)(1 - r^2), \quad (\text{A.18})$$

where $\text{Var}(x) \equiv \overline{(x - \overline{x})^2} = \overline{x^2} - \overline{x}^2$ and $\text{Cov}(y, x) \equiv \overline{yx} - \overline{x}\overline{y}$ are the variance and covariance respectively, and the linear correlation r is defined by

$$r \equiv \frac{\text{Cov}(y, x)}{\sqrt{\text{Var}(y)\text{Var}(x)}}. \quad (\text{A.19})$$

For the case $n = 2$, the fit is exact and $\chi_{\min}^2 = 0$. For the case $n = 3$, using data points $(-x, y_1)$, $(0, y_2)$, and (x, y_3) ,

$$\chi_{\min}^2 = \sum y^2 - \frac{1}{n}(\sum y)^2 - (\sum xy)^2 / \sum x^2 \quad (\text{A.20})$$

$$= (y_1^2 + y_2^2 + y_3^2) - \frac{1}{3}(y_1 + y_2 + y_3)^2 - \frac{1}{2}(y_3 - y_1)^2 \quad (\text{A.21})$$

$$= \frac{1}{6}(y_1 - 2y_2 + y_3)^2. \quad (\text{A.22})$$

Intuitively, this is the difference between the average of the two outer points and the middle point, which would coincide for an exact fit.

We now consider the SVD to show that in general χ_{\min}^2 is the sum of $(n - 2)$ squares. It is apparent from equation A.13 that

$$\chi_{\min}^2 = Y^T(1 - UU^T)Y = (U_3 \cdot Y)^2 + (U_4 \cdot Y)^2 + \dots + (U_n \cdot Y)^2, \quad (\text{A.23})$$

where $U = (U_1|U_2)$ has only the two eigenvectors of P_{\parallel} . To get the $(n - 2)$ eigenvectors of the complement, pad X with null vectors before computing the SVD or complete

U to a full basis using the Gram-Schmidt process. Again, for the case $n = 3$, the third eigenvector is $U_3 = \frac{1}{\sqrt{6}}(1, -2, 1)$. For the case $n = 4$, with regularly space points in x , the design matrix

$$X^T = \begin{pmatrix} -3 & -1 & 1 & 3 \\ 1 & 1 & 1 & 1 \end{pmatrix} \quad (\text{A.24})$$

is completed with the null eigenvectors $U_3 = \frac{1}{2}(1, -1, -1, 1)$ and $U_4 = \frac{1}{\sqrt{20}}(1, -3, 3, -1)$ or linear combinations thereof. Therefore,

$$\chi_{\min}^2 = \frac{1}{4}(y_1 - y_2 - y_3 + y_4)^2 + \frac{1}{20}(y_1 - 3y_2 + 3y_3 - y_4)^2. \quad (\text{A.25})$$

The first term is the difference in averages between the outer and inner points, while the second term is the difference between averages of y_1, y_3 , and y_2, y_4 , weighted to meet at the center. These formulas are useful for bypassing the fit process and directly computing how well hits in a track line up, for example. They are used in the linear calibration of the drift chamber time-to-distance functions.

A.2 TOF Scintillator Offsets

As described in Secs. 2.3.3 and 3.1.1, there are 16 TOF scintillators ($n=0-15$) in each sector ($s=L,R$). The TDC values from the top and bottom PMTs are labeled u_n^s and d_n^s , respectively. The two PMTs allow the measurement of both the mean time t_n^s and position p_n^s along the length of the scintillator of each hit,

$$t_n^s = \frac{1}{2}(d_n^s + u_n^s)t_{ch} \quad (\text{A.26})$$

$$p_n^s = \frac{1}{2}(d_n^s - u_n^s)t_{ch}v_{sc}, \quad (\text{A.27})$$

where $v_{sc} \approx 14.7$ cm/ns is the velocity of light in the scintillator, accounting for the average number of reflections before being detected in the PMT, and calibrated by matching the range of p_n^s to the length of the scintillator. The TDC channel resolution $t_{ch} \approx 50$ ps/ch was calibrated by adding predetermined delays to the signals from each PMT and measuring corresponding delays in the TDC channels.

Each TDC has an offset which includes the intrinsic offset of TDC electronics and delays from light propagation in the scintillator, cable, and trigger logic,

$$x_n^s = x_{n \text{ raw}}^s - x_{n \text{ off}}^s \quad \text{where} \quad x = d, u, t, p. \quad (\text{A.28})$$

The offsets $d_{n \text{ off}}^s$ and $u_{n \text{ off}}^s$ were measured with the flasher as described in Sec. 2.3.3. However, some flasher signals were missing due to attenuation and broken fibers, and this was not an absolute calibration, since not all fiber optics were the same length (due to an extra splitter box) and they were not all placed exactly in center of detector. An absolute calibration of the offsets was accomplished using cosmic ray coincidence events and the coplanarity the elastic ep events, described in the next two sections.

A.2.1 Cosmic Coincidences

The mean time offset $t_{n \text{ off}}^s$ of each paddle was calibrated absolutely using cosmic rays at low enough zenith angle Θ to pass through both a scintillator in the left sector and one in the right sector, triggering a coincidence event. Although the cosmic radiation is predominantly vertical and the distribution decreases as $\cos(\Theta)$, the rate of coincident events (1.4 Hz) was large enough for an accurate calibration of the timing offsets with only a few hours of data, taken periodically during maintenance of the SHR. The cosmic rays are predominantly high energy muons traveling near the speed of light, so the time delay between two TOF signals only depends on the distance between TOFs and it is reasonable to assume that left and right directions have same velocity distribution.

The distribution $t_i^R - t_j^L$ has two peaks, L_{ij} and R_{ij} , corresponding to cosmic rays traveling to the left and right, respectively. The peaks were enhanced by correcting for zenith angle Θ of the particle. From these two peaks we get the distance D_{ij} between the two scintillators, and the difference S_{ij} between the left and right offsets,

$$D_{ij} = ct_{ch}(R_{ij} - L_{ij}) \quad (\text{A.29})$$

$$S_{ij} = \frac{1}{2}(R_{ij} + L_{ij}). \quad (\text{A.30})$$

Let the l_i and r_i be the offsets of each scintillator in the left and right sector, respectively, then the 16×16 equations

$$\sqrt{N_{ij}}(S_{ij} = r_i - l_j) \quad (\text{A.31})$$

overdetermine each offset up to a global offset, which is insignificant because all timing in the BLAST detector is relative. The offsets are determined by a least squares solution to the above system of equations (Sec. A.1), each weighted by the number of events $N_{ij}^{R,L}$ in each peak as

$$\sigma^2 \propto \frac{1}{N_{ij}} \equiv \frac{1}{N_{ij}^R} + \frac{1}{N_{ij}^L}, \quad (\text{A.32})$$

The degeneracy of the undetermined global offset is removed by setting it to zero with the additional equations

$$\sqrt{N_i^R}(r_i = S_i^R = 0) \quad \text{and} \quad \sqrt{N_i^L}(l_i = S_i^L = 0) \quad (\text{A.33})$$

with very low weights $N_i^{L,R} = 10^{-3}$. Following Sec. A.1, with $a = (r_0, \dots, r_{15}, l_0, \dots, l_{15})$ and the rows of X and Y formed from Eqs. A.31 and A.33, we obtain from Eq. A.4 the block matrix equation

$$\begin{pmatrix} A & B \\ C & D \end{pmatrix} \begin{pmatrix} l \\ r \end{pmatrix} = \begin{pmatrix} E \\ F \end{pmatrix} \quad (\text{A.34})$$

with components

$$\begin{aligned} A_{ij} &= \delta_{ij}(\sum_k N_{ik} + N_i^R), & B_{ij} &= -N_{ij}, & E_i &= \sum_k N_{ik} S_{ik} + N_i^R S_i^R, \\ D_{ij} &= \delta_{ij}(\sum_k N_{kj} + N_j^L), & C_{ij} &= -N_{ji}, & F_i &= \sum_k N_{kj} S_{kj} + N_j^L S_j^L, \end{aligned} \quad (\text{A.35})$$

which can be solved for the offsets l_i and r_i .

This procedure was used by the ROOT macro `tmt_offsets.C` to calculate the

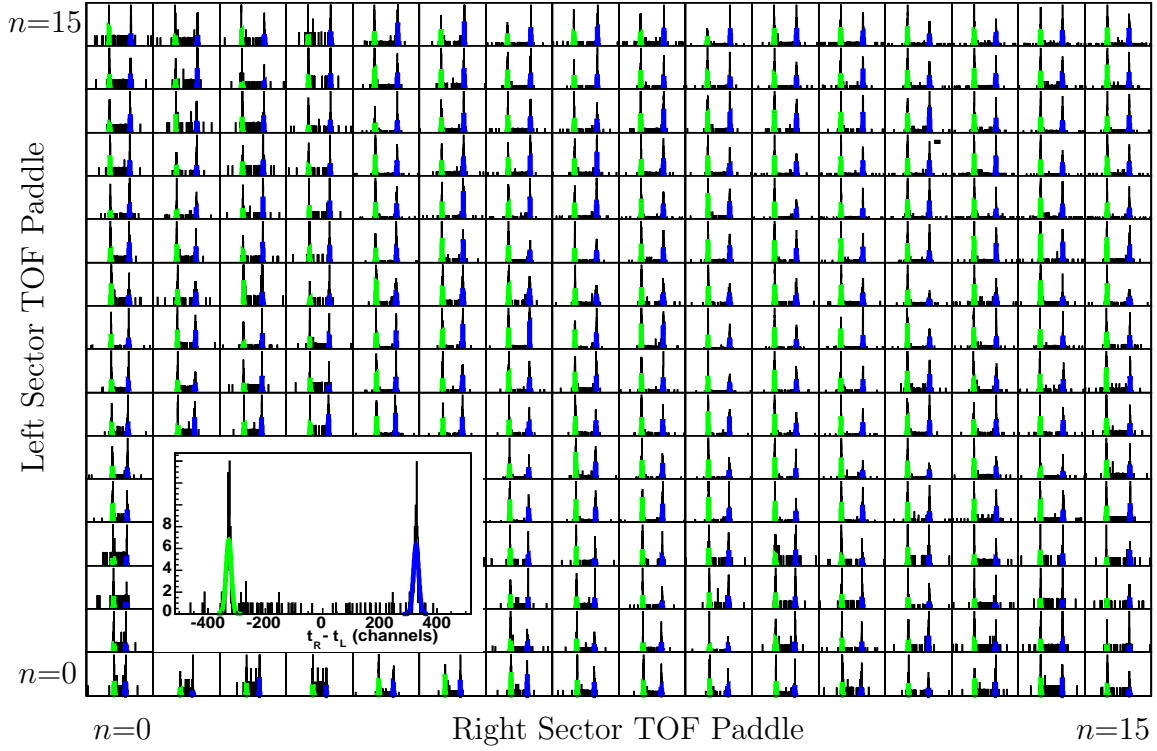


Figure A-2: Timing histograms of $t_i^R - r_j^L$ for left/right sector TOF paddle combinations from the set of cosmic runs 12865–12871. The left and right peaks correspond to particles traveling toward the left and right sectors, respectively. The spectrum of $t_{11}^R - t_{11}^L$ is enlarged in the inset.

timing offsets. The grid of peaks for each TOF paddle combination from one such calibration is shown in Fig. A-2. The RMS width of the peaks L_{ij} and R_{ij} and also the residual of the peaks $S_{ij} - (r_i - l_j)$ are histogrammed in Fig. A-3. From the latter, the uncertainty in the offsets calibration is less than 1 channel (50 ps), much better than than the timing resolution of the scintillators.

This method could be improved to calibrate each physics run from the cosmic rays in data itself. The cosmic coincidence signal is present in the data, but is washed out by the background shower events. It could be filtered using wire chamber information and strengthened by histogramming coincidences from one paddle on the left with all combinations of paddles on the right, corrected for the distance between each paddle. In this way, one could iterate between left and right sectors to improve the offset calibrations.

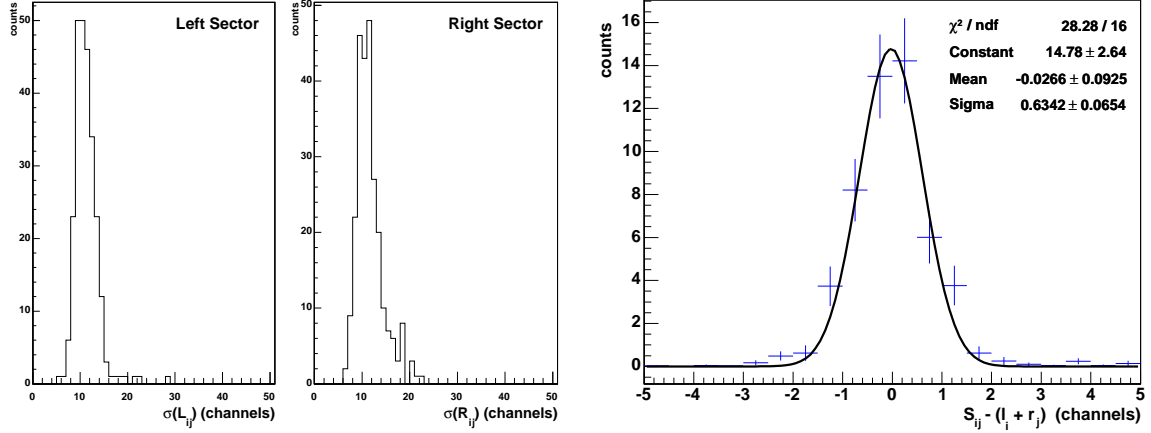


Figure A-3: left: Histogram of the widths of the left and right peaks from Fig. A-2. right: Difference of peaks S_{ij} from the expected values $r_i - l_j$ in channels. The width is the uncertainty of the offsets.

A.2.2 Elastic Coplanarity

The positional offsets of the TOFs can be calibrated using the same formalism as above with a few minor changes. The distribution of $p_i^R + p_j^L$ from elastic ep scattering events has a single coplanarity peak $S_{ij} \approx 0$. The peak is fit on top of a triangular background arising from the uniform distribution in p_i^R and p_i^L of accidental events. Letting r_i and l_i now be the positional offsets, Eq. A.31 becomes

$$\sqrt{N_{ij}}(S_{ij} = r_i + l_j), \quad (\text{A.36})$$

where N_{ij} is the number of events in each coplanarity peak. Thus the only change necessary in the formalism is $l_j \rightarrow -l_j$.

Only the paddle combinations along the elastic ridge have coplanarity peaks, but there are still enough good combinations to determine all offsets except for a global offset which can be interpreted as a rotation of the whole detector about the beamline. The global offset is determined setting S_i^R and S_i^L of Eq. A.33 to the mean of the distribution of p_n^s in each scintillator. The positional offsets were calibrated to better than 1 cm by the ROOT macro `pos_offsets.C` using this technique.

A.3 Drift Chamber Time-to-Distance Function

The drift chambers are calibrated by determining both the position and the time-to-distance (T2D) function of each sense wire (Sec. 2.3.2). The T2D function translates the TDC value for a hit into the distance the track passed from the wire. It is double-valued because one cannot determine which side of the wire the track passed without information from the other hits. For simplicity of reconstruction, the distance is defined to be in the direction of x_w , which is not perpendicular to the wire due to the 5° stereo angle. It is not even measured from the point where the ions originated because the ion drift angle is shifted by the BLAST magnetic field. The function is linear over the cell except at the fringes and within ~ 4 mm of the wire, where the velocity increases due to the stronger electric field. Three independent methods have been used to parametrize and calibrate the T2D function, and each method is described below.

A.3.1 Garfield Simulation

The T2D function was determined independent of the data using a Garfield simulation. First, the electric field in the cell was calculated from the voltages of the field, sense and guard wires. The ion velocity at each point in the cell was calculated from the electric and magnetic fields, and the gas mixture properties using the code `magboltz`. Isochrone contours were calculated by numerical integrations of the ion velocity in steps of 25 ns up to 1750 ns for initial directions outward from wire 15° apart. The distance along x_w could then be calculated geometrically for tracks with different impact angles tangent to the each TDC isochrone, as illustrated in Fig. A-4.

The T2D function calculated in this manner was parameterized by a fifth order polynomial for $t < 200$ ns and matched smoothly to a linear function at $t > 200$ ns. The coefficients were tabulated for values of the BLAST field between -4000 G and 4000 G in steps of 1000 G and for tracks with incident angles between -60° and 60° in steps of 15° with respect to the cell. During reconstruction, the T2D function was linearly interpolated to the actual magnetic field and impact angle. The only

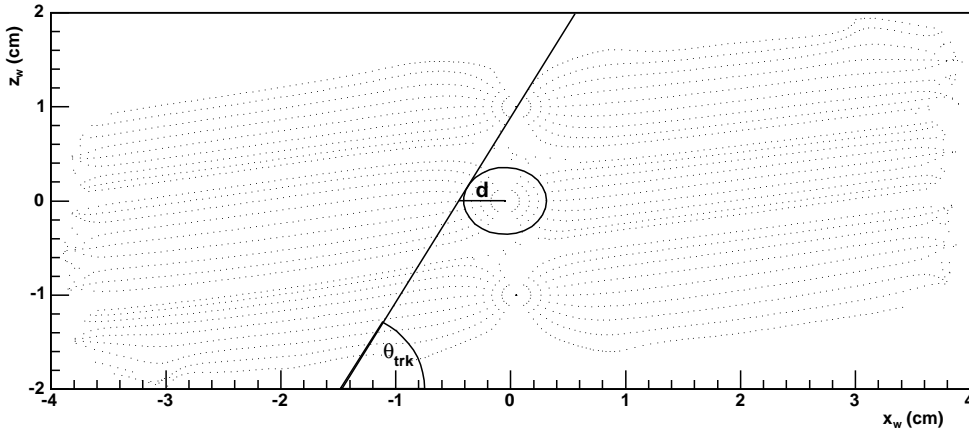


Figure A-4: Illustration of the Garfield simulation of the time-to-distance function. A track with incident angle θ_{trk} is shown tangent to the $t = 100$ ns isochrone along with the distance d returned by the T2D function.

parameters which needed calibrated were t_0 , the TDC value for which $d = 0$, and the position of the wire. The T2D function was also scaled by an empirical factor to correct for the observed ion velocity in the drift chambers.

A.3.2 Iterative Relaxation Method

The T2D function was also determined empirically [155] by an iterative relaxation method similar to the implementation used to calibrate the CLAS drift chambers at JLab [149, §3.2.2]. Tracks in the data were first reconstructed using a zeroth order T2D function. Then an improved T2D function was calculated from the distances of the simulated tracks to the wire. In each iteration, the simulated distance was histogrammed versus the TDC value of the hit, and fit to a 9th order polynomial, which was used as the T2D function in the next iteration. The approximate linear dependence of the T2D function was subtracted for convenience. After four iterations, the T2D functions relaxed to a self-consistent calibration with 20–22 MeV/c momentum resolution for the electrons. This calibration was used in reconstruction of the production ntuples for the BLAST data.

A.3.3 Least Squares Linear Calibration

The goal of the third method was to calibrate all T2D functions consistently using geometrical correlations between hits in the data. By making linear approximations, the T2D coefficients can be fit directly using the techniques of Sec. A.1. This works well because the tracks are essentially linear within each cell, and the T2D function is also linear across the whole cell except close to the wire.

The T2D function, shown in Fig. A-5, can be approximated in the linear region by

$$x = x_0 \pm d = u + vt, \quad (\text{A.37})$$

where v is the drift velocity, u is an offset, x_0 is the position of the wire in the WC coordinates, and \pm specifies which side of the wire the track passed. In one cell, there are three wires each with separate u and v coefficients on each side of the wire. Thus there are 12 coefficients per cell that must be calibrated.

Close to the wire, the slope becomes steeper,

$$d = w(t_0 - t), \quad (\text{A.38})$$

where the TDC offset t_0 is the maximum physical TDC channel, as the TDCs were run in common stop mode. The smooth transition between these two asymptotes is done with a hyperbola

$$d - d_c = \alpha(t_c - t) - \sqrt{\beta^2(t_c - t)^2 + \gamma^2}, \quad (\text{A.39})$$

where $\alpha = \frac{1}{2}(w + v)$, $\beta = \frac{1}{2}(w - v)$, and $\gamma \approx 0.105$ cm, illustrated in Fig. A-5. The point (t_c, d_c) is at the intersection of the two asymptotes,

$$t_c = \frac{wt_0 \pm (u - x_0)}{w - v} \quad \text{and} \quad d_c = w(t_0 - t_c). \quad (\text{A.40})$$

In the linear region of the cell, u and v are fitted by requiring the three hits of a stub to line up, as in Fig. A-6. This could be done by minimizing $\chi^2 = (x_0 - 2x_1 + x_2)^2$

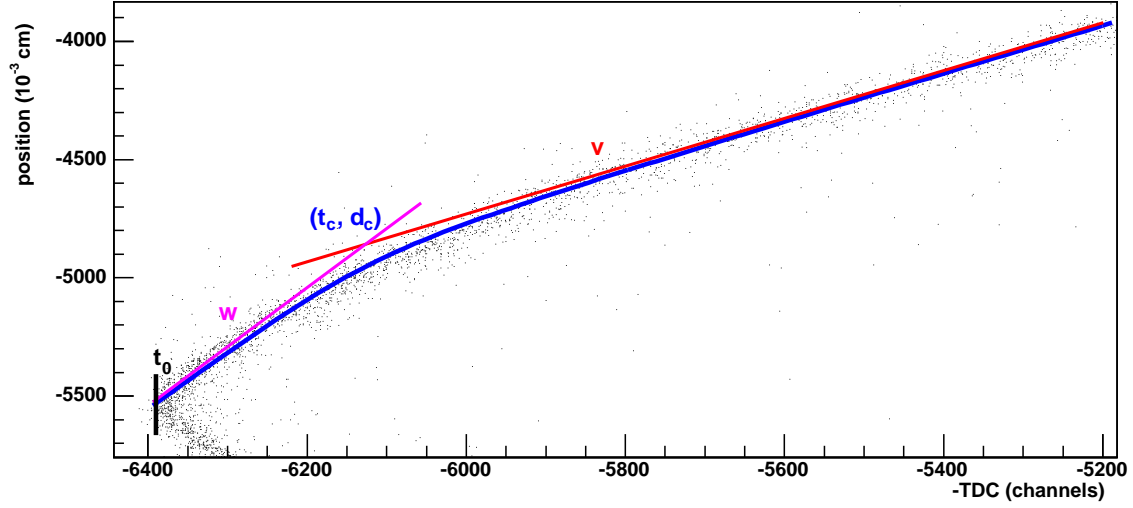


Figure A-5: Hyperbolic parametrization of the time-to-distance function. The function extends linearly to ≈ -2000 channels (4 cm from the wire).

(Sec. A.1.2). Fixing v to a constant and substituting for x_i ,

$$(u_0 - 2u_1 + u_2) + v(t_0 - 2t_1 + t_2) = 0. \quad (\text{A.41})$$

One could histogram $t_0 - 2t_1 + t_2$ and fit for the peak, giving a linear constraint on u_i . However, all three hits are linear only in a small region of the cell, especially for tracks with a low incident angle θ_{trk} , and tracks passing between the three wires.

More data can be used by considering two hits and the new variable $s \equiv \Delta z / \tan \theta_{trk}$, where Δz is the distance between the two wires labeled i and j . In this case, there are six different regions of linear stubs in a cell, as shown in Fig. A-6. Each region overlaps with the next so that they are connected across the cell, which signifies that there are enough constraints from all stub types to provide a non-degenerate solution of the calibration parameters.

If a two-hit stub lines up with the incident track angle, it satisfies the relation

$$s = \Delta x \equiv x_i - x_j \quad (\text{A.42})$$

$$= \Delta u + \Delta vt \quad (\text{A.43})$$

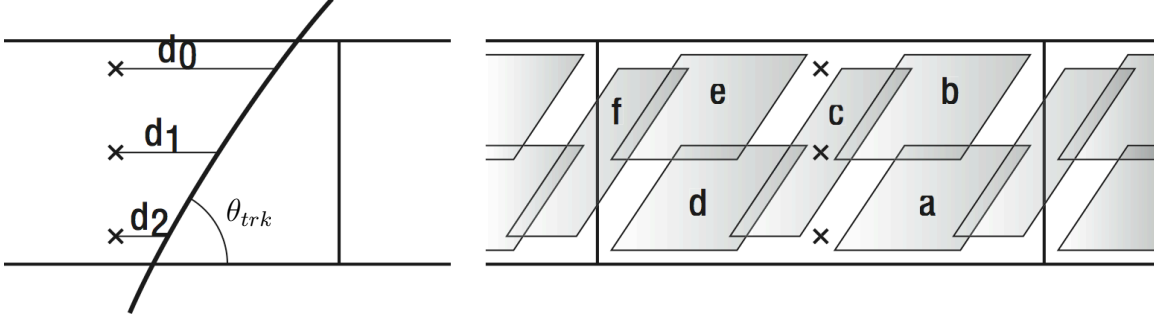


Figure A-6: Stub types used in linear calibration of the T2D function. Stub types (c) and (f) involve the two outside wires only, and are important for relating the coefficients on each side of the wire or cell boundary.

$$= \Delta u + \frac{1}{2}\Sigma t \Delta v + \frac{1}{2}\Delta t \Sigma v, \quad (\text{A.44})$$

where $\Sigma t = t_i + t_j$ and $\Delta t = t_i - t_j$, etc. This equation of a plane in $(\Sigma t, \Delta t, s)$ can be fit to the stub data for the offset Δu and the two slopes Δv and Σv using the method of Sec. A.1.1. The three fitted parameters $\langle \Delta u \rangle$, $\langle \Delta v \rangle$, $\langle \Sigma v \rangle$ provide equations to solve for the the calibration coefficients u_k , v_k . The dependence of the offset on the velocities is minimized by centering the projection over the centroid $\langle \Delta t \rangle$, $\langle \Sigma t \rangle$ of the stub data. At these coordinates, the value of s on the fitted plane is

$$\langle s \rangle \equiv \langle \Delta u \rangle + \frac{1}{2}\langle \Sigma t \rangle \langle \Delta v \rangle + \frac{1}{2}\langle \Delta t \rangle \langle \Sigma v \rangle \quad (\text{A.45})$$

After centering the offset, the three constraints per stub type are

$$\langle s \rangle = \Delta u + \frac{1}{2}\langle \Sigma t \rangle \Delta v + \frac{1}{2}\langle \Delta t \rangle \Sigma v, \quad (\text{A.46})$$

$$\langle \Delta v \rangle = \Delta v, \quad \text{and} \quad \langle \Sigma v \rangle = \Sigma v. \quad (\text{A.47})$$

The offset can be fit to better precision than the two velocities. These 18 equations per cell are linear in u_k , v_k and the least squares solution gives the calibration coefficients which do the best job of lining up each stubs in the cells. Note that the difference of Eq. A.42 from stub types (a) and (b) or types (d) and (e) is equivalent to Eq. A.43. In the calibration code, Δt is actually fit as a function of s and Σt , but the results

are the same.

Now that the stubs are evenly spread across the cell, they must be pegged down at the crossing point of each wire. We must do this using the linear region of the T2D function in order to get relations in u_k, v_k . This is done by extrapolating Eq. A.37 to the wire crossing using the TDC of the stub hit which is still in the linear region, as

$$x_i^w = u_i + v_i(t_j^w + \langle \Delta t \rangle), \quad (\text{A.48})$$

where the x^w is the coordinate of the wire crossed by the stub, t^w is the TDC value at the vertex of the other hit in the stub (Fig. A-7), and $\langle \Delta t \rangle$ is the average difference between the two TDCs, as determined above.

The nonlinear part of the T2D function is characterized by fitting the TDC pairs of stubs near the vertex where they cross over the wire, again using the method of Sec. A.1.1. Each side of the vertex is fit to a straight line and the vertex is calculated from the intersection of the two lines, as illustrated in Fig. A-7. The vertex coordinates (t_w, t_0) and slope on each side of the vertex complete the calibration of the hyperbolic T2D function of Eq. A.39. The velocity w in the hyperbolic function is the product of the slope at the vertex and the velocity v of the stub hit which is in the linear region.

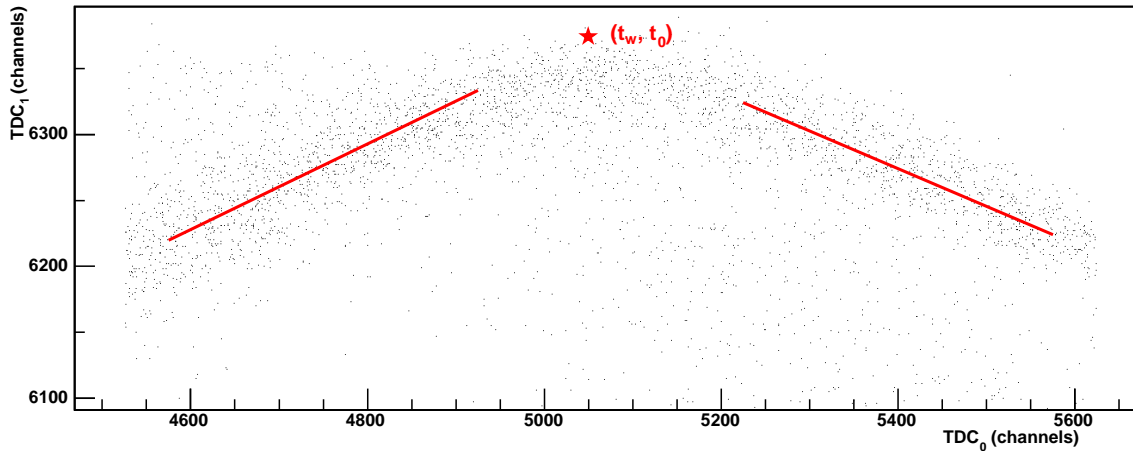


Figure A-7: Fit to the vertex of a stub crossing the wire.

This calibration method was tested against the Garfield simulation of T2D coefficients in a small forward region of the left sector drift chamber spanning two cell boundaries in each superlayer. A dramatic improvement was seen in both the momentum resolution and in the χ^2 of the track fit, shown in Fig. A-8. Compared to the Garfield calibration, the momentum resolution was reduced from 28 MeV/c to 12 MeV/c, and χ^2/ν improved from 78 to 33, in units of the 200 μm intrinsic wire resolution. Thus the effective tracking wire resolution is still on the order of 1 mm.

This calibration is being completed for all drift chamber cells. Future improvements include: adding fitted peaks from line segments, (which must be linearized), imposing a uniform hit distribution across the wire, a relative alignment of each chamber using straight cosmic tracks and hydrogen data taken with the BLAST field off, and adding ϕ and B dependence to the calibration. This method can also be iterated with either the Garfield simulation or relaxation method to account for the small variations in the T2D function from the pure hyperbolic form. Work is under way to complete the wire chamber calibration using this method.

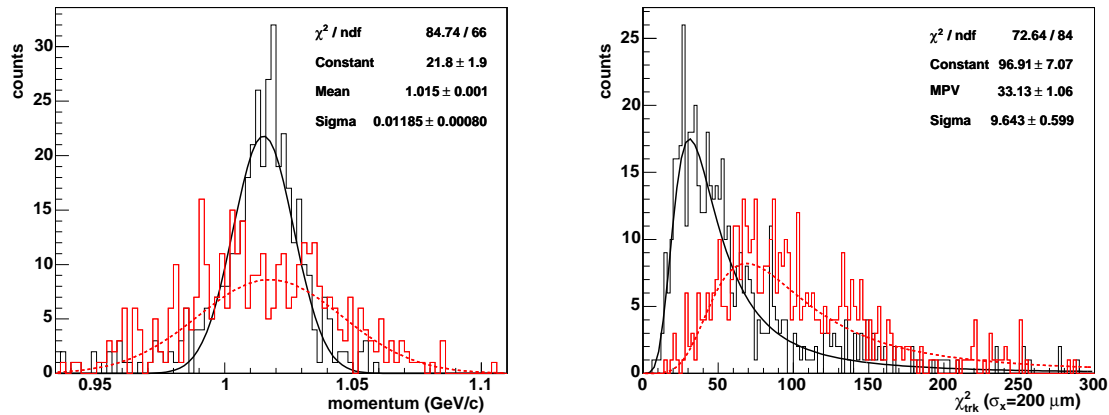


Figure A-8: Test of reconstruction in a small forward region of the left sector drift chamber using the hyperbolic T2D functions (solid black) compared to the Garfield simulation (dashed red curve). The momentum resolution (left panel) and χ^2/ν from the track fit (right panel) both improved by a factor of 2.

Appendix B

Cross Section Data

Q_c^2 (GeV ²)	Q^2 (GeV ²)	E (GeV)	E_p (GeV)	θ (°)	ϵ (1)	σ (nb/sr)	$\delta\sigma$ (nb/sr)	σ_R (1)	Ref.
(0.162)	0.1172	0.8150	0.7525	25.25	0.9061	1847	54.69	0.50478	[34]
	0.1194	0.6050	0.5414	35.15	0.8282	861.2	25.94	0.47276	[34]
	0.1555	0.3680	0.2851	75.00	0.4485	98.91	3.956	0.33715	[38]
	0.1557	0.2590	0.1760	134.99	0.0759	22.64	0.883	0.17085	[38]
	0.1558	0.5590	0.4760	45.00	0.7362	355.5	13.86	0.47894	[38]
0.191	0.1792	0.6030	0.5075	45.00	0.7350	268.1	10.99	0.42083	[38]
	0.1793	0.3510	0.2554	90.00	0.3224	48.33	2.368	0.26316	[38]
	0.1794	0.2820	0.1864	134.99	0.0755	19.74	0.7897	0.18132	[38]
	0.1794	0.2970	0.2014	119.99	0.1369	24.06	1.203	0.19478	[38]
	0.1794	0.3990	0.3034	75.00	0.4469	76.51	3.061	0.30999	[38]
	0.1794	0.4740	0.3784	60.00	0.5880	129.8	5.842	0.35363	[38]
	0.1795	0.2750	0.1794	144.99	0.0452	16.84	0.6738	0.16463	[38]
	0.1944	0.2960	0.1924	134.99	0.0752	18.38	0.9191	0.18876	[38]
	0.1945	0.7840	0.6803	35.15	0.8253	398.7	11.96	0.43793	[34]
	0.1947	0.4180	0.3142	75.00	0.4459	73.13	3.656	0.33905	[38]
	0.1947	0.6900	0.5863	40.59	0.7760	294.8	14.44	0.43338	[38]
0.1952	1.0640	0.9600	25.25	0.9042	835.3	25.82	0.46776	[34]	
0.232	0.2335	0.3310	0.2066	134.99	0.0745	12.85	0.5141	0.17213	[38]
	0.2335	0.4640	0.3395	75.00	0.4433	48.97	2.498	0.28785	[38]
	0.2336	0.6900	0.5655	45.52	0.7271	176.3	8.813	0.40555	[38]
	0.2339	0.5500	0.4253	60.00	0.5845	85.7	3.514	0.33771	[38]
	0.2350	7.0010	6.8760	4.00	0.9974	30040	842.6	0.46146	[40]

Table B.1: World data used for the extraction of G_E and G_M .

Q_c^2 (GeV ²)	Q^2 (GeV ²)	E (GeV)	E_p (GeV)	θ (°)	ϵ (1)	σ (nb/sr)	$\delta\sigma$ (nb/sr)	σ_R (1)	Ref.
0.282	0.2721	0.3640	0.2190	134.99	0.0738	9.68	0.3872	0.16158	[38]
	0.2725	0.4340	0.2888	95.00	0.2804	19.15	0.9573	0.20178	[38]
	0.2726	0.4489	0.3036	90.00	0.3170	23.55	0.5768	0.22785	[18]
	0.2726	0.4489	0.3036	90.00	0.3170	25.12	0.6153	0.24304	[18]
	0.2726	1.5777	1.4324	20.00	0.9372	762.8	16.02	0.37279	[32]
	0.2728	0.3560	0.2106	144.99	0.0441	9.043	0.4521	0.16180	[38]
	0.2728	0.6000	0.4546	60.00	0.5820	63.96	2.622	0.30048	[38]
	0.2730	0.5080	0.3625	75.00	0.4408	37.24	1.49	0.26483	[38]
	0.2915	0.3800	0.2247	134.99	0.0734	8.812	0.3525	0.16542	[38]
	0.2916	0.3990	0.2436	119.99	0.1334	10.5	0.5251	0.17338	[38]
	0.2916	0.5280	0.3726	75.00	0.4396	32.16	1.319	0.25915	[38]
	0.2922	0.6240	0.4683	60.00	0.5807	55.56	2.278	0.29781	[38]
0.2923	0.4680	0.3123	90.00	0.3159	20.55	1.048	0.22624	[38]	
0.345	0.3112	0.3960	0.2302	134.99	0.0731	7.755	0.3102	0.15489	[38]
	0.3113	0.3870	0.2211	144.99	0.0437	7.392	0.3696	0.15834	[38]
	0.3113	0.6470	0.4811	60.00	0.5795	46.61	2.33	0.24835	[38]
	0.3115	0.6900	0.5240	55.30	0.6260	56.01	2.801	0.25422	[38]
	0.3116	0.5490	0.3829	75.00	0.4383	27.83	1.085	0.22724	[38]
	0.3122	1.3640	1.1977	25.25	0.9015	358.1	8.927	0.31815	[34]
	0.3498	0.6920	0.5056	60.00	0.5771	36.94	1.884	0.24941	[38]
	0.3500	0.5880	0.4015	75.00	0.4358	22.06	0.8823	0.22742	[38]
	0.3503	0.4270	0.2403	134.99	0.0724	6.458	0.2583	0.16074	[38]
0.419	0.3890	0.8480	0.6407	50.06	0.6738	45.62	0.9317	0.23026	[34]
	0.3891	0.7360	0.5287	60.00	0.5746	30.66	1.226	0.22402	[38]
	0.3891	1.2490	1.0416	31.74	0.8478	131.6	2.577	0.25326	[34]
	0.3892	1.1420	0.9346	35.15	0.8178	107.4	2.188	0.25731	[34]
	0.3892	1.2310	1.0236	32.27	0.8433	130	2.58	0.25936	[34]
	0.3893	0.4570	0.2495	134.99	0.0717	5.123	0.2049	0.14506	[38]
	0.3894	0.4470	0.2395	144.99	0.0428	4.69	0.2345	0.14257	[38]
	0.3894	0.5560	0.3485	90.26	0.3084	11.71	0.2287	0.18485	[34]
	0.3894	0.5570	0.3495	90.00	0.3105	11.82	0.5792	0.18562	[38]

Q_c^2 (GeV ²)	Q^2 (GeV ²)	E (GeV)	E_p (GeV)	θ (°)	ϵ (1)	σ (nb/sr)	$\delta\sigma$ (nb/sr)	σ_R (1)	Ref.
0.419	0.3894	0.5570	0.3495	90.00	0.3105	11.95	0.2927	0.18766	[18]
	0.3894	0.9000	0.6925	46.56	0.7086	59.11	2.896	0.25712	[38]
	0.3894	1.9035	1.6960	20.00	0.9354	408.9	8.996	0.29244	[32]
	0.3894	3.6850	3.4775	10.00	0.9833	1751	29.03	0.28853	[36]
	0.3895	0.6960	0.4884	64.72	0.5286	25.14	0.4075	0.21402	[34]
	0.3897	0.6270	0.4193	75.00	0.4333	17.65	0.7235	0.19977	[38]
	0.3898	0.4790	0.2713	119.99	0.1305	6.218	0.3109	0.15293	[38]
	0.3903	1.5370	1.3290	25.25	0.8997	226.5	4.559	0.26844	[34]
	0.4253	3.1187	2.8921	12.47	0.9700	887.7	10.02	0.28048	[46]
	0.4280	0.4860	0.2579	134.99	0.0711	4.326	0.173	0.14901	[38]
	0.4282	0.9500	0.7218	46.55	0.7067	48.05	2.403	0.25740	[38]
	0.4287	0.6640	0.4356	75.00	0.4309	14.38	0.7046	0.20034	[38]
0.500	0.4671	0.9500	0.7011	49.51	0.6749	33.12	1.689	0.20884	[38]
	0.4672	0.9000	0.6510	53.04	0.6393	27.62	1.381	0.20142	[38]
	0.4674	0.5040	0.2549	144.99	0.0420	3.24	0.162	0.13168	[38]
	0.4675	0.5150	0.2659	134.99	0.0704	3.529	0.1765	0.13337	[38]
	0.4677	0.7000	0.4508	75.00	0.4285	11.67	0.4668	0.17162	[38]
	0.4740	9.9930	9.7400	4.00	0.9972	7593	212.6	0.23845	[40]
	0.4865	0.7170	0.4577	75.00	0.4273	10.34	0.4137	0.16663	[38]
	0.4900	0.5041	0.2430	179.99	0.0000	2.483	0.06776	0.12495	[156]
	0.5061	0.9500	0.6803	52.52	0.6424	24.26	1.189	0.20900	[38]
	0.5064	0.5430	0.2732	134.99	0.0698	2.882	0.1441	0.13048	[38]
	0.5066	0.7350	0.4650	75.00	0.4261	9.32	0.3821	0.16522	[38]
	0.5072	1.7700	1.4997	25.25	0.8970	127.3	2.574	0.22684	[34]
	0.5445	0.5700	0.2798	134.99	0.0692	2.454	0.1227	0.13179	[38]
	0.5451	0.9500	0.6595	55.60	0.6090	18.17	0.9084	0.21090	[38]
	0.5452	0.9000	0.6095	59.80	0.5670	14.2	0.7383	0.19159	[38]
0.5453	0.7690	0.4784	75.00	0.4238	7.793	0.3195	0.16493	[38]	
0.5456	0.5590	0.2683	144.99	0.0413	2.347	0.1173	0.13600	[38]	

Q_c^2 (GeV ²)	Q^2 (GeV ²)	E (GeV)	E_p (GeV)	θ (°)	ϵ (1)	σ (nb/sr)	$\delta\sigma$ (nb/sr)	σ_R (1)	Ref.
0.593	0.5788	1.1710	0.8626	44.48	0.7198	23.88	0.4752	0.16779	[34]
	0.5833	0.5970	0.2862	134.99	0.0686	2.126	0.1063	0.11981	[38]
	0.5834	0.6450	0.3341	110.71	0.1700	2.969	0.06057	0.12761	[34]
	0.5837	0.8020	0.4910	75.00	0.4215	6.573	0.3352	0.14077	[38]
	0.5837	0.8860	0.5749	64.72	0.5165	9.656	0.1985	0.15373	[34]
	0.5840	0.9500	0.6388	58.75	0.5751	13.27	0.6504	0.17302	[38]
	0.5840	1.0720	0.7608	50.06	0.6630	17.69	0.3563	0.16413	[34]
	0.5841	0.7180	0.4068	90.00	0.3002	4.77	0.1345	0.14463	[18]
	0.5841	0.7180	0.4068	90.00	0.3002	4.836	0.1811	0.14663	[18]
	0.5841	1.5220	1.2107	32.70	0.8329	48.94	0.9816	0.17914	[34]
	0.5841	2.3617	2.0505	20.00	0.9324	155	4.031	0.19252	[32]
	0.5842	1.6290	1.3177	30.24	0.8545	60.86	1.19	0.18754	[34]
	0.5843	1.0420	0.7306	51.96	0.6436	16.64	0.3373	0.16747	[34]
	0.5843	1.4310	1.1196	35.15	0.8104	42.28	0.8441	0.18162	[34]
	0.5844	0.7170	0.4056	90.26	0.2982	4.504	0.08936	0.13750	[34]
	0.5844	0.8920	0.5806	64.17	0.5218	9.945	0.1983	0.15603	[34]
	0.5844	1.5400	1.2286	32.27	0.8367	51.12	0.9907	0.18197	[34]
	0.5845	0.7180	0.4065	90.07	0.2995	4.517	0.09927	0.13746	[34]
	0.5846	0.6470	0.3354	110.29	0.1721	2.926	0.06754	0.12569	[34]
	0.5847	1.9120	1.6004	25.25	0.8953	89.17	1.781	0.18512	[34]
	0.6198	2.2380	1.9077	21.97	0.9200	109.3	1.161	0.19317	[46]
	0.6200	0.5921	0.2618	179.99	0.0000	1.411	0.03613	0.11166	[156]
	0.6213	1.1492	0.8181	47.97	0.6800	17.05	0.1656	0.16885	[46]
	0.6226	0.6240	0.2922	134.99	0.0680	1.768	0.08838	0.11739	[38]
	0.6228	0.8350	0.5031	75.00	0.4192	5.483	0.2632	0.13849	[38]
	0.6229	0.9000	0.5680	67.00	0.4923	7.652	0.3902	0.15429	[38]
	0.6230	0.8020	0.4700	80.00	0.3763	5.118	0.2559	0.14668	[38]
	0.6230	0.9500	0.6180	62.00	0.5406	9.191	0.4595	0.15804	[38]
	0.6231	2.4450	2.1129	20.00	0.9318	137.1	1.636	0.19976	[47]
	0.6232	0.6120	0.2799	144.99	0.0405	1.623	0.08116	0.11640	[38]

Bibliography

- [1] S. Eidelman *et al.* (Particle Data Group), Phys. Lett. **B592**, 1 (2004).
- [2] V. Punjabi and C. F. Perdrisat, preprint (2005), nucl-ex/0501018, submitted to PRC, nucl-ex/0501018.
- [3] O. Gayou *et al.* (Jefferson Lab Hall A), Phys. Rev. Lett. **88**, 092301 (2002), nucl-ex/0111010.
- [4] A. Afanasev, I. Akushevich, and N. Merenkov, Phys. Rev. **D64**, 113009 (2001), hep-ph/0102086.
- [5] R. G. Sachs, Phys. Rev. **126**, 2256 (1962).
- [6] T. W. Donnelly and A. S. Raskin, Annals Phys. **169**, 247 (1986).
- [7] J. J. Kelly, Phys. Rev. **C66**, 065203 (2002), hep-ph/0204239.
- [8] M. N. Rosenbluth, Phys. Rev. **79**, 615 (1950).
- [9] N. Dombey, Rev. Mod. Phys. **41**, 236 (1969).
- [10] A. I. Akhiezer *et al.*, Zhurnal Eksperimental'noi i Teoreticheskoi Fiziki **33**, 765 (1957).
- [11] R. G. Arnold, C. E. Carlson, and F. Gross, Phys. Rev. **C23**, 363 (1981).
- [12] G. Hohler *et al.*, Nucl. Phys. **B114**, 505 (1976).
- [13] O. Frisch, R.; Stern, Z. Phys. **85**, 4 (1933).

- [14] P. J. Mohr and B. N. Taylor, *The 2002 CODATA Recommended Values of the Fundamental Physical Constants*, Tech. rep., National Institute of Standards and Technology (2004), <http://physics.nist.gov/constants>.
- [15] R. Hofstadter, *Rev. Mod. Phys.* **28**, 214 (1956).
- [16] M. Breidenbach *et al.*, *Phys. Rev. Lett.* **23**, 935 (1969).
- [17] W. Albrecht *et al.*, *Phys. Rev. Lett.* **17**, 1192 (1966).
- [18] L. E. Price *et al.*, *Phys. Rev.* **D4**, 45 (1971).
- [19] P. N. Kirk *et al.*, *Phys. Rev.* **D8**, 63 (1973).
- [20] H. Gao, *Int. J. Mod. Phys.* **E12**, 1 (2003), [nucl-ex/0301002](http://arxiv.org/abs/nucl-ex/0301002).
- [21] L. N. Hand, D. G. Miller, and R. Wilson, *Rev. Mod. Phys.* **35**, 335 (1963).
- [22] I. J. J. Murphy, Y. M. Shin, and D. M. Skopik, *Phys. Rev.* **C9**, 2444 (1974).
- [23] F. Borkowski *et al.*, *Nucl. Phys.* **A222**, 269 (1974).
- [24] F. Borkowski *et al.*, *Nucl. Phys.* **B93**, 461 (1975).
- [25] G. G. Simon *et al.*, *Nucl. Phys.* **A333**, 381 (1980).
- [26] H. Gao and J. Calarco, *Precise Determination of the Proton Charge Radius*, Tech. rep., Bates Linear Accelerator Center (2004), experiment E00-02; This experiment was conditionally approved, but not completed before BLAST funding ended.
- [27] P. Mergell, U. G. Meissner, and D. Drechsel, *Nucl. Phys.* **A596**, 367 (1996), [hep-ph/9506375](http://arxiv.org/abs/hep-ph/9506375).
- [28] I. Sick, *Phys. Lett.* **B576**, 62 (2003), [nucl-ex/0310008](http://arxiv.org/abs/nucl-ex/0310008).
- [29] F. Kottmann, F. Biraben, and C. A. N. C. *et al.*, in G. Cantatore, ed., *Quantum Electrodynamics and Physics of the Vacuum, QED 2000 Second Workshop Proceedings*, N. Y. (2001), vol. 564, p. 13.

- [30] R. C. Walker *et al.*, Phys. Rev. **D49**, 5671 (1994).
- [31] J. Arrington, Phys. Rev. **C68**, 034325 (2003), nucl-ex/0305009.
- [32] M. Goitein *et al.*, Phys. Rev. **D1**, 2449 (1970).
- [33] K. M. Hanson *et al.*, Phys. Rev. **D8**, 753 (1973).
- [34] C. Berger *et al.*, Phys. Lett. **B35**, 87 (1971).
- [35] W. Bartel *et al.*, Nucl. Phys. **B58**, 429 (1973).
- [36] W. Bartel *et al.*, Phys. Rev. Lett. **17**, 608 (1966).
- [37] W. Albrecht *et al.*, Phys. Rev. Lett. **18**, 1014 (1967).
- [38] T. Janssens *et al.*, Phys. Rev. **142**, 922 (1966).
- [39] J. Litt *et al.*, Phys. Lett. **B31**, 40 (1970).
- [40] S. Stein *et al.*, Phys. Rev. **D12**, 1884 (1975).
- [41] S. Rock *et al.*, Phys. Rev. **D46**, 24 (1992).
- [42] P. Bosted *et al.*, Phys. Rev. **C42**, 38 (1990).
- [43] A. F. Sill *et al.*, Phys. Rev. **D48**, 29 (1993).
- [44] L. Andivahis *et al.*, Phys. Rev. **D50**, 5491 (1994).
- [45] D. Dutta *et al.* (JLab E91013), Phys. Rev. **C68**, 064603 (2003), nucl-ex/0303011.
- [46] M. E. Christy *et al.* (E94110), Phys. Rev. **C70**, 015206 (2004), nucl-ex/0401030.
- [47] M. I. Niculescu, *Inclusive Resonance Electroproduction Data From Hydrogen and Deuterium: Studies of Quark Hadron Duality*, Ph.D. thesis, Hampton University (1999), experiment E94-110.
- [48] I. A. Qattan *et al.*, preprint (2004), nucl-ex/0410010.

- [49] M. J. Alguard *et al.*, Phys. Rev. Lett. **37**, 1258 (1976).
- [50] B. D. Milbrath *et al.* (Bates FPP), Phys. Rev. Lett. **80**, 452 (1998), nucl-ex/9712006.
- [51] T. Pospischil *et al.* (A1), Eur. Phys. J. **A12**, 125 (2001).
- [52] M. K. Jones *et al.* (Jefferson Lab Hall A), Phys. Rev. Lett. **84**, 1398 (2000), nucl-ex/9910005.
- [53] O. Gayou *et al.*, Phys. Rev. **C64**, 038202 (2001).
- [54] D. Eyl *et al.*, Z. Phys. **A352**, 211 (1995).
- [55] S. Dieterich *et al.*, Phys. Lett. **B500**, 47 (2001), nucl-ex/0011008.
- [56] P. E. Bosted, Phys. Rev. **C51**, 409 (1995).
- [57] E. J. Brash *et al.*, Phys. Rev. **C65**, 051001 (2002), hep-ex/0111038.
- [58] J. Arrington, Phys. Rev. **C69**, 022201 (2004), the world cross section data used for fits in this paper are available on the web at http://www.jlab.org/resdata/resdata_protonff.txt, nucl-ex/0309011.
- [59] J. J. Kelly, Phys. Rev. **C70**, 068202 (2004).
- [60] J. Friedrich and T. Walcher, Eur. Phys. J. **A17**, 607 (2003), hep-ph/0303054.
- [61] D. R. Yennie, in R. Hofstadter and L. I. Schiff, eds., *Nucleon structure; proceedings of the international conference at Stanford University* (June 24-27 1963).
- [62] L. W. Mo and Y.-S. Tsai, Rev. Mod. Phys. **41**, 205 (1969).
- [63] L. C. Maximon and J. A. Tjon, Phys. Rev. **C62**, 054320 (2000), nucl-th/0002058.
- [64] J. Arrington and I. Sick, Phys. Rev. **C70**, 028203 (2004), nucl-ex/0406014.

- [65] P. A. M. Guichon and M. Vanderhaeghen, Phys. Rev. Lett. **91**, 142303 (2003), hep-ph/0306007.
- [66] J. Arrington, Phys. Rev. **C71**, 015202 (2005), hep-ph/0408261.
- [67] M. P. Rekalo and E. Tomasi-Gustafsson, preprint (2003), nucl-th/0307066.
- [68] P. G. Blunden, W. Melnitchouk, and J. A. Tjon, Phys. Rev. Lett. **91**, 142304 (2003), nucl-th/0306076.
- [69] Y. C. Chen, A. Afanasev, S. J. Brodsky, C. E. Carlson, and M. Vanderhaeghen, Phys. Rev. Lett. **93**, 122301 (2004), hep-ph/0403058.
- [70] A. Afanasev *et al.*, in P. S. A. Radyushkin, ed., *Exclusive Processes At High Momentum Transfer: Proceedings* (World Scientific, 2002), hep-ph/0208260.
- [71] J. Arrington *et al.*, *A Measurement of Two-Photon Exchange in Unpolarized Elastic Electron-Proton Scattering.*, Tech. rep., TJNAF (2005), experiment Proposal PR-05-017.
- [72] R. Gilman *et al.*, *Measurement of the Two-Photon Exchange Contribution in ep Elastic Scattering Using Recoil Polarization*, Tech. rep., TJNAF (2004), experiment E-04-019.
- [73] J. Arrington, Phys. Rev. **C69**, 032201 (2004), nucl-ex/0311019.
- [74] J. Arrington *et al.*, preprint (2004), nucl-ex/0408020.
- [75] A. Afanasev *et al.*, *Beyond the Born Approximation: A Precise Comparison of Positron-Proton and Electron-Proton Elastic Scattering in CLAS*, Tech. rep., TJNAF (2004), experiment E-04-116.
- [76] E. J. Beise, M. L. Pitt, and D. T. Spayde, Prog. Part. Nucl. Phys. **54**, 289 (2005), nucl-ex/0412054.
- [77] F. E. Maas *et al.* (A4), Phys. Rev. Lett. **93**, 022002 (2004), nucl-ex/0401019.

- [78] D. Mack *et al.*, *Measurements of Target Single-Spin Asymmetry in Elastic ep Scattering*, Tech. rep., TJNAF (2004), experiment Proposal PR-04-008.
- [79] D. Mack *et al.*, *Measurement of the Born-Forbidden Recoil Proton Normal Polarization in Electron-Proton Elastic Scattering*, Tech. rep., TJNAF (2004), experiment Proposal PR-04-009.
- [80] S. P. Wells *et al.*, *Measuring the Two-Photon Exchange Amplitude with Vector Analyzing Powers in Elastic Electron-Proton Scattering*, Tech. rep., TJNAF (2004), experiment Proposal PR-04-103.
- [81] J. Ashman *et al.* (European Muon), *Phys. Lett.* **B206**, 364 (1988).
- [82] S. J. Brodsky and G. R. Farrar, *Phys. Rev.* **D11**, 1309 (1975).
- [83] G. P. Lepage and S. J. Brodsky, *Phys. Lett.* **B87**, 359 (1979).
- [84] A. V. Belitsky, X.-D. Ji, and F. Yuan, *Phys. Rev.* **D69**, 074014 (2004), hep-ph/0307383.
- [85] J. P. Ralston and P. Jain, *Phys. Rev.* **D69**, 053008 (2004), hep-ph/0302043.
- [86] G. A. Miller, *Phys. Rev.* **C66**, 032201 (2002), nucl-th/0207007.
- [87] G. A. Miller, in P. S. A. Radyushkin, ed., *Exclusive Processes At High Momentum Transfer: Proceedings* (World Scientific, 2002), nucl-th/0206027.
- [88] F. Cardarelli and S. Simula, *Phys. Rev.* **C62**, 065201 (2000), nucl-th/0006023.
- [89] M. R. Frank, B. K. Jennings, and G. A. Miller, *Phys. Rev.* **C54**, 920 (1996), nucl-th/9509030.
- [90] G. Holzwarth, *Z. Phys.* **A356**, 339 (1996), hep-ph/9606336.
- [91] R. F. Wagenbrunn, S. Boffi, W. Klink, W. Plessas, and M. Radici, *Phys. Lett.* **B511**, 33 (2001), nucl-th/0010048.
- [92] E. L. Lomon, *Phys. Rev.* **C64**, 035204 (2001), nucl-th/0104039.

- [93] O. Gayou, *Measurement of the proton form factor ratio $\mu_p G_{Ep}/G_{Mp}$ up to $Q^2 = 5.6 \text{ GeV}^2$ by recoil polarimetry*, PhD dissertation, Université Blaise Pascal (Apr. 2002).
- [94] P. L. Chung and F. Coester, *Phys. Rev.* **D44**, 229 (1991).
- [95] F. Schlumpf, *Phys. Rev.* **D47**, 4114 (1993), hep-ph/9212250.
- [96] G. A. Miller and M. R. Frank, *Phys. Rev.* **C65**, 065205 (2002), nucl-th/0201021.
- [97] P. Kroll, M. Schurmann, and W. Schweiger, *Z. Phys.* **A338**, 339 (1991).
- [98] B.-Q. Ma, D. Qing, and I. Schmidt, *Phys. Rev.* **C65**, 035205 (2002), hep-ph/0202015.
- [99] S. Boffi *et al.*, *Eur. Phys. J.* **A14**, 17 (2002), hep-ph/0108271.
- [100] W. H. Klink, *Phys. Rev.* **C58**, 3587 (1998).
- [101] D. H. Lu, S. N. Yang, and A. W. Thomas, *Nucl. Phys.* **A684**, 296 (2001).
- [102] F. Iachello, A. D. Jackson, and A. Lande, *Phys. Lett.* **B43**, 191 (1973).
- [103] M. Gari and W. Krümpelmann, *Z. Phys.* **A322**, 689 (1985).
- [104] M. Gari and W. Krümpelmann, *Phys. Lett.* **B274**, 159 (1992).
- [105] E. L. Lomon, *Phys. Rev.* **C66**, 045501 (2002), nucl-th/0203081.
- [106] H. W. Hammer, U.-G. Meissner, and D. Drechsel, *Phys. Lett.* **B385**, 343 (1996), hep-ph/9604294.
- [107] B. Kubis and U.-G. Meissner, *Nucl. Phys.* **A679**, 698 (2001), hep-ph/0007056.
- [108] G. Holzwarth and J. Klomfass, *Phys. Rev.* **D63**, 025021 (2001), hep-ph/0009061.
- [109] A. Ali Khan *et al.* (CP-PACS), *Phys. Rev.* **D65**, 054505 (2002), hep-lat/0105015.

- [110] A. W. Thomas, Nucl. Phys. Proc. Suppl. **119**, 50 (2003), hep-lat/0208023.
- [111] M. Gockeler *et al.* (QCDSF), Phys. Rev. **D71**, 034508 (2005), hep-lat/0303019.
- [112] G. V. Dunne *et al.*, Phys. Lett. **B531**, 77 (2002), hep-th/0110155.
- [113] J. D. Ashley *et al.*, Eur. Phys. J. **A19**, 9 (2004), hep-lat/0308024.
- [114] H. H. Matevosyan, G. A. Miller, and A. W. Thomas, preprint pp. nucl-th/0501044 (2005), nucl-th/0501044.
- [115] R. G. Edwards (Lattice Hadron Physics), Nucl. Phys. Proc. Suppl. **140**, 290 (2005), hep-lat/0409119.
- [116] D. Beck *et al.*, *G⁰ experiment: Forward Angle Measurements*, Tech. rep., TJNAF (2000), experiment E-00-006.
- [117] R. Carlini *et al.*, *Qweak Experiment: A Search for Physics at the TeV Scale via a Measurement of the Proton's Weak Charge*, Tech. rep., TJNAF (2000), experiment E-02-020.
- [118] K. A. Aniol *et al.* (HAPPEX), Phys. Rev. **C69**, 065501 (2004), nucl-ex/0402004.
- [119] X. Zheng *et al.*, *Measurements of G_E^p/G_M^p using elastic $\vec{p}(\vec{e}, e'p)$ up to $Q^2 = 5.6 (\text{GeV}/c)^2$* , Tech. rep., TJNAF (2004), experiment Proposal PR-04-111.
- [120] M. Farkhondeh *et al.*, in *Proceedings of the SPIN-2004 Symposium* (2004), pESP-2004 Workshop.
- [121] G. T. Zwart, *Polarized electrons at the Bates Accelerator Center South Hall Ring: Extracted beams and internal targets*, Ph.D. thesis, Boston University (1986).
- [122] T. Zwart *et al.*, in Y. I. Makdisi, A. U. Luccio, and W. W. MacKay, eds., *15th International Spin Physics Symposium* (AIP, 2002), vol. 675, p. 1011.
- [123] W. Franklin, in *Proceedings of the SPIN-2004 Symposium* (2004).

- [124] K. A. Dow, M. Farkhondeh, and J. D. Zumbro, *South Hall Ring: Magnetic Measurements of the Lattice Dipoles*, Tech. rep., Bates Linear Accelerator Center (1993).
- [125] K. B. Unser, AIP Conf. Proc. **252**, 266 (1991).
- [126] M. H. Hurwitz, *The Compton Polarimeter at Bates*, Tech. rep., Bates Linear Accelerator Center (2003).
- [127] W. Franklin *et al.*, in *Proceedings of the SPIN-2004 Conference* (2004).
- [128] V. S. Morozov *et al.*, Phys. Rev. ST Accel. Beams **4**, 104002 (2001).
- [129] R. V. Cadman *et al.*, Phys. Rev. Lett. **86**, 967 (2001).
- [130] J. Stenger *et al.*, Phys. Rev. Lett. **78**, 4177 (1997).
- [131] A. Airapetian *et al.*, Nucl. Instrum. Methods A **540**, 68 (2005).
- [132] R. V. Cadman, *Proton-Deuteron Elastic Scattering and Three-Nucleon Forces*, Ph.D. thesis, University of Illinois at Urbana-Champaign (2001).
- [133] V. Ziskin, *Measurement of the Electric Form Factor of the Neutron at low Q^2 from a Vector Polarized Deuterium Target at BLAST*, Ph.D. thesis, Massachusetts Institute of Technology (2005).
- [134] R. J. Holt *et al.*, in *Proceedings of the Eighth International Symposium on High-Energy Spin Physics, Minneapolis, 1988* (American Institute of Physics, 1989), p. 1535.
- [135] H. Gao, R. J. Holt, *et al.*, in *Proc. Int. Wkshp. on Polarized Beams and Polarized Gas Targets, Cologne, 1995* (World Scientific, 1996), p. 67.
- [136] J. Stenger *et al.*, in *Proceedings of the International Workshop on polarized beams and targets, Cologne, 1995* (World Scientific, 1997), p. 85.
- [137] C. E. Jones *et al.*, in *Proc. Int. Wkshp. on Polarized Beams and Polarized Gas Targets, Erlangen, 1999* (unpublished, 1999), p. 204.

- [138] M. A. Miller *et al.*, in *Proc. Int. Wkshp. on Polarized Gas Targets and Polarized Beams, Urbana, 1997* (American Institute of Physics, 1998), p. 148.
- [139] C. Crawford *et al.*, in V. Derenchuk and B. von Przewoski, eds., *Proc. Int. Wkshp. on Polarized Sources and Targets, Nashville, Indiana, 2001* (World Scientific, 2001), p. 78.
- [140] B. Clasić *et al.*, *Phys. Rev. Lett.* (2005), to be submitted.
- [141] T. Walker and L. W. Anderson, *Nucl. Instrum. Methods.* **334**, 313 (1993).
- [142] J. A. Fedchak *et al.*, *Nucl. Instrum. Methods A* **391**, 405 (1997).
- [143] A. Roth, *Vacuum Technology* (Elsevier Science B. V., 1990).
- [144] C. Baumgarten *et al.*, *Eur. Phys. J. D* **18**, 37 (2002).
- [145] T. C. Black, *Design of a transverse holding-field magnet for the MIT laser-driven polarized H/D target*, Tech. rep., Massachusetts Institute of Technology (1999).
- [146] J. Slevin and W. Stirling, *Rev. Sci Instrum.* **52**, 1780 (1981).
- [147] B. Collaboration, *Bates Large Acceptance Spectrometer Toroid: Technical Design Report*, Tech. rep., Bates Linear Accelerator Center (1997).
- [148] A. Goodhue, *Analysis of Measurements of the BLAST Magnetic Field*, Tech. rep., Bates Linear Accelerator Center (2002).
- [149] B. Zhang, *Searching for short range correlations using $(e, e'NN)$ reactions*, Ph.D. thesis, Massachusetts Institute of Technology (2003).
- [150] W. H. Press, S. A. Teukolsky, W. T. Vetterling, and B. P. Flannery, *Numerical Recipes in C* (Cambridge University Press, 1988).
- [151] P. Karpus, *Vector Polarization Observables of the Deuteron*, Ph.D. thesis, University of New Hampshire (2005).

- [152] B. Tonguc, in *RICH2004 Proceedings; Nucl. Instr. and Methods A* (2005).
- [153] I. Passchier, *The charge form factor of the neutron from double polarized electron-deuteron scattering*, Ph.D. thesis, Vrije Universiteit te Amsterdam (2000).
- [154] T. Ikeda *et al.*, *Nucl. Instrum. Meth.* **A401**, 243 (1997).
- [155] C. Zhang, *Tensor Analyzing Power in Elastic Electron Deuteron Scattering Below 1 GeV*, Ph.D. thesis, Massachusetts Institute of Technology (2006).
- [156] P. Bosted *et al.*, *Phys. Rev. Lett.* **68**, 3841 (1992).